



Stability, Protection and Control of Systems with High Penetration of Converter Interfaced Generation

Final Project Report

S-56

Power Systems Engineering Research Center

*Empowering Minds to Engineer
the Future Electric Energy System*



Stability, Protection and Control of Systems with High Penetration of Converter Interfaced Generation

Final Project Report

S-56

Project Team

Sakis A. P. Meliopoulos, Project Leader
Maryam Saeedifard
Georgia Institute of Technology

Vijay Vittal
Rajapandian Ayyanar
Arizona State University

Graduate Students

Yu Liu
Sanghun Choi
Evangelos Polymeneas
Georgia Institute of Technology

Deepak Ramasubramanian
Ziwei Yu
Arizona State University

PSERC Publication 16-03

March 2016

Acknowledgements

This is the final report for the Power Systems Engineering Research Center (PSERC) research project S-56 titled “Stability, Protection and Control of Systems with High Penetration of Converter-Interfaced Generation”. We express our appreciation to PSERC and the industry advisors. We also express our appreciation to RTE for their support of the project and their close collaboration in this project. We also express our appreciation for the support provided by the National Science Foundation’s Industry / University Cooperative Research Center program.

The authors wish to recognize Thibault Prevost of RTE for his contributions to the project and his guidance in discussing and formulating the issues related to systems with high penetration of renewables.

The authors wish to recognize the postdoctoral researchers and graduate students at the Georgia Institute of Technology who contributed to the research and creation of project reports:

- Yu Liu
- Sanghun Choi
- Evangelos Polymeneas

Executive Summary

The goal of this project is to evaluate the stability, protection and control of converter-interfaced generation both at the converter level and in the bulk power system. With the increased penetration of renewable energy and decommissioning of aging thermal power plants, there is a renewed focus on converter-interfaced generation. As more of these sources appear in the transmission system, the control of converters and their representation in software have to be more accurate in order to make a reliable study of the system behavior.

This research proposes a new converter model for use in positive sequence transient stability software. The questions addressed include- Does this converter model accurately represent the electromagnetic transient operation of a power electronics converter? Does the model perform robustly in commercial positive sequence time domain software? With large system simulations, is there a significant increase in computation time with the use of this converter model? Can a large system handle an increased presence of converter-interfaced generation? Will the converter models be able to provide frequency response in the event of a contingency?

Part I: Stability, Protection and Control of Systems with High Penetration of Converter Interfaced Generation

Increasing penetration of generating units that are interfaced to power grid with power electronic devices create new challenges in the protection, control and operation of the power grid. These generating units are allowed to operate at variable or non-synchronous frequencies (e.g. wind turbines), or to operate without any rotating parts (e.g. photovoltaic cells) and they are synchronized to the power grid via power electronics. We refer to these units as Converter-Interfaced Generation (CIG). The power grid operates at a fixed frequency or a regulated frequency. The power system can easily cope with a small amount of CIGs. However, in some areas of the world, the percentage of CIGs versus synchronous machines has risen to high values and it is possible to reach 100%. High penetration levels bring serious challenges to the present protection, control and operation paradigm.

The conventional power system powered by synchronous generators has the following characteristics. (a) synchronous generators are driven by mechanical torque, so the control of the speed governor can maintain load/generation balance by controlling the frequency of the synchronous generator; (b) synchronous generators have high moment of inertia, so the oscillations of frequency and phase angle are small and slow, and transient stability of the power system can be ensured. These characteristics are absent in CIGs. In conventional systems, frequency constancy means generation/load balance. In systems with 100% CIGs this concept does not exist.

Compared to the conventional power system, a power system with high penetration of CIGs will confront the following challenges. (a) There exists no mechanical torque input to the DC link of a grid side converter, thus the control of the converter output frequency is irrelevant to load/generation balancing [2-3]. Traditional control schemes, such as area control error (ACE) become meaningless in systems with 100% CIGs. (b) CIGs do not have inertia [4-5], thus the frequency and phase angle may oscillate quickly after disturbances and in this case the operational constraints of the inverters may be exceeded to the point of damaging the inverters or causing the

shutdown of the inverters. Inverters can be protected with Low Voltage Ride Through (LVRT) function. However, in a system with high penetration of CIGs, the LVRT function practically removes a large percentage of generation for a short time (typically 0.15 to 0.2 seconds). It is not clear whether the system will gracefully recover from such an event.

One existing approach to deal with these issues is to control the converter interface such that the CIG systems behave similarly as synchronous machines with frequency responses and inertia [6-7]. However, this approach is not as good as expected because it is practically impossible to achieve high synchronizing torques due to current limitations of the inverter power electronics. For traditional power systems, synchronous machines can provide transient currents in the order of 500% to 1000% of load currents. On the contrary, the converters have to limit the transient currents to no more than approximately 170% of load currents for one or two cycles and further decrease this value as time evolves [8]. Consequently, the CIGs' imitation of synchronous machines is not quite effective.

The first important problem is the recognition that fault currents in a system with high penetration of CIGs will be much lower than conventional systems and many times may be comparable to load currents. The issue has been addressed in this project. The findings are summarized in reference [M1] listed in section 7. This reference shows the transformation of the fault currents as the penetration of CIGs goes from 0% to 100%. The reduced fault currents create protection gaps for these systems, in other words the system cannot depend on traditional protection schemes to reliably protect against all faults and abnormal conditions. We propose a new approach to protection based on dynamic state estimation.

The second important problem is the stabilization of CIGs with the power grid during disturbances. To control the CIGs such that the CIG smoothly follows the oscillations of the system and avoids excessive transients, a Dynamic State Estimation (DSE) enabled supplementary predictive inverter control (P-Q mode) scheme has been proposed, implemented and tested. The method is based on only local side information and therefore no telemetering is required and associated latencies. The method consists of the following two steps: **Step 1:** The power grid frequency as well as rate of frequency change is estimated using only local measurements and the model of the transmission circuit connecting a CIG to the power grid. **Step 2:** The power grid frequency as well as rate of frequency change are injected into the inverter controller to initiate supplementary control of the firing sequence. The supplementary control amounts to predictive control to synchronize the inverter with the motion of the power grid. Numerical experiments indicate that the supplementary control synchronizes CIGs with the power grid in a predictive manner, transients between CIGs and the power grid are minimized. One can deduct that the supplementary controls will minimize instances of LVRT logic activation.

The application of the proposed method requires an infrastructure that enables dynamic state estimation at each CIG. The technology exists today to provide the required measurements and at the required speeds to perform dynamic state estimation. In essence the method provides full state feedback for the control of the CIGs. While in this project we experimented with one type of supplementary control, the ability to provide full state feedback via the dynamic state estimation opens up the ability to use more sophisticated control methodologies. Future work should focus on utilizing the dynamic state estimation to provide full state feedback and investigate additional

control methods. The methods should be integrated with resource management, for example managing the available wind energy (in case of a WTS) or the PV energy, especially in cases that there is some amount of local storage. The dynamic state estimation based protection, should be integrated in such a system.

Part II: Development of Positive Sequence Converter Models and Demonstration of Approach on the WECC System

A voltage source representation of the converter-interfaced generation is proposed. The operation of a voltage source converter serves as a basis for the development of this model wherein the switching of the semiconductor devices controls the voltage developed on the ac side of the converter. However, the reference current determines the value of this voltage. With the voltage source representation, the filter inductance value plays an important role in providing a grounding connection at the point of coupling. A point on wave simulation served as a basis for the calibration of the proposed positive sequence model. Simulation of a simple two-machine test system and the three-machine nine-bus WSCC equivalent system validated the performance of the model with comparison against the existing boundary current injection models that are presently in use. In the existing models, the absence of the filter inductance causes significant voltage drops at the terminal bus upon the occurrence of a contingency and in a large system, it can lead to divergence of the network solution. It was found that the voltage source representation was a more realistic representation of the converter and was proposed to be used in all large-scale system studies.

The 2012 WECC 18205 bus system was used as a test system for large-scale system studies. Initially, converters replaced only the machines in the Arizona and Southern California area and the response to various system contingencies was analyzed. Carrying this forward, converters replaced all machines in the system resulting in a 100% converter-interfaced generation set. The performance of this system was found to be largely satisfactory. With the absence of rotating machines, a numerical differentiation of the bus voltage angle gave an approximate representation of the frequency. For the trip of two Palo Verde units, the frequency nadir was well above the under frequency trip setting of the WECC system and the recovery of the frequency was within 2-3 seconds enabled by the fast action of the converters. For other contingencies, the voltage response of the individual units reflected the fast control action with the achievement of steady state again within 2-3 seconds following the disturbance. Incorporation of overcurrent and overvoltage protection mechanisms ensured adherence to the converter device limits.

An induction motor drive model was also developed and tested in an independent C code written to perform a time domain positive sequence simulation. The performance of the nine bus system with and without induction motor drives was analyzed.

Project Publications:

1. Ramasubramanian, D.; Z. Yu, R. Ayyanar and Vijay Vittal. "Converter Control Models for Positive Sequence Time Domain Analysis of Converter Interfaced Generation," submitted to the *IEEE Transactions* – under review.

2. Ramasubramanian, D.; and Vijay Vittal. "Transient Stability Analysis of an all Converter Interfaced Generation WECC System," Submitted to the *Power Systems Computation Conference 2016* – abstract accepted.
3. Liu, Yu; Sakis A.P. Sakis Meliopoulos, Rui Fan, and Liangyi Sun. "Dynamic State Estimation Based Protection of Microgrid Circuits," *Proceedings of the IEEE-PES 2015 General Meeting*, Denver, CO, July 26-30, 2015.
4. Liu, Yu; Sanghun Choi, A.P. Sakis Meliopoulos, Rui Fan, Liangyi Sun, and Zhenyu Tan. "Dynamic State Estimation Enabled Predictive Inverter Control," Accepted, *Proceedings of the IEEE-PES 2016 General Meeting*, Boston, MA, July 17-21, 2016.

Student Theses:

1. Ramasubramanian, D. "*Impact of Converter Interfaced Generation on Grid Performance*," Ph.D. Thesis, Arizona State University, Tempe, AZ, 2016.
2. Weldy, Christopher. "*Stability of a 24-Bus Power System with Converter Interfaced Generation*," Master Thesis, Georgia Institute of Technology, Atlanta, GA, 2015.

Part I

Stability, Protection and Control of Systems with High Penetration of Converter Interfaced Generation

Sakis A. P. Meliopoulos, Project Leader
Maryam Saeedifard
Georgia Institute of Technology

Graduate Students
Yu Liu
Sanghun Choi
Evangelos Polymeneas
Georgia Institute of Technology

For more information about Part I, contact:

Sakis A.P. Meliopoulos
Georgia Institute of Technology
School of Electrical and Computer Engineering
777 Atlantic Dr. NW
Atlanta, Georgia 30332-0250
Phone: 404-894-2926
E-mail: sakis.m@gatech.edu

Power Systems Engineering Research Center

The Power Systems Engineering Research Center (PSERC) is a multi-university Center conducting research on challenges facing the electric power industry and educating the next generation of power engineers. More information about PSERC can be found at the Center's website: <http://www.pserc.org>.

For additional information, contact:

Power Systems Engineering Research Center
Arizona State University
551 E. Tyler Mall
Engineering Research Center #527
Tempe, Arizona 85287-5706
Phone: 480-965-1643
Fax: 480-965-0745

Notice Concerning Copyright Material

PSERC members are given permission to copy without fee all or part of this publication for internal use if appropriate attribution is given to this document as the source material. This report is available for downloading from the PSERC website.

© 2016 Georgia Institute of Technology. All rights reserved.

Table of Contents

1.	Introduction.....	1
1.1	Background	1
1.2	Motivation and Objectives	2
1.3	Organization of the Report.....	4
2.	Literature Review	5
3.	Proposed Technologies – Dynamic State Estimator	6
3.1	Dynamic State Estimator (DSE) with Local Information Only	8
3.2	Digital Signal Processor (DSP)	11
3.3	Physically-Based Inverter Modeling	11
4.	Proposed Technologies – Supplementary Predictive Inverter Control	14
4.1	DSE Enabled Supplementary Predictive Inverter Control	14
4.2	Frequency-Modulation Control.....	15
4.3	Modulation-Index and Phase-Angle Modulation Control.....	15
4.4	Switching-Sequence Modulation Control	17
5.	Simulation Results.....	25
5.1	Performance Evaluation of the Dynamic State Estimator (DSE)	25
5.2	Performance Evaluation of the Supplementary Predictive Inverter Control Enabled by Dynamic State Estimator (DSE)	33
5.2.1	Case 1: WTS Performance Without Proposed Control Strategy	35
5.2.2	Case 2: WTS Performance With Proposed Control Strategy	36
6.	Conclusions and Future Work.....	37
7.	Publications as Direct Result of this Project	38
8.	References	39
9.	Appendix A: The Quadratic Integration Method	43
10.	Appendix B: Model Description of Three-Phase Transmission Line	48
B-1:	QDM of single-section transmission line model.....	48
B-2:	QDM of multi-section transmission line model.....	49
11.	Appendix C: Model Description of Three-Phase Two-Level PWM Inverter	51
C-1:	verall Model Description.....	51
C-2:	Single Valve Model.....	55
C-3:	DC-side capacitor model	62
12.	Appendix D: Model Description of the Digital Signal Processor (DSP).....	64
D-1:	Frequency and the Rate of Frequency Change.....	64
D-2:	Positive Sequence Voltage Phasor	69

D-3: Positive-Sequence Current Phasor	70
D-4: Fundamental Frequency Real and Reactive Power.....	71
D-5: Next Zero-Crossing Time.....	71
D-6: Average DC-Input Voltage	73
13. Appendix E: Master Thesis by Christopher Weldy.....	74

List of Figures

Figure 3-1: Overall Approach for Protection, Control and Operation of a CIG.....	6
Figure 3-2: Dynamic State Estimator with Local Measurement Only	9
Figure 3-3: Dynamic State Estimation Operating on Two Consecutive Sets of Measurements ...	9
Figure 3-4: Multi-Section Transmission Line Model	10
Figure 3-5: Single-Section Three-Phase Transmission Line Model.....	10
Figure 3-6: Block Diagram of the Digital Signal Processor	11
Figure 3-7: Three-Phase Two-Level PWM Inverter Model	12
Figure 3-8: Single Valve Model	13
Figure 4-1: Block Diagram of the Supplementary Predictive Inverter Control (P-Q Mode)	14
Figure 4-2: Base Switching Sequence of the Phase A.....	19
Figure 4-3: Base Switching Sequence of the Phase B	19
Figure 4-4: Base Switching Sequence of the Phase C	20
Figure 4-5: Modulated Switching-Signal Sequence of the Phase A (SWA_UP)	22
Figure 4-6: Modulated Switching-Signal Sequence of the Phase B (SWB_UP).....	23
Figure 4-7: Modulated Switching-Signal Sequence of the Phase C (SWC_UP).....	24
Figure 5-1: Simulation System for Frequency Estimation	25
Figure 5-2: Simulation Results, 1.5-Mile Line, Local Side.....	26
Figure 5-3: Simulation Results, 1.5-Mile Line, Remote Side.....	27
Figure 5-4: Simulation Results, 2.5-Mile Line, Local Side	28
Figure 5-5: Simulation Results, 2.5-Mile-Line, Remote Side	29
Figure 5-6: Simulation Results, 4-Mile Line, Local Side.....	30
Figure 5-7: Simulation Results, 4-Mile Line, Remote Side.....	31
Figure 5-8: Test Bed for the Supplementary Predictive Inverter Control	33
Figure 5-9: Simulation Result when the Proposed Control Is Disabled	35
Figure 5-10: Simulation Results when the Proposed Control is Enabled.....	36
Figure A-1: Illustration of the Quadratic Integration Method	43
Figure B-1: The Single-Section Three-Phase Transmission Line Model.....	48
Figure B-2: Multi-section transmission line model	49
Figure C-1: Three-Phase Two-Level PWM Inverter Model.....	51
Figure C-2: The Single Valve Model.....	52

Figure C-3: Three-Phase Two-Level PWM Inverter Model with Assigned Node Numbers	53
Figure C-4: Procedure of the Generation of the SCAQCF of the Inverter Model.....	54
Figure C-5: DC-Side Capacitor Model	62
Figure D-1: Block Diagram of the Digital Signal Processor	64
Figure D-2: Cosine Function with respect to the Phase Angle	72

List of Tables

Table 5-1: Results of Side 1 32

Table 5-2: Results of Side 2 32

Table 5-3: List of the Components of the Test Bed 34

Table C-1: Assigned Node Numbers of the Three-Phase Two-Level PWM Inverter 55

1. Introduction

1.1 Background

Power systems around the world are seeing consistent increase of converter interfaced generation (CIG) capacity, which is largely due to increases in renewable energy generation (mainly wind and PV) connected to power systems through power electronic converters. For example, installed wind power capacity worldwide increased by a factor of ten between the end of 2000 and the end of 2010 [1]. Presently, the US capacity of wind farms and PV plants is 72,472 MW and 30,600 MW respectively. Some power companies around the globe have already experienced a penetration of these systems of more than 50%. This trend will continue for the foreseeable future.

The characteristics of power electronic converters are very different than conventional generation equipment connected to the power system. Power electronic limitations, CIG control modes, and decoupled mechanical inertia are differences expected to cause significant impact to the stability of the power system of the future. Because of strict current carrying capability and intolerance to abrupt transients of power electronic equipment, fault currents contributed by CIG can be significantly lower than those contributed by conventional generators. These limitations lead to fault currents that can be difficult to distinguish from maximum load currents. This makes reliable and secure protection of the power system difficult to achieve. Additionally, CIG offers control modes not available to conventional generation and CIG response times are based on electrical time constants, which are typically much shorter than the mechanical time constants of conventional generators. CIG control modes, coupled with shorter time constants will likely have an impact on the voltage response of the power system; if controlled appropriately it can be an advantage to the power system of the future. Finally, CIG does not couple mechanical inertia to the power system directly, unlike conventional generation. The mechanical inertia provided to the power system by conventional generation plays an important role in maintaining system frequency during disturbances. Since CIG does not have inertia available to help maintain the system frequency during disturbances, power systems with a high penetration of CIG will likely have to control frequency by other means and they will have different frequency response characteristics than conventional power systems.

Stability of power systems with large penetration of CIGs will be quite different than conventional systems. In conventional systems, any disturbance generates synchronizing forces for synchronous generators that allow the system to remain synchronized for a short time enough for protection systems to remove the disturbance. In CIG systems this synchronizing force does not exist. In order to maintain synchronization, new approaches will be needed. A common approach to control CIG to behave as an inertial system has serious limitations. One common approach to deal with this problem with small levels of CIG penetration is the requirement of low voltage ride through. This approach simply shuts down the CIG during a disturbance until the disturbance is removed and the CIG can start operation again. For larger penetrations, this approach may lead to temporary collapse of the system and the possibility that the system may not be able to recover.

In summary the trends in power system generation will result in systems with large penetration of CIGs and will generate problems. Problems that we have not studied well or understood at the present time.

1.2 Motivation and Objectives

The power system can easily cope with a small amount of converter interfaced generation. In some areas (locally) the power fed by converters may rise and rapidly reach 100% penetration; these areas may be remote from classical synchronous machines. In this case, grid behavior might be different from what it is today. In a far future, it may be a necessity to operate a power grid without synchronous machines. In this case, we need to investigate the important requirements that need to be specified now (considering that new units may last more than 40 years), to allow the system to operate correctly, even if this operation is completely different from today paradigm. This report provides exploratory research for defining new approaches for stability, protection, balancing control and voltage/VAr control of systems with high penetration of converter interfaced generation and evaluating these approaches.

There is an increasing penetration of generating units that are interfaced to the power grid with power electronic systems. These systems allow non-synchronous operation of the generation, this being the case of wind farms as an example. Some are completely free of rotating parts, such as solar PV farms. At the same time, they are connected to a system that operates at almost constant frequency. We will refer to these systems as Converter Interfaced Generation (CIG). The power system can easily cope with a small amount of CIG. In some areas (locally) the CIG may rise and rapidly reach 100% penetration; these areas may be remote from classical synchronous machines. In this case, grid behavior might be different from what it is today. As the case of high levels of CIG penetration becomes a possibility (islanding operation, island systems, specific areas, etc.), the following fundamental question is raised: is it possible to operate a power grid without synchronous machines? Are there important requirements that need to be specified now (considering that new units may last more than 40 years), to allow the system to operate correctly, even if this operation is completely different from today? What level of CIG penetration in terms of capacity addition can the system reliably handle? Would CIG machines be capable of supporting voltage/reactive power control and frequency control with the same efficacy as synchronous generators while their protection is effective in case of faults?

The question that has been raised and studied for years is the question of integration of renewables (which are CIGs) in the context of power/demand equilibrium taking into account the variability of weather parameters. But even if production can be fully controlled, how would the grid behave when only power converters feed it? Is the frequency still relevant when there is no physical link between load/production and frequency? Is frequency response relevant? What is the meaning and role of the Area Control Error under these conditions? Reserves? Customer Owned Resources? Primary frequency control? VAr control?

These questions regarding the present control paradigm need to be addressed and confronted to the classical way of operating a power system. New control schemes and/or operational rules may need to be defined. In addition, present protection schemes are based on a clear separation between fault currents and normal load currents. CIG limits fault currents to values comparable to load

currents. This presents a huge challenge and renders present protection schemes ineffective. Fault detection must be revisited. It is necessary that protection must be based on new principles.

It is clear that the protection and control paradigm should be quite different for the following two power systems: (a) one based on 100% synchronous machine generation, and (b) one based on 100% converter interfaced generation. The reality is that we are witnessing a transition from (a) to (b). In the near future we have to deal with a hybrid system that is closer to (a) but slowly moving to (b). The transition will be quite challenging. The stability, protection and control of the system need to be ensured in all cases.

One present approach to deal with some of these issues is focused on providing controls to the converter interfaces to make CIG-based systems behave as synchronous machines with inertia and some frequency response. This approach has limitations as during transients the converters have to limit the transient currents to no more than approximately 170% for a short duration (typically one or two cycles), and decrease this value to typical values of 110% as time evolves. This is to be compared with synchronous machines that can provide transient currents in the order of 500 to 1000% for short times and sustain it for longer period of times (tens of cycles) than converter interfaced systems. The high transient currents in synchronous machines provide strong synchronizing torques. In CIG systems the synchronizing torque concept may be irrelevant. In fact, the true need is to have at least the same level of stability for power systems than before but with less or without synchronous machine generation. The “inertia” is not a need but only a physical characteristic of historical generators. A power system mostly based on CIG could probably be controlled to be as stable as the “historical” generators.

The conventional power system powered by a synchronous generator has following characteristics: First, a synchronous generator has a mechanic torque input to its shaft. The synchronous generator generates electricity from the mechanical torque input. Thus, the primary control (speed governor) can maintain load/generation balance by controlling the frequency of the synchronous generator. Second, a synchronous generator has high moment of inertia. Thus, the frequency and voltage angle changes/oscillations of the conventional power system are small and slow. Thus, the synchronous generator can inherently ensure the transient stability of the power system and provide high transient currents that generate synchronizing torques that keep the synchronous generator in synchronism with the power system.

Compared to the conventional power system, a power system with the high penetration of CIGs will have following problems. First, there is no mechanical torque input to the DC link of a grid-side converter. As a result, the control of converter output frequency is irrelevant to load/generation balancing. Consequently, the area control error (ACE) cannot provide meaningful control information to the load/generation balancing of a power system with the high penetration of CIGs. Also, Frequency Response (β) is an irrelevant mathematical expression for the frequency stabilization of a power system with the high penetration of CIGs after a disturbance. Second, CIG does not have inertia. As a result, the frequency and voltage-angle changes of a power system with the high penetration of CIGs are fast and large and its transient current is limited. Consequently, the fault sequence and transient stability of the convention power system cannot directly be applied to a power system with the high penetration of CIGs.

We conclude that the stability analysis, autonomous controls, and protection strategies of the current power system cannot guarantee the transient stability, control and protection of a power system with the high penetration of CIGs. In other words, the operation of constraints of converters may exceed to the points of damaging the converters or causing the shutdown of CIGs unless new controls and protection strategies are developed for a power system with the high penetration of CIGs.

The objective of this study is to investigate these new challenges and identify new approaches to cope with these problems. The report provides an overview and describes new approaches that exhibit promise towards providing a robust solution to these issues. The report describes:

- The transformation of the available fault currents as the system shifts from 100% synchronous generation to 100% CIG.
- The challenges encountered in stabilizing all the CIG in a system with high penetration levels
- A proposed supplementary predictive converter control that can ensure the stability, control, and protection of a power system with high penetration of converter-interfaced generations (CIGs). This method is based upon a number of core technologies:
 - Feedback of frequency and rate of frequency change at local and remote sites.
 - High-fidelity digital signal processing (DSP)-based control information calculation.
 - High-fidelity modeling-based computer simulation studies.
 - Development of a new controller with sluggish frequency control.

The findings from above investigations are described in this report.

1.3 Organization of the Report

The report is organized as follows. Chapter 1 provides background on the electric power grid and sets up the motivation and objectives of the project. Chapter 2 provides a brief literature survey. It is recognized that there is a plethora of work addressing generation adequacy issues of renewables, which are mainly CIGs, but very limited information and studies on the protection, control and synchronization challenges for high penetration levels of renewables. Chapters 3 and 4 provide a description of the core technologies proposed to address issues of protection, control and synchronization of CIGs. Specifically, Chapter 3 presents the dynamic state estimator and Chapter 4 describes supplementary inverter controls using full state feedback from the dynamic state estimator. Chapter 5 presents numerical experiments that demonstrate the effectiveness of the proposed methods to synchronize and stabilize CIGs with the power grid during disturbance and oscillations. Finally, Chapter 6 provides a summary and identifies additional research issues to be pursued as a continuation of this project.

The report includes a number of Appendices that provide additional details of the methodologies used and the modeling approaches.

2. Literature Review

This section presents a literature review of the current technologies and known problems for electric power systems highly penetrated by renewable electricity generations. The literature is rich in methods and systems for controlling and interfacing CIGs to a stable power grid. The literature is also rich in addressing the issues of generation adequacy as more and more renewables are interconnected to the power grid. On the other hand, there is lack of work to address protection, control and stabilization issues created by high penetration levels of CIGs.

The conventional power system powered by synchronous generators has the following characteristics. (a) synchronous generators are driven by mechanical torque, so the control of the speed governor can maintain load/generation balance by controlling the frequency of the synchronous generator; (b) synchronous generators have high moment of inertia, so the oscillations of frequency and phase angle are small and slow, and transient stability of the power system can be ensured. These characteristics are absent in CIGs. In conventional systems, frequency constancy means generation/load balance. In systems with 100% CIGs this concept does not exist.

Compared to the conventional power system, a power system with high penetration of CIGs will confront the following challenges. (a) There exists no mechanical torque input to the DC link of a grid side converter, thus the control of the converter output frequency is irrelevant to load/generation balancing [2-3]. Traditional control schemes, such as area control error (ACE) become meaningless in systems with 100% CIGs. (b) CIGs do not have inertia [4-5], thus the frequency and phase angle may oscillate quickly after disturbances and in this case the operational constraints of the inverters may be exceeded to the point of damaging the inverters or causing the shutdown of the inverters. Inverters can be protected with Low Voltage Ride Through (LVRT) function. However, in a system with high penetration of CIGs, the LVRT function practically removes a large percentage of generation for a short time (typically 0.15 to 0.2 seconds). It is not clear whether the system will gracefully recover from such an event.

One existing approach to deal with these issues is to control the converter interface such that the CIG systems behave similarly as synchronous machines with frequency responses and inertia [6-7]. However, this approach is not as good as expected because it is practically impossible to achieve high synchronizing torques due to current limitations of the inverter power electronics. For traditional power systems, synchronous machines can provide transient currents in the order of 500% to 1000% of load currents. On the contrary, the converters have to limit the transient currents to no more than approximately 170% of load currents for one or two cycles and further decrease this value as time evolves [8]. Consequently, the CIGs' imitation of synchronous machines is not quite effective.

3. Proposed Technologies – Dynamic State Estimator

The basic technology for protection, control and operation is a dynamic state estimator that provides feedback to the system relays and controllers at high speeds. The dynamic state estimator that we developed provides the state feedback at rates of several thousand per second with time latencies of just a few hundreds of microseconds. The method also provides the best estimate of the frequency as well as rate of frequency change at the system (remote) side with local measurements only. Of course if telemetered data exists they can be utilized. The estimated frequency and the rate of frequency change are used to provide feedback to inverter controls. In this section we describe the method and in subsequent sections we use the dynamic state estimator for the applications.

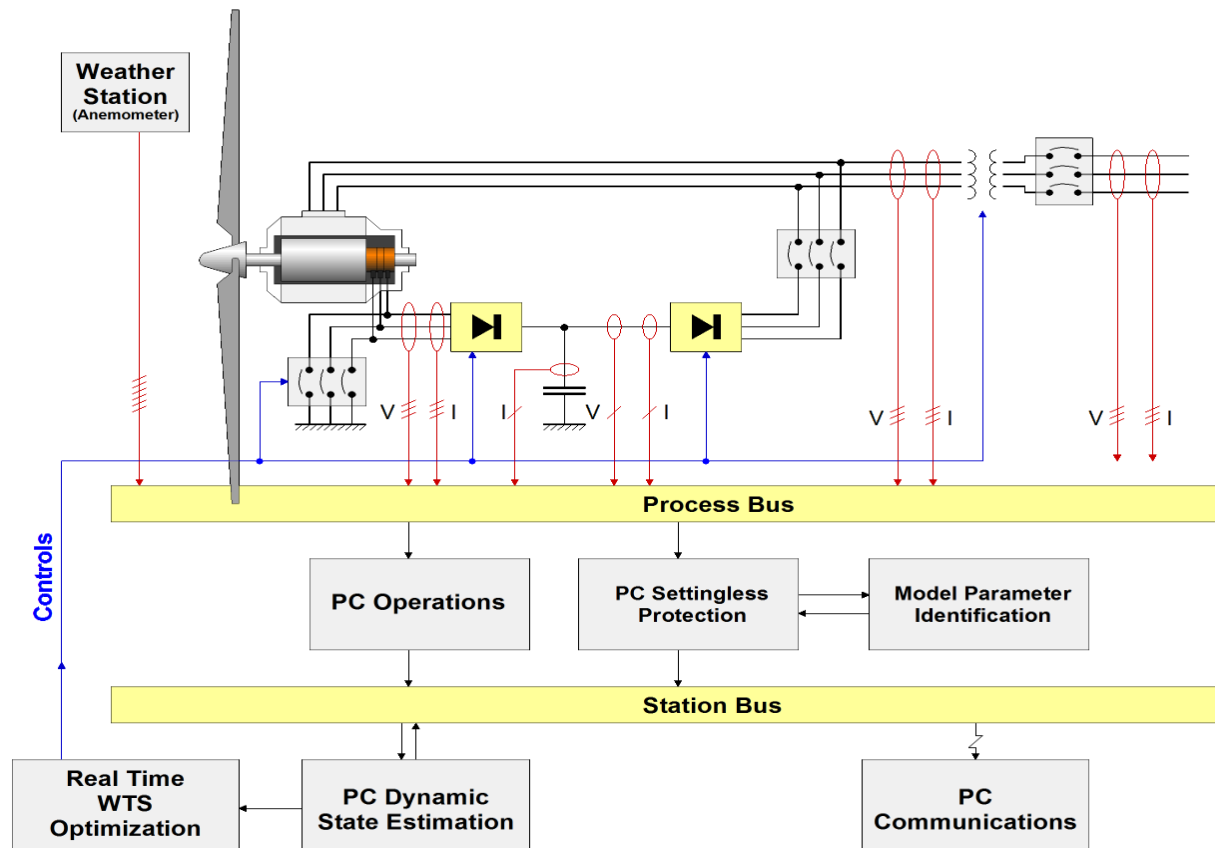


Figure 3-1: Overall Approach for Protection, Control and Operation of a CIG

The overall approach is shown in Figure 3-1. The figure shows a CIG, a wind turbine system in this case, the instrumentation for collecting data, the sampled data are collected at a process bus where the dynamic state estimation is connected to. The best estimate of the system state is utilized to provide supplementary controls to the inverters and also rectifier and/or control the storage if available. The overall scheme relies on the basic technology of the dynamic state estimator which is described next.

The Dynamic State Estimation (DSE) method requires the dynamic model of the system, the measurement models and a dynamic state estimation process. These constituent parts of the method are described next. For maximum flexibility an object oriented approach has been developed. Specifically, each device model and measurement model is a mathematical object of a specific syntax. The specific syntax is in the form of a quadratic model. Any device or measurement can be cast in this form by quadratization. The quadratization procedure is a simple procedure which introduces additional state variables to reduce nonlinearities higher than order 2 into no higher than order 2. Because most power system components are linear, the quadratization process is used for only a small number of components. The dynamic state estimator operates directly on the mathematical objects.

Device and Measurement Quadratized Model: The dynamic model of the component of interest describes all the physical laws that the component should satisfy, which usually consists of several algebraic/differential equations. In general, dynamic models of different kinds of components can be written with the same device Quadratized Dynamic Model (QDM) as shown in equation 3-1, where all the nonlinearities are reduced to no more than second order by introducing additional variables if necessary. The measurement QDM is obtained after selecting specific rows of equations corresponding to the available measurements. The QDM syntax is as follows:

Device QDM:

$$\begin{aligned}
i(t) &= Y_{eqx1} \mathbf{x}(t) + Y_{equ1} \mathbf{u}(t) + D_{eqxd1} \frac{d\mathbf{x}(t)}{dt} + C_{eqc1} \\
0 &= Y_{eqx2} \mathbf{x}(t) + Y_{equ2} \mathbf{u}(t) + D_{eqxd2} \frac{d\mathbf{x}(t)}{dt} + C_{eqc2} \\
0 &= Y_{eqx3} \mathbf{x}(t) + Y_{equ3} \mathbf{u}(t) + \left\{ \mathbf{x}(t)^T \begin{matrix} \vdots \\ F_{eqxx3}^i \\ \vdots \end{matrix} \mathbf{x}(t) \right\} + \left\{ \mathbf{u}(t)^T \begin{matrix} \vdots \\ F_{equu3}^i \\ \vdots \end{matrix} \mathbf{u}(t) \right\} + \left\{ \mathbf{u}(t)^T \begin{matrix} \vdots \\ F_{equx3}^i \\ \vdots \end{matrix} \mathbf{x}(t) \right\} + C_{feqc3}
\end{aligned} \tag{Eq. 3-1}$$

Measurements QDM:

$$\begin{aligned}
\mathbf{z}(x) &= Y_{quam,x} \mathbf{x}(t) + Y_{quam,u} \mathbf{u}(t) + D_{quam,x} \frac{d\mathbf{x}(t)}{dt} + \left\{ \mathbf{x}(t)^T \begin{matrix} \vdots \\ \mathbf{F}_{quam,xx}^i \\ \vdots \end{matrix} \mathbf{x}(t) \right\} \\
&+ \left\{ \mathbf{u}(t)^T \begin{matrix} \vdots \\ \mathbf{F}_{quam,uu}^i \\ \vdots \end{matrix} \mathbf{u}(t) \right\} + \left\{ \mathbf{u}(t)^T \begin{matrix} \vdots \\ \mathbf{F}_{quam,ux}^i \\ \vdots \end{matrix} \mathbf{x}(t) \right\} + C_{quam}
\end{aligned} \tag{Eq. 3-2}$$

where $i(t)$ is the through variables (terminal currents); $x(t)$ is the state variables, $z(t)$ is the measurements, and others are parameter matrices and vectors of the interested component.

Subsequently, the quadratized dynamic model is integrated using the quadratic method. This method is provided in Appendix A. The result of the integration is that the differential equations

are converted into algebraic equations, yielding the device and measurement model in the State and Control Algebraic Quadratic Companion Form (SCAQCF). The SCAQCF syntax for the device and measurement models is provided below.

Device SCAQCF

$$\begin{Bmatrix} i(t) \\ 0 \\ 0 \\ i(t_m) \\ 0 \\ 0 \end{Bmatrix} = Y_{eqx} \mathbf{x} + Y_{equ} \mathbf{u} + \begin{Bmatrix} \vdots \\ \mathbf{x}^T \langle F_{eqx}^i \rangle \mathbf{x} \\ \vdots \end{Bmatrix} + \begin{Bmatrix} \vdots \\ \mathbf{u}^T \langle F_{equ}^i \rangle \mathbf{u} \\ \vdots \end{Bmatrix} + \begin{Bmatrix} \vdots \\ \mathbf{u}^T \langle F_{equx}^i \rangle \mathbf{x} \\ \vdots \end{Bmatrix} - B_{eq} \quad (\text{Eq. 3-3})$$

$$B_{eq} = -N_{eqx} \mathbf{x}(t-h) - N_{equ} \mathbf{u}(t-h) - M_{eq} i(t-h) - K_{eq}$$

Measurement SCAQCF

$$\mathbf{z} = h(\mathbf{x}) = Y_{m,x} \mathbf{x} + \begin{Bmatrix} \vdots \\ \mathbf{x}^T F_{m,x}^i \mathbf{x} \\ \vdots \end{Bmatrix} + Y_{m,u} \mathbf{u} + \begin{Bmatrix} \vdots \\ \mathbf{u}^T F_{m,u}^i \mathbf{u} \\ \vdots \end{Bmatrix} + \begin{Bmatrix} \vdots \\ \mathbf{u}^T F_{m,ux}^i \mathbf{x} \\ \vdots \end{Bmatrix} + C_m \quad (\text{Eq. 3-4})$$

$$C_m = N_{m,x} \mathbf{x}(t-h) + N_{m,u} \mathbf{u}(t-h) + M_m i(t-h) + K_m$$

Appendices B and C provide examples of quadratized model relevant to this work. For example, Appendix B provides the dynamic model of a transmission line and Appendix C provides the dynamic model of an inverter. It should be understood this modeling approach applies to all model of the system.

The states are estimated using a dynamic state estimator. Three dynamic state estimators have been used: (a) weighed least squares approach, (b) constraint weighted least squares approach and (c) extended Kalman filter. We describe below the weighed least squares approach. The best estimate of the states is obtained with the following iterative algorithm:

$$x(t, t_m)^{v+1} = x(t, t_m)^v - (H^T W H)^{-1} H^T W (h(x(t, t_m)^v))$$

where $W = \text{diag}\{\dots, 1/\sigma_i^2, \dots\}$, σ_i is the standard deviation of the measurement error, and $H = \partial h(\mathbf{x}) / \partial \mathbf{x}$ is the Jacobean matrix:

3.1 Dynamic State Estimator (DSE) with Local Information Only

To illustrate the dynamic state estimator, we present a simple application case for one transmission line using only local (one side) information. The system is illustrated in Figure 3-2. Note that the system consists of a wind turbine system, a rectifier/inverter system, a step-up transformer and a transmission line that connect the WTS to the power grid. The objective of the dynamic state estimator in this case is to estimate three-phase voltages and currents, frequency, and rate of

frequency change at both local and remote side of the line. To achieve this goal the dynamic state estimation presented earlier is used.

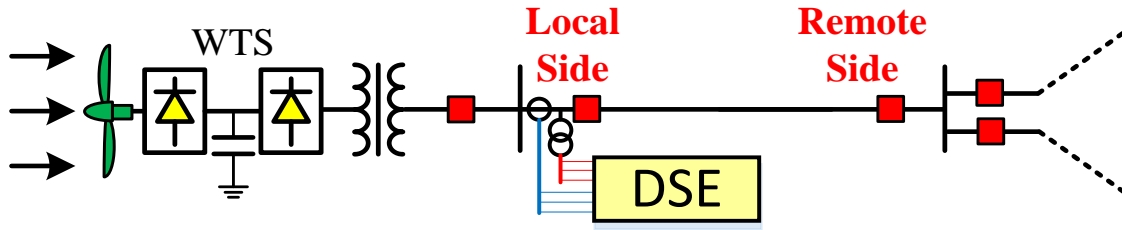


Figure 3-2: Dynamic State Estimator with Local Measurement Only

The dynamic state estimation in this case, provides the best estimate of the three phase voltages at the two ends of the line. At each execution of the method, two consecutive samples of the three phase voltages and currents (measurements) at one end of the line are used as shown in Figure 3-3. The estimated states are the three-phase voltages at both ends of the line. From the estimated states of the transmission line, all the information at both local and remote side are calculated, including three phase currents as well as frequency and rate of frequency change.

The implementation of the dynamic state estimation in this case requires that the six measurements be expressed as functions of the state. The state in this case is defined as the three phase voltages at the two ends of the line. For this purpose, the dynamic model of the line must be developed and then used to define the dynamic model of the measurements. The detailed derivation of the line model is given in Appendix B including the model of the measurements. Here we present a summary and the resulting dynamic measurement model. For accuracy, the line is segmented into a number of sections, as shown in Figure 3-4. The selected number of sections depends on the sampling rate and the total length of the line. The model of each section is shown in Figure 3-5. To simplify the drawings, mutual impedances, both inductive and capacitive, are not shown.

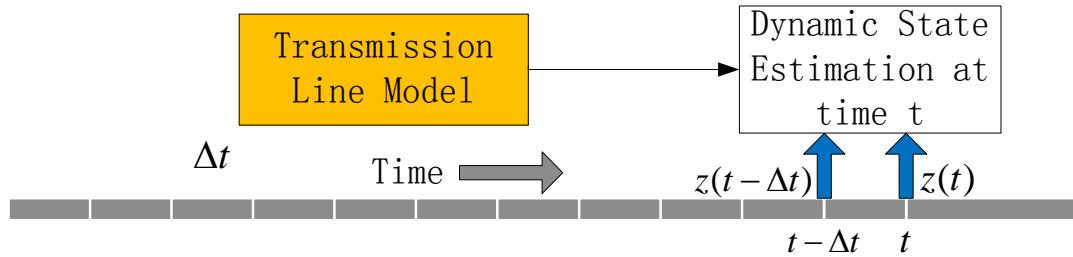


Figure 3-3: Dynamic State Estimation Operating on Two Consecutive Sets of Measurements

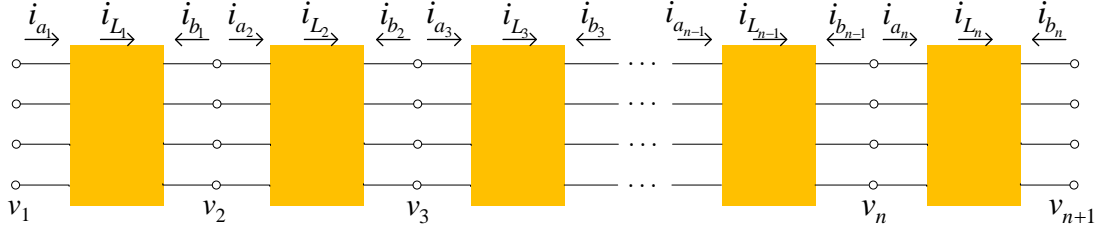


Figure 3-4: Multi-Section Transmission Line Model

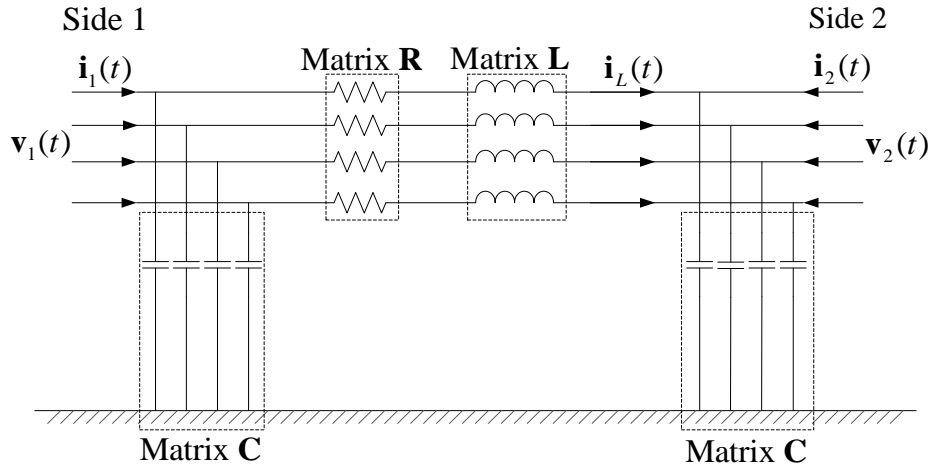


Figure 3-5: Single-Section Three-Phase Transmission Line Model

The mathematical model of each section is provided in matrix form below. This is a linear model and there is no need to quadratize it. Therefore, this is the QDM of the transmission line.

Using above measurement models, the algorithm discussed earlier is applied to provide the best estimate of the line state. It should be noted that the number of total measurements, actual and virtual is greater than the states to be estimated.

The output of the dynamic state estimator is the sampled voltage and current values at both ends of the line. From the samples, one can compute the frequency and rate of frequency change. For this purpose, a digital signal processing model was developed and it is described in section 3.2 and in Appendix D.

It has been mentioned that all models in the system have been developed in the same form, i.e. the QDM and the SCAQCF. While we do not present all the developed models, we present the inverter model because it is a rather complex model. The presentation of this model is given in section 3.3 and in Appendix C.

3.2 Digital Signal Processor (DSP)

This section presents the digital signal processor (DSP). The DSP receives the following instantaneous inputs V_{an} , V_{bn} , V_{cn} , I_a , I_b , I_c , and V_{DC} (three phase voltages and currents of the inverter and the DC voltage). The inputs are sampled data of these quantities. The DSP then calculates the following outputs:

\tilde{V}_1 : positive sequence voltage, computed from the three phase voltages

\tilde{I}_1 : positive sequence current, computed from the three phase currents

P : total real power, computed from the three phase voltages and currents

Q : total reactive power, computed from the three phase voltages and currents

f_s : average frequency, computed from the three phase voltages and currents

ZX : zero crossing time of the positive sequence voltage

$\frac{df_s}{dt}$: rate of change of frequency, computed from the three phase voltages and currents

\bar{V}_{DC} : average DC voltage, computed from DC voltage

This functional structure of the DSP is shown in Figure 3-6.

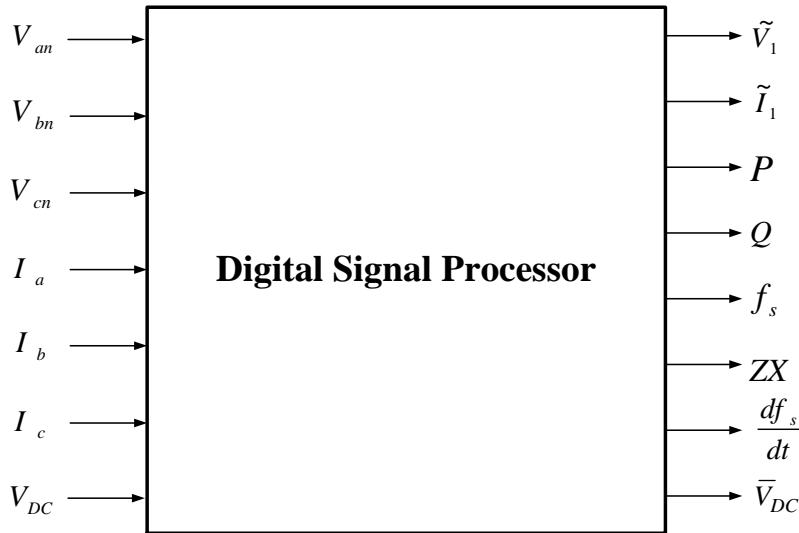


Figure 3-6: Block Diagram of the Digital Signal Processor

The detailed description of this model is provided in Appendix C.

3.3 Physically-Based Inverter Modeling

This section summarizes the inverter dynamic model. The derivation of this model is given in Appendix D. There are many inverter designs. Here we present a two-level pulse width modulation inverter. We present first the dynamical equations of the inverter model. Subsequently, the

dynamical model is integrated using the quadratic integration method. This method is presented in Appendix A. After the quadratic integration, the state and control algebraic companion form of the inverter (SCAQCF) is obtained.

A three-phase ac to dc, two-level PWM pulse width modulated inverter is shown in Figure 3-6. The inverter consists of six power electronic valves and a DC-side capacitor.

The six valves form sets of complementary valve pairs, one for each phase. Using phase A as an example, the complementary valve-model pair is SWA_H_Valve and SWA_L_Valve. A switching signal generator injects three switching signals to the three upper valve models of the inverter model. The other valves are switched by the signal circuits indicated in the figure. Each valve consists of IGBT parasite conductance and parasite capacitance, IGBT on/off conductance, a snubber circuit, an anti-parallel diode, and a current limiting circuit as shown in Figure 3-7 and 3-8.

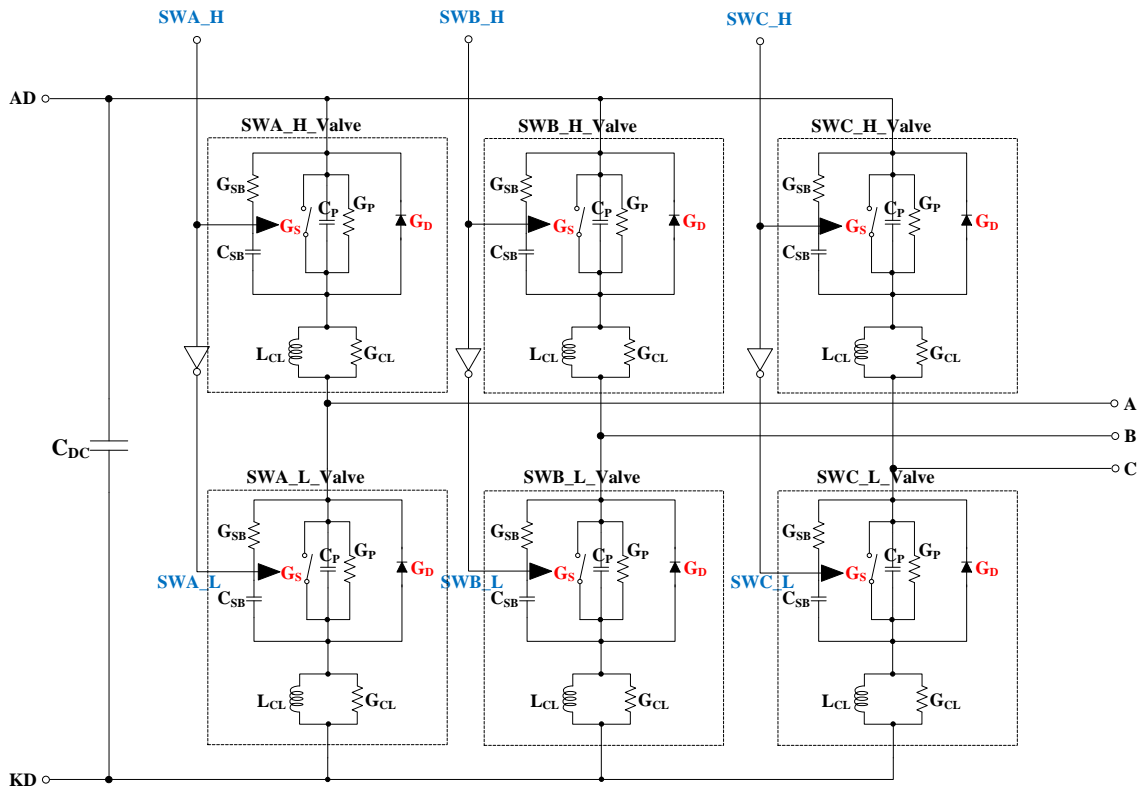


Figure 3-7: Three-Phase Two-Level PWM Inverter Model

IGBT-Conductance Determination

If ($U_S(t) == 1$), $G_S = G_{SON}$

If ($U_S(t) == 0$), $G_S = G_{SOFF}$

Anti-Parallel-Diode-Conductance Determination

If ($V_{CP}(t) \geq 0$), $G_D = G_{DOFF}$

If ($V_{CP}(t) < 0$), $G_D = G_{DON}$

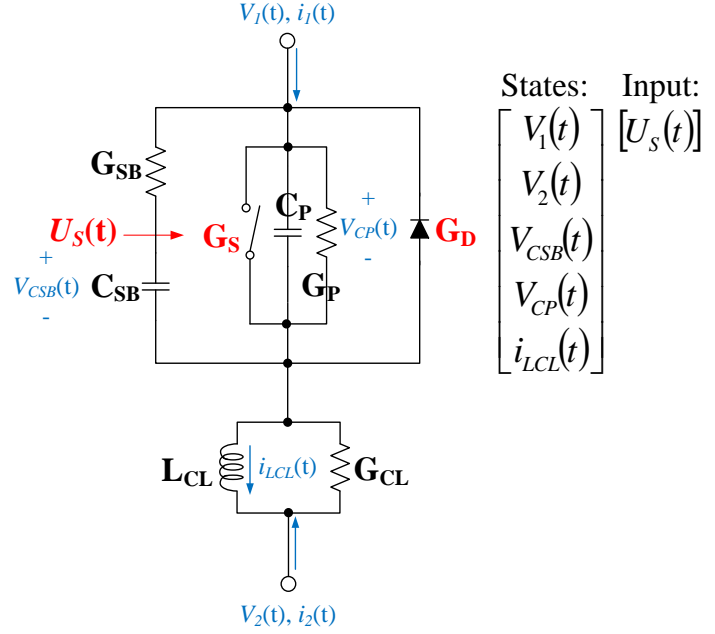


Figure 3-8: Single Valve Model

For each one of the valve states, the dynamic model of the valve has been developed and they are given in Appendix D. The models are integrated to provide the SCAQCF model for each individual valve. By combining the valve models, the overall inverter model is obtained.

Note that this model explicitly models the valve operating conditions. Based on the switching signals or the voltages across the valves, the valve operating condition is determined. This model can capture whether a valve may mis-operate (mis-fire) because of transients. This is a necessary requirement for a realistic assessment of the performance of the system under the proposed control schemes.

4. Proposed Technologies – Supplementary Predictive Inverter Control

This section presents a methodology for synchronization of CIGs during frequency swings or disturbances in the system. During these events the frequency if the system oscillates as well the voltage may experience transients. These transients may cause mis-firings of the inverter power electronics and may jeopardize the synchronization of the inverter with the system. We propose supplementary controls of the inverters to anticipate the movement of the system and synchronize with the transients of the system. The feedback is provided by the dynamic state estimator discussed in the previous section.

4.1 DSE Enabled Supplementary Predictive Inverter Control

The supplementary predictive inverter control (in P-Q mode or in P-V mode) is achieved by injection appropriate signals to modulate the switching-signal generator of the inverter. The supplementary predictive inverter control consists of frequency modulation, modulation index, phase angle modulation controls as shown in Figure 4-1. This additional control scheme supervises the inverter controller and guarantees synchronization and stability of the inverter against the power grid.

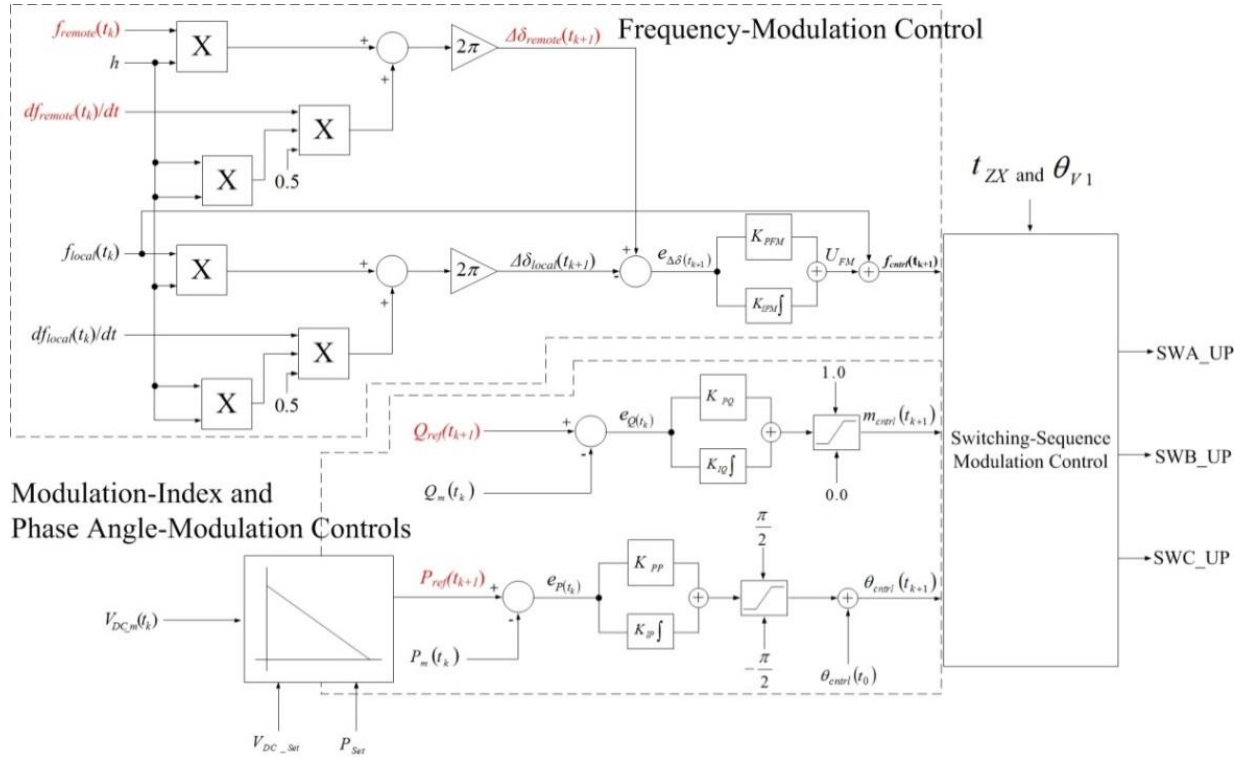


Figure 4-1: Block Diagram of the Supplementary Predictive Inverter Control (P-Q Mode)

The supplementary control scheme injects two signals into the inverter controller, as shown in Figure 4-1. One signal is the target frequency for the operation of the inverter and the other signal is the target phase angle of the inverter. Both of these signals are computed from the output of the

dynamic state estimator. The frequency signal causes a compression or expansion in time of the switching signal generated by the inverter controller while the phase angle signal cause a translation in time of the switching sequences generated by the inverter. Both the compression/expansion and translation in time are applied smoothly causing a gradual shifting towards the operation of the inverter at the target values. The details of the controls are provided next.

4.2 Frequency-Modulation Control

In this section, we present the frequency-modulation control. We first need to predict the rates of phase-angle changes of each CIG system for both the local and the remote sides, as follows:

$$t_{k+1} = t_k + h \quad (\text{Eq. 4-1})$$

$$\Delta\delta_{local}(t_{k+1}) = 2\pi \cdot \left(f_{local}(t_k) \cdot h + \frac{1}{2} \cdot \frac{df_{local}(t_k)}{dt} \cdot h^2 \right) \quad (\text{Eq. 4-2})$$

$$\Delta\delta_{remote}(t_{k+1}) = 2\pi \cdot \left(f_{remote}(t_k) \cdot h + \frac{1}{2} \cdot \frac{df_{remote}(t_k)}{dt} \cdot h^2 \right) \quad (\text{Eq. 4-3})$$

Then, we implement a closed-loop feedforward control to generate frequency-modulation control command as follows: The frequency-modulation control with respect to the one-step forward-predicted rates of phase angle changes of two CIG systems (feedforward control) is summarized as follows:

$$X(t_{k+1}) = (\Delta\delta_{remote}(t_k) - \Delta\delta_{local}(t_k)) + (\Delta\delta_{remote}(t_{k+1}) - \Delta\delta_{local}(t_{k+1}) - \Delta\delta_{remote}(t_k) + \Delta\delta_{local}(t_k)) \cdot h \quad (\text{Eq. 4-4})$$

$$\dot{X}(t_{k+1}) = -\frac{K_{IFM}}{K_{PFM}} X(t_{k+1}) + \frac{1}{K_{PFM}} U_{FM}(t_{k+1}) \quad (\text{Eq. 4-5})$$

$$f_{ctrl}(t_{k+1}) = f_{local}(t_k) + U_{FM}(t_{k+1}) \quad (\text{Eq. 4-6})$$

4.3 Modulation-Index and Phase-Angle Modulation Control

In this section, we present the modulation-index and phase-angle modulation controls using real- and reactive-power references and real- and reactive-power measurements from a digital-signal-processing (DSP) unit. We provide the modulation parameter for the P-Q control.

- a. By sending/receiving more reactive power to a power system, we can increase/decrease the voltage of a power system as described in equation 4-7. Furthermore, we can directly control the voltage of a converter-interfaced power system by controlling the modulation index m of the sinusoidal pulse width modulation (SPWM) of the switching-signal generator on behalf of the inverter control. Therefore, we can control the flow of the reactive power between the inverter and the power system by controlling the modulation index. Using the relation between the modulation index and flow of reactive power, we develop the proportional and integral (PI) control-based reactive-power control as follows:

$$V_{local} = \frac{Q \cdot X_s + V_{remote}^2}{V_{remote} \cdot \cos(\theta_{local} - \theta_{remote})} \quad (\text{Eq. 4-7})$$

$$X(t_{k+1}) = (Q_{ref}(t_{k+1}) - Q_m(t_k)) + (Q_{ref}(t_{k+1}) - Q_m(t_{k+1}) - Q_{ref}(t_k) + Q_m(t_k)) \cdot h \quad (\text{Eq. 4-8})$$

$$\dot{X}(t_{k+1}) = -\frac{K_{IQ}}{K_{PQ}} X(t_{k+1}) + \frac{1}{K_{PQ}} m_{ctrl}(t_{k+1}) \quad (\text{Eq. 4-9})$$

$$0.0 \leq m_{ctrl}(t_{k+1}) \leq 1.0 \quad (\text{Eq. 4-10})$$

- b. By controlling the phase angle of the SPWM of the switching-signal generator, we can adjust the phase-angle difference between an inverter and the power system. Therefore, we can control the flow of the real power between an inverter and the power system by controlling the phase angle θ_{local} of the SPWM as summarized in equation 4-11. For example, by defining the sinusoidal-reference signal of the phase A of the SPWM as expressed in equation 4-12, we can increase injection of real power to the power grid by increasing the phase angle, and vice versa. Using the relation between the phase angle of the SPWM and flow of the real power, we develop the proportional and integral (PI) real-power control. The real power reference is determined by the V_{DC}/P droop control.

$$P = \frac{V_{local} V_{remote} \sin(\theta_{local} - \theta_{remote})}{X_s} \quad (\text{Eq. 4-11})$$

$$S_{ref_A}(t_k) = m(t_k) \cdot \cos(2\pi \cdot f_{ctrl}(t_k) \cdot t_k + \theta_{ctrl}(t_k)) \quad (\text{Eq. 4-12})$$

$$P_{ref}(t_{k+1}) = P_{Set} + k(V_{DC_m}(t_k) - V_{DC_Set}) \quad (\text{Eq. 4-13})$$

$$X(t_{k+1}) = (P_{ref}(t_{k+1}) - P_m(t_k)) + (P_{ref}(t_{k+1}) - P_m(t_{k+1}) - P_{ref}(t_k) + P_m(t_k)) \cdot h \quad (\text{Eq. 4-14})$$

$$\dot{X}(t_{k+1}) = -\frac{K_{ip}}{K_{pp}} X(t_{k+1}) + \frac{1}{K_{pp}} \theta_{ctrl}(t_{k+1}) \quad (\text{Eq. 4-15})$$

$$-\frac{\pi}{2} \leq \theta_{ctrl}(t_{k+1}) \leq \frac{\pi}{2} \quad (\text{Eq. 4-16})$$

The above referenced target parameters are translated into switching sequence modulation control as described next.

4.4 Switching-Sequence Modulation Control

In this section, we present the switching-sequence modulation control that generates and controls switching sequences for the three upper switches of the inverter by using the three control commands, $f_{ctrl}(t_{k+1})$, $m_{ctrl}(t_{k+1})$, and $\theta_{ctrl}(t_{k+1})$, obtained from the previous sections. First, we calculate the initial-operation time for the switching-sequence modulation control using the zero-crossing time as follows:

$$t_{int} = t_{zx}(t_0) + \frac{\frac{\pi}{2} + \theta_{v1}(t_0)}{2\pi \cdot f_{local}(t_0)} \quad (\text{Eq. 4-17})$$

$$t_k = t_{int} + k \cdot h \quad (\text{Eq. 4-18})$$

Then, we generate base sinusoidal reference signals for the SPWM of the switching-signal generator based on the base frequency, 60 Hz, as follows:

$$S_{ref_A_base}(t_k) = m(t_k) \cdot \cos(2\pi \cdot f_{base} \cdot t_k) \quad (\text{Eq. 4-19})$$

$$S_{ref_B_base}(t_k) = m(t_k) \cdot \cos\left(2\pi \cdot f_{base} \cdot t_k - \frac{2\pi}{3}\right) \quad (\text{Eq. 4-20})$$

$$S_{ref_C_base}(t_k) = m(t_k) \cdot \cos\left(2\pi \cdot f_{base} \cdot t_k - \frac{4\pi}{3}\right) \quad (\text{Eq. 4-21})$$

Three-phase base switching sequences for a period expressed in the following equations are based on the base frequency, 60 Hz, and 1260 Hz of switching frequency. Figures 4-2, 4-3, and 4-4 show the three-phase base switching sequences for a full period.

$$SWA_UP_{base} = \{t_{0a}, t_{1a}, t_{2a}, \dots, t_{39a}, t_{40a}, t_{41a}\} \quad (\text{Eq.4-22})$$

$$SWB_UP_{base} = \{t_{0b}, t_{1b}, t_{2b}, \dots, t_{39b}, t_{40b}, t_{41b}\} \quad (\text{Eq. 4-23})$$

$$SWC_UP_{base} = \{t_{0c}, t_{1c}, t_{2c}, \dots, t_{39c}, t_{40c}, t_{41c}\} \quad (\text{Eq. 4-24})$$

A. Phase-A-Base Switching Sequence

Negative Edge:

$$t_{(2i)a} = \frac{i}{f_s} + f_N \left(f_s, \frac{i}{f_s}, 1.0 \right), \quad i = 0, 1, 2, \dots, 20 \quad (\text{Eq. 4-25})$$

$$f_N(a, b, c) = \text{solve}(c \cdot \cos(2\pi \cdot f_{base} \cdot t) = 2 \cdot a \cdot (t - b), t), \quad i = 0, 1, 2, \dots, 20 \quad (\text{Eq. 4-26})$$

Positive Edge:

$$t_{(2i+1)a} = \frac{i}{f_s} + f_P \left(f_s, \frac{i}{f_s}, 1.0 \right), \quad i = 0, 1, 2, \dots, 20 \quad (\text{Eq. 4-27})$$

$$f_P(a, b, c) = \text{solve} \left(c \cdot \cos(2\pi \cdot f_{base} \cdot t) = -2 \cdot a \cdot \left(t - b - \frac{1}{a} \right), t \right), \quad i = 0, 1, 2, \dots, 20 \quad (\text{Eq. 4-28})$$

B. Phase-B-Base Switching Sequence

Negative Edge:

$$t_{(2i)b} = \frac{i}{f_s} + f_N \left(f_s, \frac{i}{f_s} + \frac{1}{3 \cdot f_{base}}, 1.0 \right), \quad i = 0, 1, 2, \dots, 20 \quad (\text{Eq. 4-29})$$

Positive Edge:

$$t_{(2i+1)b} = \frac{i}{f_s} + f_P \left(f_s, \frac{i}{f_s} + \frac{1}{3 \cdot f_{base}}, 1.0 \right), \quad i = 0, 1, 2, \dots, 20 \quad (\text{Eq. 4-30})$$

C. Phase-C-Base Switching Sequence

Negative Edge:

$$t_{(2i)c} = \frac{i}{f_s} + f_N \left(f_s, \frac{i}{f_s} + \frac{2}{3 \cdot f_{base}}, 1.0 \right), \quad i = 0, 1, 2, \dots, 20 \quad (\text{Eq. 4-31})$$

Positive Edge:

$$t_{(2i+1)c} = \frac{i}{f_s} + f_P \left(f_s, \frac{i}{f_s} + \frac{2}{3 \cdot f_{base}}, 1.0 \right), \quad i = 0, 1, 2, \dots, 20 \quad (\text{Eq. 4-32})$$

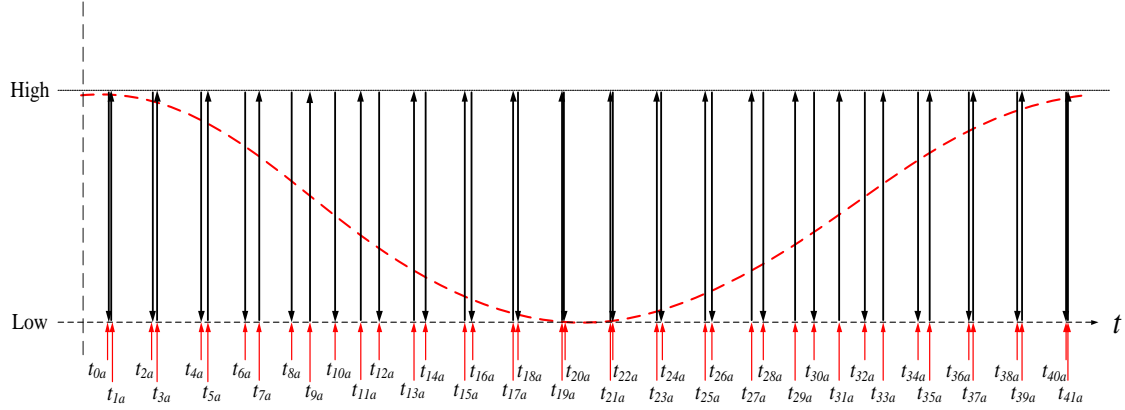


Figure 4-2: Base Switching Sequence of the Phase A

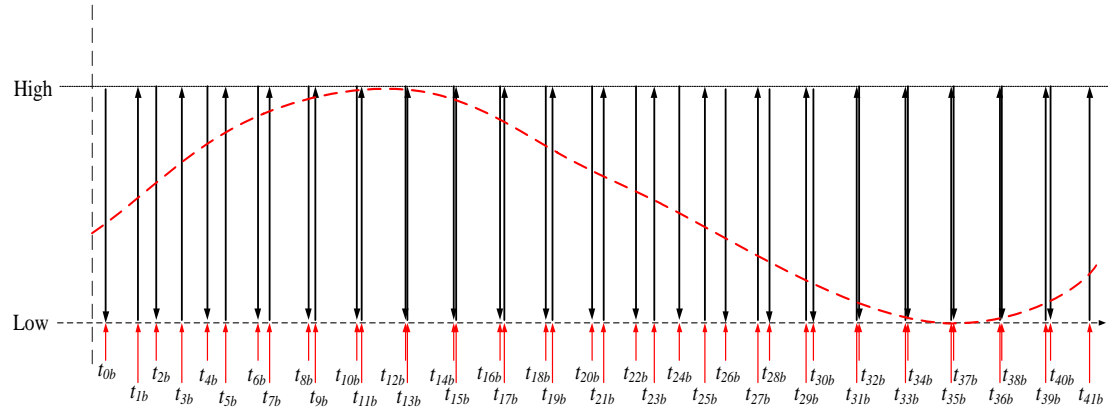


Figure 4-3: Base Switching Sequence of the Phase B

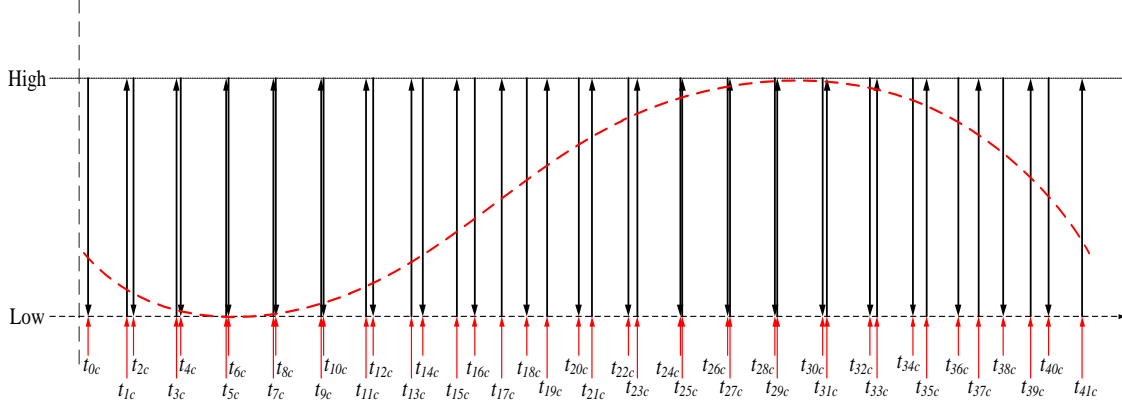


Figure 4-4: Base Switching Sequence of the Phase C

By modulating the above base switching sequences with the supplementary predictive inverter control, the proposed switching-signal generator can control real- and reactive-power flows of the system as follows:

$$SWA_UP = \{ct_{0a}, ct_{1a}, ct_{2a}, ..., ct_{39a}, ct_{40a}, ct_{41a}\} \quad (\text{Eq. 4-33})$$

$$SWB_UP = \{ct_{0b}, ct_{1b}, ct_{2b}, ..., ct_{39b}, ct_{40b}, ct_{41b}\} \quad (\text{Eq. 4-34})$$

$$SWC_UP = \{ct_{0c}, ct_{1c}, ct_{2c}, ..., ct_{39c}, ct_{40c}, ct_{41c}\} \quad (\text{Eq. 4-35})$$

A. Phase-A-Modulated Switching Sequence

Negative Edge:

$$ct_{(2i)a} = \frac{\theta_{ctrl}}{2\pi \cdot f_{ctrl}} + t_{(2i)a} \cdot m_{ctrl} + \left(\frac{1}{f_{base}} - \frac{1}{f_{ctrl}} \right), \quad i = 0, 1, 2, ..., 20 \quad (\text{Eq. 4-36})$$

Positive Edge:

$$ct_{(2i+1)a} = \frac{\theta_{ctrl}}{2\pi \cdot f_{ctrl}} + \frac{t_{(2i+1)a}}{m_{ctrl}} + \left(\frac{1}{f_{base}} - \frac{1}{f_{ctrl}} \right), \quad i = 0, 1, 2, ..., 20 \quad (\text{Eq. 4-37})$$

B. Phase-B-Modulated Switching Sequence

Negative Edge:

$$ct_{(2i)b} = \frac{\theta_{ctrl}}{2\pi \cdot f_{ctrl}} + t_{(2i)b} \cdot m_{ctrl} + \left(\frac{1}{f_{base}} - \frac{1}{f_{ctrl}} \right), \quad i = 0, 1, 2, ..., 20 \quad (\text{Eq. 4-38})$$

Positive Edge:

$$ct_{(2i+1)b} = \frac{\theta_{ctrl}}{2\pi \cdot f_{ctrl}} + \frac{t_{(2i+1)b}}{m_{ctrl}} + \left(\frac{1}{f_{base}} - \frac{1}{f_{ctrl}} \right), \quad i = 0, 1, 2, \dots, 20 \quad (\text{Eq. 4-39})$$

C. Phase-C-Modulated Switching Sequence

Negative Edge:

$$ct_{(2i)c} = \frac{\theta_{ctrl}}{2\pi \cdot f_{ctrl}} + t_{(2i)c} \cdot m_{ctrl} + \left(\frac{1}{f_{base}} - \frac{1}{f_{ctrl}} \right), \quad i = 0, 1, 2, \dots, 20 \quad (\text{Eq. 4-40})$$

Positive Edge:

$$ct_{(2i+1)c} = \frac{\theta_{ctrl}}{2\pi \cdot f_{ctrl}} + \frac{t_{(2i+1)c}}{m_{ctrl}} + \left(\frac{1}{f_{base}} - \frac{1}{f_{ctrl}} \right), \quad i = 0, 1, 2, \dots, 20 \quad (\text{Eq. 4-41})$$

Figures 4-5, 4-6, and 4-7 show the three-phase modulated switching sequences for a full period.

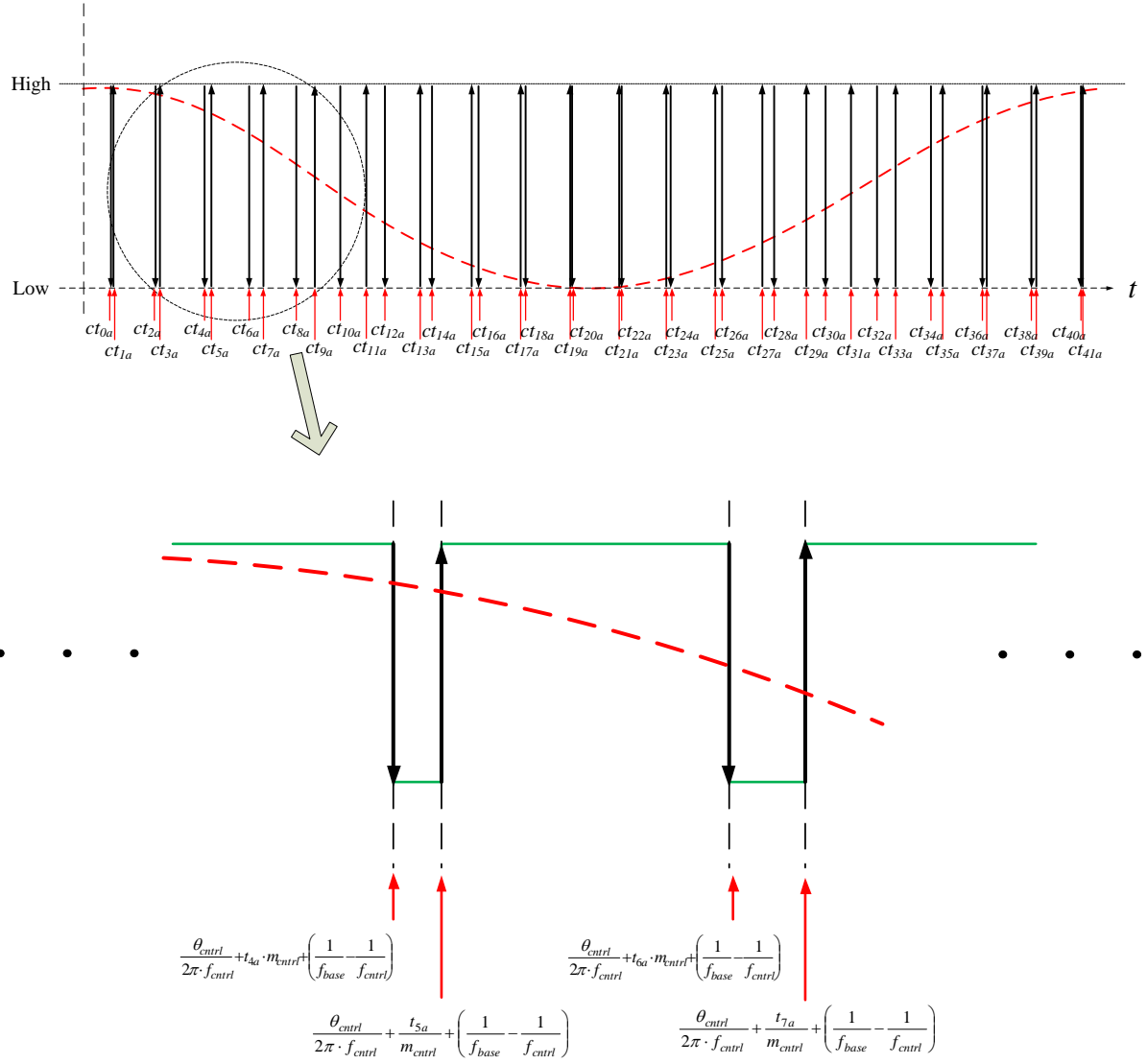


Figure 4-5: Modulated Switching-Signal Sequence of the Phase A (SWA_UP)

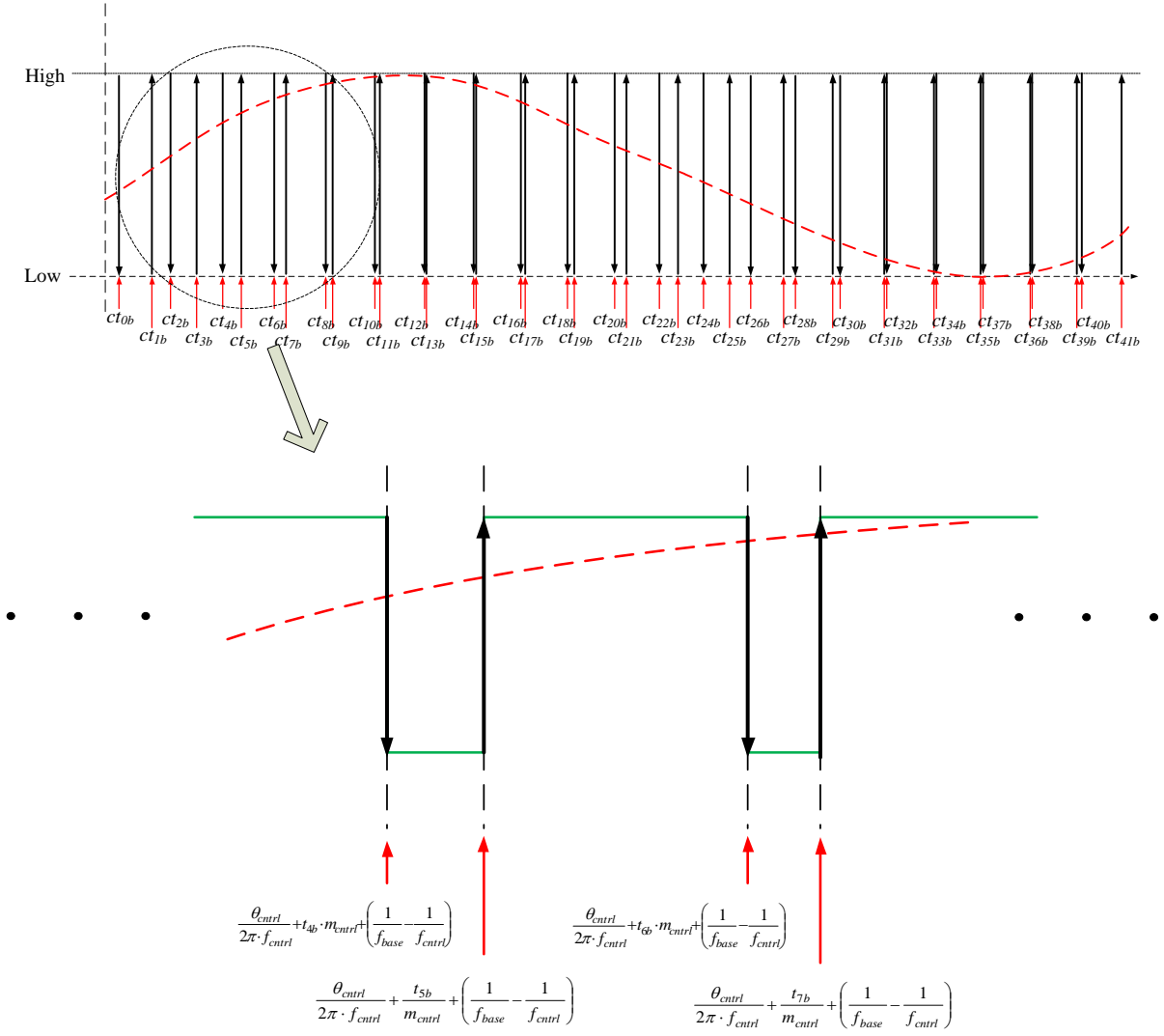


Figure 4-6: Modulated Switching-Signal Sequence of the Phase B (SWB_UP)

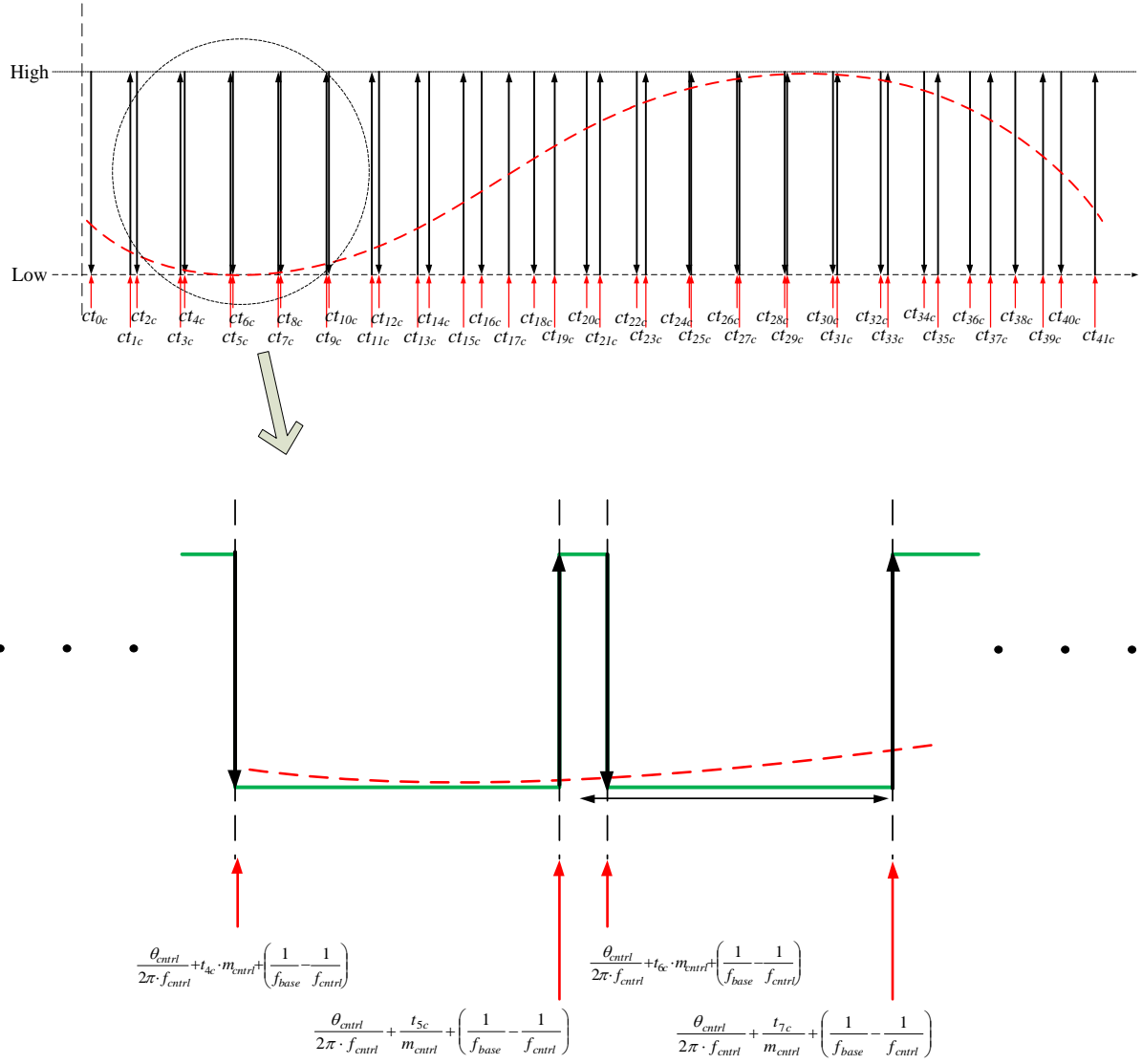


Figure 4-7: Modulated Switching-Signal Sequence of the Phase C (SWC_UP)

5. Simulation Results

In this section we present numerical experiments with the proposed methods to quantify the performance of the proposed methods.

We present first results of the dynamic state estimator. The numerical experiments have been so designed as to assess the accuracy by which the dynamic state estimator can determine frequency and rate of change of frequency of the power grid while it uses local measurements at the inverter location. The results indicate that the accuracy of the dynamic state estimator is excellent.

We also present results that quantify the performance of the supplementary inverter controls. The results indicate that the supplementary inverter controls synchronize the inverter against an oscillatory power grid and eliminates valve mis-firing during transient periods.

5.1 Performance Evaluation of the Dynamic State Estimator (DSE)

This simulation study evaluates the performance of estimating the frequency and rate of frequency change locally at the inverter as well as at the system with only local measurements. The simulation system is provided in Figure 5-1. It consists of a wind turbine system (WTS) which operates at a speed corresponding at 50 Hz. The WTS is connected to a 34.5kV transmission line via two converters and a 690V:34.5kV transformer. On the other side, the power grid is assumed to have a generator that oscillates in such a way that the frequency varies as follows: 60 ± 0.1 Hz. The source is connected to the power grid via a step up transformer and the 1.5-mile-long line.

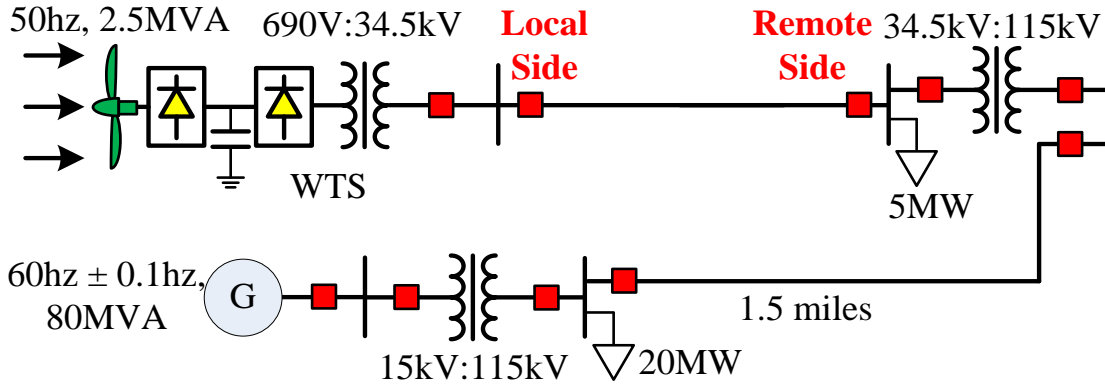


Figure 5-1: Simulation System for Frequency Estimation

One of the objectives of the dynamic state estimator is to provide the best estimate of the frequency and the rate of frequency change at the local (inverter location) and remote side (34.5kV/115kV transformer). Numerical experiments have been performed with different lengths of lines.

Figure 5-2 shows the results of the frequency and rate of frequency change, at the local side (inverter side) of the 34.5kV transmission line. The line is 1.5 miles-long. The first two channels show instantaneous values of three phase measured and DSE estimated voltages. The third and fourth channel shows the actual and estimated frequency and the fourth channel shows the error (difference). We observe that the maximum absolute error is quite small (18.87 μHz). The fifth channel shows the actual and estimated rate of frequency change and the sixth channel shows the error (difference). The error of the estimated rate of frequency change is very small (0.124 mHz/s).

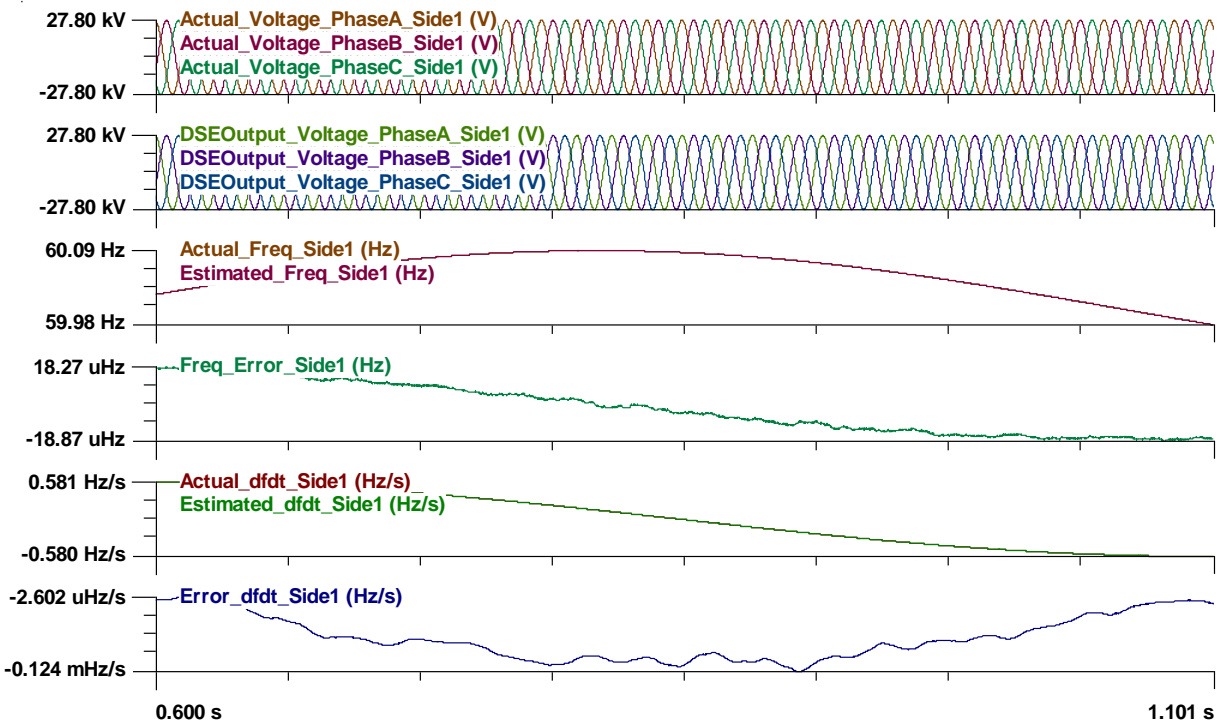


Figure 5-2: Simulation Results, 1.5-Mile Line, Local Side

Figure 5-3 shows the results of the frequency and rate of frequency change, at the remote side of the 34.5kV transmission line. The line is 1.5 miles-long. The first two channels show instantaneous values of three phase measured and DSE estimated voltages. The third and fourth channel shows the actual and estimated frequency and the forth channel shows the error (difference). We observe that the maximum absolute error is quite small (0.177 mHz). The fifth channel shows the actual and estimated rate of frequency change and the sixth channel shows the error (difference). The error of the estimated rate of frequency change is very small (1.144 mHz/s).

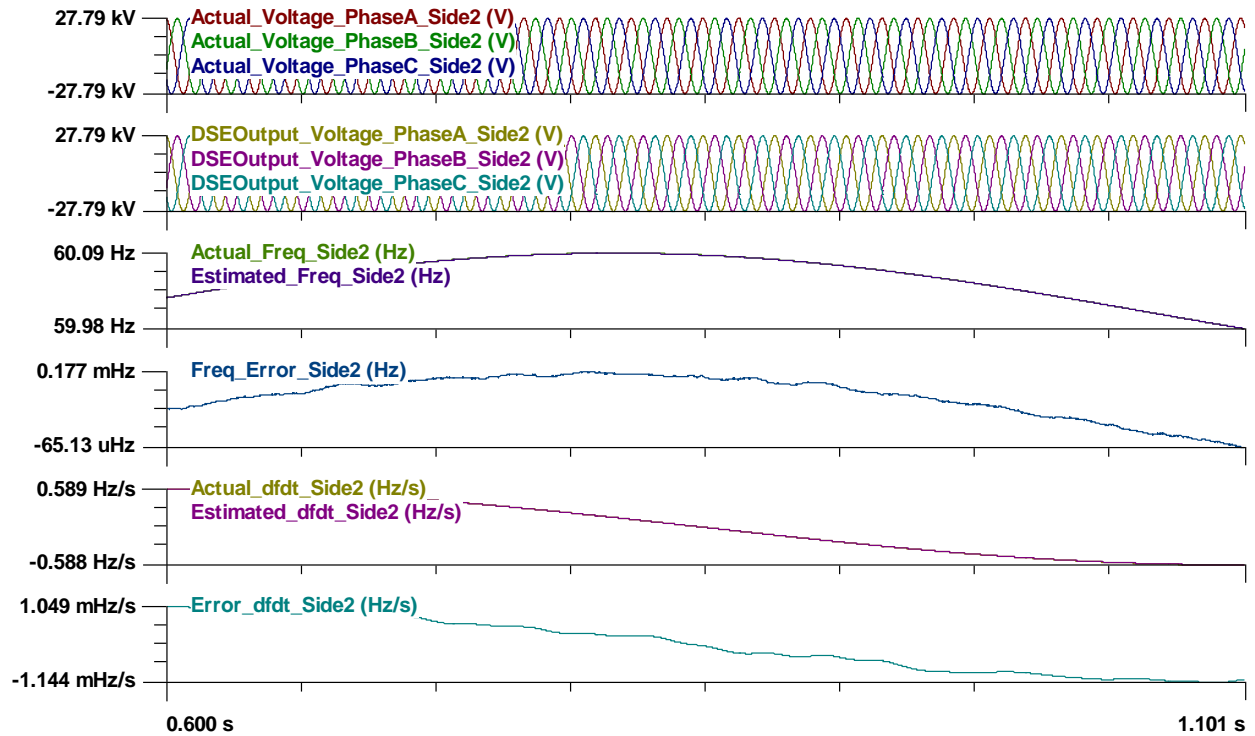


Figure 5-3: Simulation Results, 1.5-Mile Line, Remote Side

Figure 5-4 shows the results of the frequency and rate of frequency change, at the local side (inverter side) of the 34.5kV transmission line. The line is 2.5 miles-long. The first two channels show instantaneous values of three phase measured and DSE estimated voltages. The third and fourth channel shows the actual and estimated frequency and the forth channel shows the error (difference). We observe that the maximum absolute error is quite small (20.05 μHz). The fifth channel shows the actual and estimated rate of frequency change and the sixth channel shows the error (difference). The error of the estimated rate of frequency change is very small (0.128 mHz/s).

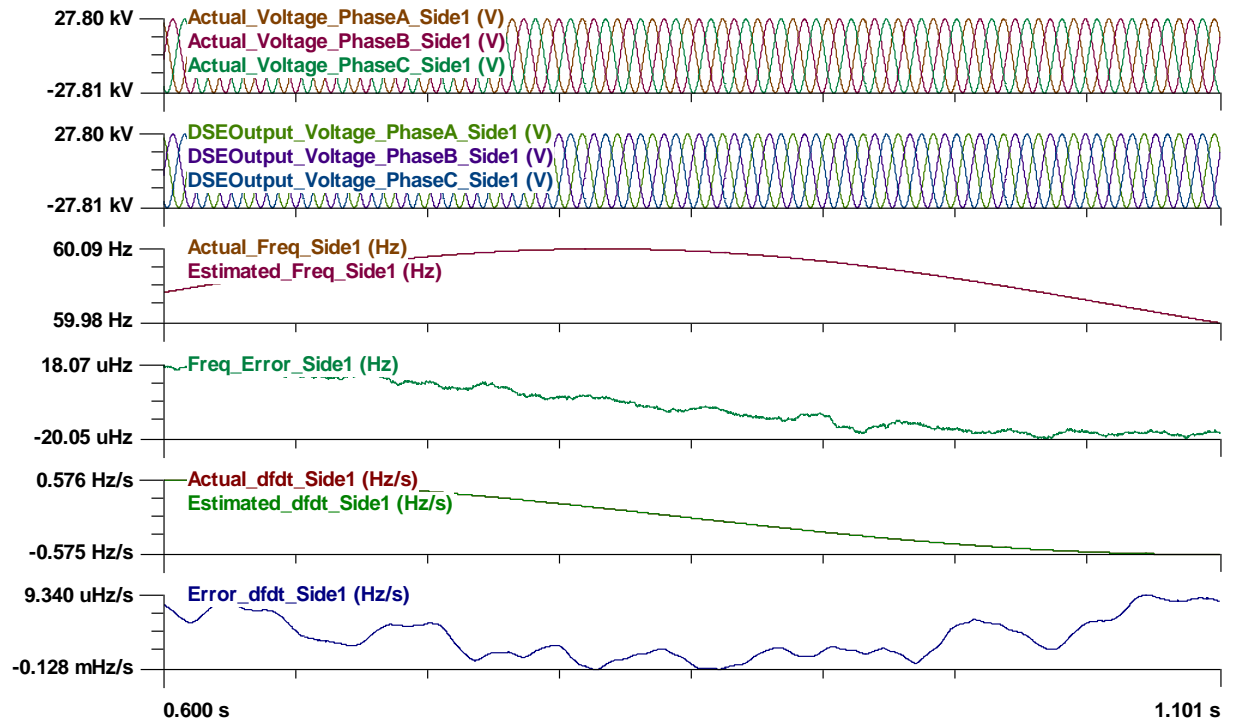


Figure 5-4: Simulation Results, 2.5-Mile Line, Local Side

Figure 5-5 shows the results of the frequency and rate of frequency change, at the remote side of the 34.5kV transmission line. The line is 2.5 miles-long. The first two channels show instantaneous values of three phase measured and DSE estimated voltages. The third and fourth channel shows the actual and estimated frequency and the forth channel shows the error (difference). We observe that the maximum absolute error is quite small (0.282 mHz). The fifth channel shows the actual and estimated rate of frequency change and the sixth channel shows the error (difference). The error of the estimated rate of frequency change is very small (1.906 mHz/s).

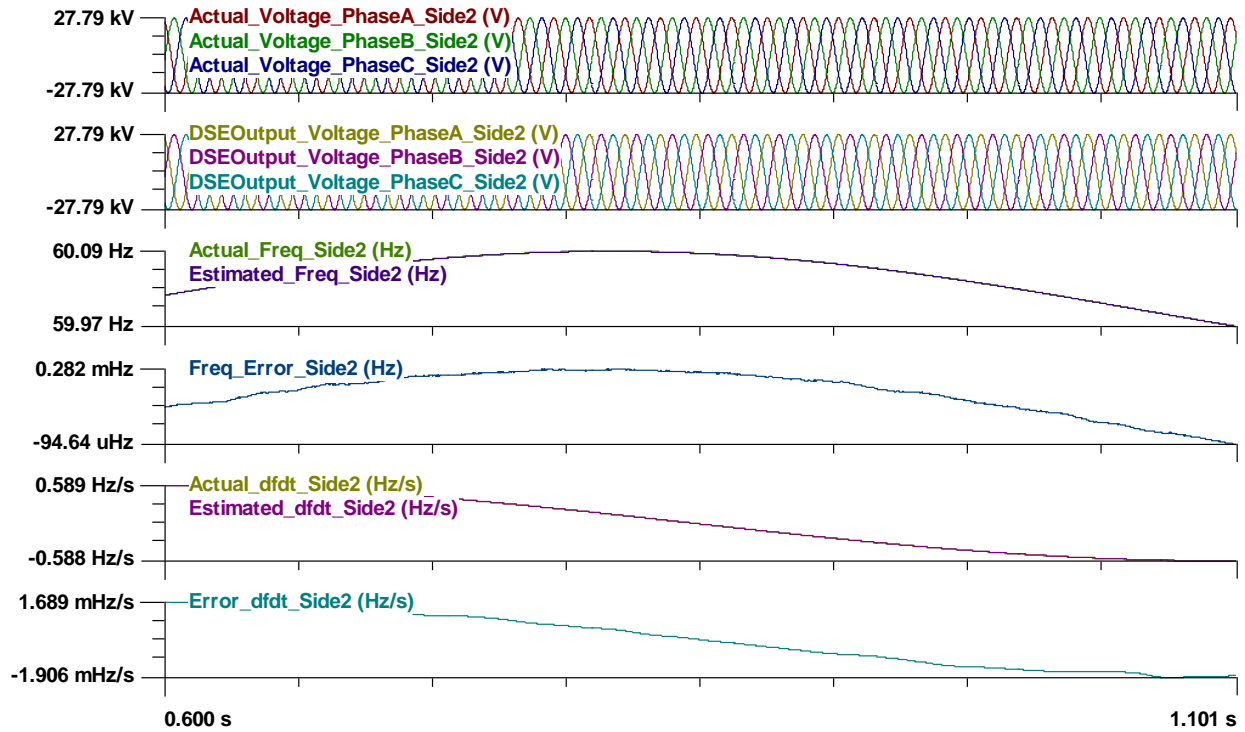


Figure 5-5: Simulation Results, 2.5-Mile-Line, Remote Side

Figure 5-6 shows the results of the frequency and rate of frequency change, at the local side (inverter side) of the 34.5kV transmission line. The line is 4.0 miles-long. The first two channels show instantaneous values of three phase measured and DSE estimated voltages. The third and fourth channel shows the actual and estimated frequency and the forth channel shows the error (difference). We observe that the maximum absolute error is quite small (18.53 μHz). The fifth channel shows the actual and estimated rate of frequency change and the sixth channel shows the error (difference). The error of the estimated rate of frequency change is very small (0.135 mHz/s).

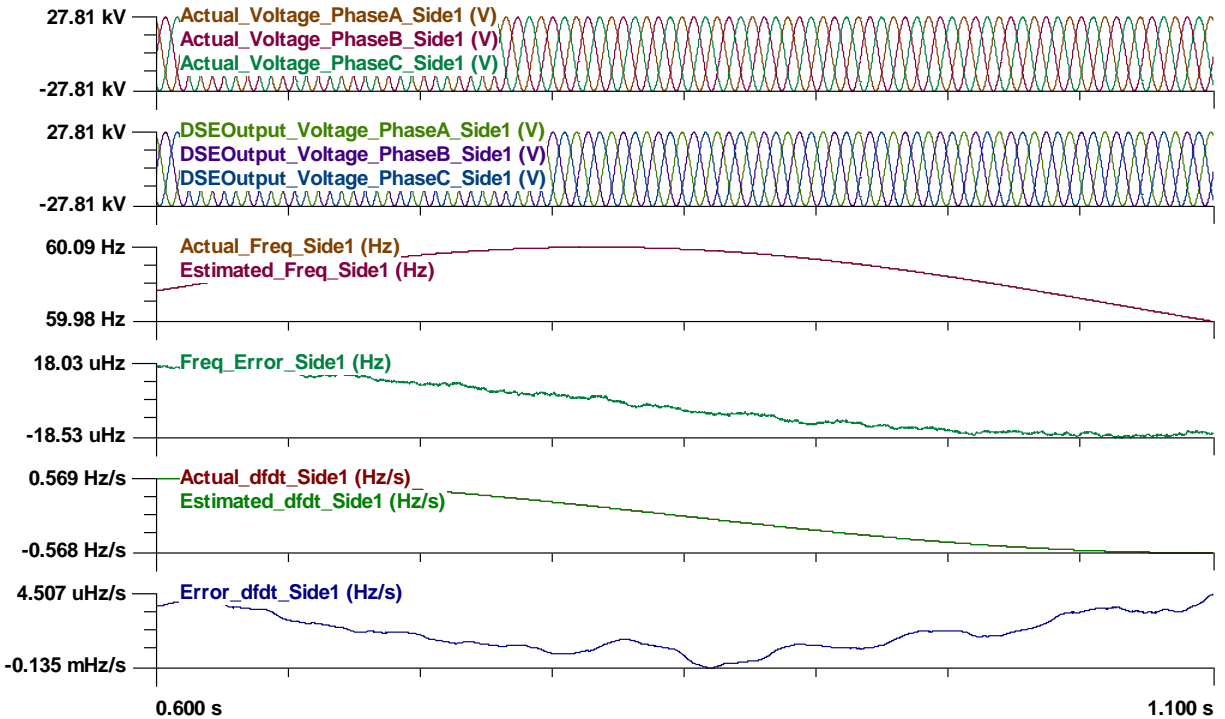


Figure 5-6: Simulation Results, 4-Mile Line, Local Side

Figure 5-7 shows the results of the frequency and rate of frequency change, at the remote side of the 34.5kV transmission line. The line is 4.0 miles-long. The first two channels show instantaneous values of three phase measured and DSE estimated voltages. The third and fourth channel shows the actual and estimated frequency and the forth channel shows the error (difference). We observe that the maximum absolute error is quite small (0.451 mHz). The fifth channel shows the actual and estimated rate of frequency change and the sixth channel shows the error (difference). The error of the estimated rate of frequency change is very small (2.896 mHz/s).

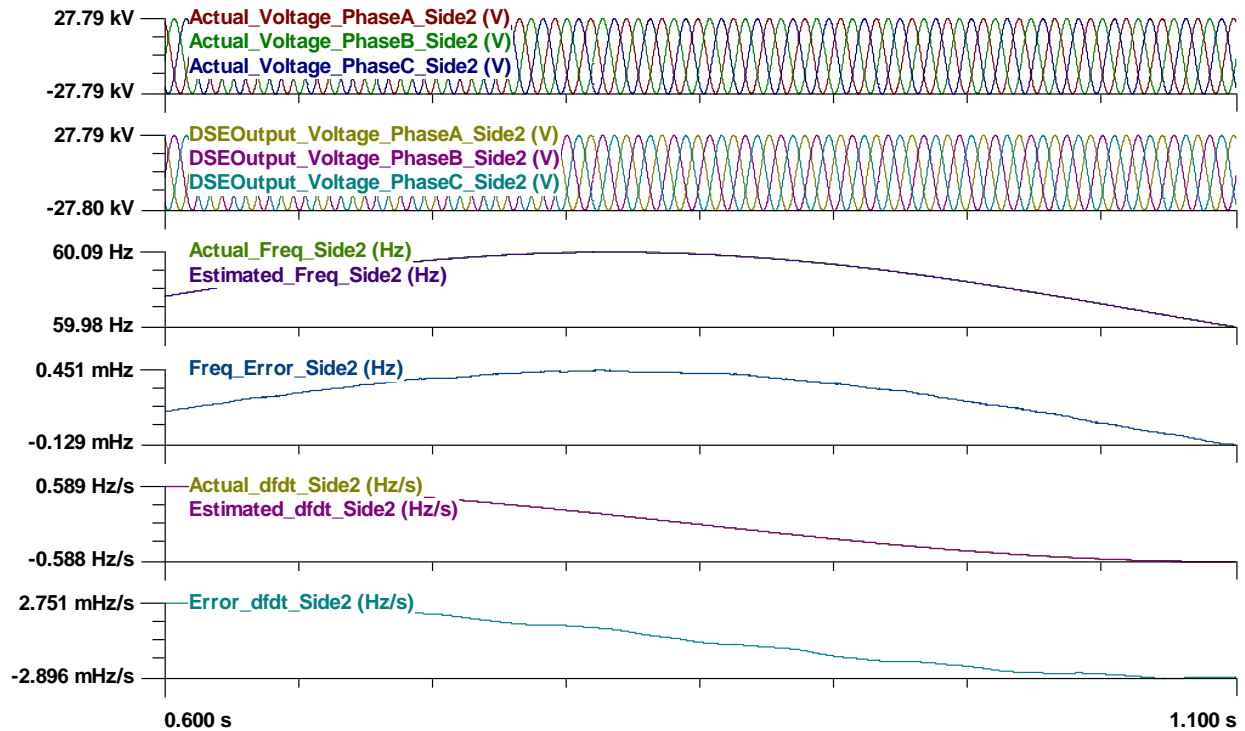


Figure 5-7: Simulation Results, 4-Mile Line, Remote Side

All results are summarized in the Tables 5-1 and 5-2. The frequency varies from 59.98~60.09 Hz, and the rate of frequency change varies from -0.6 ~ 0.6 Hz/s. From the two tables below, the maximum absolute error is within 0.001% for frequency and 0.5% for rate of frequency change. We can conclude that the proposed method can accurately estimate the local and remote side frequency as well as rate of frequency change with local information only.

Table 5-1: Results of Side 1

Case Number	Line length	Frequency Error	dFreq/dt error
1	1.5 miles	$-1.887 \times 10^{-5} \sim 1.827 \times 10^{-5}$ Hz	$-1.24 \times 10^{-4} \sim -2.602 \times 10^{-6}$ Hz/s
2	2.5 miles	$-2.005 \times 10^{-5} \sim 1.807 \times 10^{-5}$ Hz	$-1.28 \times 10^{-4} \sim 9.340 \times 10^{-6}$ Hz/s
3	4 miles	$-1.853 \times 10^{-5} \sim 1.803 \times 10^{-5}$ Hz	$-1.35 \times 10^{-4} \sim 4.507 \times 10^{-6}$ Hz/s

Table 5-2: Results of Side 2

Case Number	Line length	Frequency Error	dFreq/dt error
1	1.5 miles	$-6.513 \times 10^{-5} \sim 1.77 \times 10^{-4}$ Hz	$-1.144 \times 10^{-3} \sim 1.049 \times 10^{-3}$ Hz/s
2	2.5 miles	$-9.464 \times 10^{-5} \sim 2.82 \times 10^{-4}$ Hz	$-1.906 \times 10^{-3} \sim 1.689 \times 10^{-3}$ Hz/s
3	4 miles	$-1.29 \times 10^{-4} \sim 4.51 \times 10^{-4}$ Hz	$-2.896 \times 10^{-3} \sim 2.751 \times 10^{-3}$ Hz/s

5.2 Performance Evaluation of the Supplementary Predictive Inverter Control Enabled by Dynamic State Estimator (DSE)

Numerical experiments were carried out to evaluate the performance of the supplementary predictive inverter control. For each numerical experiment two scenarios were investigated: scenario 1: the proposed supplementary control is disabled and scenario 2: the proposed supplementary control is enabled while keeping the system conditions the same (same set of disturbances).

The numerical experiments were performed using the test system of Figure 5-8. The system consists of a type 4 wind turbine system connected to a step up transformer, a 35 kV transmission circuit, connecting to a collector substation. Part of the power grid beyond the collector substation is shown in Figure 5-8. A number of key components of this system are listed in Table 5-3. Numerical experiments with this system, by enabling the supplementary inverter control indicate that the proposed control practically eliminates valve mis-operations in the inverter when disturbances occur in the system. We present two example cases in the following subsections.

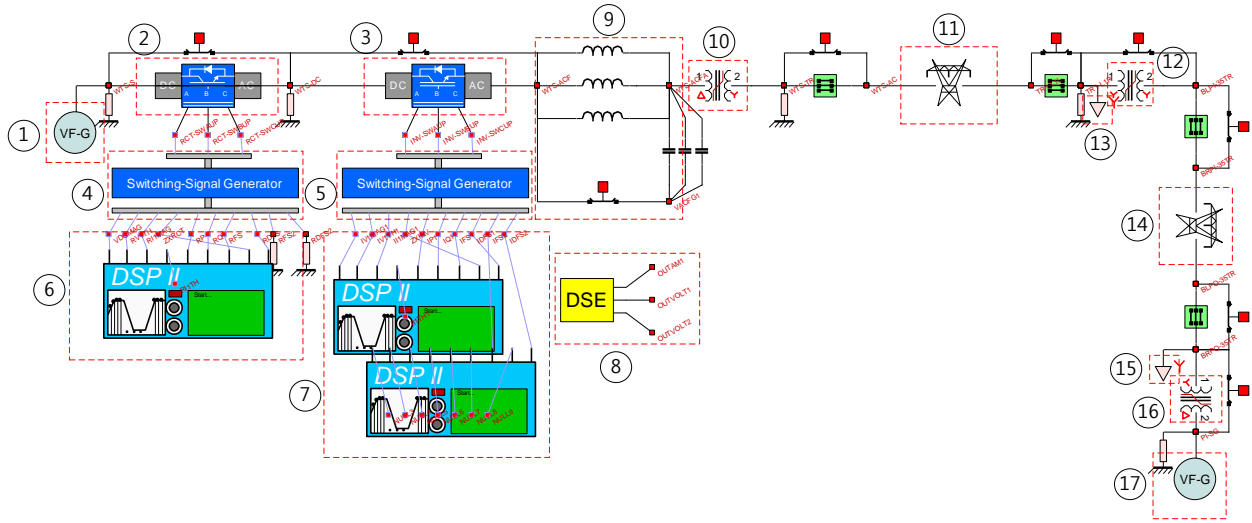


Figure 5-8: Test Bed for the Supplementary Predictive Inverter Control

Table 5-3: List of the Components of the Test Bed

Index	Component
1	Variable-Speed Wind Turbine (0.690 kV / 2.5 MVA)
2	Wind Turbine-Side Converter (0.690 kV / 2.5 MVA)
3	Grid-Side Inverter (0.690 kV / 2.5 MVA)
4	Wind Turbine-Side Converter Controller
5	Grid-Side Inverter Controller
6	Digital Signal Processor (DSP) for Wind Turbine-Side Converter Control
7	DSPs for Grid-Side Inverter Control
8	Dynamic State Estimator (DSE)
9	L-C Filter
10	Delta-Wye Transformer (0.670 kV / 34.5 kV)
11	1.5-Mile Transmission Line (34.5 kV)
12	Wye-Wye Transformer (34.5 kV / 115 kV)
13	Three-Phase Load (34.5 kV / 5 MVA)
14	1.5-Mile Transmission Line (115 kV)
15	Three-Phase Load (115 kV / 20 MVA)
16	Wye-Delta Transformer (115 kV / 15 kV)
17	Variable-Frequency Three-Phase Equivalent Voltage Source (15 kV / 80 MVA)

5.2.1 Case 1: WTS Performance Without Proposed Control Strategy

The system of Figure 5-8 was simulated under the following event: first, the grid-side inverter operates under its own controller. The wind power results in rotor speed corresponding to 50 Hz and the wind has a 10% variability. The power grid experiences an oscillation. At the remote generator, the frequency oscillation is $60\text{Hz} + 0.1\sin(2\pi \cdot t)\text{Hz}$. The grid-side inverter control is set to operate at 2 MW/0.8 kV_{DC} and 0.5 MVar (P-Q control). Any power imbalances in the system are absorbed by the conventional generation.

Simulation results are shown in Figure 5-9 over a period of 4 seconds. The first two traces show the voltages and currents at the output of the inverter. Traces 3 and 4 show the real and reactive power output of the inverter. Note the variability caused by the oscillating conditions of the power grid. Traces 5 show the local and remote phase angles of the phase A voltage at these locations. Traces 6 show the local and remote frequency. Note a small oscillation of frequency across the connecting transmission line. The last trace shows the dc voltage at the inverter input. The transients are caused by the oscillating frequency of the system and involve occasional misoperation of the valves, not shown in the graphs.

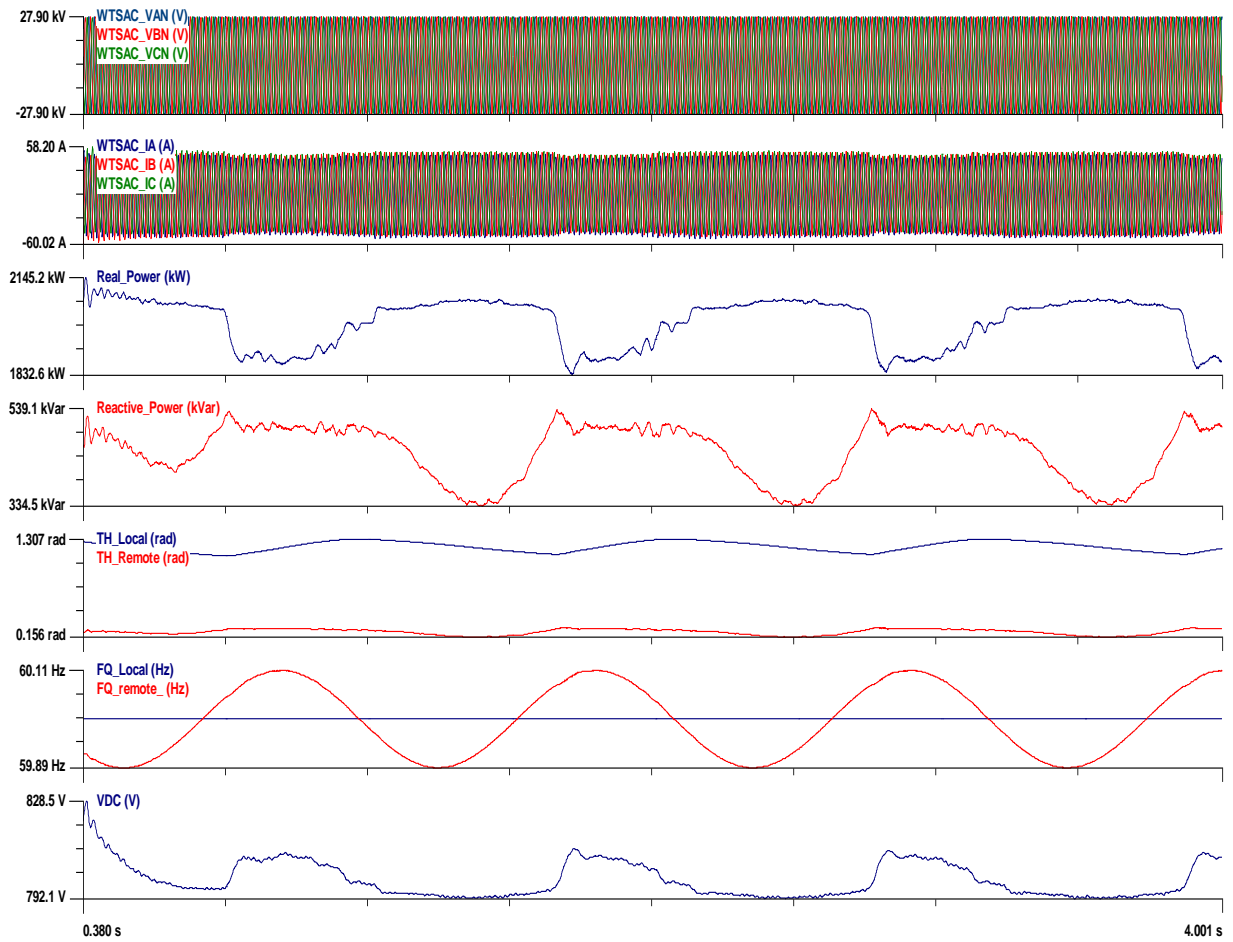


Figure 5-9: Simulation Result when the Proposed Control Is Disabled

5.2.2 Case 2: WTS Performance With Proposed Control Strategy

The system of Figure 5-8 was simulated under the following event: first, the grid-side inverter operates with the supplementary control which injects additional signal to the inverter controller. The wind power results in rotor speed corresponding to 50 Hz and the wind has a 10% variability. The power grid experiences an oscillation. At the remote generator, the frequency oscillation is $60\text{Hz} + 0.1\sin(2\pi \cdot t)\text{Hz}$. The grid-side inverter control is set to operate at 2 MW/0.8 kV_{DC} and 0.5 MVar (P-Q control). Any power imbalances in the system are absorbed by the conventional generation.

Simulation results are shown in Figure 5-10 over a period of 4 seconds. The first two traces show the voltages and currents at the output of the inverter. Traces 3 and 4 show the real and reactive power output of the inverter. Note that the real and reactive power is almost constant, less than 2% variation. Traces 5 show the local and remote phase angles of the phase A voltage at these locations – the difference is controlled to a constant value. Traces 6 show the local and remote frequency. Note the frequency difference across the connecting transmission line is practically zero. The last trace shows the dc voltage at the inverter input. The WTS “follows” and “synchronizes” with the power grid almost perfectly. No valve mis-operations were detected in this case.

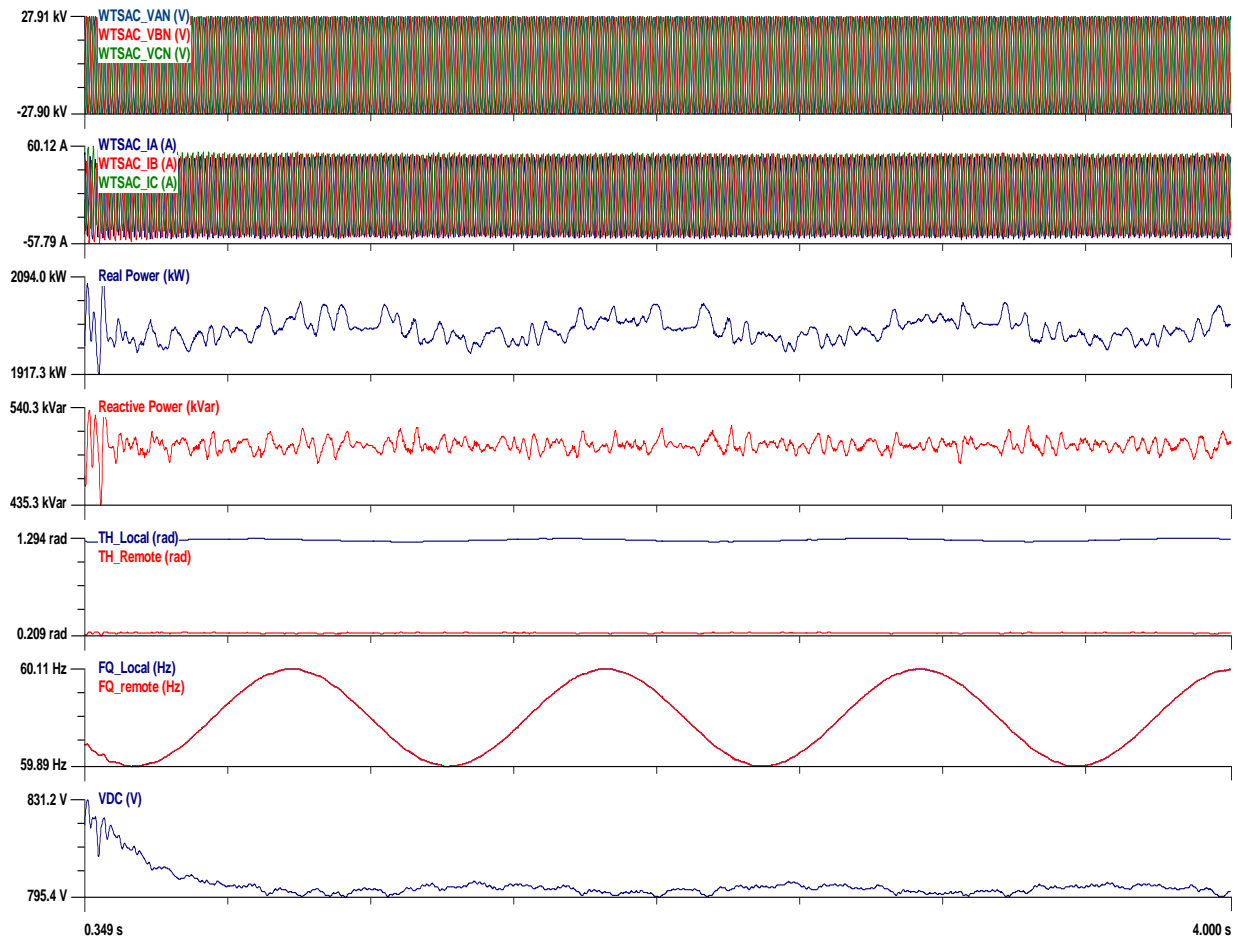


Figure 5-10: Simulation Results when the Proposed Control is Enabled

6. Conclusions and Future Work

This study investigated the issues generated from high penetration of converter-interfaced generation (CIGs) in the power grid. The following issues have been identified:

1. As CIGs are becoming a larger portion of the power grid generation, the fault current levels decrease, causing protection gaps.
2. Present day low voltage ride through strategies will cause severe problems in a system with high penetration CIGs as a disturbance may cause a large number of CIGs to temporarily shut down in ride through mode. While a small number of CIGs may be absorbed by the system, a large number (or a large proportion of the generation going into ride through mode) may result in no recovery of the system. This is unknown territory.
3. Disturbances may cause valve mis-operation in inverter systems and subsequent transients and/or oscillations among the various inverters of the system.

To address these issues, we proposed new methods for protection which do not depend on the fault current level. This protection approach is based on dynamic state estimation methods. To address the issue of stabilizing and synchronizing CIGs with the power grid we proposed and tested the use of dynamic state estimation to provide signal to the inverter controller for supplementary inverter control. The results show that the inverter is synchronized with the power grid under disturbances that may occur remotely from the CIG inverter. This method is very promising as it also eliminates oscillation between CIGs as well.

The application of the proposed method requires an infrastructure that enables dynamic state estimation at each CIG. The technology exists today to provide the required measurements and at the required speeds to perform dynamic state estimation. In essence the method provides full state feedback for the control of the CIGs. While in this project we experimented with one type of supplementary control, the ability to provide full state feedback via the dynamic state estimation opens up the ability to use more sophisticated control methodologies. Future work should focus on utilizing the dynamic state estimation to provide full state feedback and investigate additional control methods. The methods should be integrated with resource management, for example managing the available wind energy (in case of a WTS) or the PV energy, especially in cases that there is some amount of local storage. The dynamic state estimation based protection, should be integrated in such a system.

7. Publications as Direct Result of this Project

Technical Papers

- [1] Liu, Yu; Sakis A.P. Meliopoulos, Rui Fan, and Liangyi Sun. "Dynamic State Estimation Based Protection of Microgrid Circuits," *Proceedings of the IEEE-PES 2015 General Meeting*, Denver, CO, July 26-30, 2015.
- [2] Liu, Yu; Sanghun Choi, Sakis Meliopoulos, Rui Fan, Liangyi Sun, and Zhenyu Tan. "Dynamic State Estimation Enabled Predictive Inverter Control", Accepted, *Proceedings of the IEEE-PES 2016 General Meeting*, Boston, MA, July 17-21, 2016.

ECE Master Thesis

- [1] Weldy, Christopher. Master Thesis "*Stability of a 24-Bus Power System with Converter Interfaced Generation*" Georgia Institute of Technology, 2015.

8. References

- [0] Ackermann, Thomas; Editor. *Wind Power in Power Systems*, John Wiley and Sons, Ltd, second edition, 2012.
- [1] Blaabjerg, Frede; and Ke Ma. "Future on Power Electronics for Wind Turbine Systems," in *IEEE Journal of Emerging and Selected topics in Power Electronics*, vol. 1, no. 3, pp.139-152, September 2013.
- [2] Li, C.; P. Zhan, J. Wen, M. Yao, N. Li and W. J. Lee. "Offshore Wind Farm Integration and Frequency Support Control Utilizing Hybrid Multi-terminal HVDC Transmission," in *IEEE Transactions on Industry Applications*, vol. 50, no. 4, pp. 2788-2797, July/August 2009.
- [3] Miao, L.; J. Wen, H. Xie, C. Yue and W. J. Lee. "Coordinated Control Strategy of Wind Turbine Generator and Energy Storage Equipment for Frequency Support," in *IEEE Transactions on Industry Applications*, vol. 51, no. 4, pp 2732-2742, July/August 2015.
- [4] Gowaid, I. A.; A. El-Zawawi, and M. El-Gammal. "Improved inertia and frequency support from grid-connected DFIG wind farms," in *Proceeding of IEEE PES Power System Conference Exposition*, pp. 1-9. 2011.
- [5] Gonzalez-Longatt, F.M. "Activation Schemes of Synthetic Inertia Controller on Full Converter Wind Turbine (Type 4)", in *2015 IEEE Power and Energy Society General Meeting (PES 2015)*, pp. 1-5, July 26-30, 2015.
- [6] Lalor, G.; A. Mullane, and M. O'Malley. "Frequency Control and Wind Turbine Technologies," in *IEEE Transactions on Power System*, vol. 20, no. 4, pp. 1905-1913, November 2005.
- [7] Arani, M. F. M.; and E. F. El-Saadany. "Implementing virtual inertia in DFIG-based wind power generation," in *IEEE Transactions on Power System*, vol. 28, no. 2, pp. 1373-1384, June 2013.
- [8] Baran, M. E.; and N. R. Mahajan. "Overcurrent Protection on Voltage-Source-Converter-Based Multi-terminal DC Distribution Systems," in *IEEE Transactions on Power Delivery*, vol. 22, no. 1, pp. 406-412, January 2007.
- [9] Kamwa, I.; R. Grondin, and Y. Hebert. "Wide-Area Measurement Based Stabilizing Control of Large Power Systems-A Decentralized/Hierarchical Approach," in *IEEE Transactions on Power Systems*, vol. 16, no. 1, pp. 136-153, February 2001.
- [10] Fang, Xi; Satyajayant Misra, Guoliang Xue, and Dejun Yang. "Smart Grid - The New and Improved Power Grid: A Survey," in *IEEE Communications Survey & Tutorials*, vol. 14, no. 4, pp. 944-980, December 2011.
- [11] Mitter, C. S.; A. R. Hefner, D. Y. Chen, and F. C. Lee. "Insulated Gate Bipolar Transistor (IGBT) Modeling using IG-SPICE," in *IEEE Trans. on Industry Applications*, vol. 30, no. 1, pp. 24-33, August 2002.
- [12] Hefner, A. R. "A Dynamic Electro-Thermal Model for IGBT," in *IEEE Trans. on Industry Applications*, vol. 30, no. 2, pp. 394-405, August 2002.
- [13] Hefner, A. R. "Modeling Power Semiconductor Devices for Realistic Simulation," in *IEEE 4th Workshop on Computers in Power Electronics*, pp. 11-44, August 1994.

- [14] Kuang, S.; B. W. Williams, and S. J. Finney. "A Review of IGBT Models," in *IEEE Trans. on Power Electronics*, vol. 15, no. 6, pp. 1250-1266, August 2002.
- [15] Biswas, S. K.; B. Basak, and K. S. Rajashekara. "A Review of IGBT Models," in *IEEE Industry Applications Society Annual Meeting*, vol. 2, pp. 1483-1489, September 1991.
- [16] Dommel, H. W. "Digital Computer Solution of Electromagnetic Transients in Single-and Multiphase Networks," in *IEEE Transactions on Power Apparatus and Systems*, no. 4, pp. 388-399, January 2007.
- [17] Johnson, R. B. I.; B. J. Cory, and M. J. Short. "A Tunable Integration Method for the Simulator of Power System Dynamics," in *IEEE Transactions on Power Systems*, vol. 3, no. 4, pp. 1530-1537, August 2002.
- [18] Yen, K. K.; Z. Hu, and J. Andrian. "Stability Study of Parallel Predictor-Corrector Numerical Integration Algorithms and Redesign," in *IEEE Proceedings Energy and Information Technologies in the Southeast*, vol. 2, pp. 417-420, April 1989.
- [19] Van Den Bosch, P. P. J.; and H. R. Visser. "Simulation of State-Events in Power Electronic Devices," in *Fourth International Conference on Power Electronics and Variable-Speed Drives, IEEE Proceedings Energy and Information Technologies in the Southeast*, pp. 184-189, 1990.
- [20] Kato, T.; and K. Ikeuchi. "Variable Order and Variable Step-Size Integration Method for Transient Analysis Programs," in *IEEE Transactions on Power Systems*, vol. 6, no. 1, pp. 206-213, August 2002.
- [21] Kato, T.; and T. Kataoka. "Computer-Aided Analysis of a Power Electronic Circuit by a New Multi-rate Method," in *IEEE Power Electronics Specialist Conference*, vol. 2, pp. 1076-1083, May 1998.
- [22] Takano, H.; S. M. Ulhaq, and M. Nakaoka. "Computer-aided simulation technique of digitally controlled switched-mode power conversion circuits and systems using state variable matrices," in *IEEE Proceedings of the Power Conversion Conference*, vol. 1, pp. 411-418, August 1997.
- [23] Pejovic, P.; and D. Maksimovic. "PETs-a Simulation Tool for Power Electronics," in *IEEE Workshop on Computers in Power Electronics*, pp. 1-8, August 1996.
- [24] Dinavahi, V. R.; M. R. Iravani, and R. Boner. "Real-Time Digital Simulation of Power Electronic Apparatus Interfaced With Digital Controllers," in *IEEE Transactions on Power Delivery*, vol. 16, no. 4, pp. 775-781, August 2002.
- [25] Blaabjerg, F.; R. Teodorescu, M. Liserre, and A. V. Timbus. "Overview of Control and Grid Synchronization for Distributed Power Generation Systems," in *IEEE Transactions on Industrial Electronics*, vol. 53, no. 5, pp. 1398-1409, October 2006.
- [26] Saccomando, G.; and J. Svensson. "Transient operation of grid-connected voltage source converter under unbalanced voltage conditions," in *IEEE Thirty-Sixth IAS Annual Meeting Conference*, vol. 4, pp. 2419-2424, September 2001.
- [27] Agirman, I.; and V. Blasko. "A Novel Control Method of a VSC without AC Line Voltage Sensors," in *IEEE Transactions on Industry Applications*, vol. 39, no. 2, pp. 519-524, March 2003.

- [28] Teodorescu, R.; and F. Blaabjerg. "Flexible Control of Small Wind Turbines With Grid Failure Detection Operating in Stand-Alone and Grid-Connected Mode," in *IEEE Transactions on Power Electronics*, vol. 19, no. 5, pp. 1323-1332, September 2004.
- [29] Teodorescu, R.; F. Blaabjerg, U. Borup, and M. Liserre. "A New Control Structure for Grid-Connected LCL PV Inverters with Zero Steady-State Error and Selective Harmonic Compensation," in *IEEE Applied Power Electronics Conference and Exposition 2004*, vol. 1, pp. 580-586, 2004.
- [30] Song, S.; S. Kang, and N. Hahm. "Implementation and control of grid connected AC-DC-AC power converter for variable speed wind energy conversion system," in *IEEE Applied Power Electronics Conference and Exposition 2004*, vol. 1, pp. 154-158, 2003.
- [31] Zhu, H.; B. Arnet, L. Haines, E. Shaffer, and J. Lai. "Grid Synchronization Control without AC Voltage Sensors," in *IEEE Applied Power Electronics Conference and Exposition 2003*, vol. 1, pp. 172-178, 2003.
- [32] Ramos, C. J.; A. P. Martins, A. S. Araujo, and A. S. Carvalho. "Current Control in the Grid Connection of the Double-Output Induction Generator Linked to a Variable Speed Wind Turbine," in *IEEE 2002 Annual Conference of Industrial Electronics Society*, vol. 2, pp. 979-984, 2002.
- [33] Candusso, D.; I. Valero, and A. Walter. "Modelling, Control and Simulation of a Fuel Cell Based Power Supply System with Energy Management," in *IEEE 2002 Annual Conference of Industrial Electronics Society*, vol. 2, pp. 1294-1299, 2002.
- [34] Teodorescu, R.; F. Iov, and F. Walter. "Flexible Development and Test Systems for 11 kW Wind Turbine," in *IEEE 34th Annual Power Electronics Specialist Conference*, vol. 1, pp. 67-72, June 2003.
- [35] Twining, E.; and D. G. Holmes. "Grid Current Regulation of a Three-Phase Voltage Source Inverter With an LCL Input Filter," in *IEEE Transactions on Power Electronics*, vol. 18, no. 3, pp. 888-895, May 2003.
- [36] Fukuda, S.; and T. Yoda. "A Novel Current-Tracking Method for Active Filters Based on a Sinusoidal Internal Model," in *IEEE Transactions on Industrial Applications*, vol. 37, no. 3, pp. 888-895, May 2001.
- [37] Zmood, D. N.; and D. G. Holmes. "Stationary Frame Current Regulation of PWM Inverters with Zero Steady-State Error," in *IEEE Trans. on Power Electronics*, vol. 18, no. 3, pp. 814-822, May 2003.
- [38] Ciobotaru, M.; R. Teodorescu, and F. Blaabjerg. "Control of Single-Stage Single-phase PV Inverter," in *2005 European Conference on Power Electronics and Applications*, pp. 1-10, 2005.
- [39] Malesani, L.; and P. Tenti. "A Novel Hysteresis Control Method for Current-Controlled Voltage-Source PWM Inverters with Constant Modulation Frequency," in *IEEE Transactions on Industrial Applications*, pp. 88-92, February 1990.
- [40] Meliopoulos, Sakis A.P.; G. J. Cokkinides, and G. K. Stefopoulos. "Quadratic Integration Method," presented at the *International Conference on Power Systems Transients (IPST 2015)*, Paper No. IPST05 - 231, June 15-18, 2005.
- [41] Arrillaga, J.; M. H. J. Bollen, and N.R. Watson. "Power Quality Following Deregulation," in *Proceedings of the IEEE*, vol. 88, no. 2, pp. 246-261, February 2000.

- [42] Novosel, D.; V. Madani, B. Bhargave, Vu. Khoi, and J. Cole. "Dawn of the Grid Synchronization," in *IEEE Power and Energy Magazine*, vol. 6, no. 1, pp. 49-60, February 2008.
- [43] Gungor, V. C.; D. Sahin, T. Kocak, S. Ergut, C. Buccella, C. Cecati, and G. P. Hancke. "A Survey on Smart Grid Potential Applications and Communication Requirements," in *IEEE Transactions on Industrial Informatics*, vol. 9, no. 1, pp. 28-42, September 2012.
- [44] Agrawal, G. P. *Fiber-Optic Communication Systems*, John Wiley & Sons, 2002.
- [45] Kamwa, I.; S. R. Samantaray, and G. Joos. "Wide Frequency Range Adaptive Phasor and Frequency PMU Algorithms," in *IEEE Transactions on Smart Grid*, vol. 5, no. 2, pp. 569-579, February 2014.
- [46] Romano, P.; and M. Paolone. "Enhanced Interpolated-DFT for Synchrophasor Estimation in FPGAs: Theory, Implementation, and Validation of a PMU Prototype," in *IEEE Transactions on Instrumentation and Measurement*, vol. 63, no. 12, pp. 2824-2836, November 2014.
- [47] Kamwa, I.; S. R. Samantaray, and G. Joos. "Compliance Analysis of PMU Algorithms and Devices for Wide-Area Stabilizing Control of Large Power Systems," in *IEEE Transactions on Power Systems*, vol. 28, no. 2, pp. 1766-1778, April 2013.
- [48] Chen, C. "A Two-Stage Solution Procedure for Digital Power Metering According to IEEE Standard 1459-2010 in Single-Phase System," in *IEEE Transactions on Industrial Electronics*, vol. 60, no. 12, pp. 5550-5557, June 2013.

9. Appendix A: The Quadratic Integration Method

This section presents the description of the quadratic integration. The quadratic integration starts from the dynamic model of a component. We refer to this as the compact model. Then, the quadratic integration method consists of two consecutive steps [40].

First, the nonlinear differential equations of the compact model of an actual device are reformulated to fully equivalent quadratic equations by introducing additional states and algebraic equations if the nonlinear differential equations have higher-order terms than the second degree. The procedure results in the following quadratized device model:

$$\begin{aligned}
 i(t) &= Y_{eqx1} \mathbf{x}(t) + Y_{equ1} \mathbf{u}(t) + D_{eqxd1} \frac{d\mathbf{x}(t)}{dt} + C_{eqc1} \\
 0 &= Y_{eqx2} \mathbf{x}(t) + Y_{equ2} \mathbf{u}(t) + D_{eqxd2} \frac{d\mathbf{x}(t)}{dt} + C_{eqc2} \\
 0 &= Y_{eqx3} \mathbf{x}(t) + Y_{equ3} \mathbf{u}(t) + \left\{ \mathbf{x}(t)^T \left\langle F_{eqxx3}^i \right\rangle \mathbf{x}(t) \right\} + \left\{ \mathbf{u}(t)^T \left\langle F_{equu3}^i \right\rangle \mathbf{u}(t) \right\} + \left\{ \mathbf{u}(t)^T \left\langle F_{equx3}^i \right\rangle \mathbf{x}(t) \right\} + C_{feqc3}
 \end{aligned} \tag{Eq. A-1}$$

Second, the quadratized model from the first step is integrated using an implicit numerical scheme assuming that the states of the quadratized model vary quadratically within a time step h . This assumption is shown in Figure A-1.

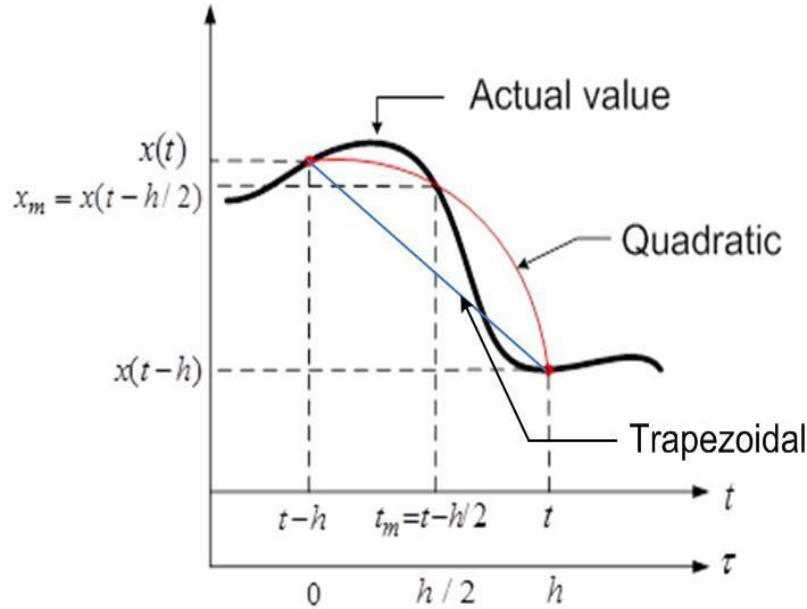


Figure A-1: Illustration of the Quadratic Integration Method

The quadratic integration method is applied to every set of equations separately in the quadratized device model. Since there are three sets of equations, each one is analyzed below to show how they can be transferred to State and Control Algebraic Quadratic Companion Form (SCAQCF). The model is obtained for a given time step h as follows:

1) Through variable equations:

$$i(t) = Y_{eqx1} \mathbf{x}(t) + Y_{equ1} \mathbf{u}(t) + D_{eqxd1} \frac{d\mathbf{x}(t)}{dt} + C_{eqc1}$$

After applying quadratic integration, we have

From time $t-h$ to t ,

$$i(t) = \left(\frac{4}{h} D_{eqxd1} + Y_{eqx1}\right) \mathbf{x}(t) + Y_{equ1} \mathbf{u}(t) - \frac{8}{h} D_{eqxd1} \mathbf{x}(t_m) + \left(\frac{4}{h} D_{eqxd1} - Y_{eqx1}\right) \mathbf{x}(t-h) + i(t-h) - Y_{equ1} \mathbf{u}(t-h)$$

From time $t-h$ to t_m ,

$$i(t_m) = \frac{1}{2h} D_{eqxd1} \mathbf{x}(t) + \left(\frac{2}{h} D_{eqxd1} + Y_{eqx1}\right) \mathbf{x}(t_m) + Y_{equ1} \mathbf{u}(t_m) + \left(\frac{1}{2} Y_{eqx1} - \frac{5}{2h} D_{eqxd1}\right) \mathbf{x}(t-h) - \frac{1}{2} i(t-h) + \frac{1}{2} Y_{equ1} \mathbf{u}(t-h) + \frac{3}{2} C_{eqc1}$$

2) Linear virtual equations:

$$0 = Y_{eqx2} \mathbf{x}(t) + Y_{equ2} \mathbf{u}(t) + D_{eqxd2} \frac{d\mathbf{x}(t)}{dt} + C_{eqc2}$$

After applying quadratic integration, we have

From time $t-h$ to t ,

$$0 = (D_{eqxd2} + \frac{h}{6} Y_{eqx2}) \mathbf{x}(t) + \frac{h}{6} Y_{equ2} \mathbf{u}(t) + \frac{2h}{3} Y_{eqx2} \mathbf{x}(t_m) + \frac{2h}{3} Y_{equ2} \mathbf{u}(t_m) + \left(\frac{h}{6} Y_{eqx2} - D_{eqxd2}\right) \mathbf{x}(t-h) + \frac{h}{6} Y_{equ2} \mathbf{u}(t-h) + h C_{eqc2}$$

From time $t-h$ to t_m ,

$$0 = -\frac{h}{24} Y_{eqx2} \mathbf{x}(t) - \frac{h}{24} Y_{equ2} \mathbf{u}(t) + (D_{eqxd2} + \frac{h}{3} Y_{eqx2}) \mathbf{x}(t_m) + \frac{h}{3} Y_{equ2} \mathbf{u}(t_m) + \left(\frac{5h}{24} Y_{eqx2} - D_{eqxd2}\right) \mathbf{x}(t-h) + \frac{5h}{24} Y_{equ2} \mathbf{u}(t-h) + \frac{h}{2} C_{eqc2}$$

3) Nonlinear equations

$$0 = Y_{eqx3} \mathbf{x}(t) + Y_{equ3} \mathbf{u}(t) + \begin{Bmatrix} \vdots \\ \mathbf{x}(t)^T \langle F_{eqxx3}^i \rangle \mathbf{x}(t) \\ \vdots \end{Bmatrix} + \begin{Bmatrix} \vdots \\ \mathbf{u}(t)^T \langle F_{equu3}^i \rangle \mathbf{u}(t) \\ \vdots \end{Bmatrix} + \begin{Bmatrix} \vdots \\ \mathbf{u}(t)^T \langle F_{equx3}^i \rangle \mathbf{x}(t) \\ \vdots \end{Bmatrix} + C_{eqc3}$$

These equations are the same under time t and time t_m

$$0 = Y_{eqx3} \mathbf{x}(t) + Y_{equ3} \mathbf{u}(t) + \begin{Bmatrix} \vdots \\ \mathbf{x}(t)^T \langle F_{eqxx3}^i \rangle \mathbf{x}(t) \\ \vdots \end{Bmatrix} + \begin{Bmatrix} \vdots \\ \mathbf{u}(t)^T \langle F_{equu3}^i \rangle \mathbf{u}(t) \\ \vdots \end{Bmatrix} + \begin{Bmatrix} \vdots \\ \mathbf{u}(t)^T \langle F_{equx3}^i \rangle \mathbf{x}(t) \\ \vdots \end{Bmatrix} + C_{eqc3}$$

$$0 = Y_{eqx3} \mathbf{x}(t_m) + Y_{equ3} \mathbf{u}(t_m) + \begin{Bmatrix} \vdots \\ \mathbf{x}(t_m)^T \langle F_{eqxx3}^i \rangle \mathbf{x}(t_m) \\ \vdots \end{Bmatrix} + \begin{Bmatrix} \vdots \\ \mathbf{u}(t_m)^T \langle F_{equu3}^i \rangle \mathbf{u}(t_m) \\ \vdots \end{Bmatrix} + \begin{Bmatrix} \vdots \\ \mathbf{u}(t_m)^T \langle F_{equx3}^i \rangle \mathbf{x}(t_m) \\ \vdots \end{Bmatrix} + C_{eqc3}$$

By restructuring and stacking the above three sets of equations into one matrix form, the standard time domain SCAQCF model is obtained:

$$\begin{Bmatrix} i(t) \\ 0 \\ 0 \\ i(t_m) \\ 0 \\ 0 \end{Bmatrix} = Y_{eqx} \mathbf{x} + Y_{equ} \mathbf{u} + \begin{Bmatrix} \vdots \\ \vdots \\ \vdots \end{Bmatrix} + \begin{Bmatrix} \vdots \\ \vdots \\ \vdots \end{Bmatrix} + \begin{Bmatrix} \vdots \\ \vdots \\ \vdots \end{Bmatrix} - B_{eq} \quad (\text{Eq. A-2})$$

$$B_{eq} = -N_{eqx} \mathbf{x}(t-h) - N_{equ} \mathbf{u}(t-h) - M_{eq} i(t-h) - K_{eq}$$

where:

$$Y_{eqx} = \begin{bmatrix} \frac{4}{h} D_{eqxd1} + Y_{eqx1} & -\frac{8}{h} D_{eqxd1} \\ D_{eqxd2} + \frac{h}{6} Y_{eqx2} & \frac{2h}{3} Y_{eqx2} \\ Y_{eqx3} & 0 \\ \frac{1}{2h} D_{eqxd1} & \frac{2}{h} D_{eqxd1} + Y_{eqx1} \\ -\frac{h}{24} Y_{eqx2} & D_{eqxd2} + \frac{h}{3} Y_{eqx2} \\ 0 & Y_{eqx3} \end{bmatrix}$$

$$Y_{equ} = \begin{bmatrix} Y_{equ1} & 0 \\ \frac{h}{6} Y_{equ2} & \frac{2h}{3} Y_{equ2} \\ Y_{equ3} & 0 \\ 0 & Y_{equ1} \\ -\frac{h}{24} Y_{equ2} & \frac{h}{3} Y_{equ2} \\ 0 & Y_{equ3} \end{bmatrix}$$

$$F_{eqx} = \begin{bmatrix} 0 & 0 \\ 0 & 0 \\ F_{eqxx3} & 0 \\ 0 & 0 \\ 0 & 0 \\ 0 & Y_{eqxx3} \end{bmatrix}$$

$$F_{equ} = \begin{bmatrix} 0 & 0 \\ 0 & 0 \\ F_{equu3} & 0 \\ 0 & 0 \\ 0 & 0 \\ 0 & Y_{equu3} \end{bmatrix}$$

$$F_{equx} = \begin{bmatrix} 0 & 0 \\ 0 & 0 \\ F_{equx3} & 0 \\ 0 & 0 \\ 0 & 0 \\ 0 & Y_{equx3} \end{bmatrix}$$

$$N_{eqx} = \begin{bmatrix} -Y_{eqx1} + \frac{4}{h}D_{eqxd1} \\ \frac{h}{6}Y_{eqx2} - D_{eqxd1} \\ 0 \\ \frac{1}{2}Y_{eqx1} - \frac{5}{2h}D_{eqxd1} \\ \frac{5h}{24}Y_{eqx2} - D_{eqxd1} \\ 0 \end{bmatrix}$$

$$N_{equ} = \begin{bmatrix} -Y_{equ1} \\ \frac{h}{6}Y_{equ2} \\ 0 \\ \frac{1}{2}Y_{equ1} \\ \frac{5h}{24}Y_{equ2} \\ 0 \end{bmatrix}$$

$$M_{eq} = \begin{bmatrix} I_{size(i(t))} \\ 0 \\ 0 \\ -\frac{1}{2}I_{size(i(t))} \\ 0 \\ 0 \end{bmatrix}$$

$$K_{eq} = \begin{bmatrix} 0 \\ hC_{eqc2} \\ C_{eqc3} \\ \frac{3}{2}C_{eqc1} \\ \frac{1}{2}hC_{eqc1} \\ C_{eqc3} \end{bmatrix}$$

$i(t)$ and $i(t_m)$: Through variables of the device model

\mathbf{x} : External and internal state variables of the device model, $\mathbf{x} = [\mathbf{x}(t), \mathbf{x}(t_m)]$

\mathbf{u} : Control variables of the device model, i.e. transformer tap, etc. $\mathbf{u} = [\mathbf{u}(t), \mathbf{u}(t_m)]$

Y_{eqx} : Matrix defining the linear part for state variables,

F_{eqx} : Matrices defining the quadratic part for state variables,

Y_{equ} : Matrix defining the linear part for control variables,

F_{equ} : Matrices defining the quadratic part for control variables,

F_{equx} : Matrices defining the quadratic part for the product of state and control variables,

B_{eq} : History dependent vector of the device model,

N_{eqx} : Matrix defining the last integration step state variables part,

N_{equ} : Matrix defining the last integration step control variables part,

M_{eq} : Matrix defining the last integration step through variables part,

K_{eq} : Constant vector of the device model.

10. Appendix B: Model Description of Three-Phase Transmission Line

This Appendix presents the model of a three phase transmission line. We introduce the model of the transmission line by two steps: first, we describe the QDM of a single-section transmission line; second, we describe the QDM of a multi-section transmission line model. This multi-section QDM can be directly used to form the SCAQCF model according to Appendix A.

B-1: QDM of single-section transmission line model

Figure B-1 gives the model of the single-section π -equivalent transmission line.

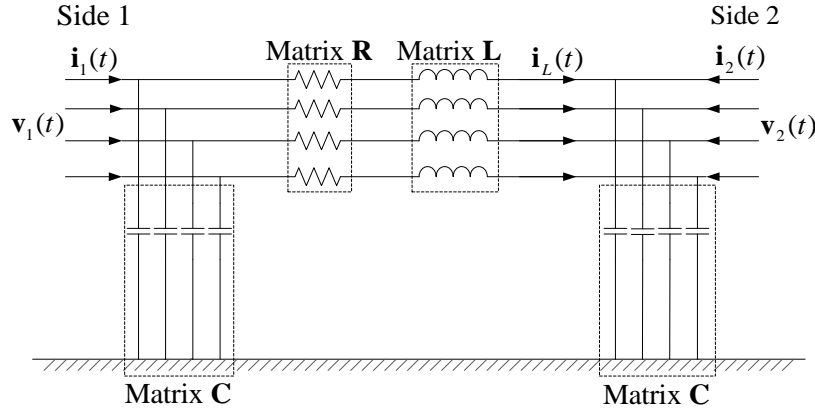


Figure B-1: The Single-Section Three-Phase Transmission Line Model

The QDM of transmission line is derived from this circuit and it is given with the following equations:

$$\begin{aligned} i_1(t) &= C \cdot \frac{dv_1(t)}{dt} + i_L(t) \\ i_2(t) &= C \cdot \frac{dv_2(t)}{dt} - i_L(t) \\ 0 &= -v_1(t) + v_2(t) + R \cdot i_L(t) + L \cdot \frac{di_L(t)}{dt} \end{aligned} \quad (\text{Eq. B-1})$$

Note that for above model equations do not include any control variables. The standard format of QDM is given in Eq. A-1. The QDM parameters of transmission lines are as follows:

$$i(t) = [i_1(t) \ i_2(t)]^T; \ x(t) = [v_1(t) \ v_2(t) \ i_L(t)]^T; \ Y_{eqx1} = \begin{bmatrix} 0 & 0 & I_4 \\ 0 & 0 & -I_4 \end{bmatrix};$$

$$D_{eqx1} = \begin{bmatrix} C & 0 & 0 \\ 0 & C & 0 \end{bmatrix}; \ Y_{eqx2} = [-I_4 \ I_4 \ R]; \ D_{eqx1} = [0 \ 0 \ L];$$

all other vectors and matrices are null; and,

$$\begin{aligned}
i(t) &= [i_{a1}(t) \quad i_{bn}(t)]^T; \quad x(t) = [v_1(t) \quad v_{n+1}(t) \quad v_2(t) \quad v_3(t) \quad \cdots \quad v_n(t) \quad i_{L1}(t) \quad i_{L2}(t) \quad \cdots \quad i_{Ln}(t)]^T; \\
Y_{eqx1} &= \begin{bmatrix} G_1 & 0 & 0 & 0 & \cdots & 0 & I_4 & 0 & \cdots & 0 \\ 0 & G_1 & 0 & 0 & \cdots & 0 & 0 & 0 & \cdots & -I_4 \end{bmatrix}; \quad D_{eqxd1} = \begin{bmatrix} C_1 & 0 & 0 & 0 & \cdots & 0 & 0 & 0 & \cdots & 0 \\ 0 & C_1 & 0 & 0 & \cdots & 0 & 0 & 0 & \cdots & 0 \end{bmatrix}; \\
Y_{eqx2} &= \begin{bmatrix} 0 & 0 & 2G_1 & 0 & \cdots & 0 & -I_4 & I_4 & \cdots & 0 \\ 0 & 0 & 0 & 2G_1 & \cdots & 0 & 0 & -I_4 & \cdots & 0 \\ \vdots & \vdots & \vdots & \vdots & \ddots & \vdots & \vdots & \vdots & \ddots & \vdots \\ 0 & 0 & 0 & 0 & \cdots & 2G_1 & 0 & 0 & \cdots & I_4 \\ -I_4 & 0 & I_4 & 0 & \cdots & 0 & R_1 & 0 & \cdots & 0 \\ 0 & 0 & -I_4 & I_4 & \cdots & 0 & 0 & R_1 & \cdots & 0 \\ \vdots & \vdots & \vdots & \vdots & \ddots & \vdots & \vdots & \vdots & \ddots & \vdots \\ 0 & I_4 & 0 & 0 & \cdots & -I_4 & 0 & 0 & \cdots & R_1 \end{bmatrix}; \quad D_{eqxd2} = \begin{bmatrix} 0 & 0 & 2C_1 & 0 & \cdots & 0 & 0 & 0 & \cdots & 0 \\ 0 & 0 & 0 & 2C_1 & \cdots & 0 & 0 & 0 & \cdots & 0 \\ \vdots & \vdots & \vdots & \vdots & \ddots & \vdots & \vdots & \vdots & \ddots & \vdots \\ 0 & 0 & 0 & 0 & \cdots & 2C_1 & 0 & 0 & \cdots & 0 \\ 0 & 0 & 0 & 0 & \cdots & 0 & L_1 & 0 & \cdots & 0 \\ 0 & 0 & 0 & 0 & \cdots & 0 & 0 & L_1 & \cdots & 0 \\ \vdots & \vdots & \vdots & \vdots & \ddots & \vdots & \vdots & \vdots & \ddots & \vdots \\ 0 & 0 & 0 & 0 & \cdots & 0 & 0 & 0 & \cdots & L_1 \end{bmatrix};
\end{aligned}$$

11. Appendix C: Model Description of Three-Phase Two-Level PWM Inverter

This Appendix presents the model of three-phase two-level PWM inverter. We introduce the model of the inverter by three steps: first, we describe the overall model of the inverter; second, we describe the single valve model; third, we describe the DC-side capacitor.

C-1: verall Model Description

In this section, we present the overall model of the three-phase two-level PWM inverter. As shown in Figure C-1, the inverter model consists of a DC-side capacitor and detail models of six-valves.

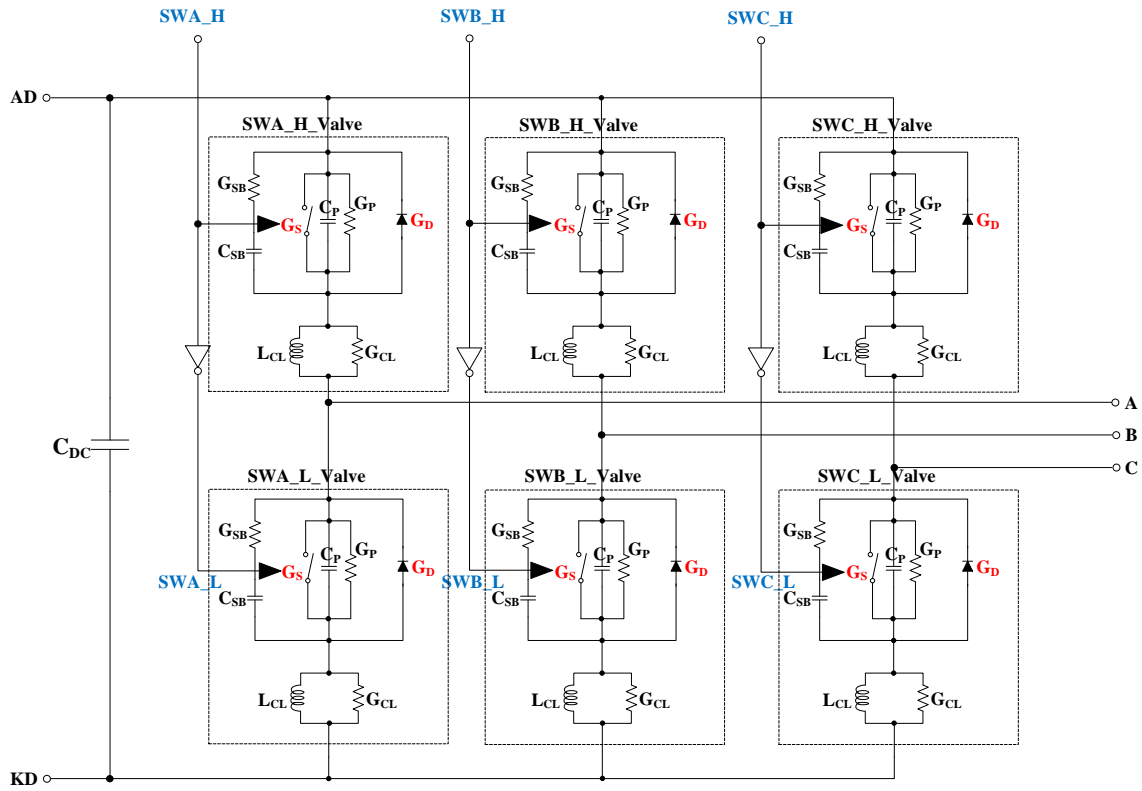


Figure C-1: Three-Phase Two-Level PWM Inverter Model

There is a complementary valve pair in each phase. For example, the complementary valve pair is SWA_H_Valve and SWA_L_Valve for phase A. Thus in this Appendix, we only show switching signals corresponding to the three-upper valves.

Each valve model consists of IGBT parasitic conductance, IGBT parasitic capacitance, IGBT-on/off conductance, a snubber circuit, an anti-parallel diode, and a current-limiting circuit as shown in Figure C-2.

IGBT-Conductance Determination

If ($U_S(t) == 1$), $G_S = G_{SON}$

If ($U_S(t) == 0$), $G_S = G_{SOFF}$

Anti-Parallel-Diode-Conductance Determination

If ($V_{CP}(t) \geq 0$), $G_D = G_{DOFF}$

If ($V_{CP}(t) < 0$), $G_D = G_{DON}$

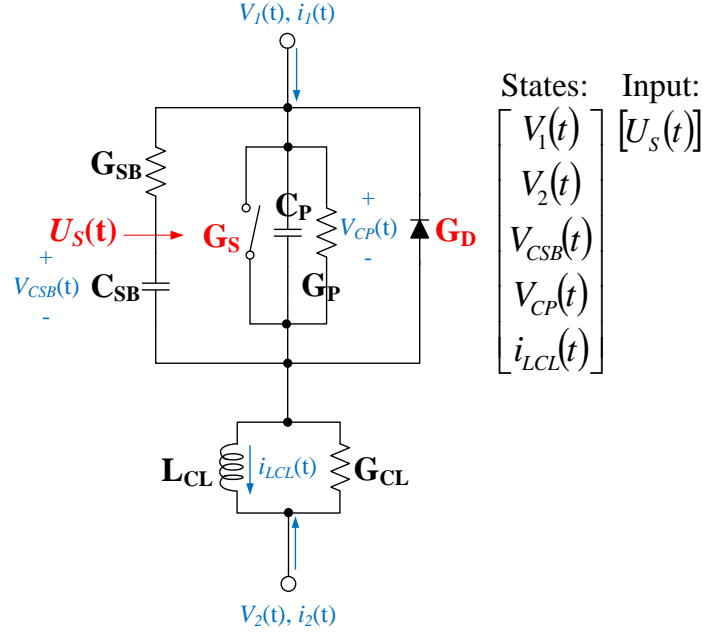


Figure C-2: The Single Valve Model

As shown in the above figure, the IGBT switch has two conduction states determined by a switching-signal input. Also, the anti-parallel diode also has two conduction states determined by the polarity of the voltage across the parasitic capacitance. The conduction state of the IGBT switch and anti-parallel diode are determined as follows:

$$G_S(t) = G_{SON} \cdot U_S(t) + G_{SOFF} \cdot (1 - U_S(t))$$

$$G_D(t) = \frac{G_{DOFF}}{2} \cdot (1 + \text{sign}(V_{CP}(t))) + \frac{G_{DON}}{2} \cdot (1 - \text{sign}(V_{CP}(t))) + (1 - \text{sign}^2(V_{CP}(t))) \cdot \left(\frac{G_{DOFF} - G_{DON}}{2} \right)$$

(Eq. C-1)

$$\text{sign}(x) = \begin{cases} 1 & \text{if } x > 0 \\ 0 & \text{if } x = 0 \\ -1 & \text{if } x < 0 \end{cases}$$

where

Therefore, each valve model has four switching states as follows:

Valve State 0: IGBT Switch: **ON** and Diode: **OFF** ($G_S = G_{SON}$ and $G_D = G_{DOFF}$),

Valve State 1: IGBT Switch: **ON** and Diode: **ON** ($G_S = G_{SON}$ and $G_D = G_{DON}$),

Valve State 2: IGBT Switch: **OFF** and Diode: **OFF** ($G_S = G_{SOFF}$ and $G_D = G_{DOFF}$),

Valve State 3: IGBT Switch: **OFF** and Diode: **ON** ($G_S = G_{SOFF}$ and $G_D = G_{DON}$).

Each valve model determines its state and control algebraic quadratic companion form (SCAQCF) of its current-time-step valve state from the predefined SCAQCFs of a single valve. By merging the SCAQCFs of six-valve and DC-side capacitor models using Kirchhoff's current law (KCL) at assigned node numbers of the inverter model as shown in Figure C-3, we generate the SCAQCF of the inverter model every time step. Figure C-4 shows the flow chart of the procedure. The above assigned node numbers are stored in the following arrays as summarized in Table C-1.

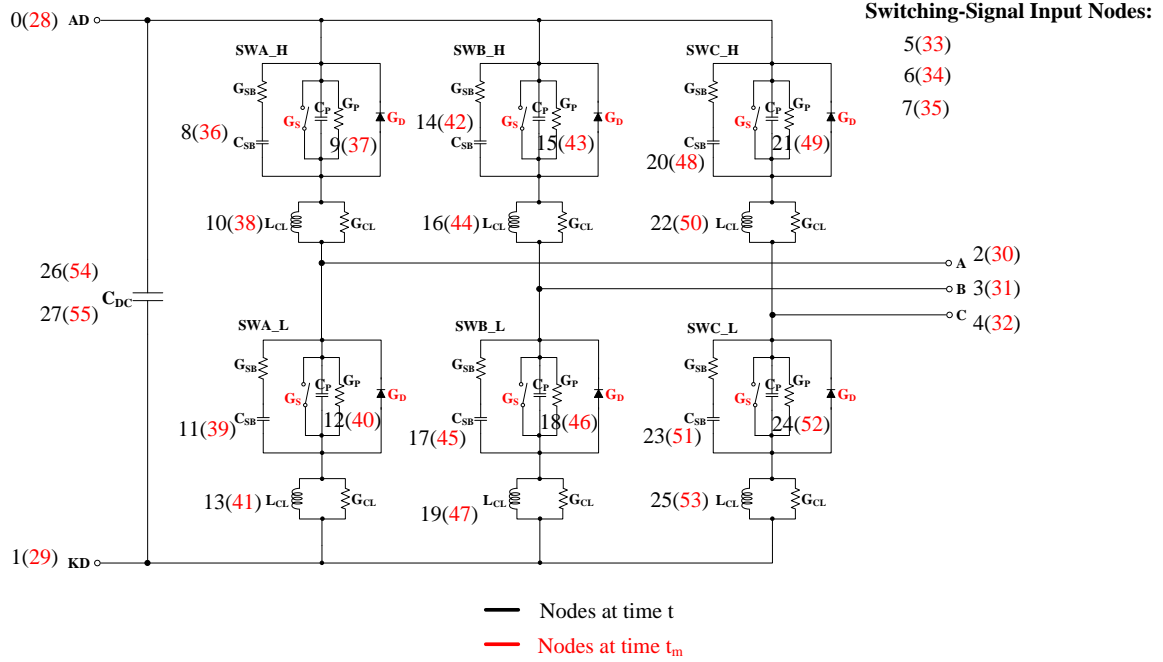


Figure C-3: Three-Phase Two-Level PWM Inverter Model with Assigned Node Numbers

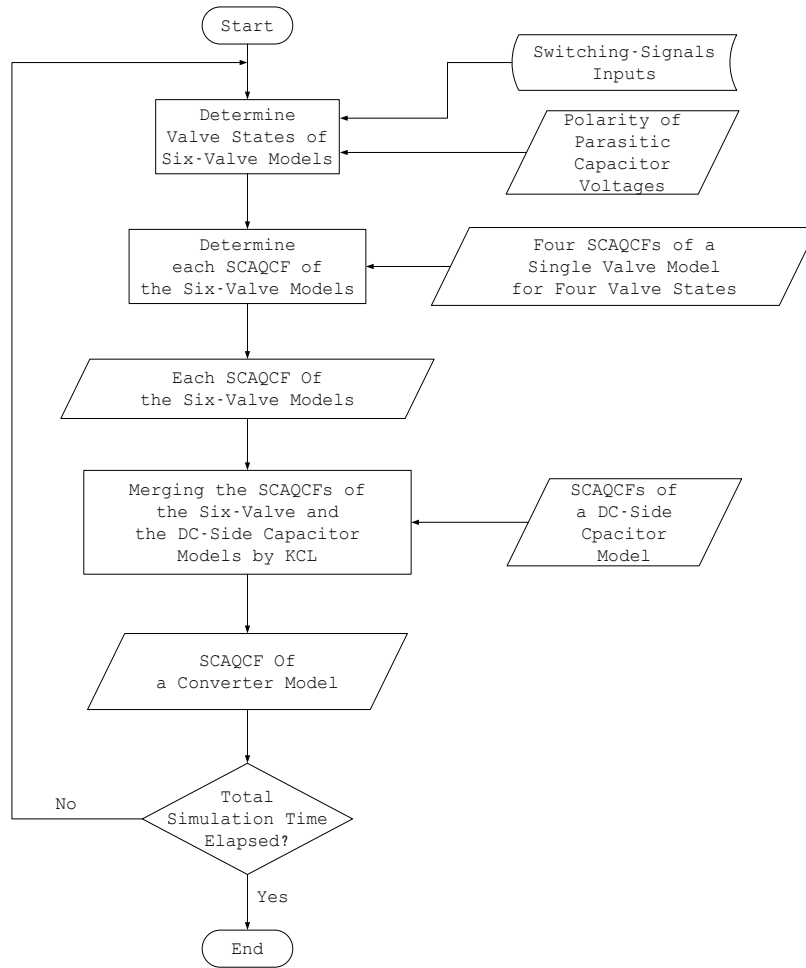


Figure C-4: Procedure of the Generation of the SCAQCF of the Inverter Model

Table C-1: Assigned Node Numbers of the Three-Phase Two-Level PWM Inverter

	t					t_m				
	External		Internal			External		Internal		
SWA_H	0	2	8	9	10	28	30	36	37	38
SWA_L	2	1	11	12	13	30	29	39	40	41
SWB_H	0	3	14	15	16	28	31	42	43	44
SWB_L	3	1	17	18	19	31	29	45	46	47
SWC_H	0	4	20	21	22	28	32	48	49	50
SWC_L	4	1	23	24	25	32	29	51	52	53

	t				t_m			
	External		Internal		External		Internal	
DC-Side Capacitor	0	1	26	27	28	29	54	55

C-2: Single Valve Model

The single valve model is provided in Figure C-2. The single valve model has four switching states. The compact models for the four valve states are:

A. Valve State 0: Switch: **ON** and Diode: **OFF** ($G_S = G_{SON}$ and $G_D = G_{DOFF}$):

$$i_1(t) = i_{LCL}(t) + G_{CL}(V_1(t) - V_{CP}(t) - V_2(t)) \quad (\text{Eq. C-2})$$

$$i_2(t) = -i_{LCL}(t) - G_{CL}(V_1(t) - V_{CP}(t) - V_2(t)) \quad (\text{Eq. C-3})$$

$$0 = -V_{CP}(t) + \frac{C_{SB}}{G_{SB}} \cdot \frac{dV_{CSB}(t)}{dt} + V_{CSB}(t) \quad (\text{Eq. C-4})$$

$$0 = -V_1(t) + V_{CP}(t) + L_{CL} \cdot \frac{di_{LCL}(t)}{dt} + V_2(t) \quad (\text{Eq. C-5})$$

$$0 = -G_{SB}(V_{CP}(t) - V_{CSB}(t)) - \textcolor{red}{G}_{SON} \cdot V_{CP}(t) - C_P \cdot \frac{dV_{CP}(t)}{dt} - G_P \cdot V_{CP}(t) \\ - \textcolor{blue}{G}_{DOFF} \cdot V_{CP}(t) + i_{LCL}(t) + G_{CL}(V_1(t) - V_{CP}(t) - V_2(t)) \quad (\text{Eq. C-6})$$

B. Valve State 1: Switch: **ON** and Diode: **ON** ($G_S = \textcolor{red}{G}_{SON}$ and $G_D = \textcolor{red}{G}_{DON}$):

$$i_1(t) = i_{LCL}(t) + G_{CL}(V_1(t) - V_{CP}(t) - V_2(t)) \quad (\text{Eq. C-7})$$

$$i_2(t) = -i_{LCL}(t) - G_{CL}(V_1(t) - V_{CP}(t) - V_2(t)) \quad (\text{Eq. C-8})$$

$$0 = -V_{CP}(t) + \frac{C_{SB}}{G_{SB}} \cdot \frac{dV_{CSB}(t)}{dt} + V_{CSB}(t) \quad (\text{Eq. C-9})$$

$$0 = -V_1(t) + V_{CP}(t) + L_{CL} \cdot \frac{di_{LCL}(t)}{dt} + V_2(t) \quad (\text{Eq. C-10})$$

$$0 = -G_{SB}(V_{CP}(t) - V_{CSB}(t)) - \textcolor{red}{G}_{SON} \cdot V_{CP}(t) - C_P \cdot \frac{dV_{CP}(t)}{dt} - G_P \cdot V_{CP}(t) \\ - \textcolor{red}{G}_{DON} \cdot V_{CP}(t) + i_{LCL}(t) + G_{CL}(V_1(t) - V_{CP}(t) - V_2(t)) \quad (\text{Eq. C-11})$$

C. Valve State 2: Switch: **OFF** and Diode: **OFF** ($G_S = \textcolor{blue}{G}_{SOFF}$ and $G_D = \textcolor{blue}{G}_{DOFF}$):

$$i_1(t) = i_{LCL}(t) + G_{CL}(V_1(t) - V_{CP}(t) - V_2(t)) \quad (\text{Eq. C-12})$$

$$i_2(t) = -i_{LCL}(t) - G_{CL}(V_1(t) - V_{CP}(t) - V_2(t)) \quad (\text{Eq. C-13})$$

$$0 = -V_{CP}(t) + \frac{C_{SB}}{G_{SB}} \cdot \frac{dV_{CSB}(t)}{dt} + V_{CSB}(t) \quad (\text{Eq. C-14})$$

$$0 = -V_1(t) + V_{CP}(t) + L_{CL} \cdot \frac{di_{LCL}(t)}{dt} + V_2(t) \quad (\text{Eq. C-15})$$

$$0 = -G_{SB}(V_{CP}(t) - V_{CSB}(t)) - G_{SOFF} \cdot V_{CP}(t) - C_P \cdot \frac{dV_{CP}(t)}{dt} - G_P \cdot V_{CP}(t) \\ - G_{DOFF} \cdot V_{CP}(t) + i_{LCL}(t) + G_{CL}(V_1(t) - V_{CP}(t) - V_2(t)) \quad (\text{Eq. C-16})$$

D. Valve State 3: Switch: **OFF** and Diode: **ON** ($G_S = G_{SOFF}$ and $G_D = G_{DON}$):

$$i_1(t) = i_{LCL}(t) + G_{CL}(V_1(t) - V_{CP}(t) - V_2(t)) \quad (\text{Eq. C-17})$$

$$i_2(t) = -i_{LCL}(t) - G_{CL}(V_1(t) - V_{CP}(t) - V_2(t)) \quad (\text{Eq. C-18})$$

$$0 = -V_{CP}(t) + \frac{C_{SB}}{G_{SB}} \cdot \frac{dV_{CSB}(t)}{dt} + V_{CSB}(t) \quad (\text{Eq. C-19})$$

$$0 = -V_1(t) + V_{CP}(t) + L_{CL} \cdot \frac{di_{LCL}(t)}{dt} + V_2(t) \quad (\text{Eq. C-20})$$

$$0 = -G_{SB}(V_{CP}(t) - V_{CSB}(t)) - G_{SOFF} \cdot V_{CP}(t) - C_P \cdot \frac{dV_{CP}(t)}{dt} - G_P \cdot V_{CP}(t) \\ - G_{DON} \cdot V_{CP}(t) + i_{LCL}(t) + G_{CL}(V_1(t) - V_{CP}(t) - V_2(t)) \quad (\text{Eq. C-21})$$

From Appendix A, the SCAQCF of a single valve is (all other matrices are null):

A. Valve State 0:

$$Y_{\text{eqs}} = \begin{bmatrix} G_{CL} & -G_{CL} & 0 & -G_{CL} & 1 & 0 & 0 & 0 & 0 & 0 \\ -G_{CL} & G_{CL} & 0 & G_{CL} & -1 & 0 & 0 & 0 & 0 & 0 \\ 0 & 0 & \frac{C_{SB}}{G_{SB}} + \frac{h}{6} & -\frac{h}{6} & 0 & 0 & 0 & \frac{2h}{3} & -\frac{2h}{3} & 0 \\ -\frac{h}{6} & \frac{h}{6} & 0 & \frac{h}{6} & L_{CL} & -\frac{2h}{3} & \frac{2h}{3} & 0 & \frac{2h}{3} & 0 \\ G_{CL} \frac{h}{6} & -G_{CL} \frac{h}{6} & G_{SB} \frac{h}{6} & -K_0 \frac{h}{6} - C_P & \frac{h}{6} & G_{CL} \frac{2h}{3} & -G_{CL} \frac{2h}{3} & G_{SB} \frac{2h}{3} & -K_0 \frac{2h}{3} & \frac{2h}{3} \\ 0 & 0 & 0 & 0 & 0 & G_{CL} & -G_{CL} & 0 & -G_{CL} & 1 \\ 0 & 0 & 0 & 0 & 0 & -G_{CL} & G_{CL} & 0 & G_{CL} & -1 \\ 0 & 0 & -\frac{h}{24} & \frac{h}{24} & 0 & 0 & 0 & \frac{C_{SB}}{G_{SB}} + \frac{h}{3} & -\frac{h}{3} & 0 \\ \frac{h}{24} & -\frac{h}{24} & 0 & -\frac{h}{24} & 0 & -\frac{h}{3} & \frac{h}{3} & 0 & \frac{h}{3} & L_{CL} \\ -G_{CL} \frac{h}{24} & G_{CL} \frac{h}{24} & -G_{SB} \frac{h}{24} & K_0 \frac{h}{24} & -\frac{h}{24} & G_{CL} \frac{h}{3} & -G_{CL} \frac{h}{3} & G_{SB} \frac{h}{3} & -K_0 \frac{h}{3} - C_P & \frac{h}{3} \end{bmatrix}$$

$$N_{\text{eqs}} = \begin{bmatrix} -G_{CL} & G_{CL} & 0 & G_{CL} & -1 \\ G_{CL} & -G_{CL} & 0 & -G_{CL} & 1 \\ 0 & 0 & -\frac{C_{SB}}{G_{SB}} + \frac{h}{6} & -\frac{h}{6} & 0 \\ -\frac{h}{6} & \frac{h}{6} & 0 & \frac{h}{6} & -L_{CL} \\ G_{CL} \frac{h}{6} & -G_{CL} \frac{h}{6} & G_{SB} \frac{h}{6} & -K_0 \frac{h}{6} + C_P & \frac{h}{6} \\ \frac{1}{2} G_{CL} & -\frac{1}{2} G_{CL} & 0 & -\frac{1}{2} G_{CL} & \frac{1}{2} \\ -\frac{1}{2} G_{CL} & \frac{1}{2} G_{CL} & 0 & \frac{1}{2} G_{CL} & -\frac{1}{2} \\ 0 & 0 & -\frac{C_{SB}}{G_{SB}} + \frac{5h}{24} & -\frac{5h}{24} & 0 \\ -\frac{5h}{24} & \frac{5h}{24} & 0 & \frac{5h}{24} & -L_{CL} \\ G_{CL} \frac{5h}{24} & -G_{CL} \frac{5h}{24} & G_{SB} \frac{5h}{24} & -K_0 \frac{5h}{24} + C_P & \frac{5h}{24} \end{bmatrix},$$

$$M_{\text{eq}} = \begin{bmatrix} 1 & 0 \\ 0 & 1 \\ 0 & 0 \\ 0 & 0 \\ 0 & 0 \\ -\frac{1}{2} & 0 \\ 0 & -\frac{1}{2} \\ 0 & 0 \\ 0 & 0 \\ 0 & 0 \end{bmatrix}$$

Where $K_0 = G_{SB} + G_{SON} + G_P + G_{DOFF} + G_{CL}$;

B. Valve State 1:

$$\begin{aligned}
 Y_{eqx} &= \begin{bmatrix} G_{CL} & -G_{CL} & 0 & -G_{CL} & 1 & 0 & 0 & 0 & 0 & 0 \\ -G_{CL} & G_{CL} & 0 & G_{CL} & -1 & 0 & 0 & 0 & 0 & 0 \\ 0 & 0 & \frac{C_{SB}}{G_{SB}} + \frac{h}{6} & -\frac{h}{6} & 0 & 0 & 0 & \frac{2h}{3} & -\frac{2h}{3} & 0 \\ -\frac{h}{6} & \frac{h}{6} & 0 & \frac{h}{6} & L_{CL} & -\frac{2h}{3} & \frac{2h}{3} & 0 & \frac{2h}{3} & 0 \\ G_{CL} \frac{h}{6} & -G_{CL} \frac{h}{6} & G_{SB} \frac{h}{6} & -K_1 \frac{h}{6} - C_P & \frac{h}{6} & G_{CL} \frac{2h}{3} & -G_{CL} \frac{2h}{3} & G_{SB} \frac{2h}{3} & -K_1 \frac{2h}{3} & \frac{2h}{3} \\ 0 & 0 & 0 & 0 & 0 & G_{CL} & -G_{CL} & 0 & -G_{CL} & 1 \\ 0 & 0 & 0 & 0 & 0 & -G_{CL} & G_{CL} & 0 & G_{CL} & -1 \\ 0 & 0 & -\frac{h}{24} & \frac{h}{24} & 0 & 0 & 0 & \frac{C_{SB}}{G_{SB}} + \frac{h}{3} & -\frac{h}{3} & 0 \\ \frac{h}{24} & -\frac{h}{24} & 0 & -\frac{h}{24} & 0 & -\frac{h}{3} & \frac{h}{3} & 0 & \frac{h}{3} & L_{CL} \\ -G_{CL} \frac{h}{24} & G_{CL} \frac{h}{24} & -G_{SB} \frac{h}{24} & K_1 \frac{h}{24} & -\frac{h}{24} & G_{CL} \frac{h}{3} & -G_{CL} \frac{h}{3} & G_{SB} \frac{h}{3} & -K_1 \frac{h}{3} - C_P & \frac{h}{3} \end{bmatrix} \\
 N_{eqx} &= \begin{bmatrix} -G_{CL} & G_{CL} & 0 & G_{CL} & -1 \\ G_{CL} & -G_{CL} & 0 & -G_{CL} & 1 \\ 0 & 0 & -\frac{C_{SB}}{G_{SB}} + \frac{h}{6} & -\frac{h}{6} & 0 \\ -\frac{h}{6} & \frac{h}{6} & 0 & \frac{h}{6} & -L_{CL} \\ G_{CL} \frac{h}{6} & -G_{CL} \frac{h}{6} & G_{SB} \frac{h}{6} & -K_1 \frac{h}{6} + C_P & \frac{h}{6} \\ \frac{1}{2} G_{CL} & -\frac{1}{2} G_{CL} & 0 & -\frac{1}{2} G_{CL} & \frac{1}{2} \\ -\frac{1}{2} G_{CL} & \frac{1}{2} G_{CL} & 0 & \frac{1}{2} G_{CL} & -\frac{1}{2} \\ 0 & 0 & -\frac{C_{SB}}{G_{SB}} + \frac{5h}{24} & -\frac{5h}{24} & 0 \\ -\frac{5h}{24} & \frac{5h}{24} & 0 & \frac{5h}{24} & -L_{CL} \\ G_{CL} \frac{5h}{24} & -G_{CL} \frac{5h}{24} & G_{SB} \frac{5h}{24} & -K_1 \frac{5h}{24} + C_P & \frac{5h}{24} \end{bmatrix} \\
 M_{eq} &= \begin{bmatrix} 1 & 0 \\ 0 & 1 \\ 0 & 0 \\ 0 & 0 \\ 0 & 0 \\ -\frac{1}{2} & 0 \\ 0 & -\frac{1}{2} \\ 0 & 0 \\ 0 & 0 \\ 0 & 0 \end{bmatrix}
 \end{aligned}$$

where $K_1 = G_{SB} + G_{SON} + G_P + G_{DON} + G_{CL}$;

C. Valve State 2:

$$\begin{aligned}
 Y_{\text{eqx}} &= \begin{bmatrix} G_{CL} & -G_{CL} & 0 & -G_{CL} & 1 & 0 & 0 & 0 & 0 & 0 \\ -G_{CL} & G_{CL} & 0 & G_{CL} & -1 & 0 & 0 & 0 & 0 & 0 \\ 0 & 0 & \frac{C_{SB}}{G_{SB}} + \frac{h}{6} & -\frac{h}{6} & 0 & 0 & 0 & \frac{2h}{3} & -\frac{2h}{3} & 0 \\ -\frac{h}{6} & \frac{h}{6} & 0 & \frac{h}{6} & L_{CL} & -\frac{2h}{3} & \frac{2h}{3} & 0 & \frac{2h}{3} & 0 \\ G_{CL}\frac{h}{6} & -G_{CL}\frac{h}{6} & G_{SB}\frac{h}{6} & -K_2\frac{h}{6} - C_P & \frac{h}{6} & G_{CL}\frac{2h}{3} & -G_{CL}\frac{2h}{3} & G_{SB}\frac{2h}{3} & -K_2\frac{2h}{3} & \frac{2h}{3} \\ 0 & 0 & 0 & 0 & 0 & G_{CL} & -G_{CL} & 0 & -G_{CL} & 1 \\ 0 & 0 & 0 & 0 & 0 & -G_{CL} & G_{CL} & 0 & G_{CL} & -1 \\ 0 & 0 & -\frac{h}{24} & \frac{h}{24} & 0 & 0 & 0 & \frac{C_{SB}}{G_{SB}} + \frac{h}{3} & -\frac{h}{3} & 0 \\ \frac{h}{24} & -\frac{h}{24} & 0 & -\frac{h}{24} & 0 & -\frac{h}{3} & \frac{h}{3} & 0 & \frac{h}{3} & L_{CL} \\ -G_{CL}\frac{h}{24} & G_{CL}\frac{h}{24} & -G_{SB}\frac{h}{24} & K_2\frac{h}{24} & -\frac{h}{24} & G_{CL}\frac{h}{3} & -G_{CL}\frac{h}{3} & G_{SB}\frac{h}{3} & -K_2\frac{h}{3} - C_P & \frac{h}{3} \end{bmatrix}, \\
 N_{\text{eqx}} &= \begin{bmatrix} -G_{CL} & G_{CL} & 0 & G_{CL} & -1 \\ G_{CL} & -G_{CL} & 0 & -G_{CL} & 1 \\ 0 & 0 & -\frac{C_{SB}}{G_{SB}} + \frac{h}{6} & -\frac{h}{6} & 0 \\ -\frac{h}{6} & \frac{h}{6} & 0 & \frac{h}{6} & -L_{CL} \\ G_{CL}\frac{h}{6} & -G_{CL}\frac{h}{6} & G_{SB}\frac{h}{6} & -K_2\frac{h}{6} + C_P & \frac{h}{6} \\ \frac{1}{2}G_{CL} & -\frac{1}{2}G_{CL} & 0 & -\frac{1}{2}G_{CL} & \frac{1}{2} \\ -\frac{1}{2}G_{CL} & \frac{1}{2}G_{CL} & 0 & \frac{1}{2}G_{CL} & -\frac{1}{2} \\ 0 & 0 & -\frac{C_{SB}}{G_{SB}} + \frac{5h}{24} & -\frac{5h}{24} & 0 \\ -\frac{5h}{24} & \frac{5h}{24} & 0 & \frac{5h}{24} & -L_{CL} \\ G_{CL}\frac{5h}{24} & -G_{CL}\frac{5h}{24} & G_{SB}\frac{5h}{24} & -K_2\frac{5h}{24} + C_P & \frac{5h}{24} \end{bmatrix}, \\
 M_{\text{eq}} &= \begin{bmatrix} 1 & 0 \\ 0 & 1 \\ 0 & 0 \\ 0 & 0 \\ 0 & 0 \\ -\frac{1}{2} & 0 \\ 0 & -\frac{1}{2} \\ 0 & 0 \\ 0 & 0 \\ 0 & 0 \end{bmatrix}
 \end{aligned}$$

where $K_2 = G_{SB} + G_{SOFF} + G_P + G_{DOFF} + G_{CL}$;

D. Valve State 3:

$$\begin{aligned}
 Y_{eqx} &= \begin{bmatrix} G_{CL} & -G_{CL} & 0 & -G_{CL} & 1 & 0 & 0 & 0 & 0 & 0 \\ -G_{CL} & G_{CL} & 0 & G_{CL} & -1 & 0 & 0 & 0 & 0 & 0 \\ 0 & 0 & \frac{C_{SB}}{G_{SB}} + \frac{h}{6} & -\frac{h}{6} & 0 & 0 & 0 & \frac{2h}{3} & -\frac{2h}{3} & 0 \\ -\frac{h}{6} & \frac{h}{6} & 0 & \frac{h}{6} & L_{CL} & -\frac{2h}{3} & \frac{2h}{3} & 0 & \frac{2h}{3} & 0 \\ G_{CL}\frac{h}{6} & -G_{CL}\frac{h}{6} & G_{SB}\frac{h}{6} & -K_3\frac{h}{6} - C_P & \frac{h}{6} & G_{CL}\frac{2h}{3} & -G_{CL}\frac{2h}{3} & G_{SB}\frac{2h}{3} & -K_3\frac{2h}{3} & \frac{2h}{3} \\ 0 & 0 & 0 & 0 & 0 & G_{CL} & -G_{CL} & 0 & -G_{CL} & 1 \\ 0 & 0 & 0 & 0 & 0 & -G_{CL} & G_{CL} & 0 & G_{CL} & -1 \\ 0 & 0 & -\frac{h}{24} & \frac{h}{24} & 0 & 0 & 0 & \frac{C_{SB}}{G_{SB}} + \frac{h}{3} & -\frac{h}{3} & 0 \\ \frac{h}{24} & -\frac{h}{24} & 0 & -\frac{h}{24} & 0 & -\frac{h}{3} & \frac{h}{3} & 0 & \frac{h}{3} & L_{CL} \\ -G_{CL}\frac{h}{24} & G_{CL}\frac{h}{24} & -G_{SB}\frac{h}{24} & K_3\frac{h}{24} & -\frac{h}{24} & G_{CL}\frac{h}{3} & -G_{CL}\frac{h}{3} & G_{SB}\frac{h}{3} & -K_3\frac{h}{3} - C_P & \frac{h}{3} \end{bmatrix} \\
 N_{eqx} &= \begin{bmatrix} -G_{CL} & G_{CL} & 0 & G_{CL} & -1 \\ G_{CL} & -G_{CL} & 0 & -G_{CL} & 1 \\ 0 & 0 & -\frac{C_{SB}}{G_{SB}} + \frac{h}{6} & -\frac{h}{6} & 0 \\ -\frac{h}{6} & \frac{h}{6} & 0 & \frac{h}{6} & -L_{CL} \\ G_{CL}\frac{h}{6} & -G_{CL}\frac{h}{6} & G_{SB}\frac{h}{6} & -K_3\frac{h}{6} + C_P & \frac{h}{6} \\ \frac{1}{2}G_{CL} & -\frac{1}{2}G_{CL} & 0 & -\frac{1}{2}G_{CL} & \frac{1}{2} \\ -\frac{1}{2}G_{CL} & \frac{1}{2}G_{CL} & 0 & \frac{1}{2}G_{CL} & -\frac{1}{2} \\ 0 & 0 & -\frac{C_{SB}}{G_{SB}} + \frac{5h}{24} & -\frac{5h}{24} & 0 \\ -\frac{5h}{24} & \frac{5h}{24} & 0 & \frac{5h}{24} & -L_{CL} \\ G_{CL}\frac{5h}{24} & -G_{CL}\frac{5h}{24} & G_{SB}\frac{5h}{24} & -K_3\frac{5h}{24} + C_P & \frac{5h}{24} \end{bmatrix}, \\
 M_{eq} &= \begin{bmatrix} 1 & 0 \\ 0 & 1 \\ 0 & 0 \\ 0 & 0 \\ 0 & 0 \\ -\frac{1}{2} & 0 \\ 0 & -\frac{1}{2} \\ 0 & 0 \\ 0 & 0 \\ 0 & 0 \end{bmatrix}
 \end{aligned}$$

where $K_3 = G_{SB} + G_{SOFF} + G_P + G_{DON} + G_{CL}$;

C-3: DC-side capacitor model

This section presents the DC-side capacitor model.

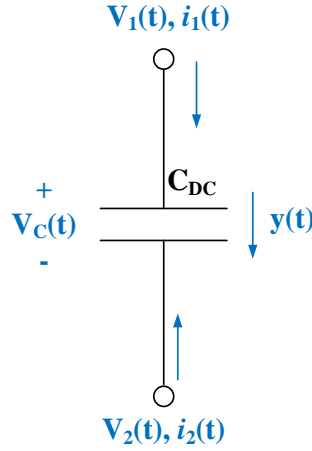


Figure C-5: DC-Side Capacitor Model

The single valve model is provided in Figure C-5. The DC-side capacitor model is:

$$i_1(t) = C_{DC} \cdot y_1(t) \quad (\text{Eq. C-22})$$

$$i_2(t) = -C_{DC} \cdot y_1(t) \quad (\text{Eq. C-23})$$

$$0 = \frac{dV_C(t)}{dt} - y_1(t) \quad (\text{Eq. C-24})$$

$$0 = V_C(t) - V_1(t) + V_2(t) \quad (\text{Eq. C-25})$$

From Appendix A, the SCAQCF of the DC-side capacitor is (all other matrices are null):

$$Y_{eqx} = \begin{bmatrix} 0 & 0 & 0 & C_{DC} & 0 & 0 & 0 & 0 \\ 0 & 0 & 0 & -C_{DC} & 0 & 0 & 0 & 0 \\ 0 & 0 & 1 & -\frac{h}{6} & 0 & 0 & 0 & -\frac{2h}{3} \\ -1 & 1 & 1 & 0 & 0 & 0 & 0 & 0 \\ 0 & 0 & 0 & 0 & 0 & 0 & 0 & C_{DC} \\ 0 & 0 & 0 & 0 & 0 & 0 & 0 & -C_{DC} \\ 0 & 0 & 0 & \frac{h}{24} & 0 & 0 & 1 & -\frac{h}{3} \\ 0 & 0 & 0 & 0 & -1 & 1 & 1 & 0 \end{bmatrix}$$

$$N_{eqx} = \begin{bmatrix} 0 & 0 & 0 & -C_{DC} \\ 0 & 0 & 0 & C_{DC} \\ 0 & 0 & -1 & -\frac{h}{6} \\ 0 & 0 & 0 & 0 \\ 0 & 0 & 0 & \frac{C_{DC}}{2} \\ 0 & 0 & 0 & -\frac{C_{DC}}{2} \\ 0 & 0 & -1 & -\frac{5h}{24} \\ 0 & 0 & 0 & 0 \end{bmatrix}$$

$$M_{eq} = \begin{bmatrix} 1 & 0 \\ 0 & 1 \\ 0 & 0 \\ 0 & 0 \\ -\frac{1}{2} & 0 \\ 0 & -\frac{1}{2} \\ 0 & 0 \\ 0 & 0 \end{bmatrix}$$

12. Appendix D: Model Description of the Digital Signal Processor (DSP)

This Appendix presents the digital signal processor (DSP). The DSP digitally filters raw analog signals into digital signals of fundamental frequency. The DSP outputs are: the positive sequence phasor of three-phase voltages (\tilde{V}_1) and currents (\tilde{I}_1), the fundamental frequency, three-phase real (P) and reactive power (Q), the actual average fundamental frequency (f_s), the next zero-crossing time from the negative to positive of the voltage positive-sequence waveform (ZX), the rate of average frequency change ($\frac{df_s}{dt}$), and DC-link average voltage (\bar{V}_{DC}). The DSP receives instantaneous value inputs V_{an} , V_{bn} , V_{cn} , I_a , I_b , I_c , and V_{DC} then calculates outputs, \tilde{V}_1 , \tilde{I}_1 , P , Q , f_s , ZX , $\frac{df_s}{dt}$, and \bar{V}_{DC} as shown in Figure D-1.

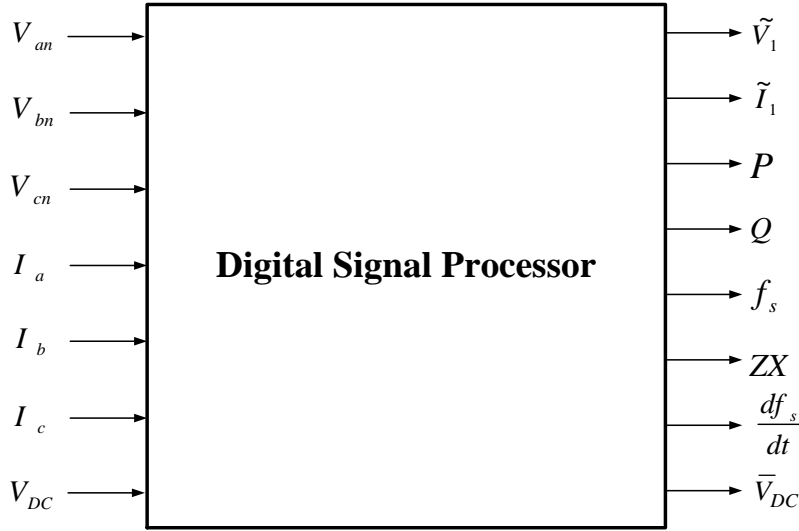


Figure D-1: Block Diagram of the Digital Signal Processor

This Appendix is arranged as follows. Section D-1 describes the calculation of frequency and the rate of frequency change; section D-2 and D-3 describes the calculation process of positive sequence voltage and current phasors; section D-4 describes the calculation of three-phase fundamental frequency real and reactive power; section D-5 describes the calculation of next zero-crossing time.

D-1: Frequency and the Rate of Frequency Change

To calculate the actual average fundamental frequency and rate of average frequency change, we are using a method based on the calculation of the rate of phase angle changes of input data, V_{an} , V_{bn} , V_{cn} , I_a , I_b , and I_c . A computationally efficient recursive implementation is described as follows. The following two sums are recursively updated every time when a new input data sample, $x(i)$, becomes available:

$$V_{1_x}(k) = \frac{1}{N} \sum_{i=k}^{k+N-1} x(i) \cos(\omega_s \cdot T_r \cdot i) \quad (\text{Eq D-1})$$

$$V_{2_x}(k) = \frac{1}{N} \sum_{i=k}^{k+N-1} x(i) \sin(\omega_s \cdot T_r \cdot i) \quad (\text{Eq. D-2})$$

$$\omega_s = 2\pi \cdot f_s \quad (\text{Eq. D-3})$$

where:

- $x(i)$: Input data samples.
 f_s : Actual average fundamental frequency. It is initialized as the nominal power frequency, 60 Hz, for the first iteration, but it is updated every recursive loop of the calculation of the average frequency.
 T_r : Sampling period of the analog-to-digital converter.
 N : Number of samples in a period $\left(= \frac{2\pi}{\omega_s T_r} \right)$.

At every sample the two sums are updated, and the phase angle, θ , is computed as follows:

$$\theta_x(k) = \tan^{-1} \left(-\frac{V_{2_x}(k)}{V_{1_x}(k)} \right). \quad (\text{Eq. D-4})$$

The actual fundamental frequency of $x(i)$ is computed from the rate of change of the above value as follows:

$$f_{s_x}(k) = f_s(k-1) + \frac{\Delta\theta_{x_k}}{2\pi T_r}. \quad (\text{Eq. D-5})$$

where $\Delta\theta_{x_k} = \theta_x(k) - \theta_x(k-1)$.

By applying the above actual fundamental frequency calculation method to the input data, V_{an} , V_{bn} , V_{cn} , I_a , I_b , and I_c , we can calculate the actual fundamental frequencies of the input data as follows:

a) $f_{s_V_{an}}(k)$:

$$V_{1_V_{an}}(k) = \frac{1}{N} \sum_{i=k}^{k+N-1} V_{an}(i) \cos(\omega_s \cdot T_r \cdot i) \quad (\text{Eq. D-6})$$

$$V_{2_V_{an}}(k) = \frac{1}{N} \sum_{i=k}^{k+N-1} V_{an}(i) \sin(\omega_s \cdot T_r \cdot i) \quad (\text{Eq. D-7})$$

$$\theta_{V_{an}}(k) = \tan^{-1} \left(-\frac{V_{2_{-}V_{an}}(k)}{V_{1_{-}V_{an}}(k)} \right) \quad (\text{Eq. D-8})$$

$$\Delta\theta_{V_{an}-k} = \theta_{V_{an}}(k) - \theta_{V_{an}}(k-1) \quad (\text{Eq. D-9})$$

$$f_{s_{-}V_{an}} = f_s(k-1) + \frac{\Delta\theta_{V_{an}-k}}{2\pi T_r} \quad (\text{Eq D-10})$$

b) $f_{s_{-}V_{bn}}(k)$

$$V_{1_{-}V_{bn}}(k) = \frac{1}{N} \sum_{i=k}^{k+N-1} V_{bn}(i) \cos(\omega_s \cdot T_r \cdot i) \quad (\text{Eq. D-11})$$

$$V_{2_{-}V_{bn}}(k) = \frac{1}{N} \sum_{i=k}^{k+N-1} V_{bn}(i) \sin(\omega_s \cdot T_r \cdot i) \quad (\text{Eq. D-12})$$

$$\theta_{V_{bn}}(k) = \tan^{-1} \left(-\frac{V_{2_{-}V_{bn}}(k)}{V_{1_{-}V_{bn}}(k)} \right) \quad (\text{Eq. D-13})$$

$$\Delta\theta_{V_{bn}-k} = \theta_{V_{bn}}(k) - \theta_{V_{bn}}(k-1) \quad (\text{Eq. D-14})$$

$$f_{s_{-}V_{bn}} = f_s(k-1) + \frac{\Delta\theta_{V_{bn}-k}}{2\pi T_r} \quad (\text{Eq. D-15})$$

c) $f_{s_{-}V_{cn}}(k)$

$$V_{1_{-}V_{cn}}(k) = \frac{1}{N} \sum_{i=k}^{k+N-1} V_{cn}(i) \cos(\omega_s \cdot T_r \cdot i) \quad (\text{Eq. D-16})$$

$$V_{2_{-}V_{cn}}(k) = \frac{1}{N} \sum_{i=k}^{k+N-1} V_{cn}(i) \sin(\omega_s \cdot T_r \cdot i) \quad (\text{Eq. D-17})$$

$$\theta_{V_{cn}}(k) = \tan^{-1} \left(-\frac{V_{2_V_{cn}}(k)}{V_{1_V_{cn}}(k)} \right) \quad (\text{Eq. D-18})$$

$$\Delta\theta_{V_{cn-k}} = \theta_{V_{cn}}(k) - \theta_{V_{cn}}(k-1) \quad (\text{Eq. D-19})$$

$$f_{s_V_{cn}} = f_s(k-1) + \frac{\Delta\theta_{V_{cn-k}}}{2\pi T_r} \quad (\text{Eq. D-20})$$

d) $f_{s_I_a}(k)$

$$V_{1_I_a}(k) = \frac{1}{N} \sum_{i=k}^{k+N-1} I_a(i) \cos(\omega_s \cdot T_r \cdot i) \quad (\text{Eq. D-21})$$

$$V_{2_I_a}(k) = \frac{1}{N} \sum_{i=k}^{k+N-1} I_a(i) \sin(\omega_s \cdot T_r \cdot i) \quad (\text{Eq. D-22})$$

$$\theta_{I_a}(k) = \tan^{-1} \left(-\frac{V_{2_I_a}(k)}{V_{1_I_a}(k)} \right) \quad (\text{Eq. D-23})$$

$$\Delta\theta_{I_{a-k}} = \theta_{I_a}(k) - \theta_{I_a}(k-1) \quad (\text{Eq. D-24})$$

$$f_{s_I_a} = f_s(k-1) + \frac{\Delta\theta_{I_{a-k}}}{2\pi T_r} \quad (\text{Eq. D-25})$$

e) $f_{s_I_b}(k)$

$$V_{1_I_b}(k) = \frac{1}{N} \sum_{i=k}^{k+N-1} I_b(i) \cos(\omega_s \cdot T_r \cdot i) \quad (\text{Eq. D-26})$$

$$V_{2_I_b}(k) = \frac{1}{N} \sum_{i=k}^{k+N-1} I_b(i) \sin(\omega_s \cdot T_r \cdot i) \quad (\text{Eq. D-27})$$

$$\theta_{I_b}(k) = \tan^{-1} \left(-\frac{V_{2-I_b}(k)}{V_{1-I_b}(k)} \right) \quad (\text{Eq. D-28})$$

$$\Delta\theta_{I_b-k} = \theta_{I_b}(k) - \theta_{I_b}(k-1) \quad (\text{Eq. D-29})$$

$$f_{s-I_b} = f_s(k-1) + \frac{\Delta\theta_{I_b-k}}{2\pi T_r} \quad (\text{Eq. D-30})$$

f) $f_{s-I_c}(k)$

$$V_{1-I_c}(k) = \frac{1}{N} \sum_{i=k}^{k+N-1} I_c(i) \cos(\omega_s \cdot T_r \cdot i) \quad (\text{Eq. D-31})$$

$$V_{2-I_c}(k) = \frac{1}{N} \sum_{i=k}^{k+N-1} I_c(i) \sin(\omega_s \cdot T_r \cdot i) \quad (\text{Eq. D-32})$$

$$\theta_{I_b}(k) = \tan^{-1} \left(-\frac{V_{2-I_b}(k)}{V_{1-I_b}(k)} \right) \quad (\text{Eq. D-33})$$

$$\Delta\theta_{I_c-k} = \theta_{I_c}(k) - \theta_{I_c}(k-1) \quad (\text{Eq. D-34})$$

$$f_{s-I_c} = f_s(k-1) + \frac{\Delta\theta_{I_c-k}}{2\pi T_r} \quad (\text{Eq. D-35})$$

Finally, we can calculate the average fundamental frequency, f_s , and rate of average frequency change as follows:

$$f_s(k) = \frac{f_{s-V_{an}}(k) + f_{s-V_{bn}}(k) + f_{s-V_{cn}}(k) + f_{s-I_a}(k) + f_{s-I_b}(k) + f_{s-I_c}(k)}{6} \quad (\text{Eq. D-36})$$

$$\frac{df_s(k)}{dt} = \frac{f_s(k) - f_s(k-1)}{T_r} \quad (\text{Eq. D-37})$$

D-2: Positive Sequence Voltage Phasor

In this section, we present the calculation of positive sequence voltage phasor \tilde{V}_1 using three-phase voltages updated every recursive loop in the previous section. First, we calculate the fundamental voltage phasors \tilde{V}_{an} , \tilde{V}_{bn} , and \tilde{V}_{cn} as follows:

$$|V_{an}(k)| = \sqrt{(V_{1_V_{an}}(k))^2 + (V_{2_V_{an}}(k))^2} \quad (\text{Eq. D-38})$$

$$|V_{bn}(k)| = \sqrt{(V_{1_V_{bn}}(k))^2 + (V_{2_V_{bn}}(k))^2} \quad (\text{Eq. D-39})$$

$$|V_{cn}(k)| = \sqrt{(V_{1_V_{cn}}(k))^2 + (V_{2_V_{cn}}(k))^2} \quad (\text{Eq. D-40})$$

$$\tilde{V}_{an}(k) = \frac{|V_{an}(k)|}{\sqrt{2}} \angle \theta_{V_{an}}(k) \quad (\text{Eq. D-41})$$

$$\tilde{V}_{bn}(k) = \frac{|V_{bn}(k)|}{\sqrt{2}} \angle \theta_{V_{bn}}(k) \quad (\text{Eq. D-42})$$

$$\tilde{V}_{cn}(k) = \frac{|V_{cn}(k)|}{\sqrt{2}} \angle \theta_{V_{cn}}(k) \quad (\text{Eq. D-43})$$

In the next step, we are calculating the positive sequence voltage phasor from the obtained fundamental frequency voltage phasors by using the symmetrical component transformation based modal decomposition. The symmetrical component transformation is expressed as follows:

$$\begin{bmatrix} \tilde{V}_1(k) \\ \tilde{V}_2(k) \\ \tilde{V}_0(k) \end{bmatrix} = \frac{1}{3} \begin{bmatrix} 1 & a & a^2 \\ 1 & a^2 & a \\ 1 & 1 & 1 \end{bmatrix} \begin{bmatrix} \tilde{V}_{an}(k) \\ \tilde{V}_{bn}(k) \\ \tilde{V}_{cn}(k) \end{bmatrix}, \text{ where } a = e^{j\frac{2\pi}{3}} \quad (\text{Eq. D-44})$$

where \tilde{V}_1 , \tilde{V}_2 , and \tilde{V}_0 are the positive, negative and zero sequence voltage phasors, respectively. By using this, we can calculate the positive-sequence voltage phasor \tilde{V}_1 , of three-phase voltages V_{an} , V_{bn} , and V_{cn} , as follows:

$$\tilde{V}_1(k) = \frac{1}{3} \cdot \left[\tilde{V}_{an}(k) + \tilde{V}_{bn}(k) \cdot e^{j\frac{2\pi}{3}} + \tilde{V}_{cn}(k) \cdot e^{j\frac{4\pi}{3}} \right] = \frac{1}{3} \cdot [V_{\alpha}(k) + jV_{\beta}(k)] \quad (\text{Eq. D-45})$$

where

$$V_\alpha(k) = \left[\frac{|V_{an}(k)|}{\sqrt{2}} \cdot \cos(\theta_{V_{an}}(k)) + \frac{|V_{bn}(k)|}{\sqrt{2}} \cdot \cos\left(\theta_{V_{bn}}(k) + \frac{2\pi}{3}\right) + \frac{|V_{cn}(k)|}{\sqrt{2}} \cdot \cos\left(\theta_{V_{cn}}(k) + \frac{4\pi}{3}\right) \right] \quad (\text{Eq. D-46})$$

$$V_\beta(k) = \left[\frac{|V_{an}(k)|}{\sqrt{2}} \cdot \sin(\theta_{V_{an}}(k)) + \frac{|V_{bn}(k)|}{\sqrt{2}} \cdot \sin\left(\theta_{V_{bn}}(k) + \frac{2\pi}{3}\right) + \frac{|V_{cn}(k)|}{\sqrt{2}} \cdot \sin\left(\theta_{V_{cn}}(k) + \frac{4\pi}{3}\right) \right] \quad (\text{Eq. D-47})$$

$$\theta_{V_1}(k) = \tan^{-1} \left(\frac{V_\beta(k)}{V_\alpha(k)} \right) \quad (\text{Eq. D-48})$$

$$|\tilde{V}_1(k)| = \frac{1}{3} \sqrt{V_\alpha(k)^2 + V_\beta(k)^2}. \quad (\text{Eq. D-49})$$

D-3: Positive-Sequence Current Phasor

In this section, we calculate the positive sequence current phasor using the same method presented in the previous section. By using three-phase currents updated every recursive loop in section D-1. We first calculate the fundamental frequency current phasors of \tilde{I}_a , \tilde{I}_b and \tilde{I}_c as follows:

$$|I_a(k)| = \sqrt{(V_{1-I_a}(k))^2 + (V_{2-I_a}(k))^2}, \quad (\text{Eq. D-50})$$

$$|I_b(k)| = \sqrt{(V_{1-I_b}(k))^2 + (V_{2-I_b}(k))^2}, \quad (\text{Eq. D-51})$$

$$|I_c(k)| = \sqrt{(V_{1-I_c}(k))^2 + (V_{2-I_c}(k))^2} \quad (\text{Eq. D-52})$$

$$\tilde{I}_a(k) = \frac{|I_a(k)|}{\sqrt{2}} \angle \theta_{I_a}(k) \quad (\text{Eq. D-53})$$

$$\tilde{I}_b(k) = \frac{|I_b(k)|}{\sqrt{2}} \angle \theta_{I_b}(k) \quad (\text{Eq. D-54})$$

$$\tilde{I}_c(k) = \frac{|I_c(k)|}{\sqrt{2}} \angle \theta_{I_c}(k) \quad (\text{Eq. D-55})$$

Then, we compute the positive sequence current phasor \tilde{I}_1 by using the symmetrical component transformation as follows:

$$\begin{bmatrix} \tilde{I}_1(k) \\ \tilde{I}_2(k) \\ \tilde{I}_0(k) \end{bmatrix} = \frac{1}{3} \begin{bmatrix} 1 & a & a^2 \\ 1 & a^2 & a \\ 1 & 1 & 1 \end{bmatrix} \begin{bmatrix} \tilde{I}_a(k) \\ \tilde{I}_b(k) \\ \tilde{I}_c(k) \end{bmatrix}, \text{ where } a = e^{j\frac{2\pi}{3}} \quad (\text{Eq. D-56})$$

$$\tilde{I}_1(k) = \frac{1}{3} \left[\tilde{I}_a(k) + \tilde{I}_b(k) \cdot e^{j\frac{2\pi}{3}} + \tilde{I}_c(k) \cdot e^{j\frac{4\pi}{3}} \right] = \frac{1}{3} \cdot [I_\alpha(k) + jI_\beta(k)] \quad (\text{Eq. D-57})$$

where

$$I_\alpha(k) = \left[\frac{|I_a(k)|}{\sqrt{2}} \cdot \cos(\theta_{I_a}(k)) + \frac{|I_b(k)|}{\sqrt{2}} \cdot \cos\left(\theta_{I_b}(k) + \frac{2\pi}{3}\right) + \frac{|I_c(k)|}{\sqrt{2}} \cdot \cos\left(\theta_{I_c}(k) + \frac{4\pi}{3}\right) \right] \quad (\text{Eq. D-58})$$

$$I_\beta(k) = \left[\frac{|I_a(k)|}{\sqrt{2}} \cdot \sin(\theta_{I_a}(k)) + \frac{|I_b(k)|}{\sqrt{2}} \cdot \sin\left(\theta_{I_b}(k) + \frac{2\pi}{3}\right) + \frac{|I_c(k)|}{\sqrt{2}} \cdot \sin\left(\theta_{I_c}(k) + \frac{4\pi}{3}\right) \right] \quad (\text{Eq. D-59})$$

$$\theta_{I_1}(k) = \tan^{-1} \left(\frac{I_\beta(k)}{I_\alpha(k)} \right) \quad (\text{Eq. D-60})$$

$$|\tilde{I}_1(k)| = \frac{1}{3} \sqrt{I_\alpha(k)^2 + I_\beta(k)^2} \quad (\text{Eq. D-61})$$

D-4: Fundamental Frequency Real and Reactive Power

In this section, we calculate the fundamental frequency three-phase real and reactive power from the extracted fundamental frequency voltage and current phasors as follows:

$$P(k) = \text{Re} \left\{ \tilde{V}_{an}(k) \cdot \tilde{I}_a^*(k) + \tilde{V}_{bn}(k) \cdot \tilde{I}_b^*(k) + \tilde{V}_{cn}(k) \cdot \tilde{I}_c^*(k) \right\} \quad (\text{Eq. D-62})$$

$$Q(k) = \text{Im} \left\{ \tilde{V}_{an}(k) \cdot \tilde{I}_a^*(k) + \tilde{V}_{bn}(k) \cdot \tilde{I}_b^*(k) + \tilde{V}_{cn}(k) \cdot \tilde{I}_c^*(k) \right\} \quad (\text{Eq. D-63})$$

D-5: Next Zero-Crossing Time

With the obtained positive sequence voltage phasor \tilde{V}_1 , we can calculate the next zero-crossing time from negative to positive. By defining that the voltage in the time domain is the cosine function, we can convert the positive sequence voltage phasor \tilde{V}_1 into the time-domain representation $V_1(t)$, as follows:

$$\tilde{V}_1(k) = |\tilde{V}_1(k)| \angle \theta_{V_1}(k) \quad (\text{Eq. D-64})$$

$$V_1(t) = \sqrt{2} \cdot |\tilde{V}_1(k)| \cdot \cos(2\pi \cdot f_s(k) \cdot t + \theta_{V_1}(k)) \quad (\text{Eq. D-65})$$

As shown in Figure. D-2, the zero crossing from negative to positive occurs in every 360° , or time $\frac{1}{f_s(k)}$ sec. Thus, we can calculate the next zero-crossing time from negative to positive, t_{n_1+1} , as follows:

$$V_1(t_{n_1+1}) = \sqrt{2} \cdot |\tilde{V}_1(k)| \cdot \cos(2\pi \cdot f_s(k) \cdot t_{n_1+1} + \theta_{V_1}(k)) = \sqrt{2} \cdot |\tilde{V}_1(k)| \cdot \cos\left(2\pi \cdot (n_1 + 1) - \frac{\pi}{2}\right) \quad (\text{Eq. D-66})$$

$$2\pi \cdot f_s(k) \cdot t_{n_1+1} + \theta_{V_1}(k) = 2\pi \cdot (n_1 + 1) - \frac{\pi}{2} \quad (\text{Eq. D-67})$$

$$t_{n_1+1} = \frac{1}{f_s(k)}(n_1 + 1) - \frac{\frac{\pi}{2} + \theta_{V_1}(k)}{2\pi \cdot f_s(k)} \quad (\text{Eq. D-68})$$

where $n_1 = \text{int}\left(\frac{\omega_s t_R + \theta_{V_1}(k)}{2\pi}\right)$ and t_R is the present time.

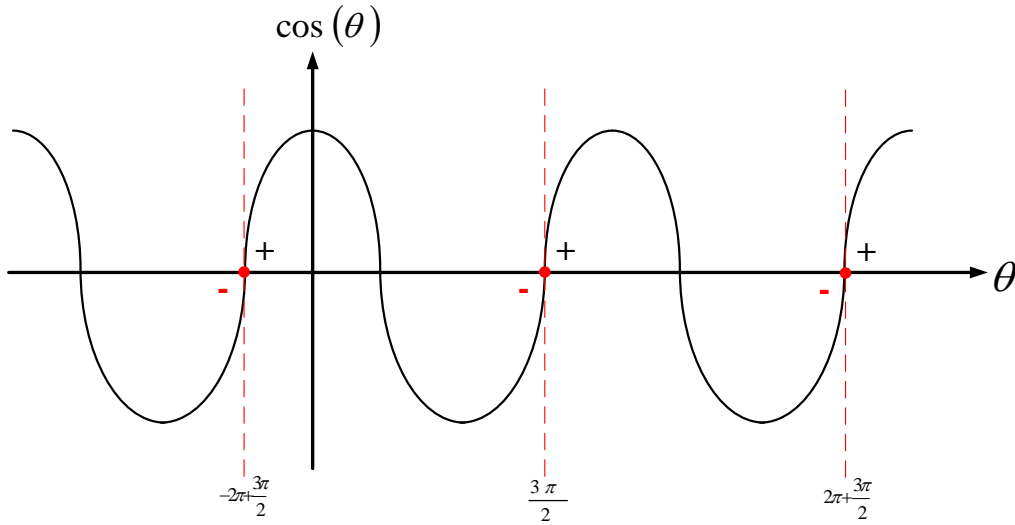


Figure D-2: Cosine Function with respect to the Phase Angle

D-6: Average DC-Input Voltage

The average DC-input voltage is computed as follows:

$$\bar{V}_{DC}(k) = \frac{1}{N} \sum_{i=k}^{k+N-1} V_{DC}(i) \quad (\text{Eq. D-71})$$

where:

- $V_{DC}(i)$: Input data sample sequence of the DC-input voltage.
 N : The number of samples in the $\frac{1}{6}$ of a period $\left(= \frac{1}{6} \cdot \frac{1}{f_s \cdot T_r}\right)$.
 T_r : Sampling period of the analog-to-digital converter.
 f_s : The actual average fundamental frequency.

13. Appendix E: Master Thesis by Christopher Weldy

This Appendix presents the summary of the Master Thesis by Christopher Weldy. The full Thesis is available on the Georgia Tech archives.

SUMMARY STABILITY OF A 24-BUS POWER SYSTEM WITH CONVERTER INTERFACED GENERATION

The objective of this Masters Thesis is to investigate the system stability implications of integration of power electronic converter interfaced generation (CIG) into conventional power systems. Due to differences between conventional generation and CIG, the power system fault currents, voltage response, and frequency response will likely change with increased penetration of CIG. This research will use state of the art software tools to perform simulations on the IEEE 24-Bus Reliability Test System (RTS-24), appropriately modified to include converter interfaced generation. Time-domain dynamic simulations and fault calculations will be performed for the system. A comprehensive set of simulations will be performed on the base case, comprised entirely of conventional generation. Conventional generation will be replaced by CIG in the model, one generating station at a time until CIG penetration is one-hundred percent. The comprehensive set of simulations will be performed at each level of CIG penetration. The results will be compared to the base case, with a focus on voltage response, frequency response, and fault current levels of the power system.

As conventional generation is replaced by CIG the system frequency declines to lower and lower minimum values in response to disturbances. Furthermore, the system voltages oscillate at higher and higher frequencies and resolve at undesirable deviations from their initial values. These undesirable results, however, can be mitigated by active and reactive power injections in response to system disturbances. To mitigate some of the issues observed in the maximum CIG power system, active and reactive power injections were modeled to represent the potential contribution to dynamic stability of the system. Use of active power injection in response to a fault can mitigate some of the additional frequency dip caused by reduction in generator inertia. Use of reactive power injection in response to a fault can mitigate some of the voltage deviation observed due to insufficient reactive power margin of available generation.

Power electronic converter rating limits have a significant impact on fault current levels in the system, but the network impedance can reduce the impact of these converter limitations at locations remote from the converter. As penetration of CIG into power systems increases, fault current levels may begin to approach load current levels. This condition may require new protection methods to maintain reliable and secure protection as power systems evolve.

Part II

Development of Positive Sequence Converter Models and Demonstration of Approach on the WECC System

Vijay Vittal
Rajapandian Ayyanar
Arizona State University

Graduate Students:
Deepak Ramasubramanian
Ziwei Yu
Arizona State University

For more information about Part II, contact:

Vijay Vittal
Director, Power Systems Engineering Research Center
Ira A. Fulton Chair Professor
Arizona State University
PO Box 875706
Tempe, AZ 85287-5706
Phone: (480) 965-1879
E-Mail: vijay.vittal@asu.edu
Phone: (480) 965-1879

Power Systems Engineering Research Center

The Power Systems Engineering Research Center (PSERC) is a multi-university Center conducting research on challenges facing the electric power industry and educating the next generation of power engineers. More information about PSERC can be found at the Center's website: <http://www.pserc.org>.

For additional information, contact:

Power Systems Engineering Research Center
Arizona State University
551 E. Tyler Mall
Engineering Research Center #527
Tempe, Arizona 85287-5706
Phone: (480) 965-1643
Fax: (480) 965-0745

Notice Concerning Copyright Material

PSERC members are given permission to copy without fee all or part of this publication for internal use if appropriate attribution is given to this document as the source material. This report is available for downloading from the PSERC website.

©2016 Arizona State University. All rights reserved.

TABLE OF CONTENTS

LIST OF FIGURES	iii
LIST OF TABLES	vii
LIST OF SYMBOLS	viii
1 INTRODUCTION	1
1.1 Background	1
1.2 Motivation and Objectives	3
1.3 Organization of the Report	5
2 LITERATURE REVIEW	6
3 MATHEMATICAL MODEL OF THE POWER SYSTEM	11
3.1 Synchronous Generator Model	11
3.1.1 The E'' Model	12
3.1.2 The E' Model	13
3.1.3 Classical Model	14
3.2 Governor Model	15
3.3 Static Exciter Model	16
3.4 Load Model	17
3.5 Network Model	18
4 MODELING OF CONVERTERS	21
4.1 The Converter Model in Commercial Software (pv1g, gewtg)	21
4.2 The Converter Control Model in Commercial Software (pv1e, ewtgfc)	23
4.3 User Defined Converter Control Model	24
4.4 Induction Motor Drive Model	30
5 SIMULATION AND RESULTS	32
5.1 Converter Model Validation in a Two Machine System	32
5.2 Results in Commercial Software	35

5.2.1	Small Scale System-Validation of Results	36
5.2.2	Large Scale System-Economy of Computation	44
5.3	Note on Boundary Current Representation of Converter	51
5.4	All CIG WECC system	52
5.4.1	Generation Outage (100% CIG penetration)	52
5.4.2	Dc Voltage Dip and Subsequent Recovery (100% CIG penetration)	57
5.4.3	Line Fault followed by Outage (100% CIG penetration)	59
5.4.4	Bus Fault (100% CIG penetration)	59
5.4.5	Line Reconnection (100% CIG penetration)	62
5.5	Induction Motor Drive Model	64
6	CONCLUSION AND FUTURE RESEARCH	68
	REFERENCES	70
	APPENDICES	75
A	EPCL CODE FOR USER DEFINED CONVERTER CONTROL MODEL	75
B	THREE GENERATOR EQUIVALENT SYSTEM DATA	83
B.1	Power flow solution	83
B.2	Dynamic data	83

LIST OF FIGURES

Figure 1.1	Sources of electricity generation in U.S. in 2013 [1]	1
Figure 3.1	E'' model equivalent circuit	12
Figure 3.2	E' model equivalent circuit	14
Figure 3.3	Droop characteristic	15
Figure 3.4	Governor based on droop characteristics	16
Figure 3.5	Static exciter basic framework	17
Figure 3.6	Machine and network reference frames for machine i	19
Figure 4.1	Modeling solar photovoltaic plants in PSLF [2]	21
Figure 4.2	Modeling wind turbine-generators in PSLF [3]	22
Figure 4.3	Converter model in PSLF [4]	23
Figure 4.4	Converter control model in PSLF [4]	24
Figure 4.5	User defined converter control model	25
Figure 4.6	Variation of Q_{limit} with V_t	26
Figure 4.7	Conversion from windup to anti-windup limit	27
Figure 4.8	Inner current control loop in PLECS to generate PWM reference voltage wave	28
Figure 4.9	Boundary current converter representation for positive sequence simulation	28
Figure 4.10	Voltage source converter representation for positive sequence sim- ulation	29
Figure 4.11	Modified active power controller for voltage source converter rep- resentation	29
Figure 4.12	Control diagram of induction motor speed control drive	31
Figure 5.1	Two machine system	32
Figure 5.2	Comparison of the converter active power output between PLECS and positive sequence simulation	33
Figure 5.3	Phase voltage waveforms at the converter terminal from PLECS . .	34
Figure 5.4	Line current waveforms at the converter terminal from PLECS . .	34
Figure 5.5	Converter active power output for different PLL gains	35

Figure 5.6	Three machine nine bus equivalent system	36
Figure 5.7	Comparison of the active power output of converter at bus 1 between PLECS and the ‘epcgen’ model in PSLF with synchronous machines at buses 2 and 3	37
Figure 5.8	Comparison of the reactive power output of converter at bus 1 between PLECS and the ‘epcgen’ model in PSLF with synchronous machines at buses 2 and 3	38
Figure 5.9	Comparison of the terminal voltage of converter at bus 1 between PLECS and the ‘epcgen’ model in PSLF with synchronous machines at buses 2 and 3	39
Figure 5.10	Sensitivity of the terminal voltage of converter at bus 1 for positive sequence voltage source representation to different values of filter inductor	40
Figure 5.11	Active power output of the converters for an all CIG system with increase in active power load	41
Figure 5.12	Reactive power output of the converters for an all CIG system with increase in active power load	42
Figure 5.13	Frequency response of an all CIG system with increase in reactive power load	42
Figure 5.14	Voltage magnitudes of an all CIG system with increase in reactive power load	43
Figure 5.15	Active power output of the converters for an all CIG system with increase in reactive power load	43
Figure 5.16	Reactive power output of the converters for an all CIG system with increase in reactive power load	44
Figure 5.17	Power flow in the WECC system [5]	45
Figure 5.18	Active power generation in the Arizona area due to trip of two Palo Verde units	46
Figure 5.19	Total generation in Southern California area due to trip of two Palo Verde units	47
Figure 5.20	System frequency due to trip of two Palo Verde units	47
Figure 5.21	Active power flow to Southern California from Arizona with the opening of a tie line between Arizona and Southern California following a line fault	48

Figure 5.22 Active power flow to Southern California from LADWP with the opening of a tie line between Arizona and Southern California following a line fault	49
Figure 5.23 Active power flow from Southern California to San Diego with the opening of a tie line between Arizona and Southern California following a line fault	49
Figure 5.24 Active power output of a unit at Four Corners for a bus fault close to the unit	50
Figure 5.25 Terminal voltage of a unit at Four Corners for a bus fault close to the unit	50
Figure 5.26 Magnitude of converter current for a voltage source representation of the converter for a bus fault close to the unit	51
Figure 5.27 Frequency across five generation areas for the trip of two Palo Verde units (droop coefficient of each CIG unit is R_p)	53
Figure 5.28 Active power output in four areas of WECC following the trip of two Palo Verde units	54
Figure 5.29 Behavior of the third Palo Verde unit for the trip of two other Palo Verde units	55
Figure 5.30 Frequency across five generation areas for the trip of two Palo Verde units (droop coefficient of each CIG unit is $2R_p$)	55
Figure 5.31 Frequency across five generation areas for the trip of two Palo Verde units (droop coefficient of each CIG unit is $R_p/2$)	56
Figure 5.32 Frequency across five generation areas for the trip of two Palo Verde units followed by the reduction in dc voltage by 1% and its subsequent recovery	58
Figure 5.33 Behavior of the third Palo Verde unit for the trip of two other Palo Verde units followed by the reduction in dc voltage by 1% and its subsequent recovery	58
Figure 5.34 Arizona active power flow with the opening of a tie line between Arizona and Southern California following a line fault	59
Figure 5.35 Southern California active power flow with the opening of a tie line between Arizona and Southern California following a line fault	60

Figure 5.36 Active power flow from Arizona to Southern California with the opening of a tie line between Arizona and Southern California following a line fault	60
Figure 5.37 Active power of a Four Corner unit for a three phase bus fault near the unit	61
Figure 5.38 Terminal voltage of a Four Corner unit for a three phase bus fault near the unit	61
Figure 5.39 Current of a Four Corner unit for a three phase bus fault near the unit	62
Figure 5.40 Current of a Four Corners unit for a line re-closure near the unit . .	63
Figure 5.41 Current of a Four Corners unit located one bus away	63
Figure 5.42 Current of a Four Corners unit located one bus away for lower maximum current	64
Figure 5.43 Total Arizona active power for line re-closure	64
Figure 5.44 Speed of induction motor for both the presence and absence of a constant speed drive for a 10 MW load increase	65
Figure 5.45 Load torque of induction motor for both the presence and absence of a constant speed drive for a 10 MW load increase	65
Figure 5.46 Active power consumed by induction motor for both the presence and absence of a constant speed drive for a 10 MW load increase	66
Figure 5.47 Reactive power consumed by induction motor for both the presence and absence of a constant speed drive for a 10 MW load increase	66

LIST OF TABLES

Table 5.1	Converter-controller parameter values for three generator equivalent system	37
Table B.1	Power Flow Solution for the three generator equivalent system . . .	83
Table B.2	Generator dynamic data for the three generator equivalent system .	83
Table B.3	Exciter dynamic data for the three generator equivalent system . . .	83
Table B.4	Governor dynamic data for the three generator equivalent system . .	84

LIST OF SYMBOLS

Symbol	Description
AC	Alternating current
ACE	Area control error
AZ	Arizona
CIG	Converter interfaced generation
d/dt	Time derivative
D	Speed damping coefficient in synchronous machine
DC	Direct current
DFIG	Doubly-fed induction generator
DSA	Dynamic security assessment
e	Denotes the error signal in an exciter
e''	Complex value of voltage behind subtransient reactance in the dq frame
e''_d, e''_q	d and q axis components of the voltage behind subtransient reactance
E'	Voltage behind transient reactance in a synchronous machine in abc frame
E'_d, E'_q	d and q axis components of the transient voltage
E_d, E_q	d and q axis components of internal converter voltage
E''	Voltage behind subtransient reactance in a synchronous machine in abc frame
$ E $	Magnitude of internal converter voltage
E_{FD}	Synchronous machine stator voltage corresponding to field voltage
EMF	Electro motive force
EWTFGC	PSLF wind turbine controller model
EXAC4, EXST1	AC and static exciter models in PSLF
f	Denotes the feedback signal in exciter
$f()$	Function denoting a differential equation
fmetr	Frequency meter model in PSLF
FACTS	Flexible AC transmission system
$g()$	Function denoting an algebraic equation
GE	General electric
GENCLS	Classical machine model in PSLF
GENROU	Detailed synchronous machine model in PSLF
GENTPF	Synchronous machine model in PSLF
GEWTG	PSLF GE wind generator model

H	Inertia constant of synchronous machine
H_{ind}	Inertia constant of induction motor
i_d, i_q	Current along the d and q axis
i_{ds}, i_{qs}	d and q axis stator current components of an induction motor
I	Current injected by the machine into the network in the abc frame
\bar{I}	Vector of network currents
I_{Pcmd}, I_{Qcmd}	Active and reactive current commands in converter controller
IEEE	Institute of Electrical and Electronics Engineers
kV	Unit of voltage (kilo volts)
K_a	Exciter gain
K_f	Feedback gain in exciter
K_i, K_p	Integral and proportional in converter controller
K_{ip}	Integral gain in converter controller active power loop
K_{limit}	Anti-windup proportional gain in converter controller
L'_d, L'_q	Synchronous machine transient inductances along the d and q axis
L''_d, L''_q	Synchronous machine subtransient inductances along the d and q axis
LADWP	Los Angeles Department of Water and Power
LVPL	Low voltage power logic
m	Amplitude modulation ratio in converter
M	Transformed reduced admittance matrix
MW,MVAR	Units of active and reactive power (mega watts and mega vars)
MPPT	Maximum power point tracking
P	Power
P_{cmd}	Active power command generated by converter controller
P_e	Output electrical power of machine
P_g	Scheduled generator output power at rated speed
P'_g	Final achieved steady state power at frequency ω_p
P_m	Input mechanical power of a synchronous machine
P_{max}	Maximum active power of a power source
P_{ord}	Reference active power signal for converter controller in PSLF
P_{ref}	Reference set point power for the governor
PI	Proportional Integral
PSLF	Positive sequence load flow
PSS	Power system stabilizer

PSS/E	Power system simulator for engineering
PV	Photo voltaic
PV1G,PV1E	PSLF converter models
Q_{cmd}	Reactive power command generated by converter controller
Q_g	Generated reactive power
Q_{max}, Q_{min}	Maximum and minimum reactive power of a power source
r	Synchronous machine stator resistance
R	Droop coefficient for thermal governor
R_p	Active power droop coefficient in converter controller
R_q	Reactive power droop coefficient in converter controller
R_r	Rotor resistance of an induction motor
RPS	Renewable portfolio standards
s	Represents complex frequency $j\omega$ in Laplace domain
s_i	Indicates the i^{th} state in a block diagram
s_{ind}	Slip of an induction motor
SOCAL	Southern California
T	Transformation matrix
T_1, T_2	Time constants of the lead lag block in a governor
T_{1pv}, T_{2pv}	Time constants of the lead lag block in converter controller
T_a	Exciter time constant
T_b, T_c	Time constants of the lead lag block in a exciter
T_e	Electrical torque of an induction motor
T_{ed}, T_{eq}	Converter voltage time constants
T_f	Feedback time constant in exciter
T_r	Transducer time constant
T_D, T_Q	Converter current time constants
T_G	Time constant of the first order time delay block in a governor
T_{Gpv}	Time constant of the first order time delay block in converter controller
T_m	Input mechanical torque of a synchronous machine
T'_o	Time constant of stator circuit in an induction motor
TGOV1	Governor model in PSLF
u	Vector of input/control variables
$var flg$	Flag setting in PSLF converter controller model
v'_d, v'_q	Induction motor stator voltage along the d and q axis

v_d, v_q	Synchronous machine stator voltage along the d and q axis
v_D, v_Q	Synchronous machine stator voltage along the D and Q axis
\bar{V}	Vector of network voltages
V_{dc}	Converter dc voltage
V_{ref}	Reference voltage level
V_{sch}	Scheduled voltage
V_t	Terminal voltage of generator in abc frame
V_T	Converter carrier voltage
VSC	Voltage source converter
WECC	Western electricity coordinating council
x	Vector of state variables in a system
\dot{x}	Vector of time derivatives of the state variables
x_d, x_q	d and q axis synchronous reactance of a synchronous machine
x'_d, x'_q	d and q axis transient reactance of a synchronous machine
x''_d, x''_q	d and q axis subtransient reactance of a synchronous machine
x''	Subtransient reactance of a synchronous machine
x_ℓ	Synchronous machine leakage reactance
X_m	Induction motor mutual reactance
X_r	Induction motor rotor reactance
y	Vector of network variables
\bar{Y}	Reduced network admittance matrix
δ	Torque angle of synchronous machine
λ_d, λ_q	d and q axis flux linkage along the air gap of a synchronous machine
λ_D, λ_Q	d and q axis flux linkage of the synchronous machine damper windings
ϕ	Internal voltage angle of converter
τ'_{d0}, τ'_{q0}	d and q axis components of the open circuit transient time constant
τ''_{d0}, τ''_{q0}	d and q axis components of the open circuit subtransient time constant
ω	Rotor speed of a synchronous generator
ω_p	Steady state frequency achieved by the droop controller after a disturbance
ω_{ref}	Value of rotor speed for which zero electrical power produced
$\omega_{r_{ind}}$	Speed of the rotor of an induction motor
ω_R	Rated rotor speed of a synchronous machine
ω_S	Synchronous rotor speed
Δ	Indicates a small change in a quantity

1. Introduction

1.1 Background

Fossil fuel fired steam power plants form the backbone of the electric power infrastructure. In 2013, in the United States alone, fossil fuel power plants have contributed close to 67% of the total 4 trillion kilowatt-hours of electricity generation, Figure 1.1 [1]. The

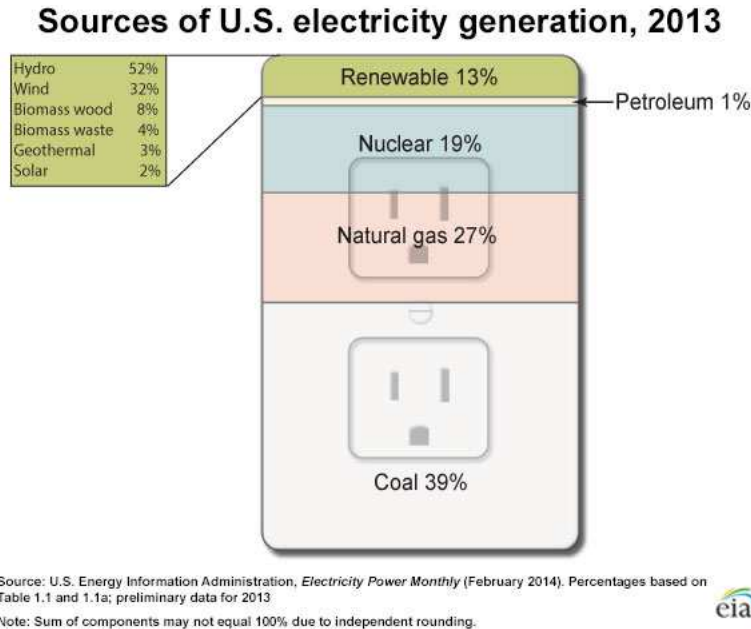


Figure 1.1: Sources of electricity generation in U.S. in 2013 [1]

contribution of coal to power generation has been steadily shrinking due to the increased production of electricity from natural gas, nuclear and wind resources. As it can be seen from Figure 1.1, presently natural gas and coal fired power plants provide the maximum contribution for the generation of electricity. This generation resource portfolio however will soon have to have a different profile as the predicted reserves of coal, natural gas and petroleum are set to last only for another 100 years or so [6, 7]. These figures bring about the need to explore different viable options of power generation. Further, with more stringent environmental considerations and emission controls, there is a need and requirement for cleaner energy generation sources. These sources, at present, represent the remaining 32% of the electrical energy generated. While nuclear power is considered to be a clean and efficient energy source, there are many concerns with regard to the safe operation of a nuclear power plant. The recent incident in Japan in 2011 has resulted in many coun-

tries, such as Germany, Australia, Portugal and Switzerland, restructuring their nuclear policy [8–10]. With the stacking of such odds, the electrical energy extracted from renewable energy sources will have to rise from the present 13% to a significant proportion of the total electricity energy generated.

The present power system is dominated by synchronous machines which generate electricity at an almost constant frequency of 60Hz/50Hz. These large machines are the work horses of the power grid and are interconnected with each other through transmission lines, thereby enabling the transfer of power to load centers located far away from the generation sources. The machines operate in synchronism with each other and thus give rise to an inherent ‘in-built’ torque known as the *synchronizing torque*. Within a certain range of operation, this torque is able to keep the generators in synchronism with each other, upon the occurrence of a disturbance. Further, due to the internal electromagnetic field in these machines, there is an inherent *damping torque* too which serves to damp out certain oscillations that may arise [11].

The development of a nation brings about an increase in the standard of living of a majority of its population. This results in an increase in electricity consumption resulting in a situation wherein the large generators are now forced to operate at a point close to their maximum capacity [12] if new sources of generation cannot be quickly added. A higher operating point reduces the synchronizing torque and can cause the machines to lose synchronism with each other even upon the occurrence of small disturbances. Thus, with generators operating close to their maximum capacity, the system stability margin reduces. Two effective solutions leading to the increase in the stability margins are the expansion of the transmission network and the commissioning of new generating plants. These solutions are however time consuming and require long term planning. In the short term, the reduction in the stability margin can be tackled to a large extent with the addition of precise control equipment such as the power system stabilizer (PSS) and FACTS devices. While these control equipment increase the speed of response to a disturbance, they serve to increase the operating range of the synchronous machine.

In recent years, there has been an increase in generation from converter interfaced sources. These converter interfaced sources do not operate in a synchronous manner and thus an almost constant frequency output is provided by the converter through stringent control. While some of these sources such as wind farms and tidal energy sources contain rotating parts, there are sources which are static in nature too, such as solar farms and fuel cells. All these sources will be referred to as converter interfaced generation (CIG).

The power system already has a small penetration of CIG sources which can be easily accommodated and tolerated due to the large presence of synchronous machines. However, due to technology improvements and requirements to meet renewable portfolio standards (RPS), the penetration level of CIGs in some areas of the power system can and will rise within a short period of time. Presently, this boom of CIG has taken place predominantly at the distribution level.

Many utilities are now investing in alternate sources of energy resulting in the connection of CIGs at the transmission level. This connection to the bulk power system presents a significant challenge with respect to the operation of the power system. Supplementary storage devices or control mechanisms have to be usually included to reduce the effect of the uncertainty in the power source (wind, solar and tidal). The converters, usually voltage source converters (VSC), decouple the source of power from the network. Thus the mass and inertia of a rotating machine like a wind turbine will now be electrically isolated from the network. In order to utilize the kinetic energy of the rotating wind turbine, extra control algorithms have to be built into the converter operation. Further, to promote maximum utilization of these renewable energy sources, many of them operate using a maximum power point tracking (MPPT) algorithm. This reduces the number of sources that can be scheduled by the system operator.

Taking this technology one step further, there is a prospect of even interfacing synchronous machines through converters. A large number of the future synchronous machines would be powered by gas turbines. From a thermodynamic point of view, a large gas turbine is more efficient when compared to a combination of smaller turbines. However due to compressor-turbine material stress constraints, a larger turbine would be required to operate at a lower speed. Thus, interfacing the synchronous machine to the grid through a converter releases it from operating at a fixed speed and can bring about an increase in the efficiency of the overall power system. Further, the reduced requirement of the auxiliary systems will result in an economic gain.

1.2 Motivation and Objectives

The increase in CIG penetration brings about significant challenges to the operation of a power system. Various paradigms that have been set in stone for conventional synchronous machine operation may now have to be revisited and revised. Equipment and control requirements may have to be specified considering the fact that these new CIGs may last for more than 30-40 years. It is akin to rebuilding the power system as it would have been done when the first synchronous machine was connected to the AC power grid.

The objectives of the proposed research work are as given below:

1. *Examination of the efficacy of CIGs to provide frequency control.* In large systems, with the increased penetration of CIGs, their ability to provide frequency control under the occurrence of load/generation changes will be investigated. Further, with their fast response and lack of inertia, the existing concepts of primary frequency response are to be examined.
2. *Full control of variable resources on a large scale.* The variability of wind and solar power has to be overcome by using multiple storage devices with a combination of precise control spanning the entire length and breadth of the large power system.
3. *Dynamic behavior of the power grid.* Even with full control of CIGs, the dynamic behavior of the power grid with only power converters feeding power into the grid will be examined.
4. *Behavior of various load profiles.* Nowadays, the impact of power converters is felt at the load end too with the advent of power drives and solid state electronic devices. The impact of these loads on the network supplied with CIGs will be examined.
5. *Transient and steady state stability.* The stability of the power grid, which until now relied largely on the natural operation of the synchronous machine, will be re-evaluated under the presence of CIGs.
6. *Reactive power support.* The present grid code does not allow for converters at the distribution level to control voltage. However, the converters at the transmission level will have to regulate the voltage at their buses. This would result in converters with increased ratings. The ability of converters to regulate the voltage and provide reactive power support is to be examined.
7. *Development of accurate dynamic models to represent CIG.* Commercial software have dynamic models representing the converters and their associated control blocks. However these control blocks are complex while the converter models do not seem to be robust with respect to system configuration. As part of this project, simple and accurate converter models will be developed that represent the behavioral patterns of a practical converter. Further, integration of the developed models in commercial software will be explored.

Upon completion of this research work, a better handle on the operational aspect of the power grid with a large penetration of CIGs would be obtained. Further, the behavior of the large scale power system with these distributed generation sources will be examined and validated under the existence of the proposed control schemes and stability profiles.

1.3 Organization of the Report

Following this introductory chapter, Chapter 2 will discuss an overview of the work present in literature. Subsequent to this, the modeling of conventional power system components will be presented in Chapter 3 while Chapter 4 covers the modeling of converters and their associated control mechanisms. The testing of the converter models along with proposed control strategies on systems of varying degrees of complexity will be shown in Chapter 5. Chapter 6 concludes this report.

2. Literature Review

Solid state switching converters form the backbone of the new age power systems. The presence of these solid state switches in the power generation system can be traced back to 1951 with the appearance of the first static exciter [13]. These excitation systems had a fast transient response and made the alternator self-regulating. Until 1961, these exciters were applied only to small generators with applications predominantly in aircraft and ship power systems. In 1961, the first static excitation system was developed for application to large land based steam turbine generators [14]. The success of these static excitation systems brought about a change in the definitions for excitation systems [15].

With the help of many design refinements through the passage of time and with improvements in technology, the basic framework of the static exciter nowadays is different from the one proposed in 1961. Although these excitation systems gave the desired transient response, they are known to cause problems with regard to steady state stability [16]. This goes to show that solid state switch devices, even while acting in a background capacity are known to cause instability in power systems. The development of PSS and FACTS devices has however alleviated this scenario to a certain extent.

The transformation of the power grid and the advent of CIG sources will bring the solid state switch to the foreground in the power system. This calls for a detailed study of the control of converter sources. Though this topic is a relatively new one, a lot of research activity has already been devoted to it starting from the micro second level control of the switching signals, driving through the millisecond control of the production of the reference signals and ending at an analysis of the effects of these sources on the power system.

The study of the behavior of the bulk power system is usually undertaken at a millisecond level. It can thus be safely assumed that the micro second level switching actions of the converter switches occur as expected. With this in the bag, the onus is now to obtain the appropriate reference signals at the millisecond level. The rapid growth of microgrids has ensured that there is adequate literature on this aspect of control. As microgrids are designed to be self-sufficient and can be expected to island from the main grid, voltage and frequency control within the microgrid is of prime importance. The presence of diesel generators in microgrids is quite common and with this aspect [17] discusses the frequency and voltage control in a small system when an unintentional islanding of the microgrid occurs. The vital point raised by the authors of this paper is that under certain conditions,

renewable energy sources will have to operate in a derated manner. This can bring about more control and also provide a reserve margin as shown in the paper.

With an increased penetration of CIG in the transmission system, it would be worthwhile to have these sources contribute to the frequency recovery. Reference [18] presents few of the key issues that surround this ideology. One of the issues mentioned is that since renewable energy sources are variable, they cannot be considered as reserves. Due to this variability, many utilities are hesitant to include these sources into the dispatchable set of sources. Further, unlike synchronous alternators which have a large mass, wind turbines are comparatively small and their inertia contribution is thus relatively small. Their contribution can only help during the intervening time it takes for the slower acting conventional units to react. The authors mention the necessity of designing primary and secondary frequency response control loops which would act with the presence of minimal storage devices. Also, concerns have been raised about the lack of accurate dynamic models to represent these sources. The most significant aspect shown by this paper is that with the addition of wind generators to the system, the total inertia of the system is shown to increase with the conditional clause that the inertia of the wind turbines is *time dependent*. Few other papers, [19–22], have tackled the issue of getting wind turbine machines to participate in system frequency regulation. These papers discuss a variety of control mechanisms and strategies specific to wind turbines. Though the concept of these mechanisms are sound, their testing and validation has been performed only on small systems.

One of the aims of this project is to explore the possibility of operating a CIG grid in the same manner as the present grid. This would prevent a requirement for a large scale change in terminology and metrics. Similar to primary frequency response in the conventional power grid, the concept of applying droop control to renewable sources has been widely discussed in [23–29]. However, as with previous literature, these papers discuss the control strategies within a specified microgrid. The concept of derating renewable sources is further explored in [24] wherein the possibility of a frequency reserve margin from wind generators is made possible. Also, the authors propose to continuously vary the droop coefficient with variation in wind velocity. In order to improve the accuracy of existing droop control, [25] proposes an addition of a supplementary control loop while [28] introduces cascaded control loops of angle, frequency and power in order to improve the power sharing accuracy in microgrids. The conventional frequency droop control loop is augmented with an angle quantity to improve its accuracy.

Most of the above literature is based on wind turbine generator machines. Since these

are rotating machines with some amount of kinetic energy, it is easier to control them for frequency response. However with photovoltaic sources few other issues arise. These are succinctly described in [30]. The authors state that if PV sources are to contribute to frequency response, then, three options are available: (1) Continue operation of PV at MPPT with energy storage devices; (2) Utilize a load bank to dump the surplus power; and (3) Make the PV sources dispatchable. The authors of [31] analyze that the best return on investment is obtained by operating the sources as dispatchable sources. In order to tackle the input power fluctuation, [32] proposes a fuzzy based frequency control for PV systems while [33] proposes the use of an electric double layer capacitor to maintain a spinning reserve.

Presently, utility scale solar plants have the capability to curtail their power output on the directive of the system operator. In addition, if curtailed, they also have the ability to increase their output if required [34]. It is thus not unrealistic to assume that in the future, with increased penetration of renewable resources, solar plants (and wind farms) can be scheduled to operate at an operating point below their maximum power output thereby providing a reserve margin to the system. Further, with the increase in renewable energy, energy storage elements will have a significant presence and thus also contribute to the reserve margin.

It has thus been established that there exists sufficient literature describing the possibilities of frequency recovery in the presence of CIG. However, as mentioned before, these techniques have only been tested on small systems. As these sources start appearing in the transmission system, the long distances and the requirement to transfer reactive power may play a role in deciding the stability of the system. With renewable resources, the question of variability and adequacy of reserve comes into the picture. The aim of approaching close to 100% CIG in the power system includes the possibility of having conventional synchronous machines also interfaced to the network via converters. Hydro power plants and gas turbine units can be hooked onto the grid in this manner. For these sources, variability and adequacy of reserve is no longer a major issue. However the issue of reactive power support over long transmission lines still exists. This can be a deciding factor in the stability of the system. According to the authors of [35], CIGs providing reactive power support can increase the probability of islanding especially when the penetration of CIGs is high. However if the power grid has to function in a stable manner, CIGs will have to be called on to provide reactive power support as has been analyzed in [36] with the possibility of wind turbines providing reactive power support to improve rotor angle

stability.

Analysis of the behavior of these sources in a large power system has turned up very few articles in the literature. Further, with most converter based units appearing in the distribution system, it is assumed that these units will have negligible impact on the behavior of the bulk power system. The authors of [37] have analyzed the effect of these units and have arrived at the conclusion that the effects are strongly dominated by the type of distributed generator technology. The authors have used the small standard New England Test System in their work with the maximum penetration of additional CIG being around 33%. According to the authors, raising the penetration level above this value was considered unrealistic as it would require a reconsideration of the classical power system concepts. A maximum penetration level of 30% was considered even in [12].

The first inkling of an analysis of a large power system with CIGs is provided by [38] wherein the impact of wind generators on the primary frequency control of the British transmission grid has been analyzed. Though these generators are assumed to not have any frequency control capability, an analysis of the amount of reserve required has been carried out. Subsequent to this, [11] and [39] have analyzed the effect on the transient and small signal stability of the power system due to increased penetration of DFIG based wind turbines. Further, a control strategy has been proposed by the authors in [39] to alleviate the impact of wind turbines in large power systems. However, though the system considered is large, the total penetration of CIG is quite low.

With the consideration of a large system for analysis, namely the Western Electricity Coordinating Council (WECC) system, [40] examined the impact of PV sources on the small signal and transient stability. A portion of the conventional generation was replaced to include the PV sources. However the PV sources were added only to those parts of the system that contained relatively large amounts of conventional generation. It has also been assumed that the reactive power support decreases with increase in CIG as most of the sources are rooftop PV which are not allowed to regulate voltage as per the existing grid code. The utility scale PV sources however provide reactive power support. The analysis has been carried out with a maximum penetration of 20% by the authors. Further, the PV sources were assumed to operate in a constant power mode. It was shown that these sources can be both beneficial and detrimental to the behavior of the grid. The exact effect depends on the location of the disturbance and the location of the PV sources.

The analysis in [41] is with regard to the impact that CIGs will cause on the modes of oscillation of the power system. The authors tackle the task of analyzing the behavior

of a future WECC system, year 2020 and 2022, with an increased penetration of CIGs. The impact of these devices on the existing electromechanical modes has been analyzed. Following this, it was further analyzed that certain modes in the inter area frequency range arise that are entirely due to CIGs. This aspect of operation is vital for future high penetration schemes.

In [42], a renewable penetration of 53% has been assumed and it has been shown that for most contingencies, the system is stable and the behavior abides by the grid code. The effect of converter based sources contributing to frequency response has also been explored. However, the renewable sources were again spread across the system and not concentrated in a particular area.

It can thus be seen that there has been little work done with regard to examining the behavior of large systems with increased penetration of CIGs. This project aims to study this aspect of large system with close to 100% penetration of CIGs. Along the way some control strategies for the safe and stable operation of such systems will also be proposed. Further, there has been little work done with regard to consideration of detailed representation of loads. Reference [43] discusses the stability of a CIG based microgrid along with a converter interfaced load. With the growing popularity of converter based motor drives, the analysis of converter interfaced loads are as important as CIGs for a future grid which this project aims to tackle. By tackling such issues the objectives of the project would be satisfied.

3. Mathematical Model of the Power System

The power system is considered by some to be the largest man-made machine in the world. With a vast network of transmission lines spanning across large geographical areas, interspersed with generators and load centers all operating at almost the same frequency and in unison most of the time, it is indeed a large machine. Due to its size and complexity, detailed mathematical models of its components are required to study its behavior using computer simulations. The general equations of the nonlinear power system can be described by a set of differential and algebraic equations as in (3.1) [44]:

$$\begin{aligned}\dot{x} &= f(x, y, u) \\ 0 &= g(x, y)\end{aligned}\tag{3.1}$$

where, x is the vector of states, y is the vector of network variables and u is the vector of inputs/control signals. The functions f and g represent the right hand sides of the differential and algebraic equations respectively.

The differential equations represent the dynamics of each member device of the power system. These equations usually represent the section of the power system which is behind the network bus and not represented in the power flow. As an example, these equations can represent the dynamic behavior of the internal operation of a synchronous generator. The network variables of the vector y , bus voltage for example, depict the boundary between the device and the network. The algebraic equations of the function g link each device to one another through the network admittance matrix.

Simulation of large power systems involves a significant computational burden. To this end, commercial software such as PSLF, PSS/E and DSA Tools are employed. In this project, PSLF has been used to run the simulations. In the following sections of the chapter, the mathematical models of few important devices, as used by PSLF, will be discussed.

3.1 Synchronous Generator Model

In a large power system, depending on the system size, complexity, study criteria and area of disturbance, models with different levels of simplification are utilized. Three commonly used models are discussed below in increasing order of simplicity.

3.1.1 The E'' Model

This model is also known as the ‘*voltage behind subtransient reactance model*’. It is derived from the full model with the following assumptions:

1. The transformer voltage terms, $\dot{\lambda}_d$ and $\dot{\lambda}_q$, are considered negligible in the stator voltage equations when compared with the speed voltage terms $\omega\lambda_d$ and $\omega\lambda_q$.
2. Additionally, in the stator voltage equations, the variation of ω is considered negligible *i.e.* $\omega \cong \omega_R$.

The stator voltage equations get modified as shown in (3.2) upon incorporation of the above assumptions.

$$\begin{aligned} v_d &= -ri_d - \omega\lambda_q - \dot{\lambda}_d \\ v_q &= -ri_q + \omega\lambda_d - \dot{\lambda}_q \end{aligned} \implies \begin{cases} v_d &= -ri_d - \omega_R\lambda_q \\ v_q &= -ri_q + \omega_R\lambda_d \end{cases} \quad (3.2)$$

3. The subtransient reactances along the d and q axis are assumed to be equal *i.e.* $L_d'' = L_q''$.

It should be noted that both the field circuit effects and the damper winding effects are represented in this generator model.

Representing all flux linkages as corresponding generated EMFs, the final stator voltage equations are,

$$\begin{aligned} v_d &= -ri_d - i_q x'' + e_d'' \\ v_q &= -ri_q + i_d x'' + e_q'' \end{aligned} \quad (3.3)$$

The EMF $e'' = e_q'' + je_d''$ is known as the voltage behind the subtransient reactance and the equivalent circuit of the generator in the abc frame is as shown in Figure 3.1. With the

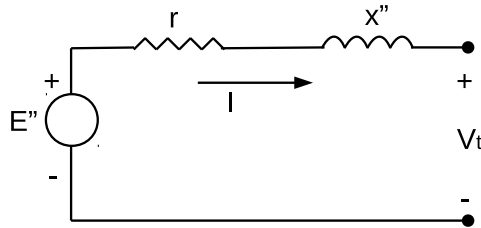


Figure 3.1: E'' model equivalent circuit

stator voltage equations defined, the remaining dynamic equations describing the machine can be derived as in Chapter 4 of [44]. In salient pole machines, in addition to the damper

winding, a fictitious short circuited winding is assumed to be present on the q axis to mimic the field circuit winding in the d axis.

The final equations obtained as are given below:

$$\dot{\lambda}_D = \frac{1}{\tau_{d0}''} \sqrt{3} E_q' - \frac{1}{\tau_{d0}''} \lambda_D + \frac{1}{\tau_{d0}''} (x_d' - x_\ell) i_d \quad (3.4)$$

$$\begin{aligned} \sqrt{3} \dot{E}_q' = \frac{\sqrt{3}}{\tau_{d0}'} E_{FD} + \frac{(x_d - x_d') (x_d'' - x_\ell)}{\tau_{d0}' (x_d' - x_\ell)} i_d - \frac{\sqrt{3}}{\tau_{d0}'} \left[1 + \frac{(x_d - x_d') (x_d' - x_d'')}{(x_d' - x_\ell)^2} \right] E_q' \\ + \frac{(x_d - x_d') (x_d' - x_d'')}{\tau_{d0}' (x_d' - x_\ell)^2} \lambda_D \end{aligned} \quad (3.5)$$

$$\dot{\lambda}_Q = \frac{-1}{\tau_{q0}''} \sqrt{3} E_d' - \frac{1}{\tau_{q0}''} \lambda_Q + \frac{1}{\tau_{q0}''} (x_q' - x_\ell) i_q \quad (3.6)$$

$$\begin{aligned} \sqrt{3} \dot{E}_d' = \frac{-(x_q - x_q') (x_q'' - x_\ell)}{\tau_{q0}' (x_q' - x_\ell)} i_q - \frac{\sqrt{3}}{\tau_{q0}'} \left[1 + \frac{(x_q - x_q') (x_q' - x_q'')}{(x_q' - x_\ell)^2} \right] E_d' \\ - \frac{(x_q - x_q') (x_q' - x_q'')}{\tau_{q0}' (x_q' - x_\ell)^2} \lambda_Q \end{aligned} \quad (3.7)$$

$$2H\dot{\omega} = T_m - e_q'' i_q / 3 - e_d'' i_d / 3 - D\omega \quad (3.8)$$

$$\dot{\delta} = \omega - 1 \quad (3.9)$$

These differential equations are supported by the following algebraic equations

$$e_q'' = \frac{x_d'' - x_\ell}{x_d' - x_\ell} \sqrt{3} E_q' + \frac{x_d' - x_d''}{x_d' - x_\ell} \lambda_D \quad (3.10)$$

$$e_d'' = \frac{x_q'' - x_\ell}{x_q' - x_\ell} \sqrt{3} E_d' - \frac{x_q' - x_q''}{x_q' - x_\ell} \lambda_Q \quad (3.11)$$

This simplified model is the most detailed model used in power system transient stability simulations and its model name in PSLF is GENROU.

3.1.2 The E' Model

While the previous model accounted for the subtransient circuit effects, this model considers those effects as negligible. The remaining two assumptions with regard to the transformer voltages and the variation of ω still hold for the two axis model.

With the absence of the subtransient circuit, this model is also known as the ‘*voltage behind transient reactance model*’. The equivalent circuit for the model is as shown in

Figure 3.2. As a further approximation, the model can be represented as a voltage behind

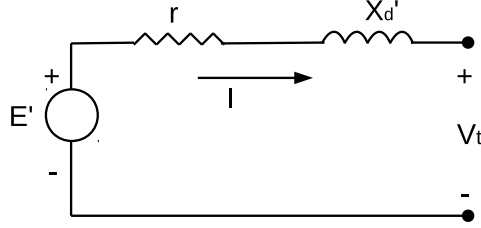


Figure 3.2: E' model equivalent circuit

the d axis transient reactance. The detailed reasoning behind this approximation along with the complete derivation of the dynamic equations can be obtained from Chapter 4 of [44].

The final dynamic equations are as given below:

$$\dot{E}'_q = \frac{1}{\tau'_{d0}} (E_{FD} - E'_q + (x_d - x'_d) I_d) \quad (3.12)$$

$$\dot{E}'_d = \frac{1}{\tau'_{q0}} (-E'_d - (x_q - x'_q) I_q) \quad (3.13)$$

$$2H\dot{\omega} = T_m - (E'_d I_d + E'_q I_q) + (L'_q - L'_d) I_d I_q - D\omega \quad (3.14)$$

$$\dot{\delta} = \omega - 1 \quad (3.15)$$

3.1.3 Classical Model

This is the most simple model for the synchronous machine. The significant assumptions made for the development of this model are as given below:

1. The air gap flux is constant. Thus the effects of armature reaction are neglected.
2. The voltage behind the transient reactance is constant.
3. The motion of the rotor of the machine coincides with the angle of the voltage behind the transient reactance.
4. No damper windings exist.
5. Input mechanical power P_m is constant.

Since constant flux constant voltage is assumed, no excitation system can be used for a generator represented by this model. Further, since the motion of the mechanical rotor

angle is assumed to coincide with the internal voltage angle, no governor model can be used with this machine representation.

The equations representing this model are as given below:

$$2H\dot{\omega} = P_m - P_e \quad (3.16)$$

$$\dot{\delta} = \omega - 1 \quad (3.17)$$

where, P_e is the electrical power injected into the network at the terminals of the machine. The value of this quantity can be obtained by using the network admittance matrix. In PSLF, this model goes by the name of GENCLS.

In simulations it is common to take one synchronous machine as the reference machine. This is done to avoid the dependency of the rotor angles δ on each other. Thus the angular velocity differential equations ($d\delta/dt$) are written using relative angles instead of absolute angles.

3.2 Governor Model

The main function of a governor is to vary the input power to the generator in accordance to the variation in frequency. While governors may have additional tasks depending on the type of fuel used, the main operational loop of all governors remains similar. To bring about primary frequency response, a droop controller is made use of in governors. The operational characteristic of droop controllers is as shown in Figure 3.3. At the rated

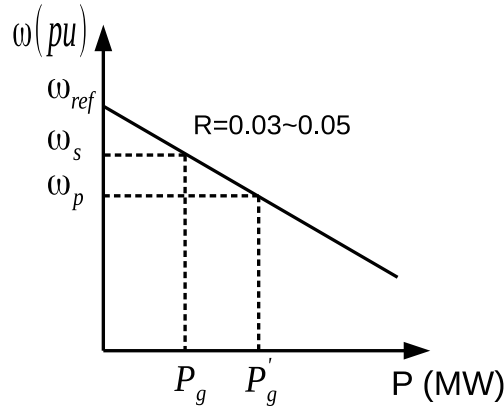


Figure 3.3: Droop characteristic

frequency of $\omega_s = 1.0pu$ the output of the generator is the scheduled power P_g . With a drop in frequency, the characteristic makes the governor increase the active power thereby arresting the fall in frequency. Eventually a steady state frequency ω_p is attained with an increased power output of P'_g .

Based on this characteristic, a simple governor model can be derived as shown in Figure 3.4. The differential equations describing the dynamic behavior of this governor are as given by (3.18)-(3.20).

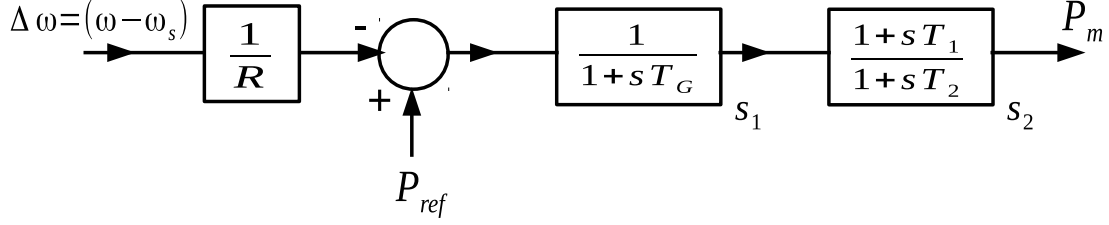


Figure 3.4: Governor based on droop characteristics

$$\frac{ds_1}{dt} = \frac{1}{T_G} \left[P_{ref} - \frac{\Delta\omega}{R} - s_1 \right] \quad (3.18)$$

$$\frac{ds_2}{dt} = \frac{1}{T_2} \left[s_1 - s_2 - s_1 \frac{T_1}{T_2} \right] \quad (3.19)$$

$$P_m = s_2 + s_1 \frac{T_1}{T_2} \quad (3.20)$$

In PSLF, a governor model very similar to this model is present under the model name of TGOV1.

3.3 Static Exciter Model

Any realistic generator model, E'' or two axis model, has to have an associated excitation system model to represent the exciter. While a handful of generators across the system continue to have a DC exciter, the static exciter and the brushless AC exciter are the most common exciters nowadays.

The basic framework of a static exciter model is shown in Figure 3.5 with the dynamic equations given by (3.21)-(3.26).

$$\frac{ds_1}{dt} = \frac{1}{T_r} (V_t - s_1) \quad (3.21)$$

$$e = V_{ref} - s_1 - f \quad (3.22)$$

$$\frac{ds_2}{dt} = \frac{1}{T_b} \left[e - s_2 - e \frac{T_c}{T_b} \right] \quad (3.23)$$

$$\frac{ds_3}{dt} = \frac{dE}{dt} = \frac{1}{T_a} \left[K_a \left[s_2 + e \frac{T_c}{T_b} \right] - E \right] \quad (3.24)$$

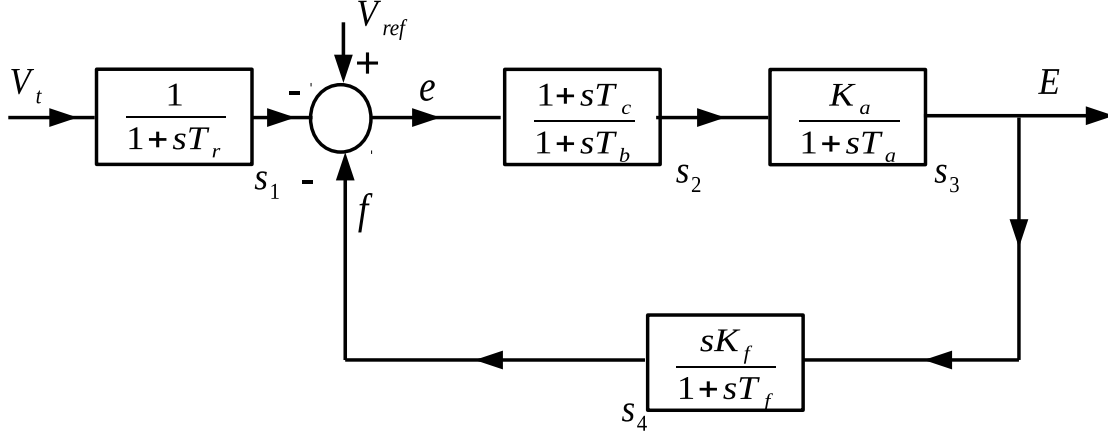


Figure 3.5: Static exciter basic framework

$$\frac{ds_4}{dt} = \frac{1}{T_f} \left[\frac{-K_f}{T_f} E - s_4 \right] \quad (3.25)$$

$$f = s_4 + E \frac{K_f}{T_f} \quad (3.26)$$

In AC and DC exciters, the signal E is the input excitation to the exciter and the armature voltage of the exciter becomes the input excitation to the synchronous machine. In static exciters, the signal E can be directly applied as the input excitation to the synchronous machine field winding and under these circumstances, this signal can be denoted as E_{FD} . In PSLF, the AC and static exciters models EXAC4 and EXST1 are used.

3.4 Load Model

While nonlinear loads are represented by differential equations depicting their dynamic behavior, static loads have been traditionally represented by either an *exponential* model or a *polynomial* model. Both models can represent a load as either constant power, constant current or constant impedance. Usually a complex mix of all three types of load are present in the system at any given point in time. However, if for some reason no detailed load information exists, then active power loads are represented as constant current loads while reactive power loads are represented as constant impedance loads [16].

Often even active power loads are represented as constant impedance loads. With this representation, all static loads can be absorbed into the system admittance matrix [44]. The current injection into the network now comes from only those components that have been represented by dynamic equations. The load buses can now be eliminated from the network equations using matrix reduction techniques [44].

Since all generator models are representative of a voltage behind reactance model, the generator reactance too can be absorbed into the admittance matrix and thereby represent the generator internal bus as being directly hooked onto the network.

3.5 Network Model

While running a power flow algorithm, the slack bus angle is usually set to zero and taken as the reference for all other bus angles. In dynamic simulations the slack bus voltage phasor is considered to coincide with the Q axis of the synchronously rotating network frame of reference with the D axis leading the Q axis by 90° .

The network equations of (3.1) i.e. $g(x, y) = 0$ describe the transmission network in relation to the bus quantities and injections as given by (3.27) & (3.28).

$$\bar{I} = \bar{Y}\bar{V} \quad (3.27)$$

where,

$$\bar{I} \triangleq \begin{bmatrix} \bar{I}_1 \\ \bar{I}_2 \\ \dots \\ \bar{I}_n \end{bmatrix} \text{ and } \bar{V} \triangleq \begin{bmatrix} \bar{V}_1 \\ \bar{V}_2 \\ \dots \\ \bar{V}_n \end{bmatrix} \quad (3.28)$$

To complete Ohm's law, \bar{Y} is the reduced admittance matrix of the network.

Since a network reduction has already been performed, \bar{I} and \bar{V} are vectors of length $nx1$ wherein it is assumed that there are n buses in the system at which a device is present with its behavior described by a set of differential equations. Correspondingly, the matrix \bar{Y} is of size nxn . When each phasor of \bar{I} , \bar{V} and \bar{Y} is projected into its components onto the DQ frame, then the length of the vectors become $2nx1$ while the size of the reduced admittance matrix becomes $2nx2n$.

Each synchronous machine is said to have a dq axis which rotates in synchronism with the rotor of that machine [45]. Due to the different loading levels of each machine, the dq axis of any particular machine will be displaced from the network DQ axis by an angle equal to the torque angle δ of that particular machine. Figure 3.6 shows the displacement between the two reference frames for any individual machine i . The relationship between the network and machine frame quantities, as given by (3.29), can be easily obtained by inspection of Figure 3.6.

$$\begin{aligned} V_{Qi} + jV_{Di} &= (V_{qi} \cos \delta_i - V_{di} \sin \delta_i) + j(V_{qi} \sin \delta_i + V_{di} \cos \delta_i) \\ \Rightarrow V_{D,Q} &= V_{d,q} e^{j\delta_i} \end{aligned} \quad (3.29)$$

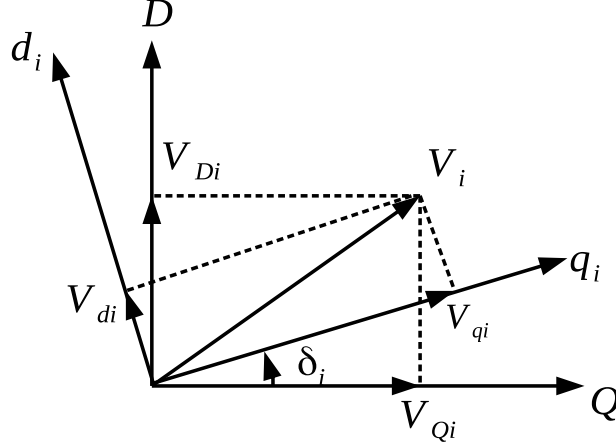


Figure 3.6: Machine and network reference frames for machine i

Therefore, (3.27) can now be rewritten as,

$$I_{D,Q} = Y V_{D,Q} \Leftrightarrow V_{D,Q} = Y^{-1} I_{D,Q} \quad (3.30)$$

Since the aim of a dynamic simulation is to observe the behavior of the devices connected to the network, it is preferred that the machine reference frame is maintained throughout the simulation. Thus (3.30) has to be converted from the network frame to the machine frame. The procedure as given in [44] is discussed below.

Using the transformation factor defined in (3.29), a transformation matrix T can be formed for the entire network. Since the transformation factor for each bus is independent of the other buses, the matrix T will be a diagonal matrix of size $n \times n$ as given,

$$T = \begin{bmatrix} e^{j\delta_1} & 0 & \dots & 0 \\ 0 & e^{j\delta_2} & \dots & 0 \\ \dots & \dots & \dots & \dots \\ 0 & 0 & \dots & e^{j\delta_n} \end{bmatrix} \quad T^{-1} = \begin{bmatrix} e^{-j\delta_1} & 0 & \dots & 0 \\ 0 & e^{-j\delta_2} & \dots & 0 \\ \dots & \dots & \dots & \dots \\ 0 & 0 & \dots & e^{-j\delta_n} \end{bmatrix} \quad (3.31)$$

The vector of voltages in the network and machine frame of reference is given by,

$$V_{D,Q} = \begin{bmatrix} V_{Q1} + jV_{D1} \\ V_{Q2} + jV_{D2} \\ \dots \\ V_{Qn} + jV_{Dn} \end{bmatrix} \quad V_{d,q} = \begin{bmatrix} V_{q1} + jV_{d1} \\ V_{q2} + jV_{d2} \\ \dots \\ V_{qn} + jV_{dn} \end{bmatrix} \quad (3.32)$$

Using the transformation matrix T , the two voltage vectors can be related as

$$\begin{aligned} V_{D,Q} &= T V_{d,q} \\ V_{d,q} &= T^{-1} V_{D,Q} = T^* V_{D,Q} \end{aligned} \quad (3.33)$$

Similar equations can be written to relate the current vectors of both frames of reference.

To transform (3.30), the relations in (3.33) are used.

$$I_{D,Q} = YV_{D,Q} \implies TI_{d,q} = YTV_{d,q} \quad (3.34)$$

Upon premultiplying by T^{-1} ,

$$I_{d,q} = (T^{-1}YT) V_{d,q} \triangleq MV_{d,q} \Leftrightarrow V_{d,q} = M^{-1}I_{d,q} \quad (3.35)$$

where,

$$M \triangleq (T^{-1}YT) \quad (3.36)$$

Thus (3.35) gives the desired relation between the currents and voltages of each device connected by the network, in the machine frame of reference.

If each device is represented as a Thévenin source, then the solution of the differential equations will give the values of the voltage vector of (3.35). In order to proceed to the next time step, (3.35) is now solved to obtain the values of the current vector. These new values of the current vector are then used in the next time step to obtain the solution of the differential equations. If the devices are represented as Norton sources, then the solution of the differential equations would return the values of the current vector and (3.35) would have to be solved to obtain the values of the voltage vector.

Since the transformation matrix T depends on the torque angle of the machine, the transformation plays an important role in the dynamic simulation.

In the following chapter, the modeling of the converters and their corresponding control strategies will be discussed.

4. Modeling of Converters

The previous chapter discussed the mathematical modeling aspects of the ‘*conventional*’ power system. Recently, due to the increasing addition of renewable sources of energy, converter models are being included into all commercial software. These models however differ in complexity from one software vendor to another. In addition, the development of generic models had been stalled for quite some time due to non negotiable proprietary information held by the manufacturers. In PSLF, the converter models and their associated control models are mainly representative of GE’s converter models for wind and solar applications [2, 3, 46], though, some manufacturer independent wind models also exist. The basic framework of connecting a converter based source to the grid in PSLF is as shown in Figure 4.1 [2] for a solar photovoltaic source and in Figure 4.2 [3] for a wind turbine-generator.

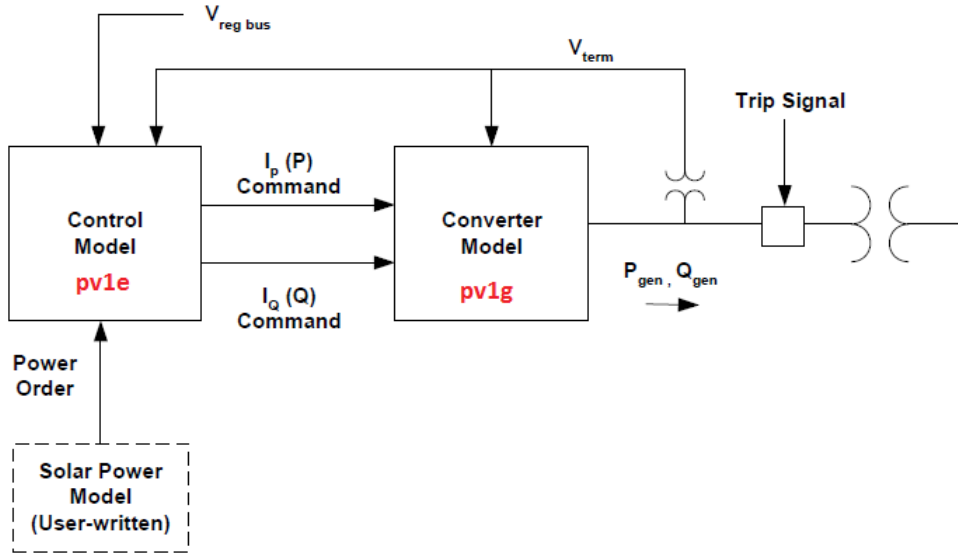


Figure 4.1: Modeling solar photovoltaic plants in PSLF [2]

4.1 The Converter Model in Commercial Software (pv1g,gewtg)

The converter is the interface between the source of power and the network. In PSLF, the models *pv1g* and *gewtg* represent the converter model for solar photovoltaic and wind applications respectively. There is minimal difference between the two models. Figure 4.3 shows the block diagram of this converter model [4]. In PSLF, the converter is represented as a current source which injects the required current into the network. The active and

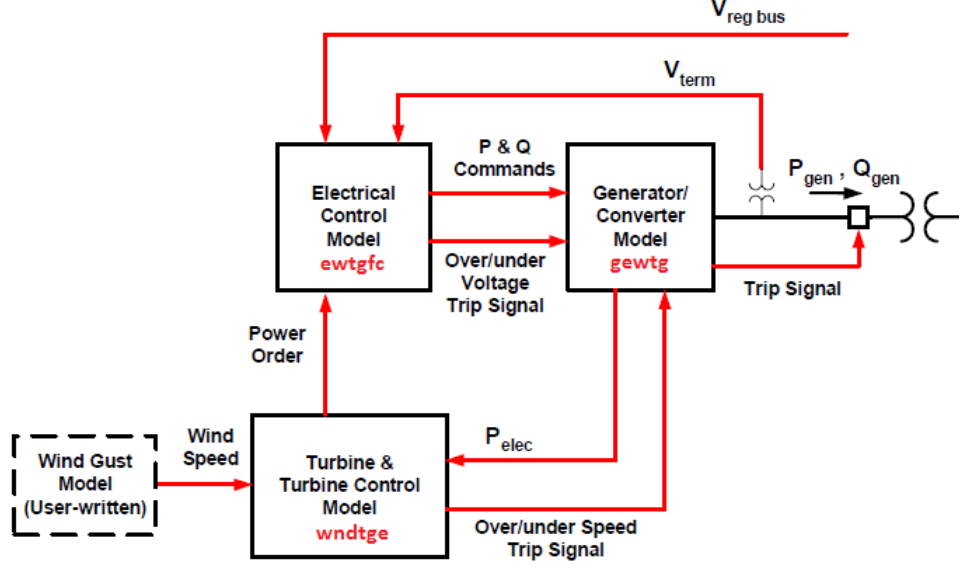


Figure 4.2: Modeling wind turbine-generators in PSLF [3]

reactive current commands are issued from the control block. The model receives the individual current commands and injects a complex current into the network. The 20ms time constant represents the switching of the solid state switches within the converter.

Apart from representing the switching action of the converter, built into this block is the behavior of few limiting devices. The low voltage power logic (LVPL) uses the terminal voltage to control the upper limit on the active power injected. If the bus voltage of the converter falls below a certain value, due to the occurrence of a disturbance, the LVPL block will reduce the upper limit as per the characteristic shown. Within a range of low voltage values, the active current upper limit is varied in a linear fashion. If the voltage falls below the lower boundary of the range, the active current upper limit is made zero. In the normal operating voltage range, the LVPL block does not affect the active current upper limit. All settings in the LVPL block can be set by the user.

Further, two algebraic current limiters are present in this block. The *high voltage reactive current management* section is instrumental in reducing the reactive power injected if the terminal voltage rises above a certain user defined limit. The user also has the freedom to set the rate at which the reactive power is ramped down. The *low voltage active current management* section takes care of reducing the active power injected while the voltage falls below a certain value. Its function is similar to the LVPL block.

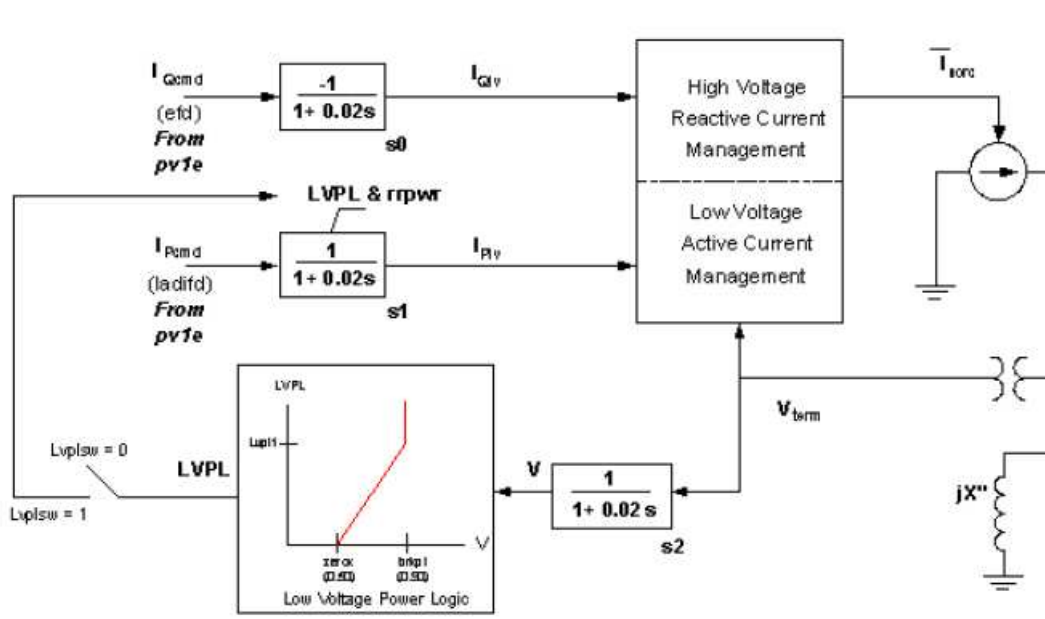


Figure 4.3: Converter model in PSLF [4]

4.2 The Converter Control Model in Commercial Software (pv1e,ewtgfc)

The control model is responsible for generating the active and reactive current commands for the converter model. The block diagram of this model is depicted in Figure 4.4 [4]. The bottom section of the model shows the calculation of the active current command. The reference active power, P_{ord} , can be either set by the user using an external user-written dynamic model or the value scheduled in the power flow. This feature thus allows for the inclusion of a governor type model to set the active power as will be shown later on in this report.

The model allows for three different ways of setting the reactive current command. These various modes can be toggled using the *varflg* parameter as shown in the block diagram. These different ways are:

1. PV VAr controller emulator: This emulator is nothing but a voltage regulator. The terminal voltage is compared to its reference value and the desired amount of reactive power is calculated using a PI controller.
2. Power factor regulator: The converter can be operated at a desired power factor and the reactive power is calculated based on the required power factor and the active

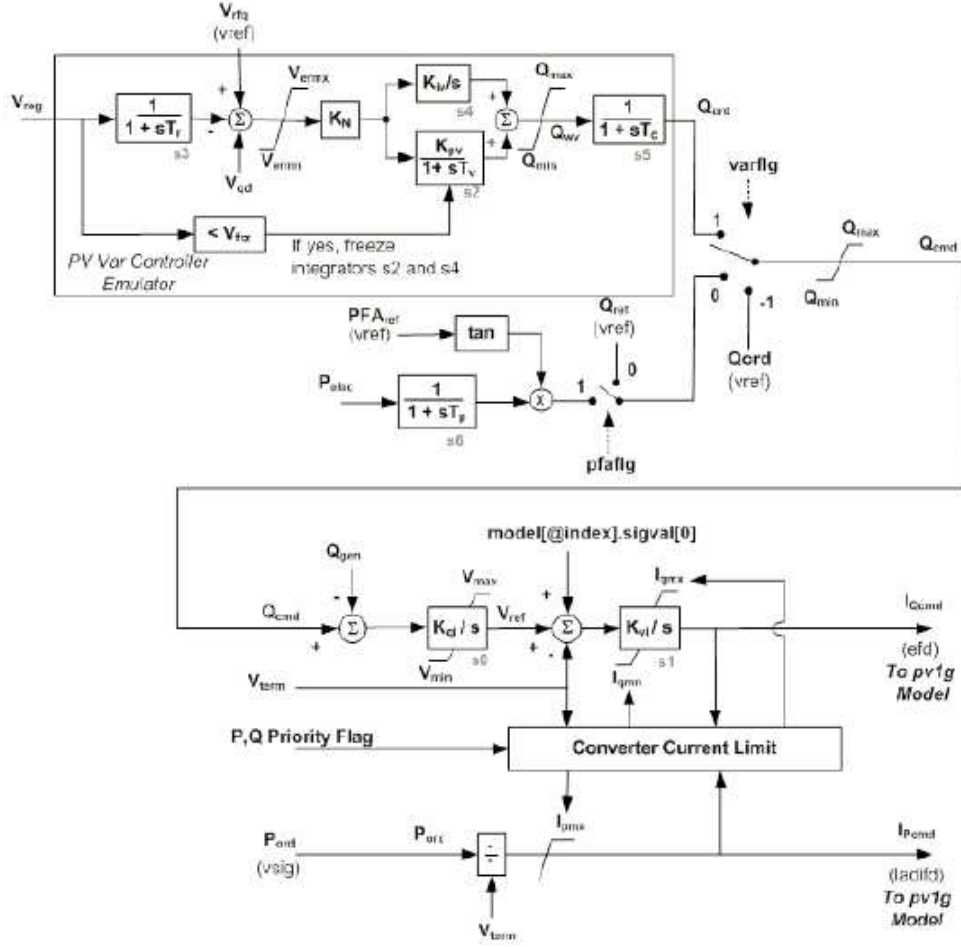


Figure 4.4: Converter control model in PSLF [4]

power.

3. User defined reactive power: The user has an option to provide a value of required reactive power.

The converter current limit block ensures that all current commands are within certain limits. The details of the operation of this limiter are provided in [2].

4.3 User Defined Converter Control Model

While the control model described in the previous section was found to work as per design and specifications, it was deemed to be complex. With the aim of achieving close to 100% CIG penetration, a requirement arises for simpler control structures bearing in mind that the stability of the system hinges upon the interaction of these controls with one

another. In addition, as different manufacturers would have their own variation of control architecture, a simple control was used to focus on the model of the converter. With this objective, a controller as shown in Figure 4.5 was designed for the converter.

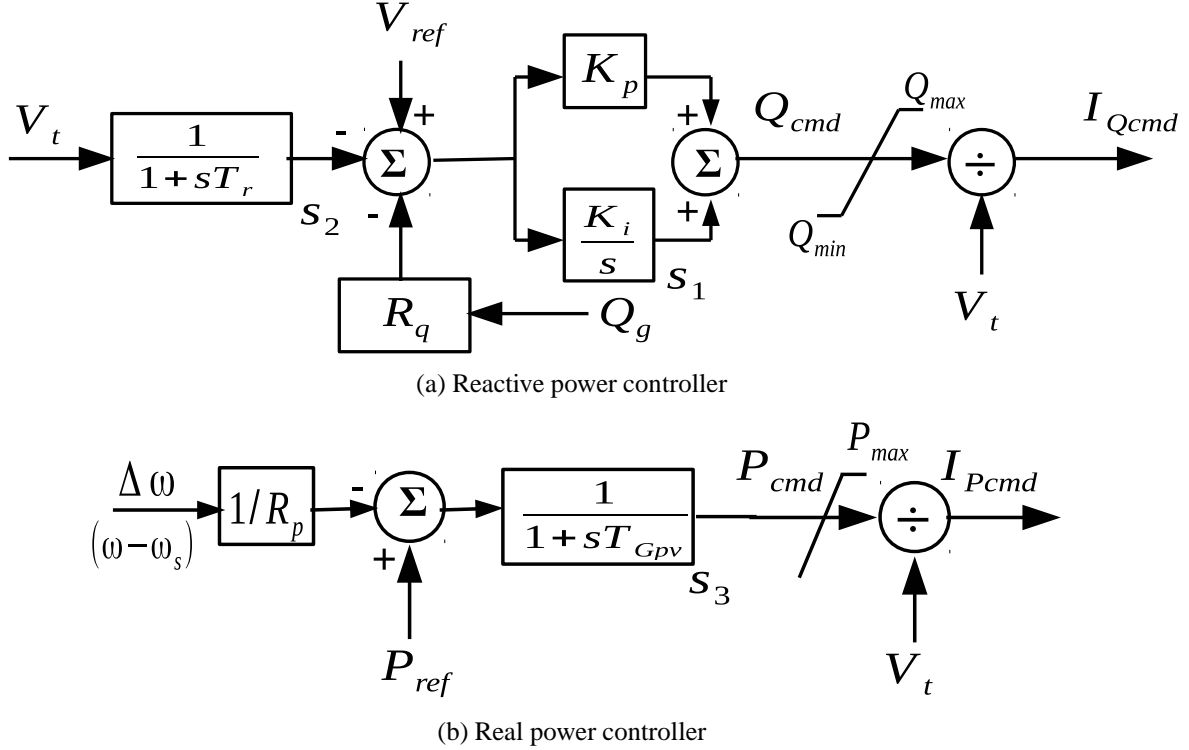


Figure 4.5: User defined converter control model

The effective real power order (Figure 4.5(b)) is a combination of the power setpoint and the active power droop coefficient while the reactive power order (Figure 4.5(a)) is obtained from the voltage error along with a reactive power droop. The QV droop is instrumental in obtaining a stable operation between converters when multiple converters are connected to the same bus. The active power droop coefficient is denoted as R_p and the reactive power droop coefficient is denoted as R_q . The equations describing the behavior of the controller are given by (4.1) to (4.5).

$$\frac{ds_1}{dt} = K_i [V_{ref} - s_2 - R_q Q_g] \quad (4.1)$$

$$\frac{ds_2}{dt} = (1/T_r) * [V_t - s_2] \quad (4.2)$$

$$\frac{ds_3}{dt} = (1/T_{Gpv}) * [P_{ref} - (\Delta\omega/R_p) - s_3] \quad (4.3)$$

$$Q_{cmd} = s_1 + K_p [V_{ref} - s_2 - R_q Q_g] \quad (4.4)$$

$$P_{cmd} = s_3 \quad (4.5)$$

Limits have been imposed on the maximum active and reactive power and minimum reactive power deliverable. In choosing the limits for the reactive and active power, it has been assumed that the converter can withstand an instantaneous MVA of 1.7 times its rating. Further, it has been assumed that at a terminal voltage level of 0.75pu, the minimum operable power factor is 0.4. As the voltage dips, the limits of the converter control will change to allow for more reactive power to be delivered while curtailing the active power delivered to meet the MVA rating. Though a terminal voltage of 0.75pu has been chosen as the minimum voltage, the maximum deliverable reactive power is maintained constant for voltages below 0.8pu as shown in Figure 4.6. The value of q_{max_1} is taken from the

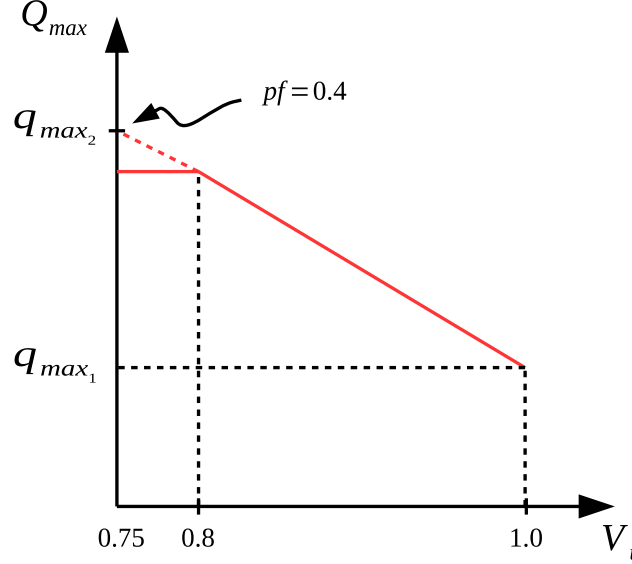


Figure 4.6: Variation of Q_{limit} with V_t

power flow but is assumed to be the value of maximum reactive power at a voltage level of 1.0pu. The value of q_{max_2} is obtained as given by (4.6).

$$q_{max_2} = \sqrt{\frac{(1.7 * MVA)^2}{1 + \left(\frac{1}{\tan \cos^{-1} 0.4}\right)^2}} \quad (4.6)$$

Therefore, at any voltage level V_t above 0.8pu, the value of q_{max} is obtained as given by (4.7).

$$q_{max} = q_{max_1} + \frac{q_{max_2} - q_{max_1}}{0.8 - 1.0} (V_t - 1.0) \quad (4.7)$$

The value of q_{min} is maintained constant as specified in the power flow while the maximum active power is obtained as in (4.8) to maintain the MVA rating.

$$p_{max} = \sqrt{(1.7 * MVA)^2 - q_{max}^2} \quad (4.8)$$

Since an integrator is present in the reactive power loop, the windup limit has been converted to an anti-windup limit as per the scheme mentioned in [47]. The block diagram of this conversion is as shown in Figure 4.7 where the value of K_{limit} is appropriately chosen.

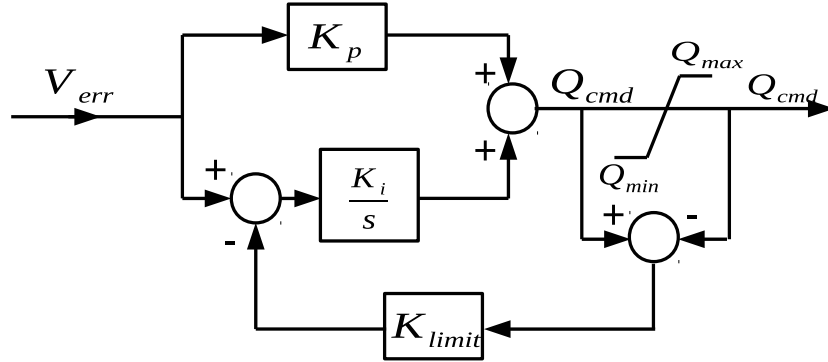


Figure 4.7: Conversion from windup to anti-windup limit

To model the converter, a voltage source representation of the converter has been proposed in this research work. The voltage source representation has first been modeled at the electromagnetic transient level using the PLECS [48] software package. This modeling has then been used as a basis for the development of a positive sequence phasor model which is required for large scale grid simulation. Using the PLECS software package, a detailed switching model of the converter has been simulated. The control mechanism described in Figure 4.5 is used to generate the current commands which are then used as shown in Figure 4.8 to generate the reference voltage wave to obtain the pulse width modulated signals. A 5 microsecond time step has been used for the simulation. The fast inner current control loops are required in the electromagnetic transient simulation to obtain the magnitude and phase angle of the PWM reference voltage wave. This detail of modeling the voltage source converter and its control is however not suitable for the simulation of large networks as it would require a smaller time step of simulation to accurately capture the inner loop behavior and this would considerably increase the time duration of simulation.

Due to the effect of grid impedance on the operation of the inner current control loop [49], a wide variety of inner current control loops are used in practical inverters with the

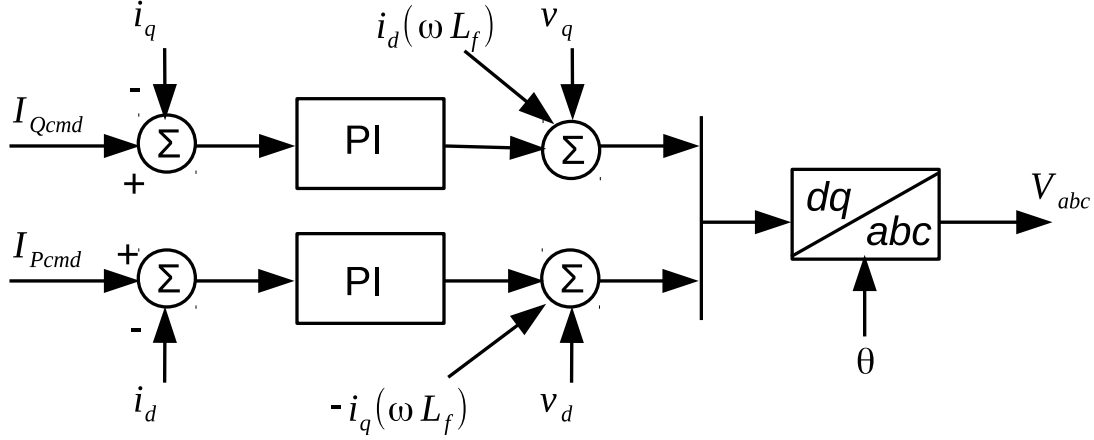


Figure 4.8: Inner current control loop in PLECS to generate PWM reference voltage wave

common characteristic of response times that are very fast in relation to the bandwidth proposed for grid level controls. Accordingly, the grid level modeling used in this project represents the behavior of the inner control loops by simple time constants. Hence, two alternatives can be considered for modeling the converters in positive sequence:

- With the assumption that the inner current control loop is very quick, the converter is modeled as a specified current boundary condition on the positive sequence network solution model. This representation has been referred to as the boundary current representation wherein the values of i_q and i_d from Figure 4.10 are the boundary currents as shown in Figure 4.9.
- As the converter is a voltage source converter with a voltage source on the dc side, the converter is modeled as a Thévenin voltage source described by Figure 4.10 and (4.9) and the active power controller is modeled as shown in Figure 4.11.

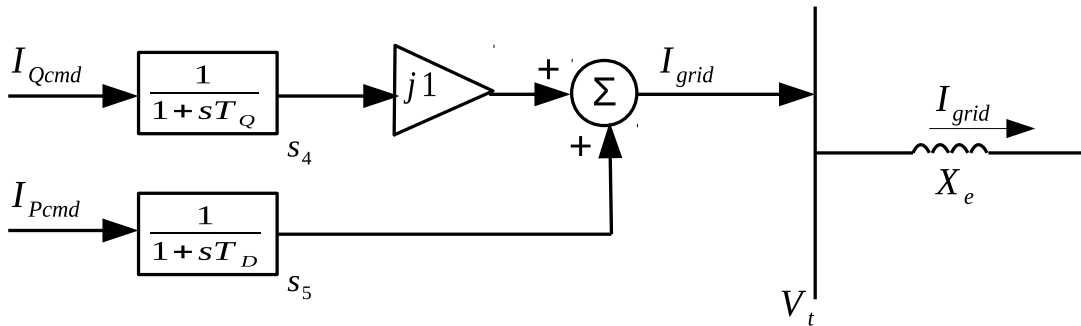


Figure 4.9: Boundary current converter representation for positive sequence simulation

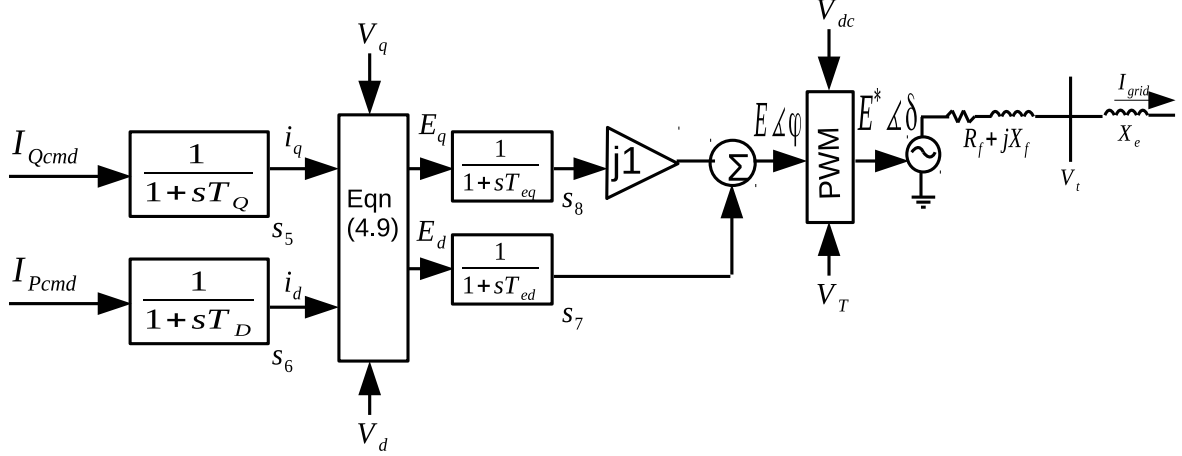


Figure 4.10: Voltage source converter representation for positive sequence simulation

$$\begin{aligned} E_d &= V_d + i_d R_f - i_q X_f \\ E_q &= V_q + i_q R_f + i_d X_f \end{aligned} \quad (4.9)$$

The converter representation includes the effect of the dc voltage and the amplitude modu-

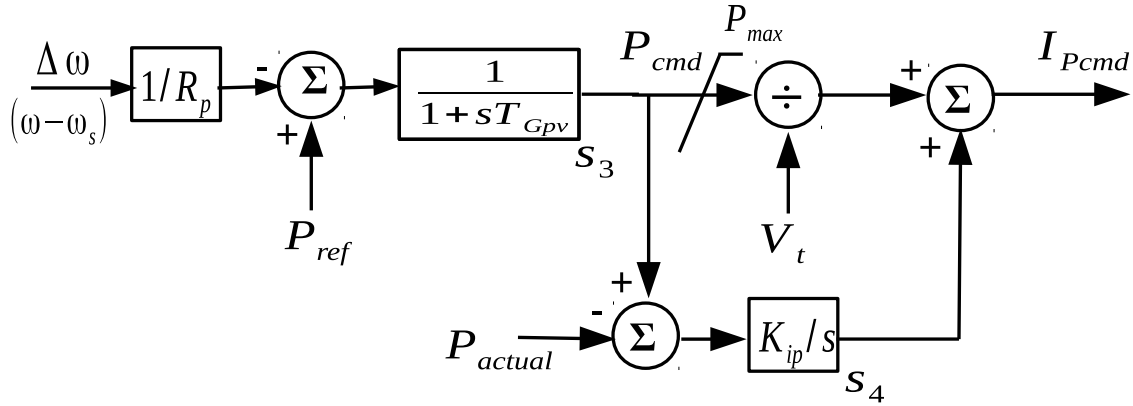


Figure 4.11: Modified active power controller for voltage source converter representation

lation ratio m of the pulse-width modulation control depicted by the PWM block in Figure 4.10. To achieve a steady state modulation ratio of 0.6, the carrier voltage (V_T) and dc voltage (V_{dc}) are initialized to be:

$$V_T = \frac{\sqrt{E_d^2 + E_q^2}}{0.6}; V_{dc} = \frac{\sqrt{E_d^2 + E_q^2}}{0.5 * 0.6} \quad (4.10)$$

At every time step, the values of E_d and E_q from (4.9) are used in the following manner:

- magnitude and angle of the required internal voltage is obtained as $|E| = \sqrt{E_d^2 + E_q^2}$ and $\phi = \tan^{-1}(E_q/E_d)$

- The modulation index is calculated as $m = |E|/V_T$. The value of m is limited to be between 0.4 and 1.0.
- The phase voltage values are then obtained as $E_{a,b,c} = 0.5mV_{dc} \cos(\omega_s t + \phi - 120i)$ where ω_s is 377 rad/s and $i = 0, 1, 2$
- value of E_d^* and E_q^* ($E^* \angle \delta$) is obtained by applying Park's transformation on $E_{a,b,c}$.

A lower steady state modulation ratio will require a higher dc voltage magnitude to maintain the same ac voltage and would restrict the lower band gap of the modulation ratio. A steady state modulation ratio of 0.6 has been chosen to allow for a sufficient range of values for the transient modulation ratio.

In addition, two protection schemes have been incorporated:

- As the converters have a hard current limit, an instantaneous overcurrent protection has been implemented with a cut-off current of 1.7 pu [2].
- A time dependent overvoltage protection has also been implemented. If the voltage at the terminal V_t rises 0.15 pu more than the steady state voltage for more than 0.1s, the converter is tripped.

The implementation of this converter and its associated controller for positive sequence time domain simulation was carried out in PSLF [50] by writing an EPCL code as given in Appendix A. EPCL is PSLF's in-built programming language.

4.4 Induction Motor Drive Model

The need for precise speed control of induction motors has resulted in the development of speed control power electronic drives. In a futuristic grid, both the generation source and the loads could be interfaced through converters. It is thus important to simultaneously develop positive sequence models for converter interfaced loads.

The equations representing the induction motor are as developed in [16] given here by (4.11)-(4.13). As a squirrel cage induction motor is assumed to be used, the rotor side equations of the machine are not present and only the stator equations are required along with the swing equation of the machine.

$$\frac{d\omega_{r_{ind}}}{dt} = \frac{1}{2H_{ind}} (T_m - T_e) \quad (4.11)$$

$$T_o' \frac{dv_d'}{dt} = -v_d' - \frac{X_m^2}{X_r} i_{qs} + \frac{sX_r v_q'}{R_r} \quad (4.12)$$

$$T_o' \frac{dv_q'}{dt} = -v_q' + \frac{X_m^2}{X_r} i_{ds} - \frac{sX_r v_d'}{R_r} \quad (4.13)$$

The control diagram of the speed control drive model is shown in Figure 4.12 [51]. The

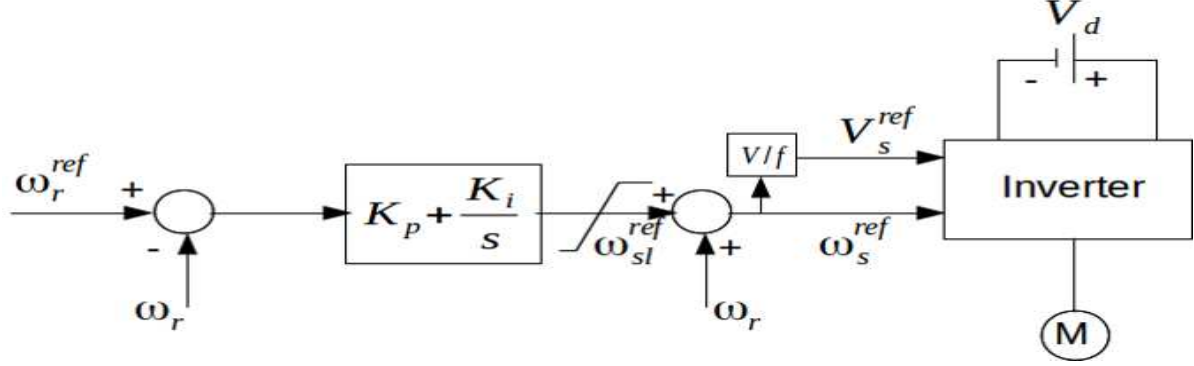


Figure 4.12: Control diagram of induction motor speed control drive

rectifier for the drive was considered to be an uncontrolled full bridge diode rectifier while the sinusoidal pulse-width modulation reference signal, denoted by V_s^{ref} and ω_s^{ref} , was generated to maintain constant flux inside the motor and maintain a constant rotor speed of ω_r^{ref} .

In the following chapter, a discussion of the results verifying the performance of this converter control for various system configurations and the induction motor drive model is recorded.

5. Simulation and Results

The performance of the converter and its associated control was first validated with the performance of the converter in PLECS by using a simple test system. Following this, the performance of the converter was analyzed in a 3 generator system and the 2012 WECC system.

5.1 Converter Model Validation in a Two Machine System

A C code was written to simulate the time domain dynamic response of the converter representation shown in Figures. 4.5 and 4.10. A simple test system as shown in Figure 5.1 was constructed to compare the behavior of the converter model in positive sequence with its behavior in PLECS. The loads were treated as constant admittance loads. For the

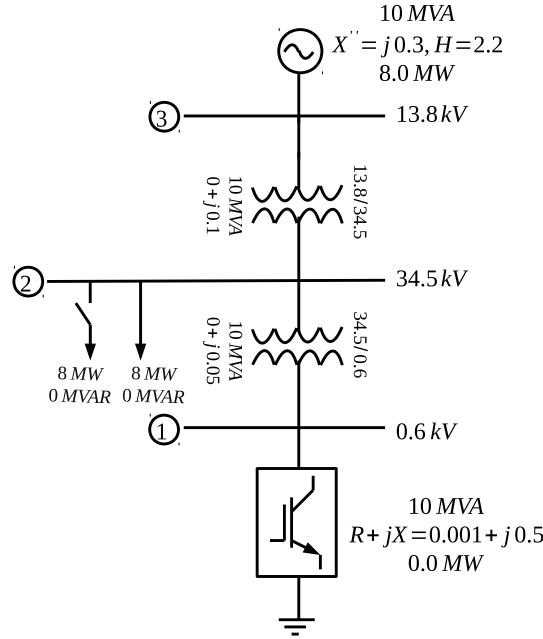


Figure 5.1: Two machine system

simulation, the synchronous machine was represented by a round rotor *genrou* model with an inertia constant $H = 2.2$ s along with an associated governor and static exciter model. To observe the response of the converter, an additional 8MW was switched on at $t = 1$ s at bus 2. Following this, at $t = 1.1$ s, the reference command to the converter (P_{ref} in Figure 4.5(b)) was changed from 0MW to 8MW.

In the PLECS simulation, a 5 kHz switching frequency was used to obtain the pulse width modulated waveform. The reactive power loop had gains of 4.0 and 20.0 respec-

tively for the proportional and integral controllers in both PLECS and the positive sequence simulation. The active power integral controller in the positive sequence simulation had a gain of 0.5.

The comparison between the PLECS simulation and the positive sequence model is shown by the active power output of the converter in Figure 5.2. Further, Figures. 5.3 and 5.4 show the 3 phase voltage and current waves at the converter terminals. From these figures it can be seen that the response of the converter is completed in approximately 50ms and the demand is quickly met. However, the positive sequence response differs from

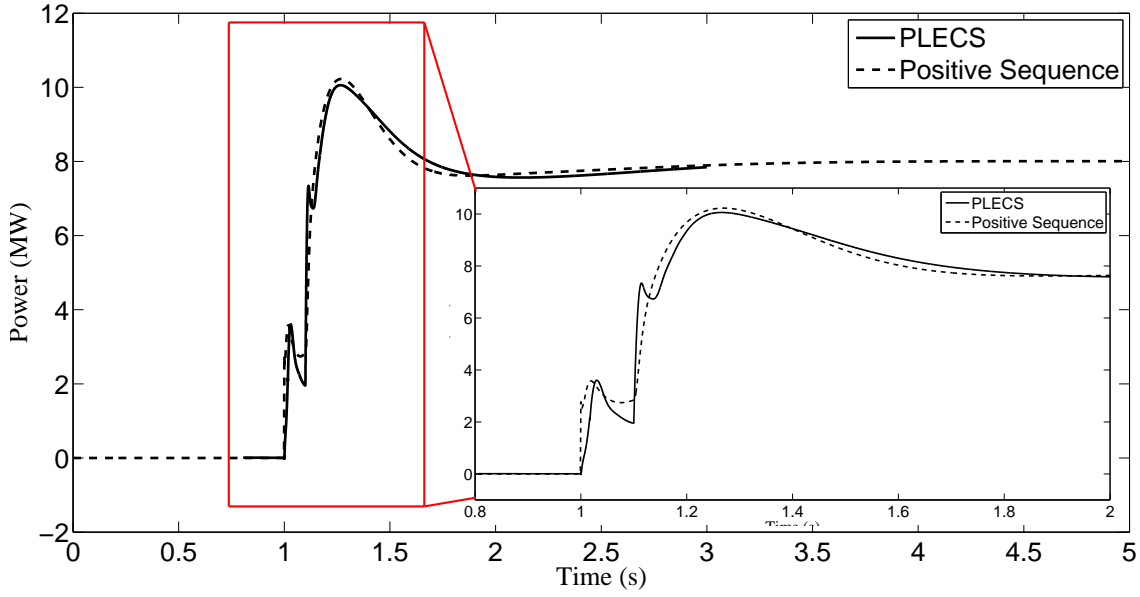


Figure 5.2: Comparison of the converter active power output between PLECS and positive sequence simulation

the PLECS model response at the instant of disturbance. One reason for this difference is the fact that in PLECS, a differential equation model is used to depict the filter inductors of the converter whereas in the positive sequence model, the filter inductor is represented algebraically as a simple reactance. Hence the PLECS response to a disturbance shows a small finite time constant as opposed to the instantaneous response obtained from the positive sequence simulation. This representation of the inductor is required for the point on wave type of simulation carried out in PLECS whereas the phasor simulation is unable to represent this feature. Secondly, as the PLECS simulation works on instantaneous values of voltage and current, a phased locked loop is required to track the phase angle of the voltage at the converter terminal and a small time constant is associated with this tracking.

As expected, the response of the converter to the step change in P_{ref} is completed

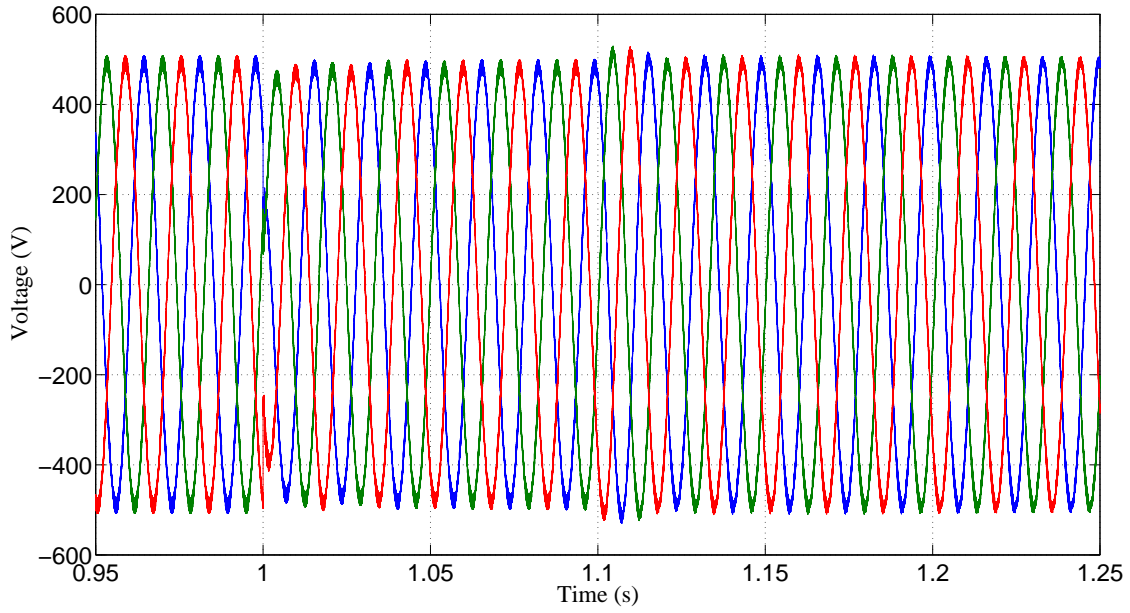


Figure 5.3: Phase voltage waveforms at the converter terminal from PLECS

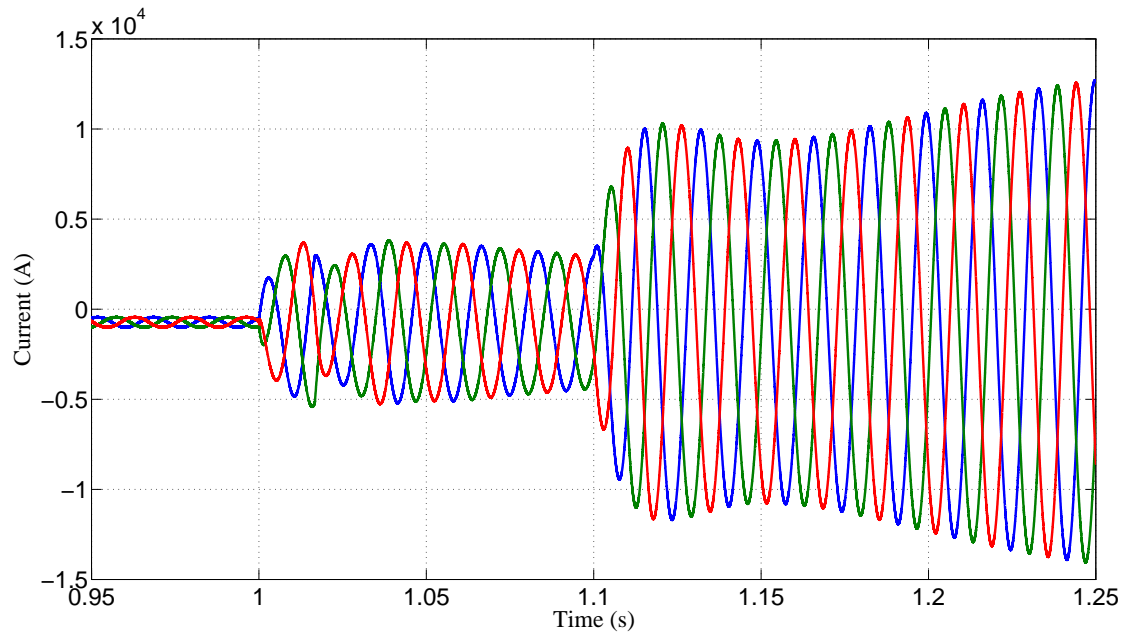


Figure 5.4: Line current waveforms at the converter terminal from PLECS

in approximately 50ms. The 0.1s delay in triggering the change in reference command is used to simulate a transfer trip situation. This scenario therefore depicts the natural response of the converter model to a change in the reference command.

The simplified positive sequence model representing the converter as a controlled volt-

age source without the explicit representation of the inner current control loop shows the same behavioral trend as the electromagnetic transient simulation. Thus while simulating large systems, this simplified model can be utilized.

The behavior of the PLL is intertwined with the value of the filter inductor and the gains of the inner current control loop. In order to restrict the percentage of ripple in the output current, the value of the filter inductor is decided based on the switching frequency. In addition, the switching frequency imposes a limit on the current loop bandwidth. Further, the PLL bandwidth should generally be lower than 60Hz in grid connected applications. In this project, the value of the filter inductor was so chosen as to restrict the current ripple to a maximum of 5%.

The sensitivity of the converter response to the PLL gain is as shown in Figure 5.5. Indirectly, the sensitivity of the converter response to the value of the filter inductor is also conveyed by the same curve. It can be seen that as the PLL becomes slower (lower gain), its effect is reflected in the performance of the converter in the few milliseconds following the disturbance. For this value of filter inductance, a faster PLL makes the system unstable. The next section will discuss the implementation of the simplified time domain converter

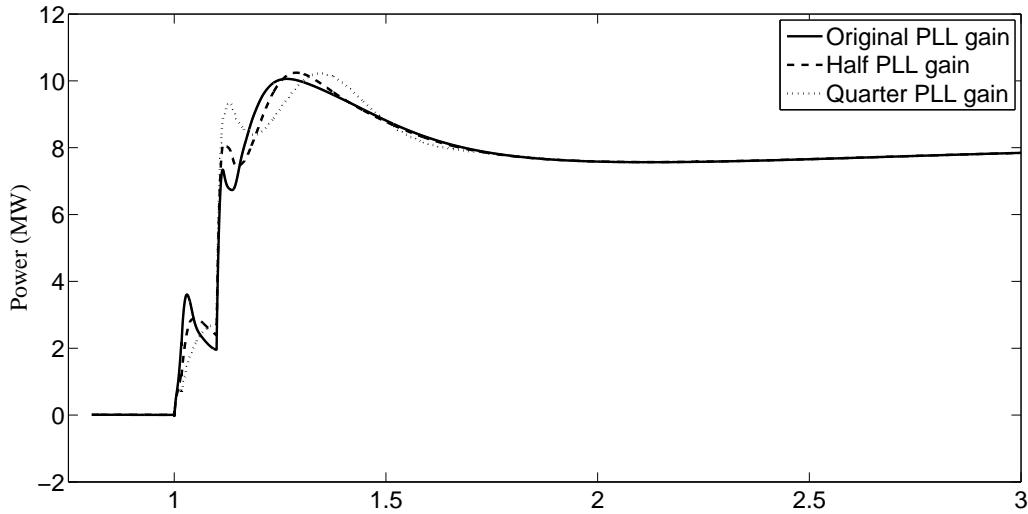


Figure 5.5: Converter active power output for different PLL gains

model in commercial positive sequence time domain simulation software.

5.2 Results in Commercial Software

The two positive sequence converter models namely, the boundary current injection and the voltage source representation of the converter, were implemented with the ‘user written model’ feature of the large scale grid simulation program PSLF.

5.2.1 Small Scale System-Validation of Results

A three machine nine bus equivalent system [44] shown in Figure 5.6 was used to validate the performance of the developed converter controller model in PSLF. This system

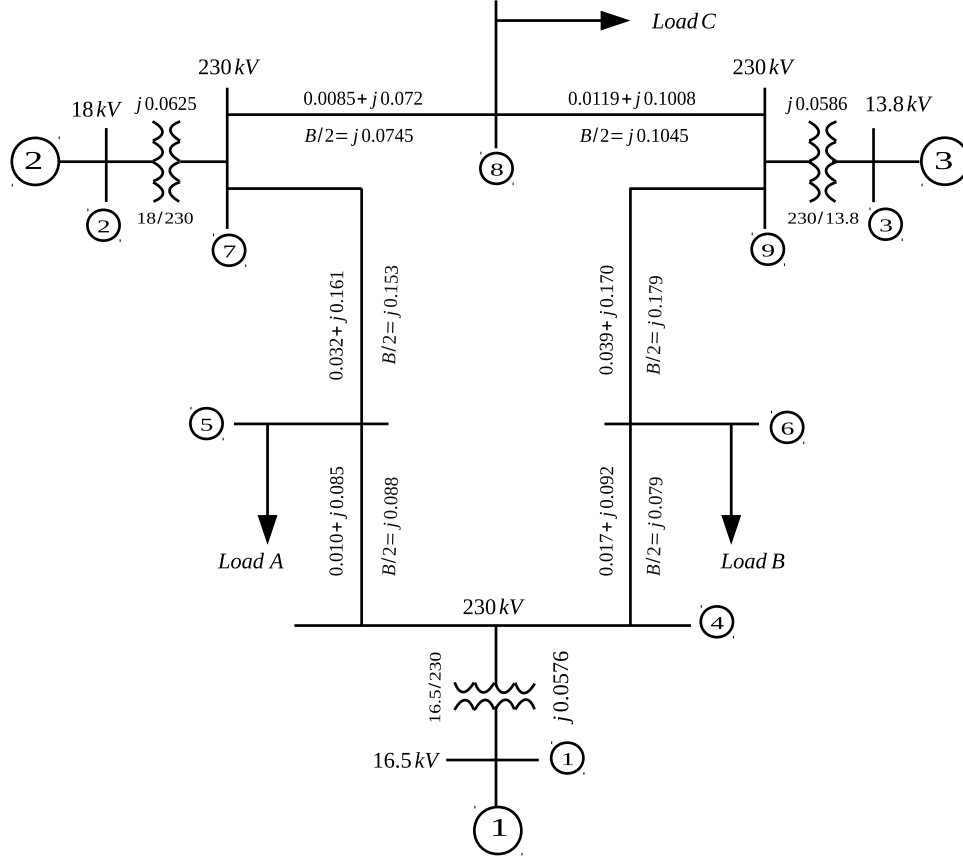


Figure 5.6: Three machine nine bus equivalent system

consists of 9 buses, 3 generators and 3 static loads. Though the size of the system is small, it is sufficient to showcase a variety of stability concepts. The powerflow solution of this network, power consumed by the load at buses 5, 6 and 8 and the dynamic data is given in Appendix B.

From the structure of the system it can be seen that any type of fault will significantly affect all three sources. However the purpose of this system is to analyze the effect of small disturbances that occur frequently in the power system. The load in a system is continuously changing and the generation sources have to appropriately adjust their load setpoints to meet the demand. Thus, the behavior of the converter model to an increase in load was compared with its behavior in PLECS for the same disturbance.

With the loads treated as constant admittance, the load at bus 6 was increased by 10MW

at $t=5$ s. The proportional and integral gains of the PI controller in the reactive power loop were taken as 1.0 and 5.0 respectively while the integral gain in the active power loop was 0.5. The remaining controller parameter values used for this simulation were as tabulated in Table 5.1.

Table 5.1: Converter-controller parameter values for three generator equivalent system

Parameter	Value
T_r	0.02
R_{vq}	0.0
R_p	0.05
T_Q	0.01
T_D	0.01
T_{Gpv}	0.01
T_{ed}	0.01
T_{eq}	0.01

In the first scenario, the machine at bus 1 was replaced with a converter while the machines at buses 2 and 3 were retained as synchronous machines. Figure 5.7 shows the active power output of the converter at bus 1.

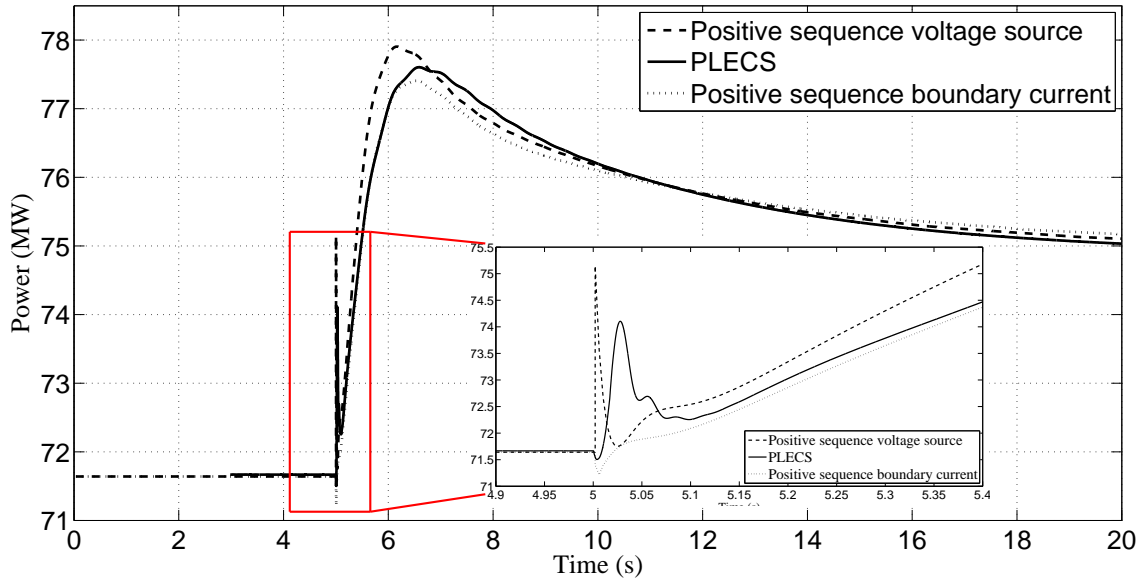


Figure 5.7: Comparison of the active power output of converter at bus 1 between PLECS and the 'epcgen' model in PSLF with synchronous machines at buses 2 and 3

The PLECS response has been compared with both the voltage and boundary current representation of the converter in positive sequence. The figure inset shows the response

of the models at the instant of disturbance. Though both the PLECS response and the boundary current response have a dip in the active power at the instant, the boundary current response fails to capture the transient that occurs in the first 0.1s after the disturbance. The response from the voltage source representation however is able to capture this transient. The difference in rise time between the voltage source representation response and the PLECS response can be attributed to the difference between the point on wave modeling in PLECS wherein a differential $R+sL$ model is used in PLECS for the filter inductor whereas in the positive sequence phasor model the filter is represented by its algebraic fundamental frequency resistance and reactance in the Thévenin impedance.

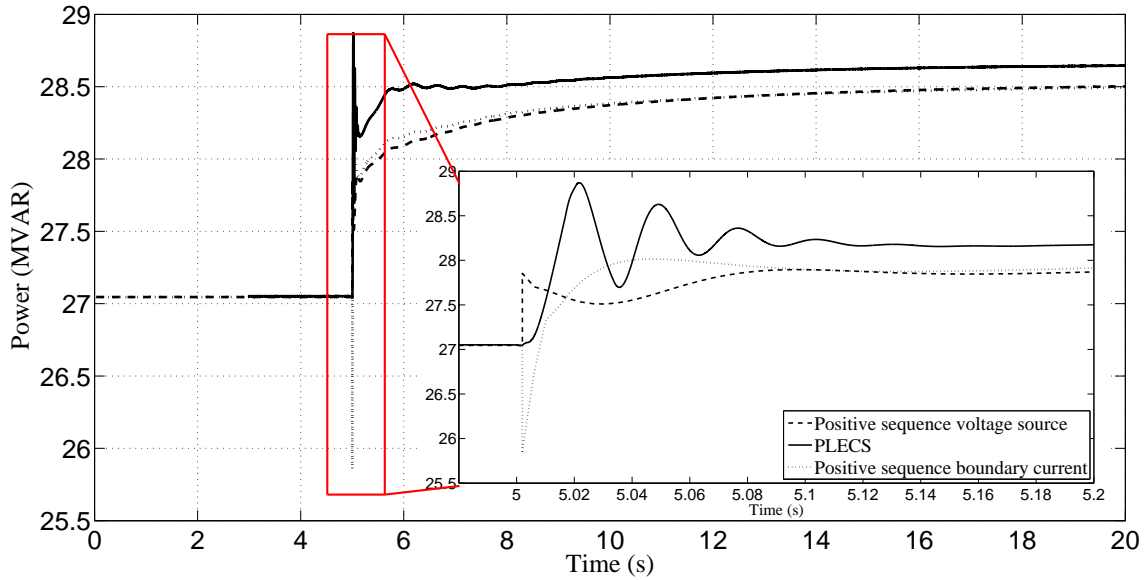


Figure 5.8: Comparison of the reactive power output of converter at bus 1 between PLECS and the ‘epcgen’ model in PSLF with synchronous machines at buses 2 and 3

The reactive power response and terminal voltage are shown in Figures. 5.8 and 5.9 respectively. It can be immediately observed from these figures that the voltage source representation response is the more acceptable positive sequence phasor approximation to the point on wave simulation. From the inset of Figure 5.8 it can be seen that the reactive power trajectory of the boundary current simulation is evidently inconsistent with the result from the PLECS simulation. The trajectory produced by the voltage source positive sequence model, while not reproducing the oscillatory component of the electromagnetic response, is consistent with the PLECS simulation in the direction of its initial change. This difference in the response at the instant of disturbance justifies the use of the voltage source representation as the model of choice for the simulation of large systems.

The difference in the terminal voltage between the voltage source representation and

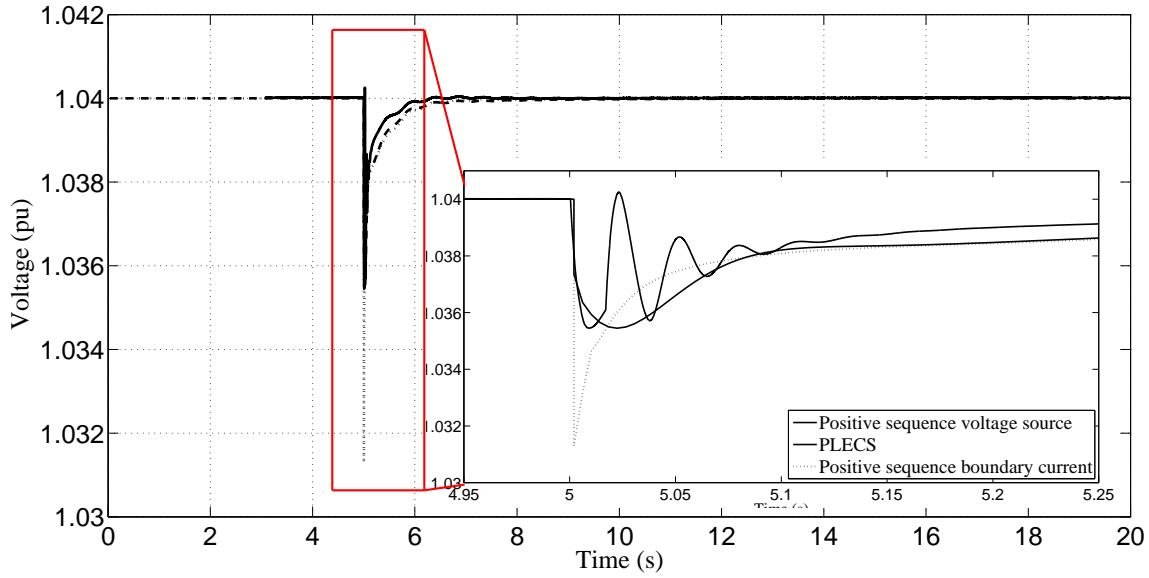


Figure 5.9: Comparison of the terminal voltage of converter at bus 1 between PLECS and the 'epcgen' model in PSLF with synchronous machines at buses 2 and 3

the boundary current representation at the instant of disturbance can be attributed to the presence of the filter inductor. In both the voltage source representation and the PLECS response, the presence of the filter inductor provides a connection to ground and thereby reduces the voltage dip as can be seen from Figure 5.9.

The sensitivity of the terminal voltage to the value of the filter inductor is as shown in Figure 5.10. It can be seen that as the per unit value of the filter inductor increases, the nadir of the terminal voltage decreases. The boundary current representation of the converter is akin to a voltage source representation with a very high value of filter inductance as voltage sources are represented by their Norton equivalent in positive sequence time domain simulation software. Thus, as the value of the filter inductor increases, the impedance to ground increases thereby causing a higher voltage drop at the terminal bus.

It could be argued that the nadir of the terminal voltage can be affected by the control mechanism used for the boundary current source representation. However to achieve the same nadir as the electromagnetic transient simulation response, an exceptionally high value of control gains would be required. This would however still not represent the first peak obtained and it could make the control structure unstable. Practically, a wide range of control techniques for converter interfaced generation exists. The intricacies of the control structure vary with the type of energy source and the manufacturer of the equipment used to harness said energy source. These control techniques can however become quite complicated and since the focus of this research was to be on the representation of the

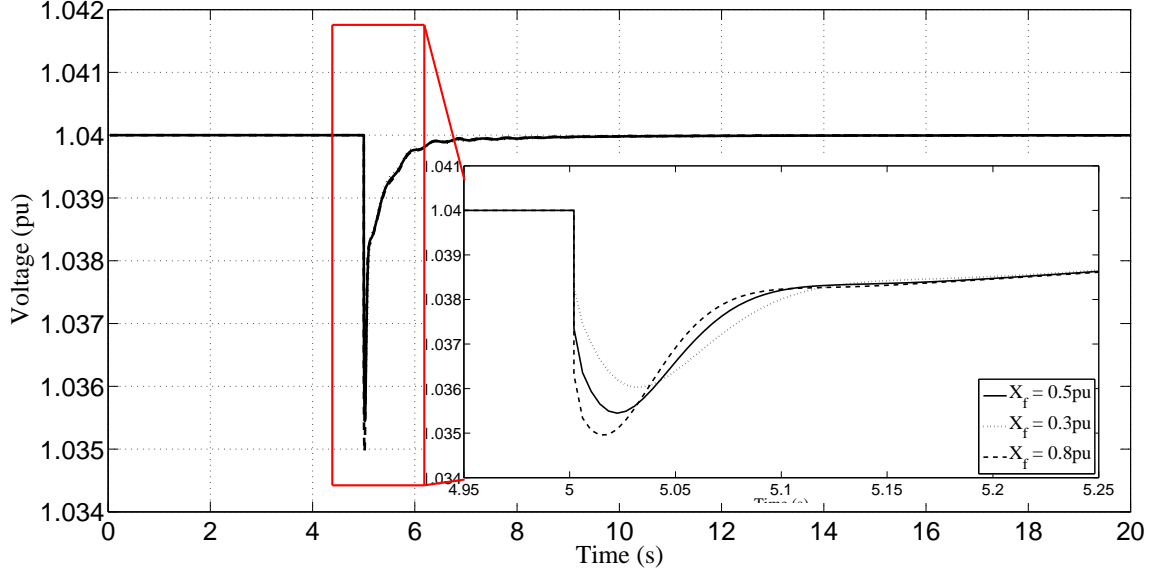


Figure 5.10: Sensitivity of the terminal voltage of converter at bus 1 for positive sequence voltage source representation to different values of filter inductor

converter, a simplified control structure was used.

In order to look at an all CIG system, the machines at buses 2 and 3 were also replaced with both forms of the positive sequence converter model. The instantaneous rise in the active power of the voltage source representation can be calculated on the same lines as the distribution of impact calculation for synchronous machines.

Based on the electrical distance between the internal voltage source of the converter and the disturbance point, the instantaneous response of a converter at bus i for an impact at bus k can be obtained as:

$$P_{i\Delta}(0^+) = \left(P_{sik} / \sum_{j=1}^n P_{sjk} \right) P_{L\Delta}(0^+) \quad i = 1, 2, \dots, n \quad (5.1)$$

where

$$P_{sik} = V_i V_k (B_{ik} \cos \delta_{ik0} - G_{ik} \sin \delta_{ik0}) \quad (5.2)$$

and $P_{L\Delta}(0^+)$ is the load impact at bus k . The entire derivation of (5.1) is available in [44]. Though the PLECS response is not instantaneous, the peak of the first oscillation falls at around the same value as the instantaneous response as can be seen from Figure 5.7. Thus (5.1) can be used to obtain the approximate peak value of the converter response following a disturbance.

For the same load increase of 10 MW at bus 6 at $t=1$ s, the active power output from the converters is as shown in Figure 5.11 while Figure 5.12 shows the reactive power

output. With the final steady state values being almost the same, the behavior of the models at the instant of disturbance becomes the deciding factor. It can be seen that in an all CIG system too, the boundary current representation response instantaneously moves in a direction opposite to what would be expected while the response from the voltage source representation is as expected and it conforms to (5.1).

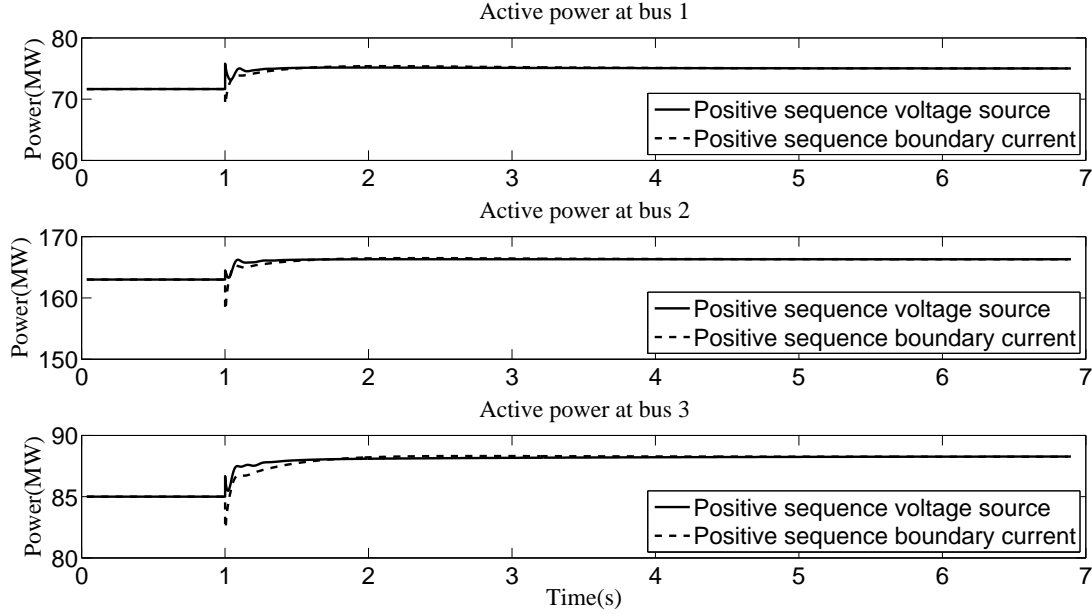


Figure 5.11: Active power output of the converters for an all CIG system with increase in active power load

To further compare the two positive sequence converter representations, the reactive power load at bus 6 was increased by 10MVAR at $t=1$ s while the active part remained unchanged, in an all CIG system. In a synchronous machine, the rotor speed gives an indication of the network frequency. However since converters are static sources, an approximate network frequency is obtained by performing a numerical differentiation of the bus voltage angle. In PSLF, the dynamic model *fmetr* performs this task. With the load change as mentioned, Figure 5.13 shows the frequency response. This response was obtained at bus 5.

The figure shows a large difference in transient frequency between the two converter representations. A possible explanation can be as follows: for the boundary current representation of the converter, at the instant of disturbance, the bus voltage angles can experience a step change which upon differentiation can produce a large change in frequency. In the voltage source representation however, the bus voltage angles does not change drastically.

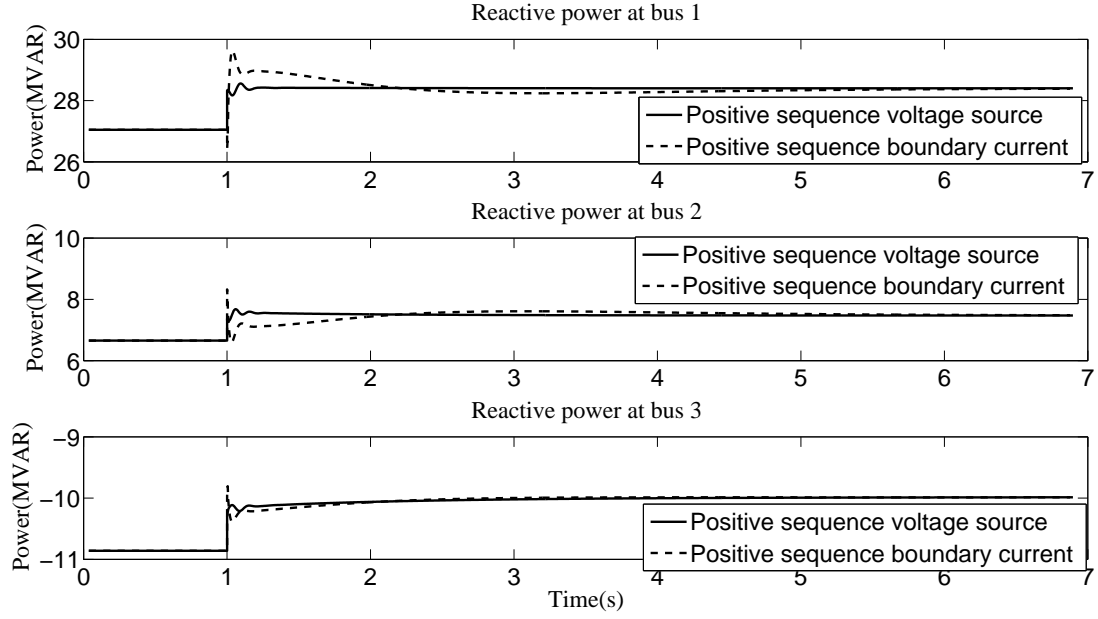


Figure 5.12: Reactive power output of the converters for an all CIG system with increase in active power load

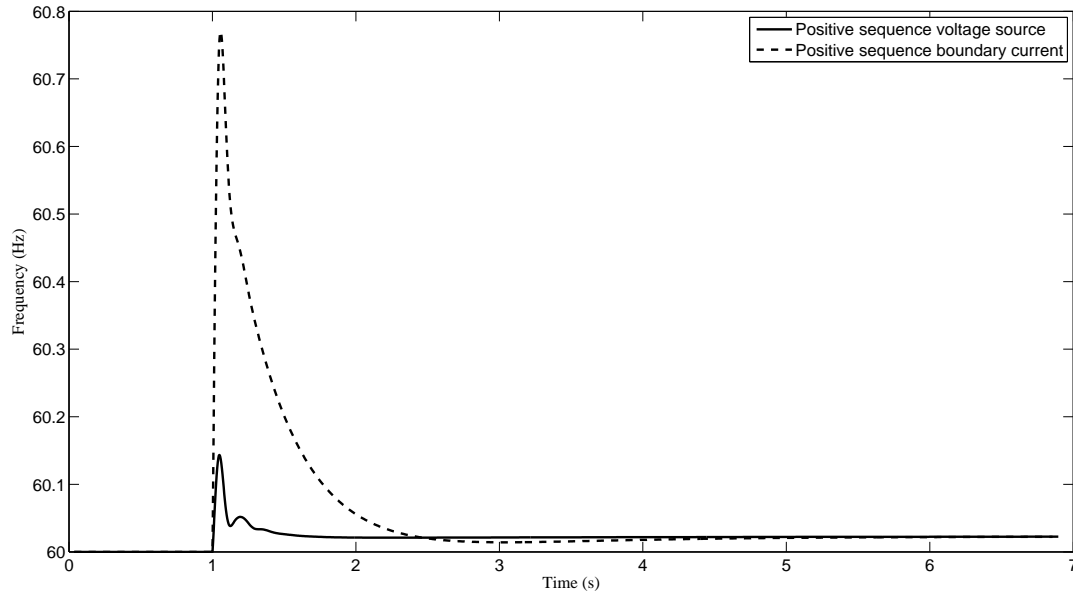


Figure 5.13: Frequency response of an all CIG system with increase in reactive power load

The plot of the voltage magnitude at the terminals of the converters and at the load bus is as shown in Figure 5.14. It can be seen that the drop in voltage magnitude at the terminals of the converters is around 0.02pu while the drop at the load bus is around 0.03pu. For a 10 MVAR increase in load, this is a nominal decrease in voltage magnitude and the fast action

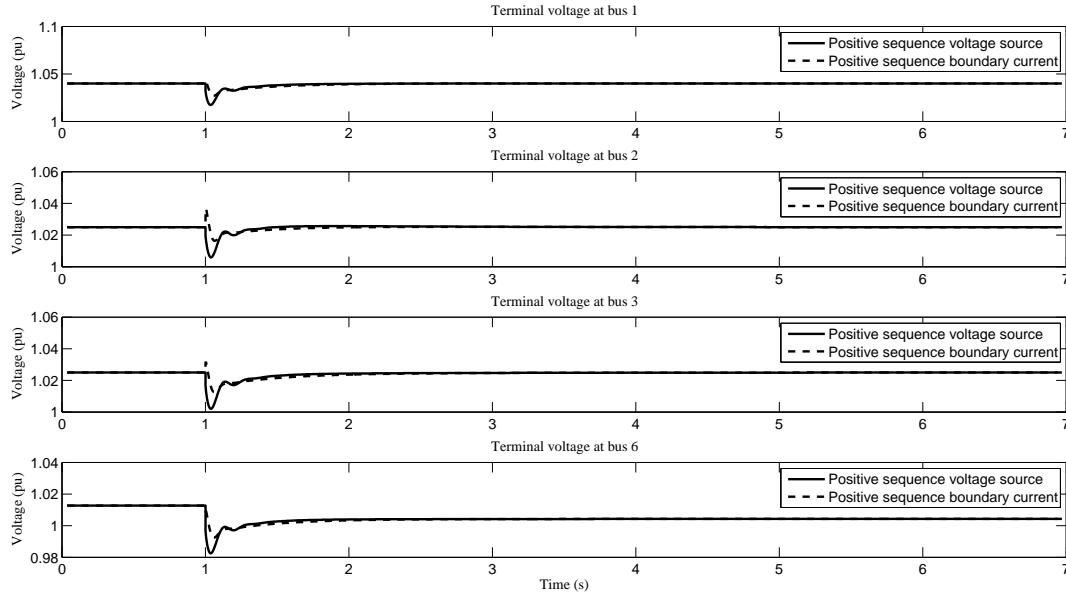


Figure 5.14: Voltage magnitudes of an all CIG system with increase in reactive power load

of the converters bring the voltage back to the pre-contingency value within 1s. Due to the increase in load, the voltage at the load bus is lower, as expected. The change in active and reactive power of the converters are shown in Figures 5.15 and 5.16 respectively.

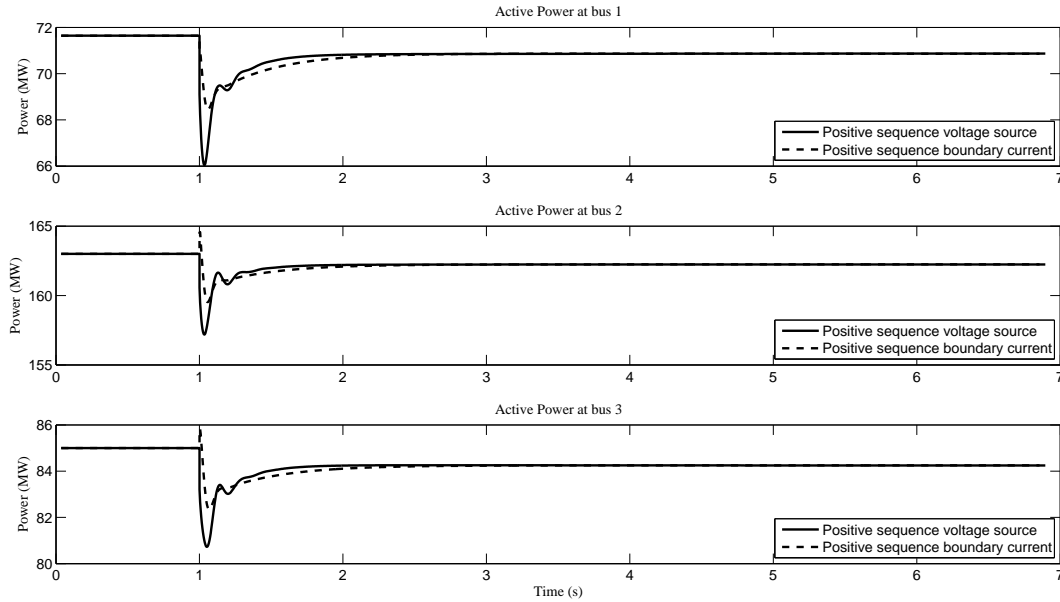


Figure 5.15: Active power output of the converters for an all CIG system with increase in reactive power load

It has thus been established that the voltage source representation of the converter is the

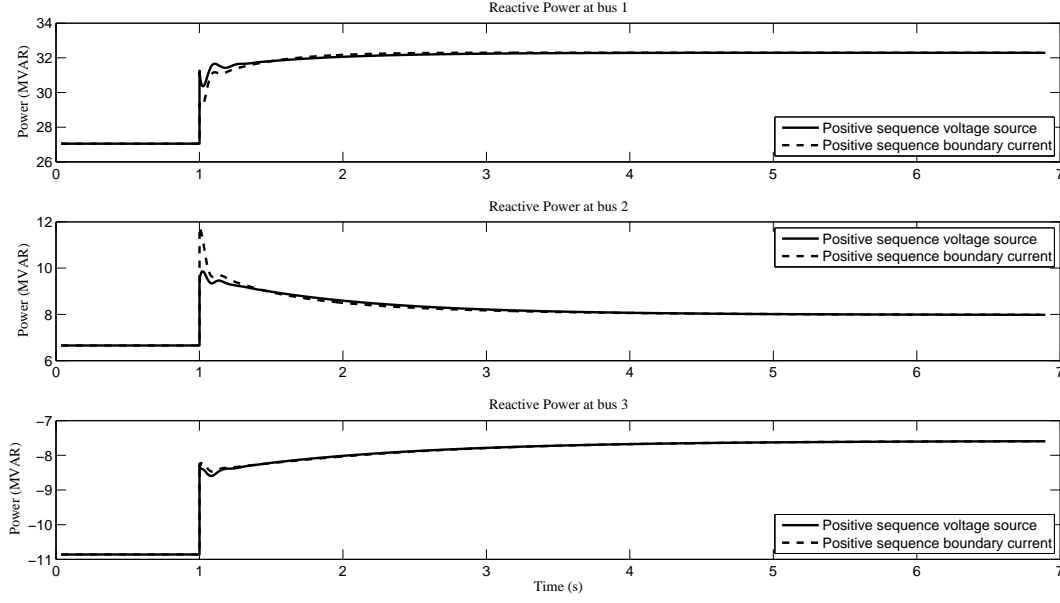


Figure 5.16: Reactive power output of the converters for an all CIG system with increase in reactive power load

more appropriate representation in positive sequence phasor simulations of large systems.

5.2.2 Large Scale System-Economy of Computation

To ensure that this model is practical in a large scale system, the WECC 2012 system has been used. At this stage, it is important to test the robustness and numerical behavior of the model when large number of converters are present in the system. This system has 18205 buses, 13670 lines and 3573 generators. The total generation is 176 GW while the total load is 169 GW. The power flow diagram of the system is as shown in Figure 5.17 [5]. To obtain a sizable presence of converters, all the generators in the Arizona and Southern California area (528 units) were replaced with converters represented by the proposed voltage source representation. This accounted for 24.3% of the total system generation with 25.6 GW in Arizona and 17 GW in Southern California.

For a CIG to take part in frequency regulation, a reserve margin has to be present. As per the associated material for the WECC system operating case [5], all areas of the system have a defined amount of headroom available for frequency regulation. This reserve is however not distributed equally among all generators in the area, with few generators operating without a governor. In this project, the maximum active power deliverable by a CIG unit has been assumed to be equal to the MW rating of the turbine of the generator which the CIG replaces while the MVA rating of the CIG has been assumed to be the

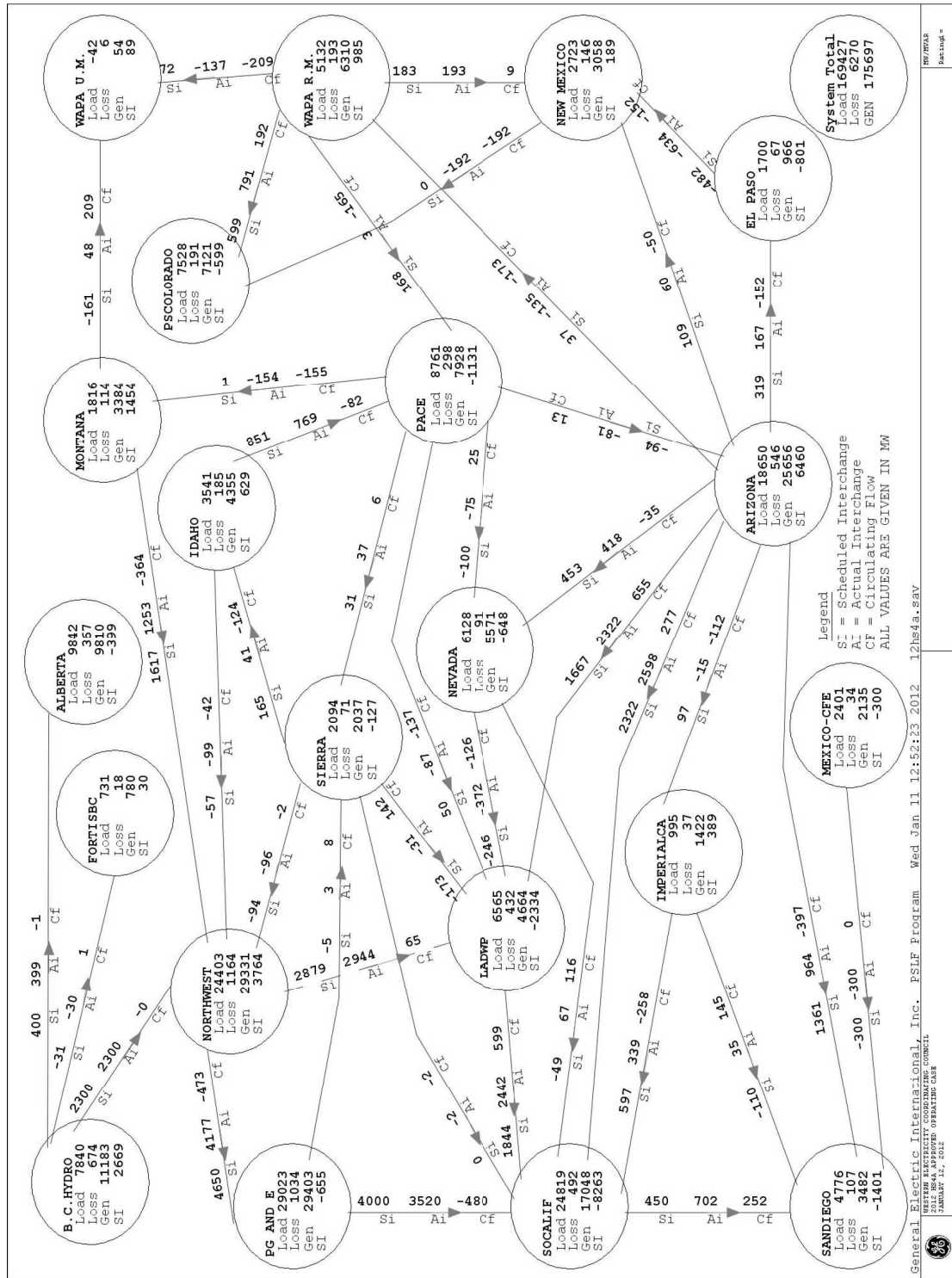


Figure 5.17: Power flow in the WECC system [5]

same as the MVA rating of the generator. If the CIG replaces a generator without an associated governor, then it has been assumed that the CIG too cannot take part in frequency regulation.

Thus, with an available headroom on almost all converter interfaced sources, the value of the droop coefficient R_p was taken to be the same as that used by the governor of the synchronous machine it replaced while R_q was taken to be 0.05pu on a machine MVA base. The reactive power PI controller gains of all converters were set to $K_p=1.0$ and $K_i=5.0$ while the active power integral controller had a gain of $K_{ip}=0.5$. The values of all other parameters were kept the same as in Table 5.1.

This initial penetration of 24.3% is used to test the numerical stability of the converter model for three system contingencies.

Generation Outage (24.3% CIG penetration)

At $t=15$ s, two of the Palo Verde units were tripped resulting in a generation outage of 2755 MW. Fig 5.18 shows the power output from the remaining sources in the Arizona area while the effect on the adjacent area of Southern California has been shown in Figure 5.19.

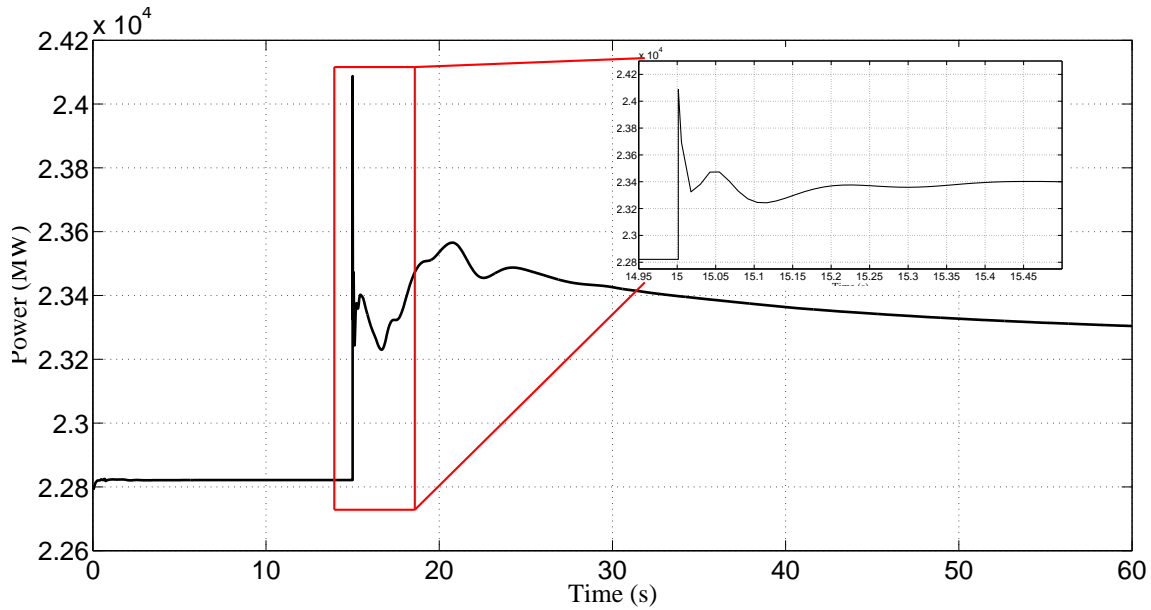


Figure 5.18: Active power generation in the Arizona area due to trip of two Palo Verde units

The system frequency plot is shown in Figure 5.20. It can be seen that the reduction in frequency is quickly arrested due to the fast action of the converters and the system has no problem in absorbing the substantial CIG presence.

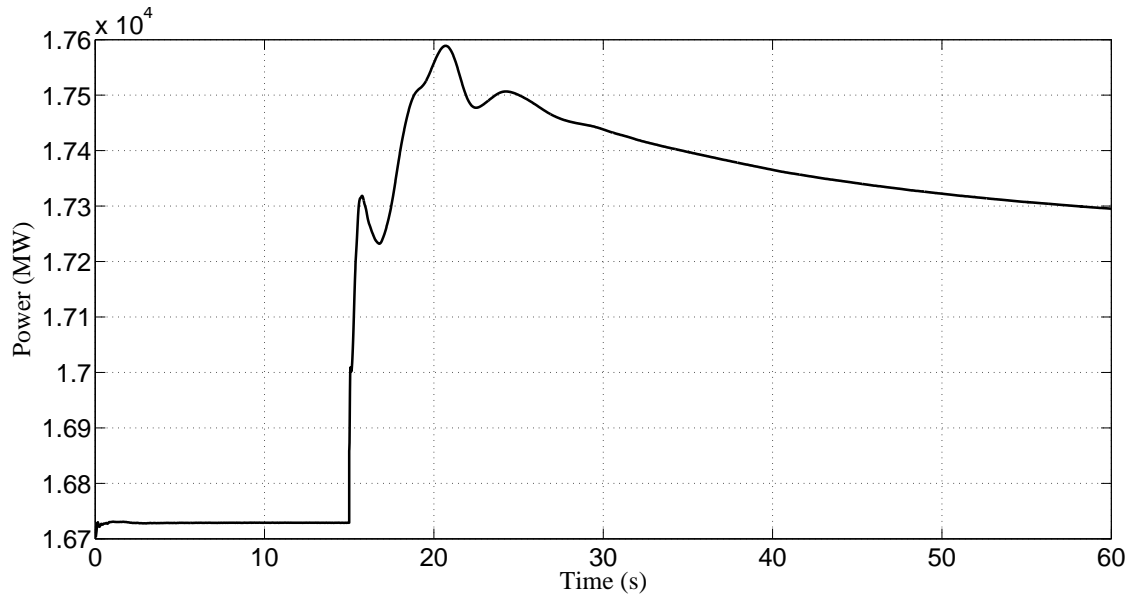


Figure 5.19: Total generation in Southern California area due to trip of two Palo Verde units

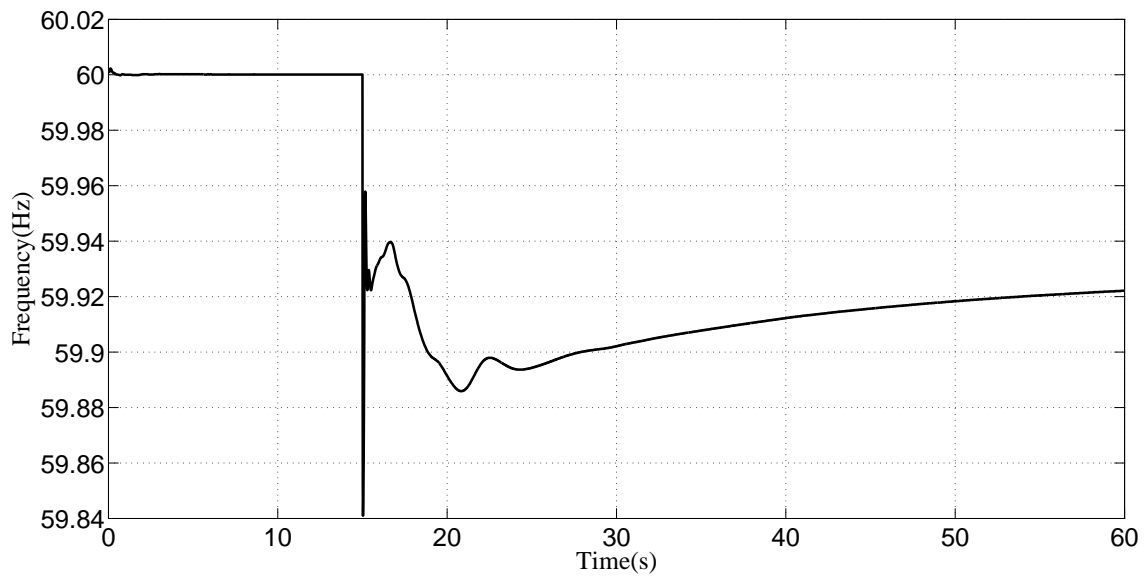


Figure 5.20: System frequency due to trip of two Palo Verde units

In terms of computation time, PSLF took 7:04 minutes to run this 60 second simulation with the first 20 seconds of simulation taking 1:52 minutes. In comparison to this, when all machines were represented in the conventional manner, the same 60 second simulation took 6:41 minutes with the first 20 seconds of simulation being completed in 1:39 minutes. Both simulations were run on a machine with an i7 processor and 16.0 gb of RAM with a simulation time step of 0.0041s.

Line Fault followed by Outage (24.3% CIG penetration)

A three phase fault was applied on a tie line between Arizona and Southern California at $t=15\text{s}$. Subsequently, at $t=15.1\text{s}$, the breakers at both ends of the line were opened. The initial flow on the line was 1408.6 MW and 134.4 MVAR from the Arizona side. Figures. 5.21, 5.22 and 5.23 show the changes in the power transfer between Southern California and the areas of Arizona, Los Angeles Department of Water and Power (LADWP) and San Diego. Negative values indicate that the power flow is into Southern California while positive values indicate power flow out of the region. The opening of the line causes a reduction in flow between Arizona and Southern California as expected.

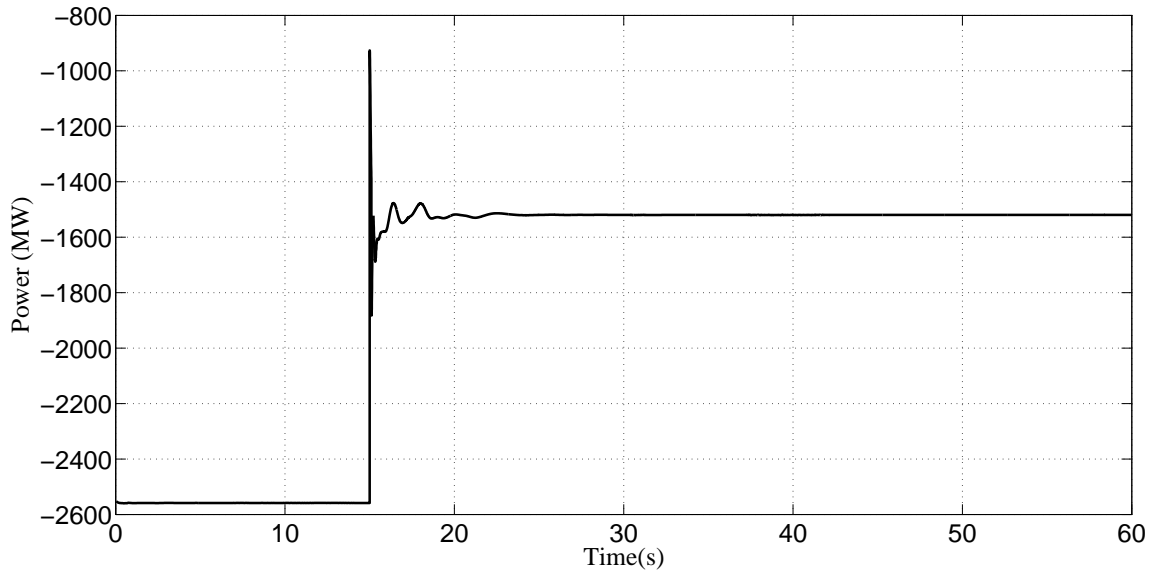


Figure 5.21: Active power flow to Southern California from Arizona with the opening of a tie line between Arizona and Southern California following a line fault

It should be noted that only the voltage source representation of the converter was able to function reliably following the fault. The boundary current representation of the converters resulted in frequent non convergence issues with regard to the network solution following the occurrence of the fault.

Bus Fault (24.3% CIG penetration)

The third contingency carried out on the WECC system was applying a bus fault for 0.1s at $t=15\text{s}$ near the Four Corners generation plant in the Arizona area. The active power and terminal voltage of one of the units is as shown in Figures. 5.24 and 5.25. From the active power plot the familiar damped rotor angle oscillations can be observed from the output of the synchronous machine. In addition, it can also be seen that a large electronic

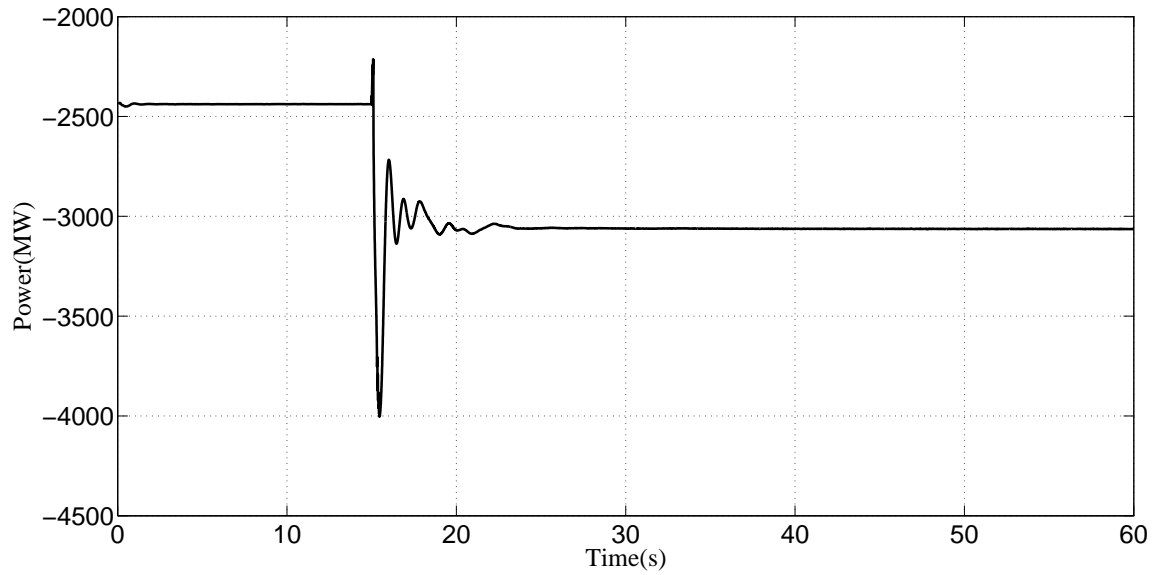


Figure 5.22: Active power flow to Southern California from LADWP with the opening of a tie line between Arizona and Southern California following a line fault

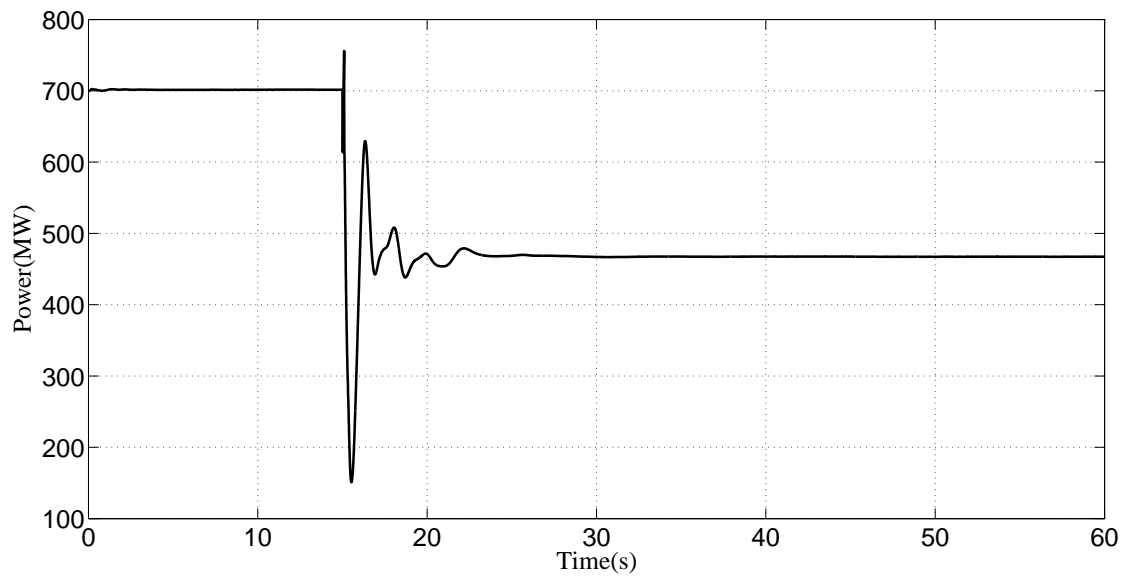


Figure 5.23: Active power flow from Southern California to San Diego with the opening of a tie line between Arizona and Southern California following a line fault

source brings about a highly damped response. However, the voltage dip in the converter response is larger than that of the corresponding synchronous machine. The value of the filter inductor along with the absence of a sub-transient capability influences the magnitude of this dip in voltage. The magnitude of the converter current for the voltage source representation is as shown in Figure 5.26. The current is well within its short time current rating of 1.7pu. It has also been observed that for few other significant bus faults, the

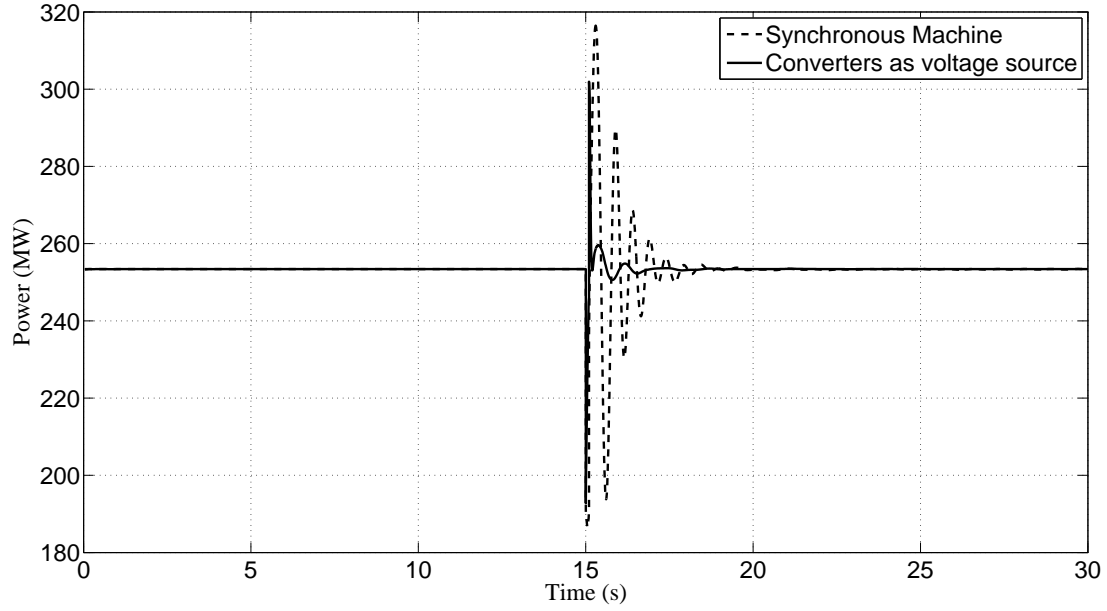


Figure 5.24: Active power output of a unit at Four Corners for a bus fault close to the unit

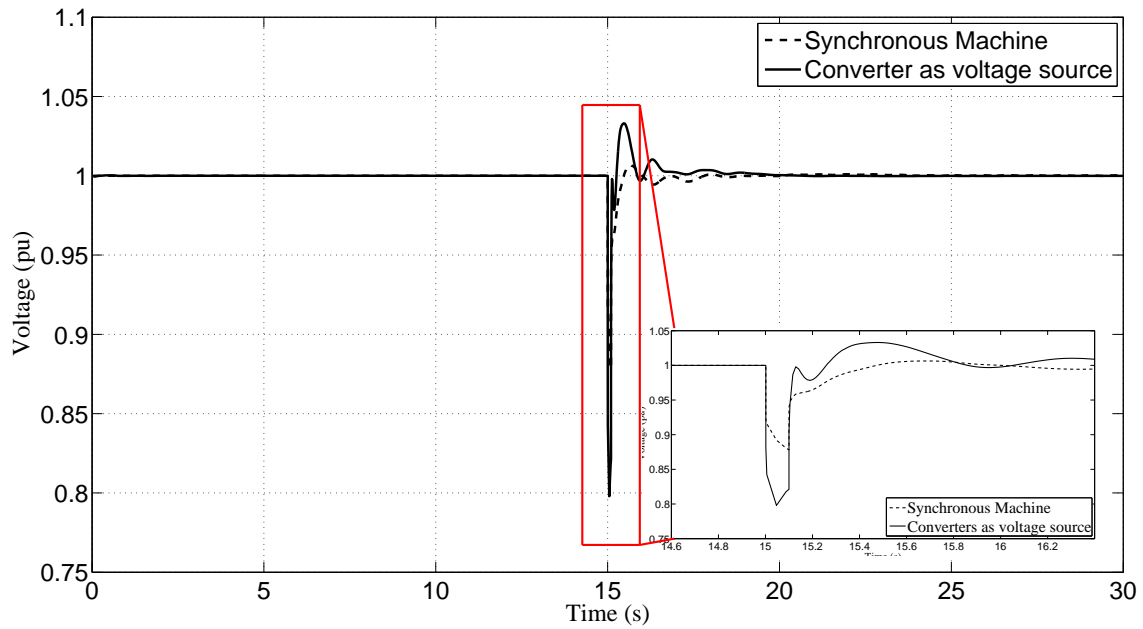


Figure 5.25: Terminal voltage of a unit at Four Corners for a bus fault close to the unit

network solution diverges when the boundary current representation is used.

The performance of the developed converter model and its associated control structure has been validated for a large system by these three contingencies. The simulation is numerically stable and not computationally intensive.

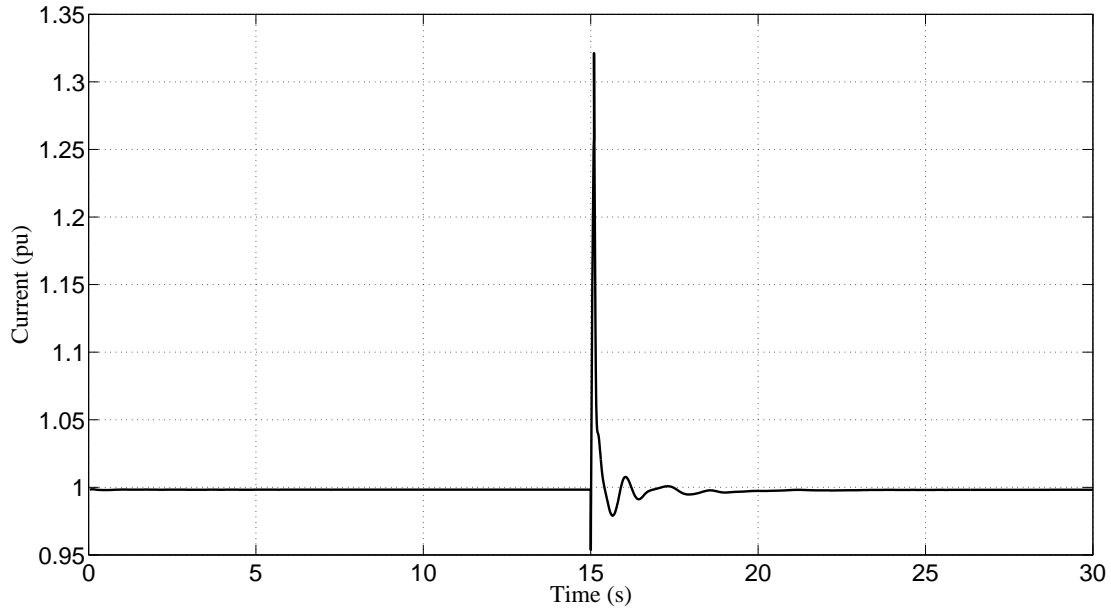


Figure 5.26: Magnitude of converter current for a voltage source representation of the converter for a bus fault close to the unit

5.3 Note on Boundary Current Representation of Converter

In order to study the effect of large penetration of converter interfaced generation in the power system, it is very important that the computer simulation models have a reliable representation of the converter. Based on the results of the previous two sections, it has been shown that the boundary current representation is not a suitable representation due to the following reasons:

1. It is unable to capture the transient that occurs in the first 100ms following a disturbance.
2. The initial change of the reactive power trajectory does not conform with the expected change.
3. The absence of the filter inductor results in a larger voltage dip as compared to the voltage source representation and the PLECS response.
4. The network solution fails to converge for simulations of certain contingencies in large systems.

In each case mentioned above, the voltage source representation is consistent with the properties of these devices and is thus a more appropriate approximation of the electro-

magnetic transient model for positive sequence simulations.

In the following section, the behavior of the WECC system will be shown for a 100% CIG penetration.

5.4 All CIG WECC system

In this scenario, all the conventional synchronous machine models in the dynamic file of the WECC system were replaced and represented by the voltage source representation of the converter. With this replacement, the only rotating machines in the system were the induction motor loads and 3 wound rotor induction generators. The 3 induction generators represent 3 wind turbine units. The remaining wind units (33 in number) were represented by the boundary current injection converter model as they were already present in the dynamic file as a converter interfaced source.

Thus, the entire generation set (barring the 3 wound rotor induction generator wind models) were converter interfaced. With a total system generation of 176 GW, the three wound rotor wind generators produce 0.34 GW. The value of the droop coefficient R_p for the converter was taken to be the same as the value of the droop coefficient in the governor of the synchronous machine the converter replaced. This results in a varied value of active droop across the system. The value of coefficient R_q was taken as 0.05pu on a machine MVA base while the PI controller in the reactive power loop had a proportional gain of 1.0 and an integral gain of 5.0. The value of K_{ip} was taken as 0.5. The converters have the value of R_f as 0.004pu and X_f as 0.05pu on a self MVA base.

The behavior of this all CIG system has been analyzed for the following contingencies:

5.4.1 Generation Outage (100% CIG penetration)

The tripping of two Palo Verde units is considered to be a significant event in the WECC system. Figure 5.27 shows the frequency response of the system following the trip of two of the units resulting in a loss of 2755 MW of generation at $t=15$ s. The under frequency trip setting of relays in WECC are set at 59.5 Hz [52]. When all machines are synchronous machines, the frequency response of the entire system is calculated as (5.3) [42],

$$f = \frac{\sum_{i=1}^n MVA_i \omega_i}{\sum_{i=1}^n MVA_i} \quad (5.3)$$

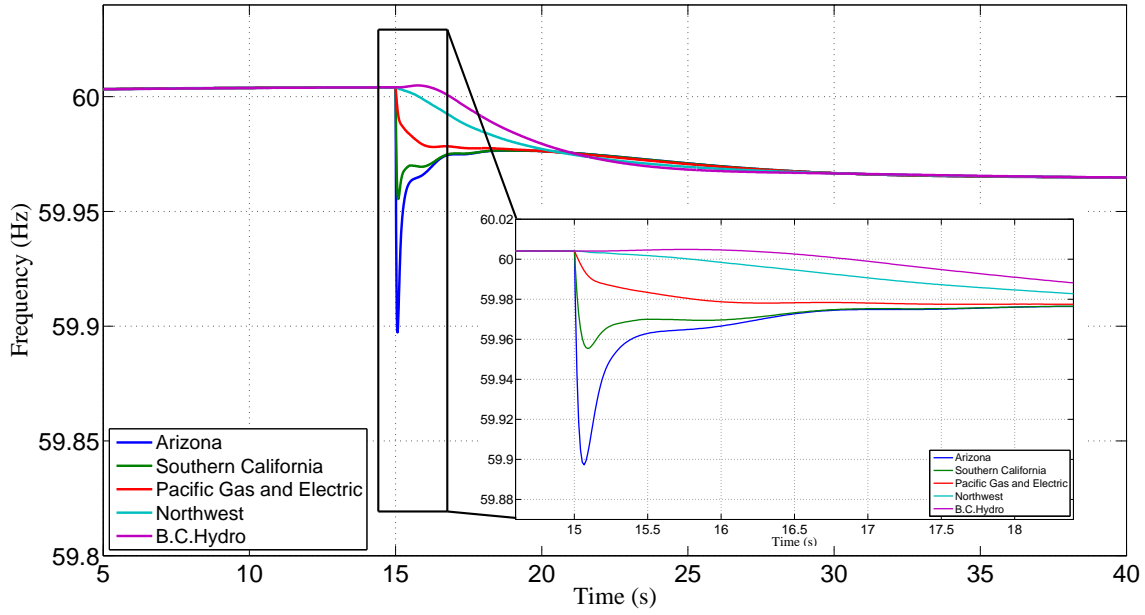


Figure 5.27: Frequency across five generation areas for the trip of two Palo Verde units (droop coefficient of each CIG unit is R_p)

where MVA_i is the rating of the machine, ω_i is the speed of the machine and n is the number of synchronous machines. However in a system where all sources are interfaced through converters, the speed of rotation of a machine (if present) behind the converter will not give any picture of the system frequency as it is electrically decoupled from the network. Thus an approximate frequency has been obtained by performing a numerical differentiation of the bus voltage angle. The plots in Figure 5.27 show the calculated frequency in the five major generating areas of the WECC system which account for 63.4% of the total system generation while Figure 5.28 shows the actual active power in four of these areas.

It can be seen that the largest excursion in frequency occurs in the Arizona area as expected. Further, even with the total inertia of the system being close to zero, the frequency nadir is well above the under frequency trip setting. The fast action of the converters and their associated control help in arresting the rate of decrease of frequency and bring about a steady state operation quickly. The frequency settles at 59.965 Hz. Due to the highly meshed network, the bus voltage angles in different parts of the network change in varied ways and this can also be observed from the frequency plot.

As the third unit at Palo Verde is the closest to the outage, the response of the converter representing this unit can be informative. The active power, reactive power, terminal volt-

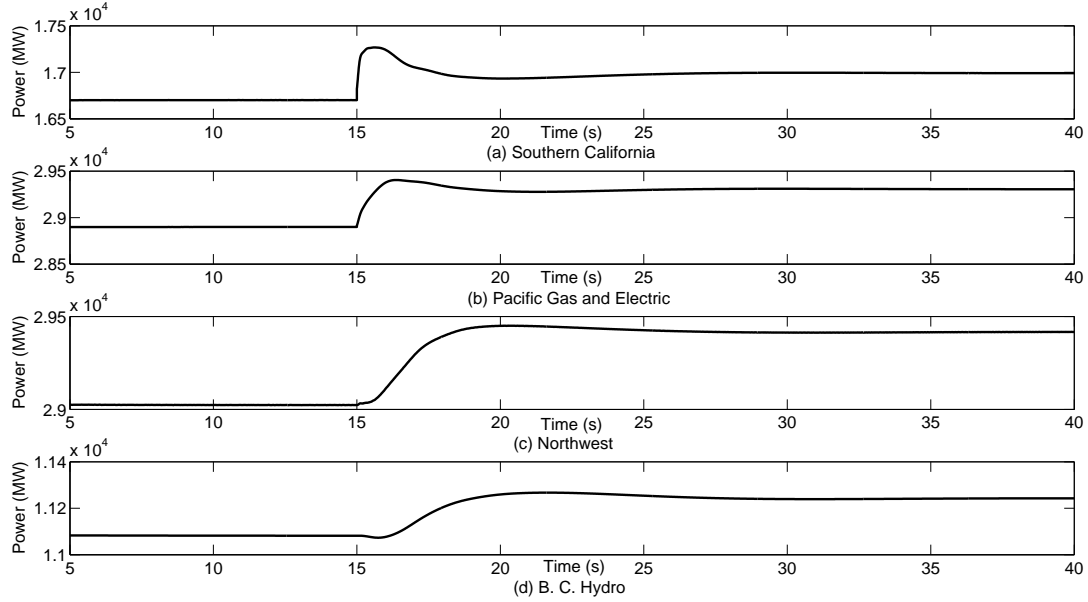


Figure 5.28: Active power output in four areas of WECC following the trip of two Palo Verde units

age and current of the converter representing the third Palo Verde unit is as shown in Figure 5.29. It can be seen that the converter response is quick and none of the limits are violated. The converter current is well within its maximum rating and the voltage control loop maintains the voltage at the pre-fault value. As the Palo Verde units are operated close to their maximum active power limit, there is very little reserve margin available.

To observe the effect of the active power droop coefficient, two further simulations were run. In the first, the values of the droop coefficient were doubled while in the second they were halved. Thus, if we denote R_p as the droop coefficient of each CIG unit for the plot in Figure 5.27, the values of the droop coefficients were made $2R_p$ and $R_p/2$ in order to observe the effect of droop. Individual CIG units may still have different values of droop as the coefficient R_p takes on different values for each unit as mentioned at the start of this section. The frequency plots of Figures. 5.30 and 5.31 show the performance for the trip of two Palo Verde units when the values of the droop coefficient were $2R_p$ and $R_p/2$ respectively.

It can be observed that changing the value of the coefficient changes the final steady state value of the frequency. When the coefficient value is increased, it signifies that the same change in active power will cause a greater reduction in frequency while when the coefficient value is decreased, the reduction in frequency is lower. In Figure 5.30, the frequency settles around 59.933 Hz while in Figure 5.31, the frequency settles at 59.982

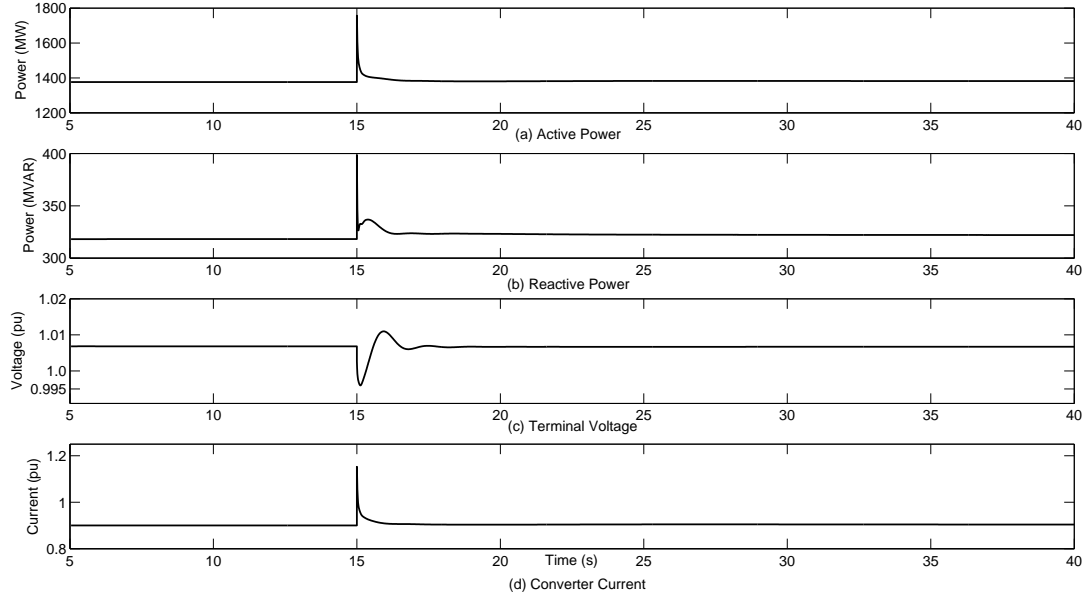


Figure 5.29: Behavior of the third Palo Verde unit for the trip of two other Palo Verde units

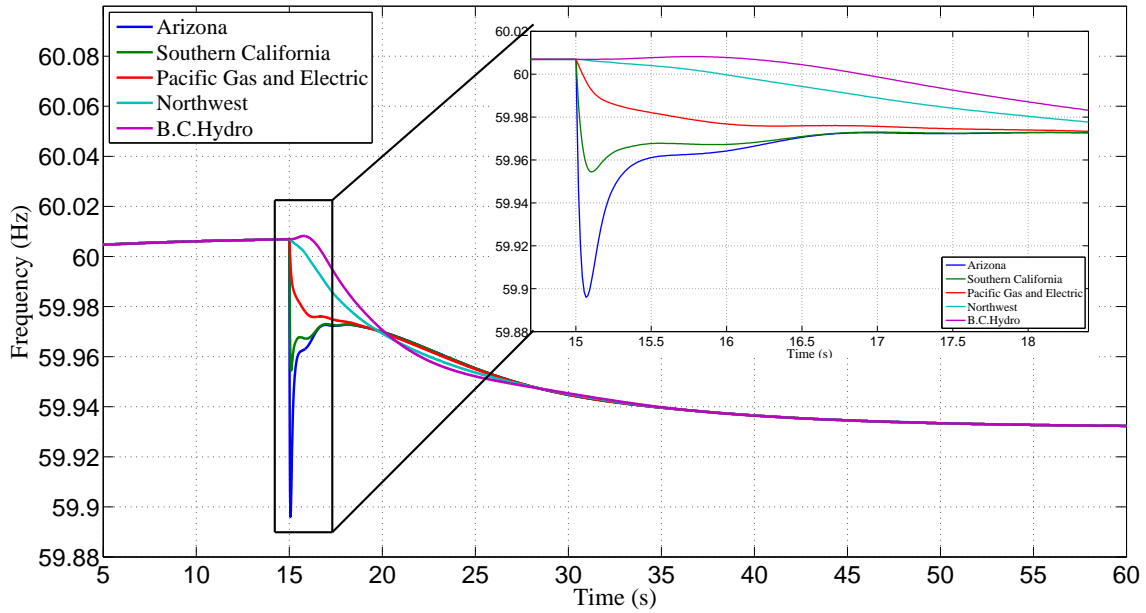


Figure 5.30: Frequency across five generation areas for the trip of two Palo Verde units (droop coefficient of each CIG unit is $2R_p$)

Hz. This is in comparison to the settling frequency of 59.965 Hz in Figure 5.27. The frequency nadir changes slightly with change in the value of the droop coefficient. With droop coefficient R_p , the frequency nadir is 59.8973 Hz. With a droop value of $2R_p$, the

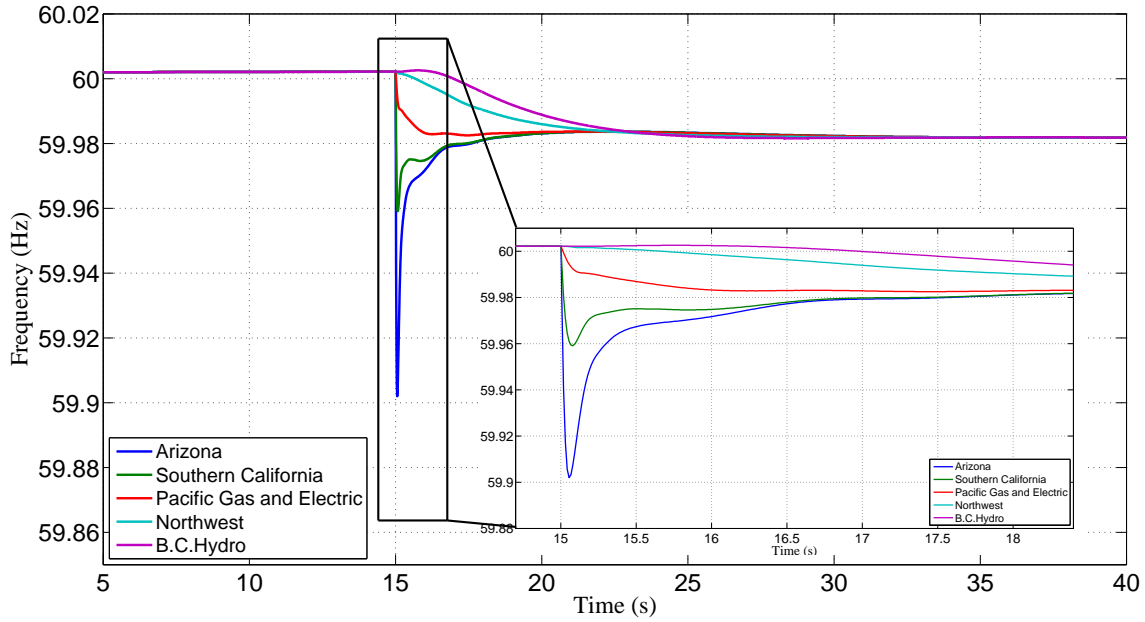


Figure 5.31: Frequency across five generation areas for the trip of two Palo Verde units (droop coefficient of each CIG unit is $R_p/2$)

nadir is 59.896 Hz while with a droop value of $R_p/2$, the nadir is 59.902 Hz.

In addition, this comparison brings to light the fact that although CIG units are fast acting, a finite time is required to bring about a steady state operation as rotating elements are still present in the system in the form of induction motors. The inertia of these motors play a role in the transient behavior of the system. There is also a difference in settling time with different values of droop coefficients and this can be seen from all frequency plots.

In all subsequent scenarios, the value of the droop coefficient has been assumed to be R_p .

In terms of computation time, with a droop coefficient R_p , PSLF took 8:10 minutes to run the 40 second simulation of this generation outage scenario with the first 20 seconds of simulation taking 3:52 minutes. The simulation was run on a machine with an i7 processor and 16.0 gb of RAM with a simulation time step of 0.0041s. It can be concluded that an all CIG system is capable of providing a stable frequency response through the fast action of the controllers and the simulation is numerically stable too.

5.4.2 Dc Voltage Dip and Subsequent Recovery (100% CIG penetration)

In all of the above scenarios, the dc voltage has been assumed to be constant, implying a battery as a source of power. However, even for units of a size as low as 100 MVA, the assumption of a battery as a constant source of power is not realistic. A practical source can either be a gas or hydro turbine (synchronous machine) or a solar/wind farm. Such sources would require a capacitor on the dc bus to maintain a constant voltage input to the inverter. However, a disturbance in the network would cause fluctuations in the current levels causing the dc voltage across the capacitor and thus across the converter switches to vary. It is hence important to study the effect of this variable dc voltage on the system behavior.

At $t=15$ s, two Palo Verde units are tripped resulting in a generation outage of 2755MW. With a capacitor on the dc link, the immediate response to this contingency would be an increase in the converter current and a decrease in capacitor voltage. Gradually as the active power control reacts (with synchronous machine control being the slowest), the capacitor voltage will be restored. To simulate this situation, the dc voltage on all CIG units participating in frequency regulation was reduced by 1%, 20ms after the generation outage. Gradually, over the subsequent 10s, the dc voltage was restored. The frequency plot for this scenario is as shown in Figure 5.32 while Figure 5.33 shows the active power, reactive power, terminal voltage and current of the third Palo Verde unit.

The sudden reduction in generation at $t=15$ s causes the frequency to drop to 59.89 Hz in the Arizona area. The subsequent reduction in dc voltage causes the terminal voltage of CIG units to drop by a larger extent when compared to the terminal voltage drop for just the trip of the units. This can be observed by comparing Figure 5.33(c) with Figure 5.29(c). This drop in voltage results in a reduction of load (voltage dependent load) thereby causing the frequency to rise. The voltage drop also results in the tripping of a motor due to activation of the under voltage load shedding relay at the motor terminals. The subsequent recovery of the dc voltage and its effect on the system is apparent from Figure 5.33.

The results of this scenario are a set of conservative results as the dc voltage has been assumed to drop only on those CIG units that take part in frequency regulation. In reality, the voltage would drop at all units. However, the recovery of the voltage is possible only on units that take part in frequency regulation. Further, for a dc voltage drop greater than 1%, multiple converters trip due to overcurrent and multiple motors trip due to under voltage.

In practice, the size of the capacitor at the dc bus would have to be designed so as to

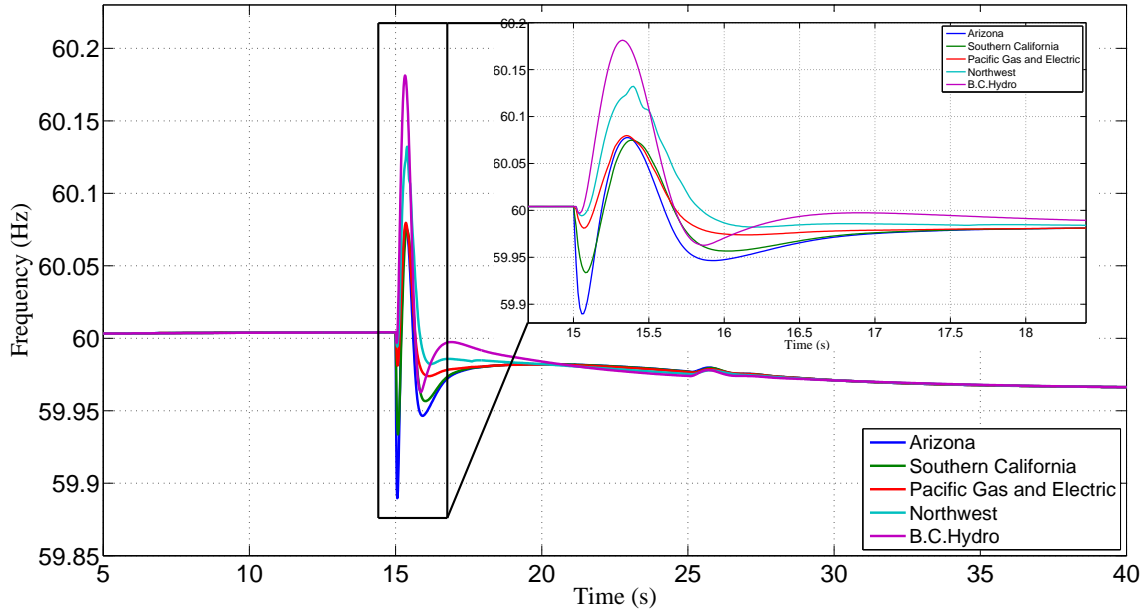


Figure 5.32: Frequency across five generation areas for the trip of two Palo Verde units followed by the reduction in dc voltage by 1% and its subsequent recovery

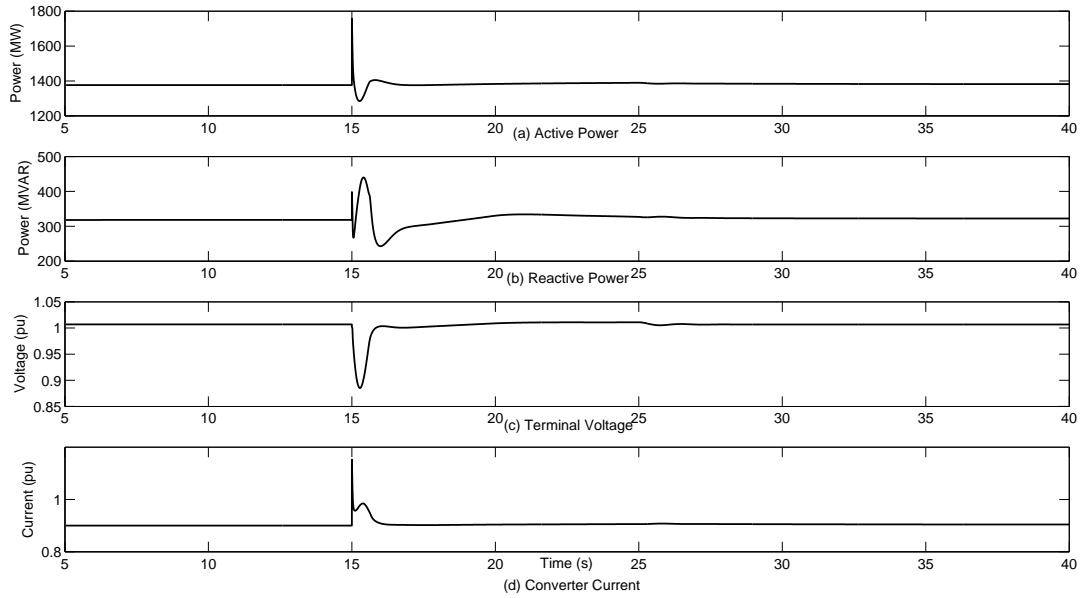


Figure 5.33: Behavior of the third Palo Verde unit for the trip of two other Palo Verde units followed by the reduction in dc voltage by 1% and its subsequent recovery

restrict the drop in voltage to less than 1%. Additionally, fast acting units may have to be brought online to support the voltage and in order to maintain the system reliability, a coordinated, well designed wide area control action may be required.

In the following two contingencies, the dc voltage is assumed to remain constant throughout the entire scenario.

5.4.3 Line Fault followed by Outage (100% CIG penetration)

A fault on a transmission line followed by the tripping of the line can be a significant contingency on the system especially if the line is a tie line between two areas and has a considerable amount of power transfer across it. At $t=15$ s a three phase fault was applied for 0.05s at the midpoint of a line between the Arizona and Southern California areas. The line was subsequently tripped at both ends. Modern protection devices are able to clear the fault and isolate the corresponding elements within 4 cycles [53]. The initial flow of power on the line was 1408.6 MW and 134.4 MVAR from the Arizona side. Figures. 5.34, 5.35 and 5.36 show the active power in the Arizona area, Southern California area and the flow between these two areas respectively. The figures show that the response is satisfactory.

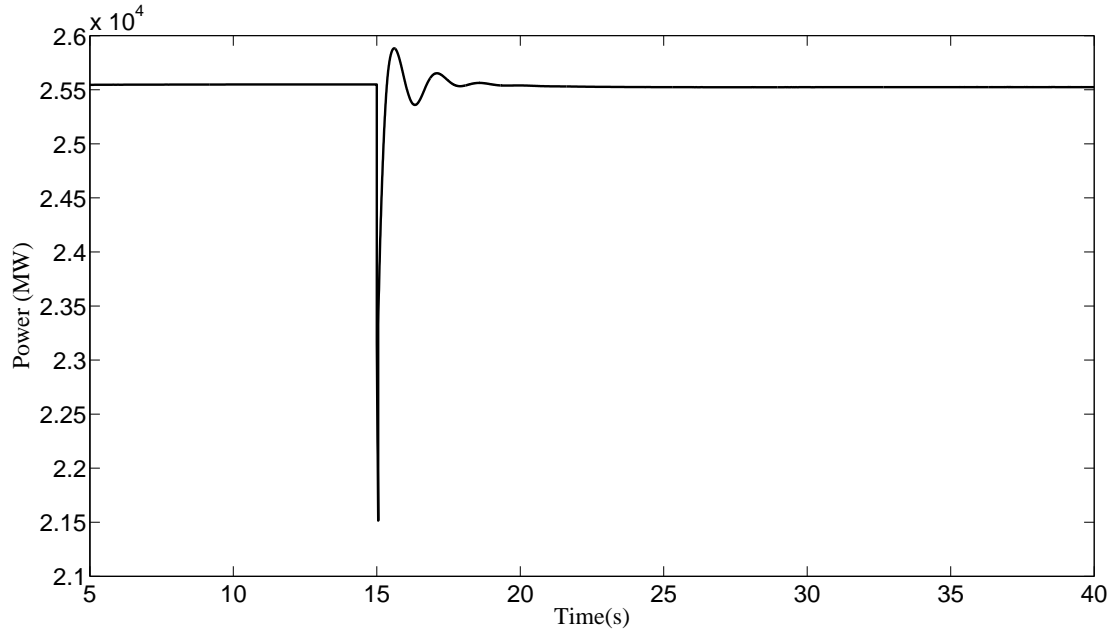


Figure 5.34: Arizona active power flow with the opening of a tie line between Arizona and Southern California following a line fault

5.4.4 Bus Fault (100% CIG penetration)

A three phase fault for 0.05 seconds at $t=15$ s was applied at a bus close to the Four Corners generating plant in the Arizona area. Six converters in the New Mexico area tripped due to overcurrent upon the occurrence of the fault. The active power, terminal voltage and current of the converter at Four Corners is as shown in Figures. 5.37, 5.38

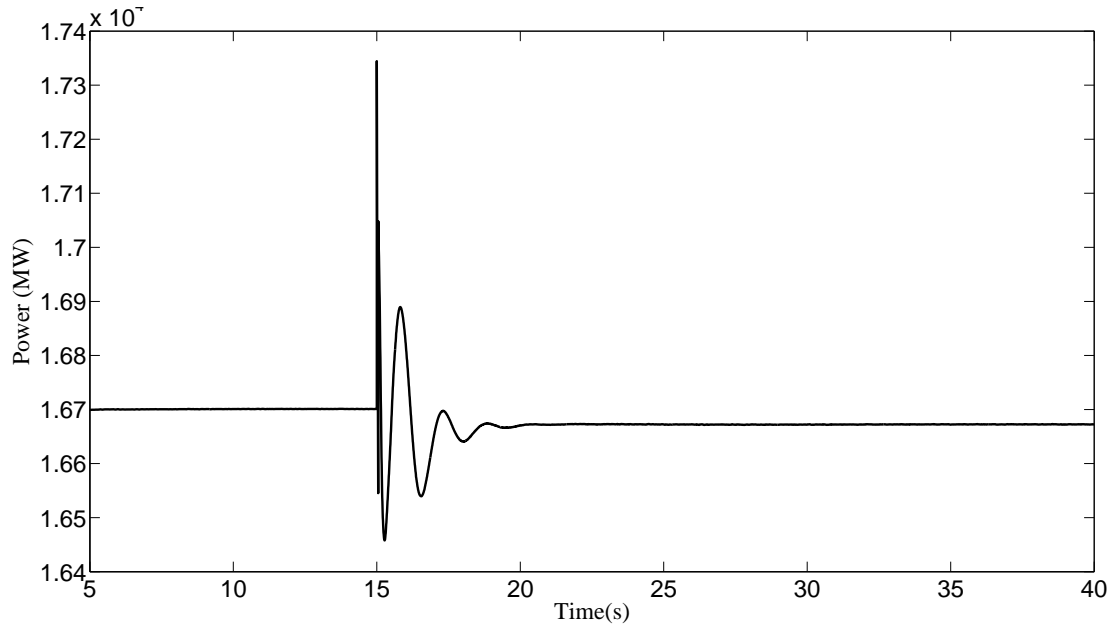


Figure 5.35: Southern California active power flow with the opening of a tie line between Arizona and Southern California following a line fault

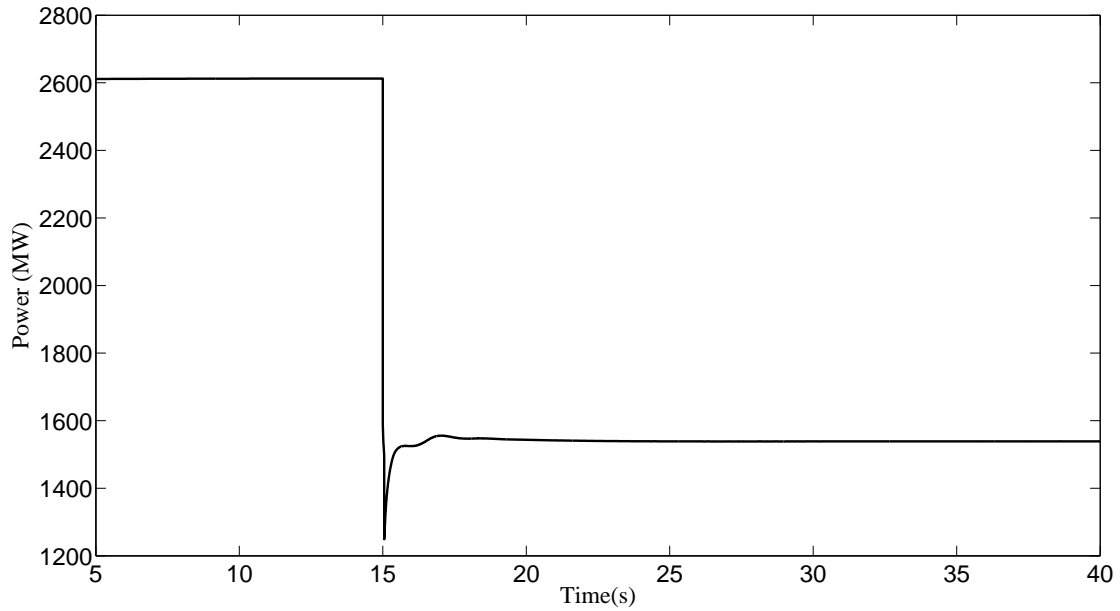


Figure 5.36: Active power flow from Arizona to Southern California with the opening of a tie line between Arizona and Southern California following a line fault

and 5.39. It can be seen from Figure 5.38 that the terminal voltage falls by 0.12pu almost instantaneously thereby reducing the active power produced at the terminals of the converter by around 50 MW as can be seen from Figure 5.37. However, from the increase

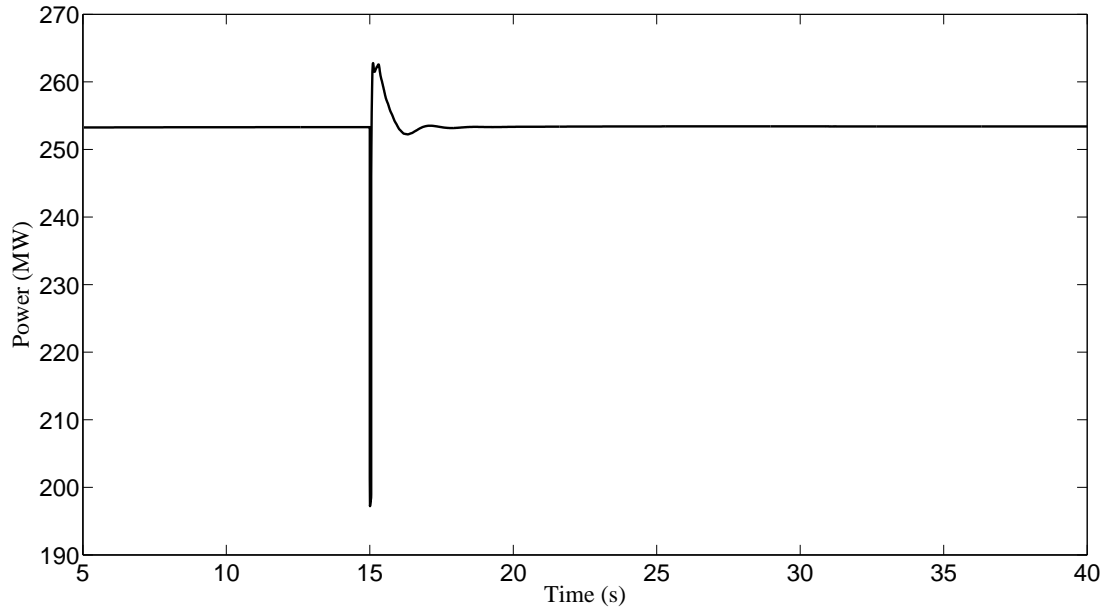


Figure 5.37: Active power of a Four Corner unit for a three phase bus fault near the unit

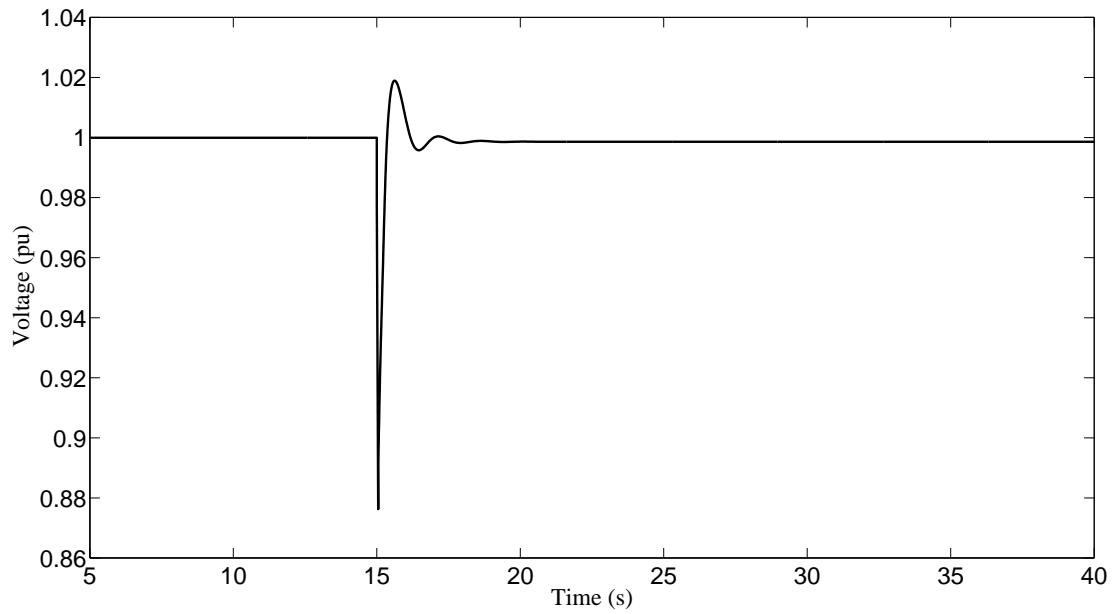


Figure 5.38: Terminal voltage of a Four Corner unit for a three phase bus fault near the unit

in current in Figure 5.39, it can be inferred that the reactive power produced increases to bring the voltage level back to 1.0pu within 3 seconds. The absence of an oscillatory mode for a fault close to a source is a significant observation that can be made from this scenario.

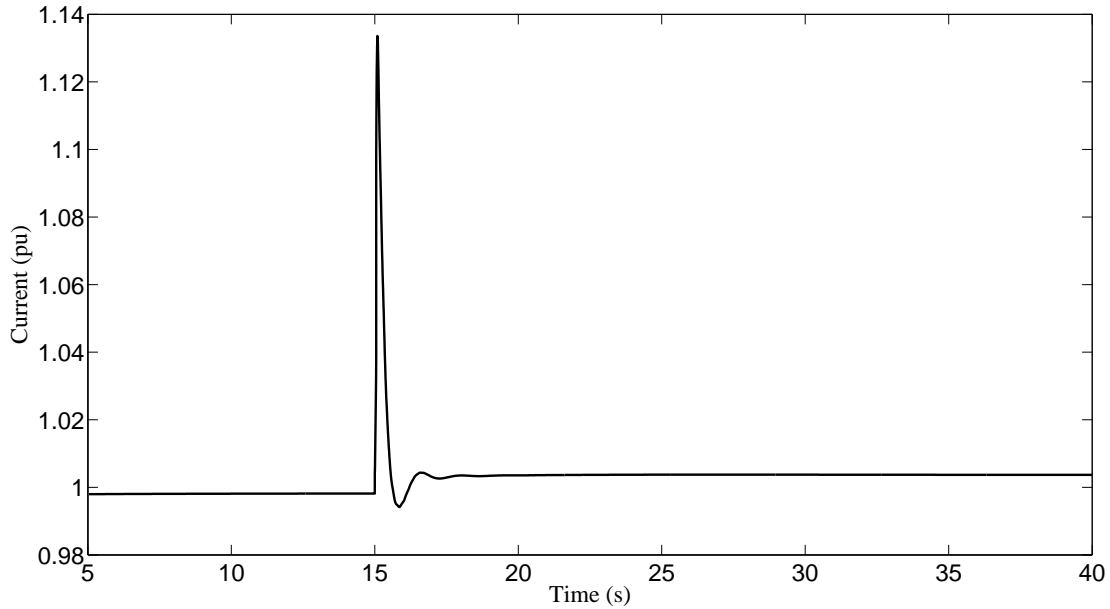


Figure 5.39: Current of a Four Corner unit for a three phase bus fault near the unit

5.4.5 Line Reconnection (100% CIG penetration)

To observe the effect of a line re-closure over large terminal bus voltage angles, the line between Moenkopi and Four Corners was initially outaged and the power flow was solved. This resulted in an angle difference of around 40 degrees between the buses. During the simulation, at $t = 15\text{s}$, the line was reclosed. The current of one of the Four Corners units, located near the line is as shown in Figure 5.40. It can be seen from the figure that the current rises to 1.5pu at the instant of re-closure but regains its pre-disturbance value within a second. The maximum value of current has been taken to be 1.7pu in this case. The current of another Four Corners unit located one bus away from this unit is as shown in Figure 5.41. It can be seen from the figures that the converters have no problem in dealing with the line re-closure and the performance is satisfactory. In order to observe the behavior with a lower current rating, the maximum current of the just the Four Corners units were set as 1.4pu. With this setting, the simulation was run once again. This time, due to the lower current setting and due to the overcurrent trip mechanism, the unit located closer to the line tripped while the remaining units took up the surplus power. This can be seen from the current of the Four Corners unit located one bus away as shown in Figure 5.42.

The total active power output from the Arizona area for both values of maximum current is as shown in Figure 5.43. From the figures, it can be seen that the system is capable

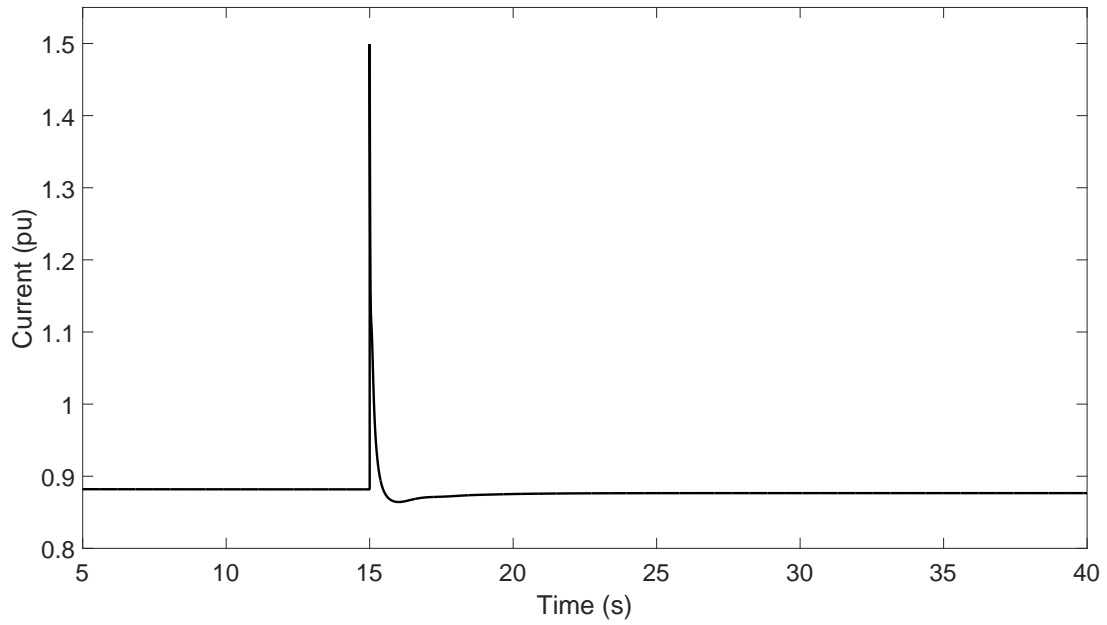


Figure 5.40: Current of a Four Corners unit for a line re-closure near the unit

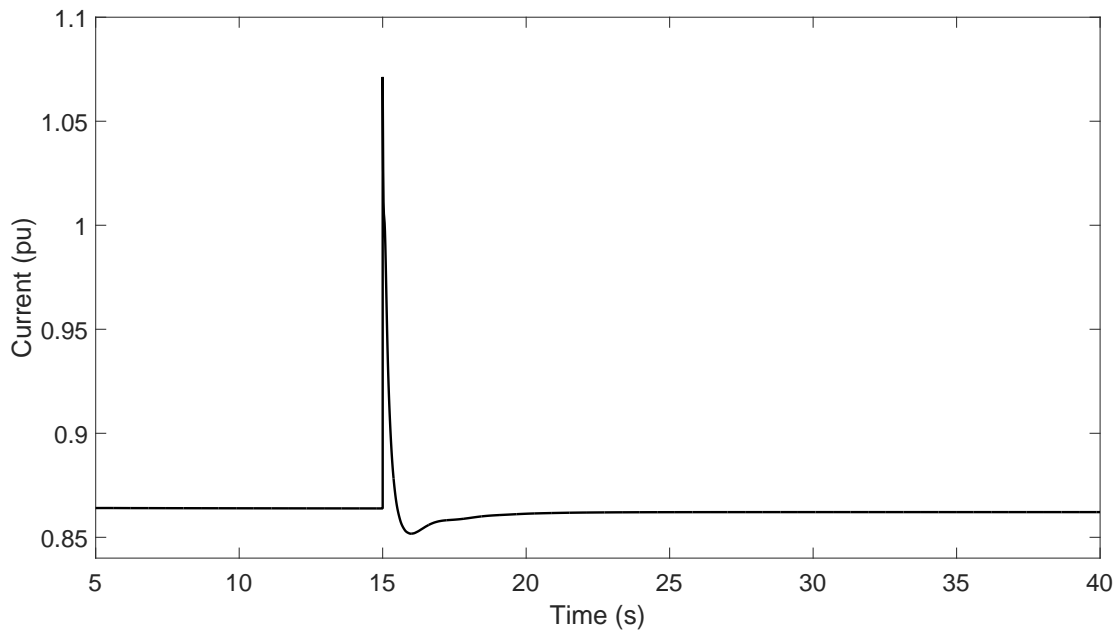


Figure 5.41: Current of a Four Corners unit located one bus away

of withstanding the re-closure of a large line. The results of this section show that the preliminary tests on the performance of an all CIG system are positive.

The next section describes the performance of the induction motor drive model

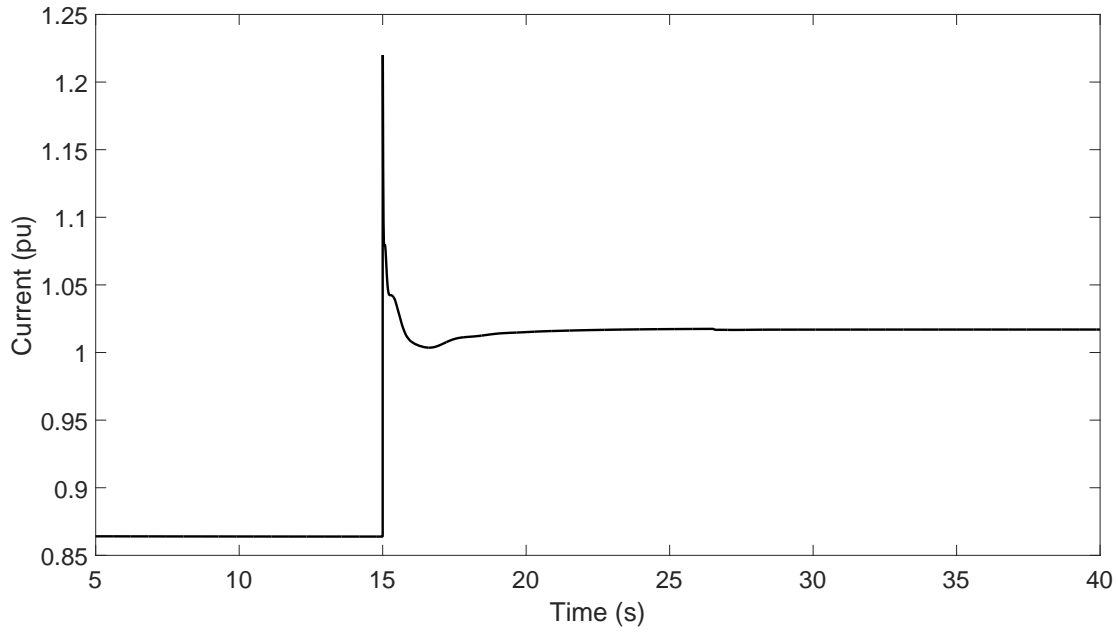


Figure 5.42: Current of a Four Corners unit located one bus away for lower maximum current

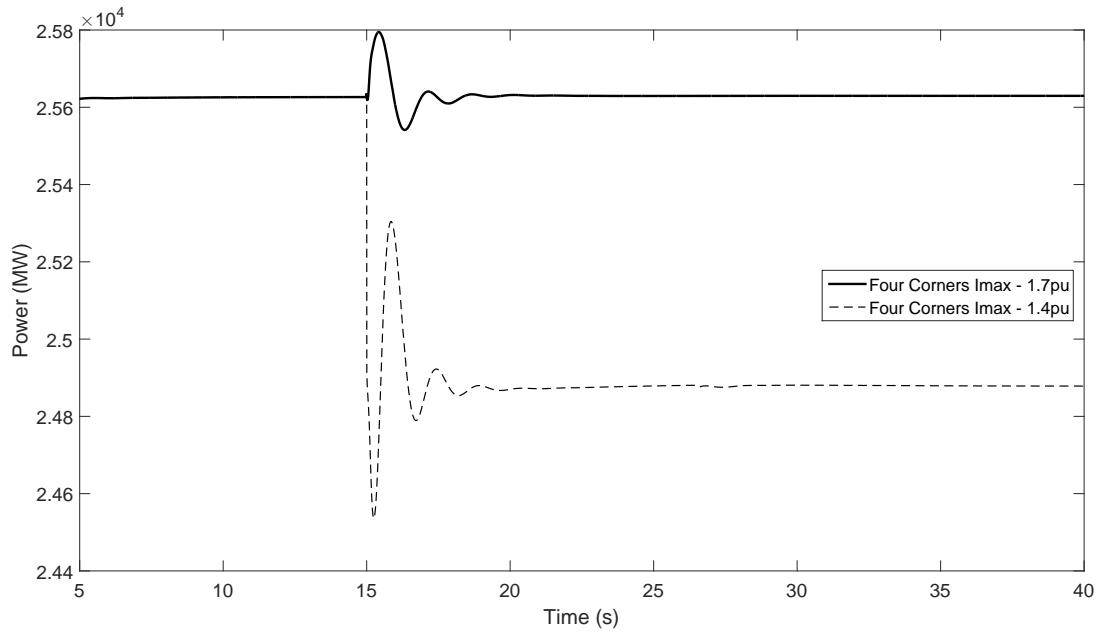


Figure 5.43: Total Arizona active power for line re-closure

5.5 Induction Motor Drive Model

The validation of the motor speed drive model was carried out in an independently developed, in-house C program capable of performing positive sequence time domain simulations. The network of Figure 5.6 was used as a test system and the static load at

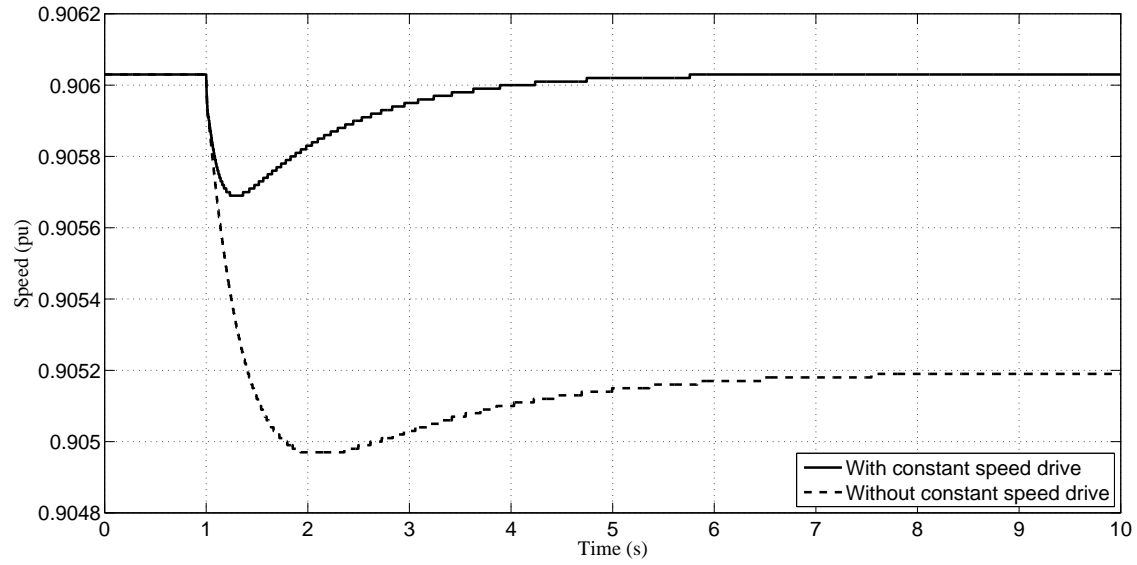


Figure 5.44: Speed of induction motor for both the presence and absence of a constant speed drive for a 10 MW load increase

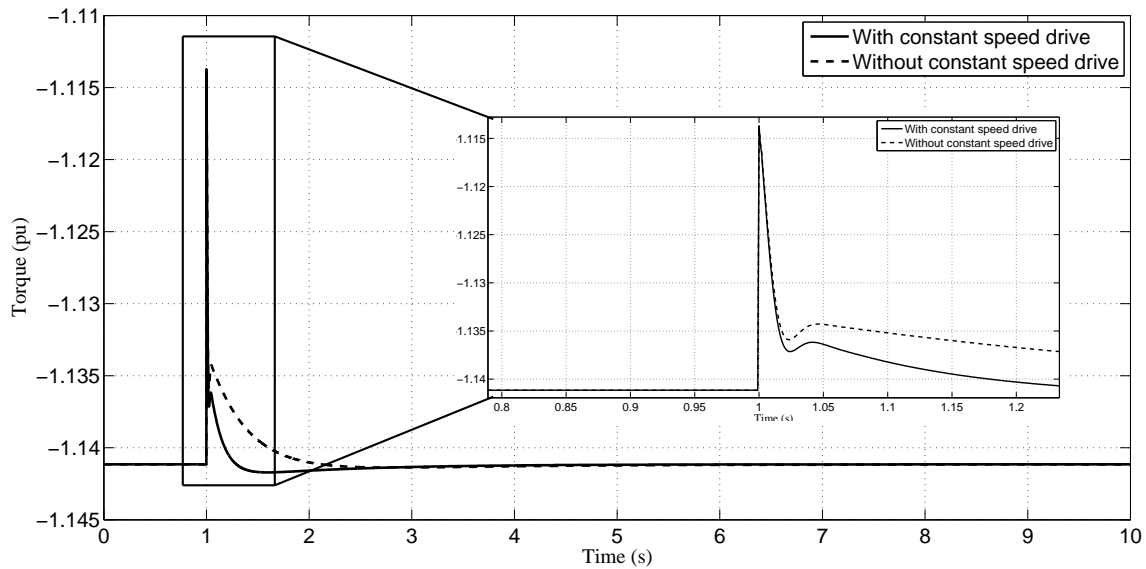


Figure 5.45: Load torque of induction motor for both the presence and absence of a constant speed drive for a 10 MW load increase

bus 5 was replaced by an induction motor with an inertia $H=1.2$ s. In order to obtain the value of slip and the reactive power consumed by the motor for a given active power load, the procedure of incorporating the equations of the motor into the Newton Raphson power flow algorithm as detailed in [54] was made use off.

For an active power load increase of 10 MW at bus 6 at $t=1$ s, Figure 5.44 shows the

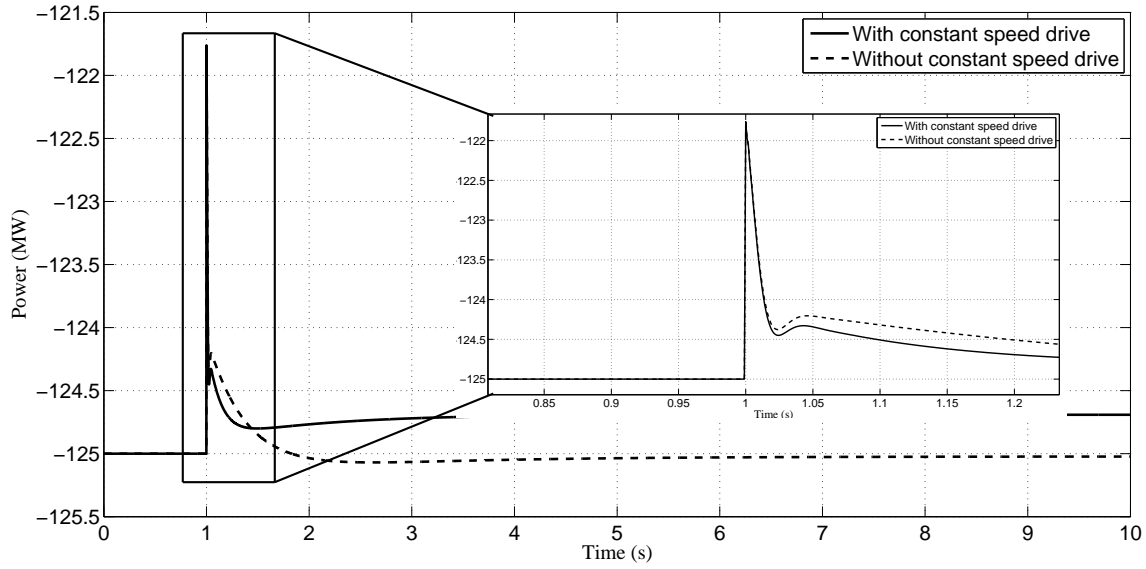


Figure 5.46: Active power consumed by induction motor for both the presence and absence of a constant speed drive for a 10 MW load increase

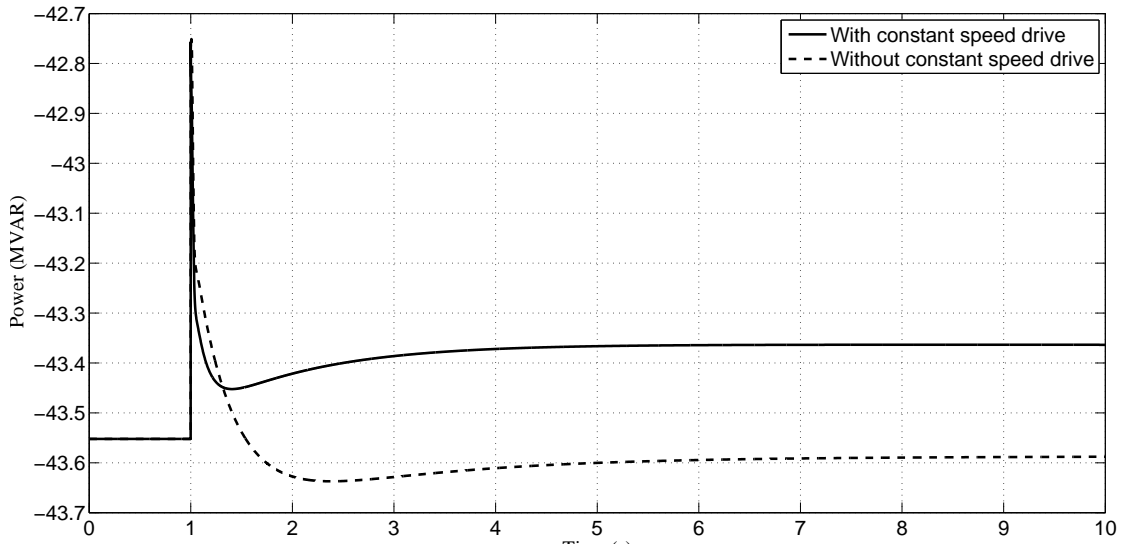


Figure 5.47: Reactive power consumed by induction motor for both the presence and absence of a constant speed drive for a 10 MW load increase

speed of the induction motor for both the presence and absence of the constant speed drive. The proportional and integral controller gains of the drive were 5.0 and 4.0 respectively. It can be seen that the positive sequence constant speed drive model is able to maintain the speed of the motor at the pre-contingency value. The load torque on the motor is shown in Figure 5.45.

The negative value indicates that it is a load on the system. As the load on the induction motor has not changed, the load torque is expected to remain the same and it can be seen that is the case. However, due to the change in speed, the electrical power drawn by the motor from the network would have changed to maintain the same level of torque. This can be seen from Figures 5.46 and 5.47 wherein the active and reactive power consumed by the motor is shown.

When a motor is enabled with a constant speed drive, the active power consumed reduces as the speed is maintained at a higher value when compared to the drop in speed without a drive. A load increase in the system reduces the voltage magnitude at all uncontrolled buses in the system and this causes the speed of the motor to drop. However, when the motor is enabled with a constant speed drive, the speed is maintained by ensuring that the flux in the air gap remains constant. Thus, if the terminal voltage drops, then the frequency of the inverter output is also reduced to maintain the value of flux thereby maintaining the speed.

6. Conclusion and Future Research

The future grid will be served by sources of energy whose characteristics will be decoupled from the network due to the presence of an interface converter. For the scope of this project, these sources are known as converter interfaced generation (CIG). With an increasing penetration of such sources, the behavior of the bulk power system has been analyzed. To do this, reliable models for the converter and its control were developed for use in commercial grade software to showcase the complex interactions of these models with one another.

The goals achieved by this research work are listed as below:

1. A reliable converter model based on the voltage source representation of the converter was developed by using an electromagnetic transient level model of the converter as a basis.
2. A straightforward control structure for the converter was developed.
3. The converter model and its associated control was incorporated into the commercial software PSLF using 'user written models' after being tested on an independently developed, in-house C code capable of performing positive sequence time domain simulations on small test systems.
4. The greater accuracy of the voltage source representation of the converter over the boundary current injection representation was showcased.
5. The behavior of the large WECC system with all converter interfaced sources was analyzed under various contingent situations and the behavior was found to be largely satisfactory with the converters contributing to both frequency regulation and reactive power support.
6. A positive sequence model for an induction motor speed control drive was developed and its performance was observed in a small all CIG test system.

During the course of this research work, new questions were raised which can lead to avenues for future research work such as:

1. When the dc voltage of the inverter dropped by more than 1% upon the occurrence of a contingency, widespread tripping of induction motors due to undervoltage and

converters due to overcurrent occurred. It is possible that a well coordinated wide area control strategy could increase the system reliability by bringing voltage support units online quickly.

2. As a planning problem, a capacitor of appropriate size will have to be placed on the dc bus to reduce the voltage drop. Further, it is possible that different locations in the system can withstand different amounts of drop in voltage on the dc bus. This problem would have to be analyzed and addressed.
3. Until now, the source behind the inverter has not been modeled. However, it is important to model these sources as the recovery of the dc side voltage depends on the characteristics and control of the source. Development of a complete positive sequence model of the source and its associated converter for use in commercial time domain simulation software is the need of the hour.
4. For large systems, a robust analytical tuning procedure of the controller gains is required. This would ensure the maximum utilization of the converter bandwidth and bring about a healthy system operation.
5. Currently, the stress on the blades of a steam turbine determines the operating frequency range of the system. With an all CIG system, an optimal frequency range is yet to be determined.
6. The behavior of induction motors and their associated drive mechanism has been tested only on a small system. Their behavior and interaction with CIG in a large system is yet to be seen.

References

- [1] “Electricity in the United States,” U.S. Energy Information Administration, April 10, 2013, [Online]: http://www.eia.gov/energyexplained/index.cfm?page=electricity_in_the_united_states [Accessed: August 10, 2014].
- [2] K. Clark, N. W. Miller, and R. Walling, “Modeling of GE solar photovoltaic plants for grid studies,” GE Energy, Tech. Rep. 1.1, April 2010.
- [3] N. W. Miller, W. W. Price, and J. J. Sanchez-Gasca, “Dynamic modeling of ge 1.5 and 3.6 wind turbine-generators,” GE Power Systems, Tech. Rep. 3.0, October 2003.
- [4] *PSLF User’s Manual*, General Electric International, Inc., 2013.
- [5] “Associated material for 2012 HS4A approved operating case,” Western Electricity Coordinating Council, January 2012.
- [6] I. Kolesnikov, “World reserves of fossil fuels,” 2013, [Online]: <http://knoema.com/smsfgud/world-reserves-of-fossil-fuels> [Accessed: August 10, 2014].
- [7] S. Shafiee and E. Topal, “When will fossil fuel reserves be diminished?” *Energy Policy*, vol. 37, no. 1, pp. 181 – 189, 2009.
- [8] A. Breidthardt, “German government want nuclear exit by 2022 at latest,” Reuters, May 30, 2011, [Online]: <http://uk.reuters.com/article/2011/05/30/us-germany-nuclear-idUKTRE74Q2P120110530> [Accessed: August 10, 2014].
- [9] “Nuclear power: When the steam clears,” *The Economist*, March 24, 2011, [Online]: <http://www.economist.com/node/18441163> [Accessed: August 10, 2014].
- [10] J. Chandler, “Is this the end of the nuclear revival,” *The Sydney Morning Herald*, March 19, 2011, [Online]: <http://www.smh.com.au/environment/energy-smart/is-this-the-end-of-the-nuclear-revival-20110318-1c0i9.html> [Accessed: August 10, 2014].
- [11] D. Gautam, V. Vittal, and T. Harbour, “Impact of increased penetration of dfbg-based wind turbine generators on transient and small signal stability of power systems,” *IEEE Trans. Power Syst.*, vol. 24, no. 3, pp. 1426–1434, Aug 2009.

- [12] A. Azmy and I. Erlich, "Impact of distributed generation on the stability of electrical power system," in *2005 IEEE Power Engineering Society General Meeting*, June 2005, pp. 1056–1063.
- [13] H. Storm, "Static magnetic exciter for synchronous alternators," *Transactions of the American Institute of Electrical Engineers*, vol. 70, no. 1, pp. 1014–1017, July 1951.
- [14] L. M. Domeratzky, A. Rubenstein, and M. Temoshok, "A static excitation system for industrial and utility steam turbine-generators," *Transactions of the American Institute of Electrical Engineers Power Apparatus and Systems, Part III.*, vol. 80, no. 3, pp. 1072–1077, April 1961.
- [15] I. Report, "Proposed excitation system definitions for synchronous machines," *IEEE Trans. Power App. Syst.*, vol. PAS-88, no. 8, pp. 1248–1258, Aug 1969.
- [16] P. Kundur, *Power System Stability and Control*, N. Balu and M. Lauby, Eds. McGraw-Hill Education, 1994.
- [17] S. Mishra, D. Ramasubramanian, and P. Sekhar, "A seamless control methodology for a grid connected and isolated pv-diesel microgrid," *IEEE Trans. Power Syst.*, vol. 28, no. 4, pp. 4393–4404, Nov 2013.
- [18] H. Bevrani, A. Ghosh, and G. Ledwich, "Renewable energy sources and frequency regulation: survey and new perspectives," *IET Renewable Power Generation*, vol. 4, no. 5, pp. 438–457, September 2010.
- [19] R. de Almeida and J. Peças Lopes, "Participation of doubly fed induction wind generators in system frequency regulation," *IEEE Trans. Power Syst.*, vol. 22, no. 3, pp. 944–950, Aug 2007.
- [20] I. Erlich and M. Wilch, "Primary frequency control by wind turbines," in *2010 IEEE Power and Energy Society General Meeting*, July 2010, pp. 1–8.
- [21] J. F. Conroy and R. Watson, "Frequency response capability of full converter wind turbine generators in comparison to conventional generation," *IEEE Trans. Power Syst.*, vol. 23, no. 2, pp. 649–656, May 2008.
- [22] A. Attya and T. Hartkopf, "Control and quantification of kinetic energy released by wind farms during power system frequency drops," *IET Renewable Power Generation*, vol. 7, no. 3, pp. 210–224, May 2013.

- [23] T. Vandoorn, B. Meersman, J. De Kooning, and L. Vandevelde, "Transition from islanded to grid-connected mode of microgrids with voltage-based droop control," *IEEE Trans. Power Syst.*, vol. 28, no. 3, pp. 2545–2553, Aug 2013.
- [24] K. Vidyanandan and N. Senroy, "Primary frequency regulation by deloaded wind turbines using variable droop," *IEEE Trans. Power Syst.*, vol. 28, no. 2, pp. 837–846, May 2013.
- [25] R. Majumder, B. Chaudhuri, A. Ghosh, R. Majumder, G. Ledwich, and F. Zare, "Improvement of stability and load sharing in an autonomous microgrid using supplementary droop control loop," *IEEE Trans. Power Syst.*, vol. 25, no. 2, pp. 796–808, May 2010.
- [26] Y. A. R. I. Mohamed and E. El-Saadany, "Adaptive decentralized droop controller to preserve power sharing stability of paralleled inverters in distributed generation microgrids," *IEEE Trans. Power Electron.*, vol. 23, no. 6, pp. 2806–2816, Nov 2008.
- [27] E. Barklund, N. Pogaku, M. Prodanovic, C. Hernandez-Aramburo, and T. Green, "Energy management in autonomous microgrid using stability-constrained droop control of inverters," *IEEE Trans. Power Electron.*, vol. 23, no. 5, pp. 2346–2352, Sept 2008.
- [28] S. Ashabani and Y.-R. Mohamed, "General interface for power management of micro-grids using nonlinear cooperative droop control," *IEEE Trans. Power Syst.*, vol. 28, no. 3, pp. 2929–2941, Aug 2013.
- [29] G. Diaz, C. Gonzalez-Moran, J. Gomez-Aleixandre, and A. Diez, "Scheduling of droop coefficients for frequency and voltage regulation in isolated microgrids," *IEEE Trans. Power Syst.*, vol. 25, no. 1, pp. 489–496, Feb 2010.
- [30] H. Xin, Y. Liu, Z. Wang, D. Gan, and T. Yang, "A new frequency regulation strategy for photovoltaic systems without energy storage," *IEEE Trans. Sustain. Energy*, vol. 4, no. 4, pp. 985–993, Oct 2013.
- [31] W. Omran, M. Kazerani, and M. Salama, "Investigation of methods for reduction of power fluctuations generated from large grid-connected photovoltaic systems," *IEEE Trans. Energy Convers.*, vol. 26, no. 1, pp. 318–327, March 2011.

- [32] M. Datta, T. Senjyu, A. Yona, T. Funabashi, and C.-H. Kim, "A frequency-control approach by photovoltaic generator in a pv-diesel hybrid power system," *IEEE Trans. Energy Convers.*, vol. 26, no. 2, pp. 559–571, June 2011.
- [33] N. Kakimoto, S. Takayama, H. Satoh, and K. Nakamura, "Power modulation of photovoltaic generator for frequency control of power system," *IEEE Trans. Energy Convers.*, vol. 24, no. 4, pp. 943–949, Dec 2009.
- [34] M. Morjaria and D. Anichkov, "'Grid Friendly" utility-scale PV plants," White Paper, First Solar, Aug 2013.
- [35] M. A. Eltawil and Z. Zhao, "Grid-connected photovoltaic power systems: Technical and potential problemsa review," *Renewable and Sustainable Energy Reviews*, vol. 14, no. 1, pp. 112 – 129, January 2010.
- [36] E. Vittal, M. O'Malley, and A. Keane, "Rotor angle stability with high penetrations of wind generation," *IEEE Trans. Power Syst.*, vol. 27, no. 1, pp. 353–362, Feb 2012.
- [37] J. Slootweg and W. Kling, "Impacts of distributed generation on power system transient stability," in *2002 IEEE Power Engineering Society Summer Meeting*, vol. 2, July 2002, pp. 862–867.
- [38] R. Pearmine, Y. H. Song, and A. Chebbo, "Influence of wind turbine behaviour on the primary frequency control of the british transmission grid," *IET Renewable Power Generation*, vol. 1, no. 2, pp. 142–150, June 2007.
- [39] D. Gautam, L. Goel, R. Ayyanar, V. Vittal, and T. Harbour, "Control strategy to mitigate the impact of reduced inertia due to doubly fed induction generators on large power systems," *IEEE Trans. Power Syst.*, vol. 26, no. 1, pp. 214–224, Feb 2011.
- [40] S. Eftekharnajad, V. Vittal, G. Heydt, B. Keel, and J. Loehr, "Impact of increased penetration of photovoltaic generation on power systems," *IEEE Trans. Power Syst.*, vol. 28, no. 2, pp. 893–901, May 2013.
- [41] J. Quintero, V. Vittal, G. Heydt, and H. Zhang, "The impact of increased penetration of converter control-based generators on power system modes of oscillation," *IEEE Trans. Power Syst.*, vol. 29, no. 5, pp. 2248–2256, Sept 2014.

- [42] N. W. Miller, M. Shao, S. Pajic, and R. D'Aquila, "Western wind and solar integration study phase 3 - frequency response and transient stability," NREL, Tech. Rep. NREL Report No. SR-5D00-62906, Dec 2014.
- [43] N. Bottrell, M. Prodanovic, and T. Green, "Dynamic stability of a microgrid with an active load," *IEEE Trans. Power Electron.*, vol. 28, no. 11, pp. 5107–5119, Nov 2013.
- [44] P. Anderson and A. Fouad, *Power system control and stability*. IEEE Press, 2003.
- [45] J. M. Undrill, "Structure in the computation of power-system nonlinear dynamical response," *IEEE Trans. Power App. Syst.*, vol. PAS-88, no. 1, pp. 1–6, January 1969.
- [46] K. Clark, R. Walling, and N. Miller, "Solar photovoltaic (pv) plant models in pslf," in *2011 IEEE Power and Energy Society General Meeting*, July 2011, pp. 1–5.
- [47] A. Ghoshal and V. John, "Anti-windup schemes for proportional integral and proportional resonant controller," in *National Power Electronic Conference*, 2010.
- [48] "PLECS," Plexim Electrical Engineering Software, <http://www.plexim.com/home>.
- [49] S. Yang, Q. Lei, F. Peng, and Z. Qian, "A robust control scheme for grid-connected voltage-source inverters," *IEEE Trans. Ind. Electron.*, vol. 58, no. 1, pp. 202–212, Jan 2011.
- [50] "PSLF," GE Energy Consulting, <http://www.geenergyconsulting.com/practice-area/software-products/pslf>.
- [51] B. K. Bose, *Modern Power Electronics and AC Drives*. Prentice Hall PTR, 2002.
- [52] "Frequency response initiative report - the reliability role of frequency response," NERC, Tech. Rep., Oct 2012.
- [53] M. Seelig, "Impact of new generator circuit-breaker technologies on power plant availability and profitability," *Proceedings CEPSI*, 2000.
- [54] D. Ruiz-Vega, T. Asiain Olivares, and D. Olguin Salinas, "An approach to the initialization of dynamic induction motor models," *IEEE Trans. Power Syst.*, vol. 17, no. 3, pp. 747 – 751, Aug 2002.

Appendix A. EPCL Code for User Defined Converter Control Model

```

/* *****/
/* ***** epcgen model for converter along with associated control *****/
/* *****/

```

/ Model comments and data description*

This model depicts the converter as a voltage source and thus has xsrc as 0.05

Model Input Parameters

```

rsrc    0.0
xsrc    0.05
Tr      Voltage transducer time constant (sec)
Kp      Proportional Gain
Ki      Integral Gain
Kip     Integral Gain in active power loop
Klimit  Anti-windup gain
Rq      Q-V droop coefficient
TQ      Q time delay (sec)
Rp      P-f droop coefficient
Tg      Time constant (sec)
Tl      Lead time constant (sec)
T2      Lag time constant (sec)
TD      P time delay (sec)
Ted     Ed time delay (sec)
Teq     Eq time delay (sec)
MWcap   Maximum MW cap for the governor part of the converter
Pmax    Maximum Active power
Qmax    Maximum Reactive Power
Qmin    Minimum Reactive Power
dV      Voltage variation for trip
dt      Time for voltage variation
Imax    Max Current
Tfl     1.0 - indicates that governor is active
        0.0 - indicates that governor is not active

```

Sample Input dynamic data record:

```
epcgen Busno. "Bus Name" kV "id" : #9 mva=100.0 "convepc_v.p" 5.0 "rsrc" 0.004 "xsrc" 0.05 "Tr" 0.02...
```

****** End of comments */*

```

define INIT 2
define SORC 3
define ALGE 4
define RATE 5

```



```

define OUTP 7
define NETW 8

@mx = dypar[0].cmi
@k = model[@mx].k
@bus=model[@mx].bus
@mode = dypar[0].mode
@kgen = genbc[@k].kgen

switch (@mode)

case SORC:

    if (epcgen[@mx].er>0.)
@delat=arctan(epcgen[@mx].ei/epcgen[@mx].er)
    elseif (epcgen[@mx].er<0. and epcgen[@mx].ei>=0.)
        @delat=arctan(epcgen[@mx].ei/epcgen[@mx].er)+(1.570796327*2)
    elseif (epcgen[@mx].er<0. and epcgen[@mx].ei<0.)
        @delat=arctan(epcgen[@mx].ei/epcgen[@mx].er)-(1.570796327*2)
    elseif (epcgen[@mx].er=0. and epcgen[@mx].ei>0.)
        @delat=1.570796327
    elseif (epcgen[@mx].er=0. and epcgen[@mx].ei<0.)
        @delat=-1.570796327
    endif

    /* Using Vdc to get the required voltage */
    @E = sqrt((epcgen[@mx].s6*epcgen[@mx].s6)+(epcgen[@mx].s7*epcgen[@mx].s7))
    @Vdc = epcgen[@mx].v12

    /* dropping Vdc 0.02s after Paloverde trip
    if (dypar[0].time>=15.02 and dypar[0].time<=25.02)
        if (epcgen[@mx].Tfl=1.0)
            @drop=1.0/100
            @Vdc = ((dypar[0].time-15.02)*(1/10.0)*@drop*epcgen[@mx].v12)+((1.0-@drop)*epcgen[@mx].v12)
        endif
    endif */

    @VT = epcgen[@mx].v13
    @wst = 2*(22/7)*60*dypar[0].time
    @m = @E/@VT

    if (@m>1.0)
        @m=1.0
        /*logterm("Max modulation index at bus ",busd[@bus].extnum,"<")*/
    endif
    if (@m<0.4)
        @m=0.4
        /*logterm("Min modulation index at bus ",busd[@bus].extnum,"<")*/
    endif

    if (epcgen[@mx].s6>0.)

```

```

@delt1=arctan(epcgen[@mx].s7/epcgen[@mx].s6)
elseif (epcgen[@mx].s6<0. and epcgen[@mx].s7>=0.)
    @delt1=arctan(epcgen[@mx].s7/epcgen[@mx].s6)+(1.570796327*2)
elseif (epcgen[@mx].s6<0. and epcgen[@mx].s7<0.)
    @delt1=arctan(epcgen[@mx].s7/epcgen[@mx].s6)-(1.570796327*2)
elseif (epcgen[@mx].s6=0. and epcgen[@mx].s7>0.)
    @delt1=1.570796327
elseif (epcgen[@mx].s6=0. and epcgen[@mx].s7<0.)
    @delt1=-1.570796327
endif

@Va = 0.5*@m*@Vdc*cos((@wst)+@delt1)
@Vb = 0.5*@m*@Vdc*cos((@wst)+@delt1-2.094395102)
@Vc = 0.5*@m*@Vdc*cos((@wst)+@delt1+2.094395102)

@Ed = (2/3)*((@Va*cos(@wst))+(@Vb*cos(@wst-2.094395102))+(@Vc*cos(@wst+2.094395102)))
@Eq = (-2/3)*((@Va*sin(@wst))+(@Vb*sin(@wst-2.094395102))+(@Vc*sin(@wst+2.094395102)))

epcgen[@mx].angle= 1.570796327+ @delt

epcgen[@mx].ed=@Ed
epcgen[@mx].eq=@Eq

break

case NETW:

break

case ALGE:

break

case RATE:

@vmon = volt[@bus].vm

@mibase = gens[@kgen].mibase

/* Setting of the limits */

@x=epcgen[@mx].Imax

@Qmax1=epcgen[@mx].Qmax
@Qmax2=sqrt(pow((@x*@mibase),2)/1.19047) /* 0.4 power factor */
@deninv=2.0

if (@vmon>0.8)
    @qmax=@Qmax1-((@Qmax2-@Qmax1)*(@vmon-1.0)*4.0) /* Qmax according to voltage */
else

```

```

        @qmax=@Qmax1-((@Qmax2-@Qmax1)*(0.8-1.0)*4.0)    /*Qmax according to voltage*/
    endif
    @qmin=epcgen[@mx].Qmin
    @lim=pow((@x*@mvabase),2)-pow(@qmax,2)
    if (@lim<0.0)
        @qmax=0.9*@x*@mvabase
        @lim=pow((@x*@mvabase),2)-pow(@qmax,2)
    endif
    @pmax=sqrt(@lim)    /* to preserve the MVA*/

    /* Voltage Transducer */

    epcgen[@mx].ds1 = (@vmon-epcgen[@mx].s1)/epcgen[@mx].Tr

    @verr = genbc[@k].vref-epcgen[@mx].s1-(epcgen[@mx].Rq*gens[@kgen].qgen/@mvabase)

    /* PI Block */

    epcgen[@mx].ds0 = epcgen[@mx].Ki*(@verr-(epcgen[@mx].Klimit*epcgen[@mx].v3))
    @prop = epcgen[@mx].Kp*@verr

    @Qcmd = @prop+epcgen[@mx].s0

    @a=@Qcmd
    if ((@Qcmd*@mvabase)>@qmax)
        @Qcmd=@qmax/@mvabase
    endif

    if ((@Qcmd*@mvabase)<@qmin)
        @Qcmd=@qmin/@mvabase
    endif
    epcgen[@mx].v3=@a-@Qcmd

    @Iqcmd = -@Qcmd/epcgen[@mx].s1

    /* Q time delay */

    epcgen[@mx].ds4 = (@Iqcmd-epcgen[@mx].s4)/epcgen[@mx].TQ

    /* Governor time constant */

    @perr = genbc[@k].pref-(netw[@bus].f/(1.0*epcgen[@mx].Rp))
    epcgen[@mx].ds2 = (@perr-epcgen[@mx].s2)/epcgen[@mx].Tg

    /* Lead lag block */

    epcgen[@mx].ds3 = (epcgen[@mx].s2-epcgen[@mx].s3-(epcgen[@mx].s2*epcgen[@mx].T1/epcgen[@mx].T2))
        / epcgen[@mx].T2

    @Pcmd = (epcgen[@mx].s3+(epcgen[@mx].s2*epcgen[@mx].T1/epcgen[@mx].T2))*epcgen[@mx].MWcap/@mvabase

```

```

    if ((@Pcmd*@mvabase)>@pmax)
        @Pcmd=@pmax/@mvabase
    endif

    if (epcgen[@mx].Tfl=0.0)
        @Pcmd=genbc[@k].pref*epcgen[@mx].MWcap/@mvabase
    endif

    @Ipcmd = (@Pcmd/epcgen[@mx].s1)+epcgen[@mx].s8

    /* P time delay */

    epcgen[@mx].ds5 = (@Ipcmd-epcgen[@mx].s5)/epcgen[@mx].TD

    /* Calculating the inner voltage */

    if (epcgen[@mx].er>0.)
        @delt=arctan(epcgen[@mx].ei/epcgen[@mx].er)
    elseif (epcgen[@mx].er<0. and epcgen[@mx].ei>=0.)
        @delt=arctan(epcgen[@mx].ei/epcgen[@mx].er)+(1.570796327*2)
    elseif (epcgen[@mx].er<0. and epcgen[@mx].ei<0.)
        @delt=arctan(epcgen[@mx].ei/epcgen[@mx].er)-(1.570796327*2)
    elseif (epcgen[@mx].er=0. and epcgen[@mx].ei>0.)
        @delt=1.570796327
    elseif (epcgen[@mx].er=0. and epcgen[@mx].ei<0.)
        @delt=-1.570796327
    endif

    @vq=(-epcgen[@mx].er*sin(@delt))+(epcgen[@mx].ei*cos(@delt))
    @vd=(epcgen[@mx].er*cos(@delt))+(epcgen[@mx].ei*sin(@delt))

    @iq=epcgen[@mx].s4
    @id=epcgen[@mx].s5

    @ed=@vd+(@id*epcgen[@mx].rsrc)-(@iq*epcgen[@mx].xsrc)
    @eq=@vq+(@iq*epcgen[@mx].rsrc)+(@id*epcgen[@mx].xsrc)

    epcgen[@mx].ds6 = (@ed-epcgen[@mx].s6)/epcgen[@mx].Ted
    epcgen[@mx].ds7 = (@eq-epcgen[@mx].s7)/epcgen[@mx].Teq

    epcgen[@mx].ds8 = epcgen[@mx].Kip*(@Pcmd-(gens[@kgen].pgen/@mvabase))

    /* set variables for output file */
    epcgen[@mx].v0 = gens[@kgen].pgen
    epcgen[@mx].v1 = gens[@kgen].qgen
    epcgen[@mx].v2 = volt[@bus].vm

    /* remaining output variables */
    epcgen[@mx].v4=@Qcmd*@mvabase
    epcgen[@mx].v5=@Pcmd*@mvabase

```

```

epcgen[@mx].v6=@iq
epcgen[@mx].v7=@id
epcgen[@mx].v8=sqrt((epcgen[@mx].itr*epcgen[@mx].itr)+(epcgen[@mx].iti*epcgen[@mx].iti))
epcgen[@mx].v9=sqrt((@id*@id)+(@iq*@iq))

/* Setting the trip settings */
/* Overcurrent trip */

if (dypar[0].time>8.0)
if (epcgen[@mx].v8 > epcgen[@mx].Imax)
gens[@kgen].st=0
epcgen[@mx].v11=dypar[0].time
logterm("Tripping_converter_at_bus",busd[@bus].extnum,"_due_to_overcurrent<")
endif
endif

/* Over voltage trip */
if (dypar[0].time>8.0)
if ((@vmon-genbc[@k].vref)>epcgen[@mx].dV)
if(epcgen[@mx].v10=0.0)
epcgen[@mx].v10=dypar[0].time
/*logterm("Over voltage timer started at bus ",busd[@bus].extnum,"<")*/
endif
if ((dypar[0].time-epcgen[@mx].v10) > epcgen[@mx].dt)
gens[@kgen].st=0
logterm("Tripping_converter_at_bus",busd[@bus].extnum,"_due_to_overvoltage<")
endif
endif
endif

if ((@vmon-genbc[@k].vref)<epcgen[@mx].dV and epcgen[@mx].v10>0.0)
epcgen[@mx].v10=0.0
/*logterm("Over voltage timer reset at bus ",busd[@bus].extnum,"<") */
endif
endif

break

case INIT:

@mvabase = gens[@kgen].mbase
@pgen = gens[@kgen].pgen/@mvabase
@qgen = gens[@kgen].qgen/@mvabase

epcgen[@mx].s1 = volt[@bus].vm
genbc[@k].vref = epcgen[@mx].s1+(epcgen[@mx].Rq*@qgen)

epcgen[@mx].s0 = @qgen
@iqcmd = -@qgen/epcgen[@mx].s1
epcgen[@mx].s4 = @iqcmd
epcgen[@mx].v3=0.0

```

```

genbc[@k].pref = @pgen*@mvabase/epcgen[@mx].MWcap
epcgen[@mx].s2 = @pgen*@mvabase/epcgen[@mx].MWcap
epcgen[@mx].s3 = epcgen[@mx].s2*(1-(epcgen[@mx].T1/epcgen[@mx].T2))
@pcmd = @pgen
@ipcmd = @pcmd/epcgen[@mx].s1
epcgen[@mx].s5 = @ipcmd

/* Calculating the inner voltage */

if (epcgen[@mx].er > 0.)
@delt=arctan(epcgen[@mx].ei/epcgen[@mx].er)
elseif (epcgen[@mx].er < 0. and epcgen[@mx].ei >= 0.)
@delt=arctan(epcgen[@mx].ei/epcgen[@mx].er)+(1.570796327*2)
elseif (epcgen[@mx].er < 0. and epcgen[@mx].ei < 0.)
@delt=arctan(epcgen[@mx].ei/epcgen[@mx].er)-(1.570796327*2)
elseif (epcgen[@mx].er = 0. and epcgen[@mx].ei > 0.)
@delt=1.570796327
elseif (epcgen[@mx].er = 0. and epcgen[@mx].ei < 0.)
@delt=-1.570796327
endif

@vq=(-epcgen[@mx].er*sin(@delt))+(epcgen[@mx].ei*cos(@delt))
@vd=(epcgen[@mx].er*cos(@delt))+(epcgen[@mx].ei*sin(@delt))

@iq=epcgen[@mx].s4
@id=epcgen[@mx].s5

@ed=@vd+(@id*epcgen[@mx].rsrc)-(@iq*epcgen[@mx].xsrc)
@eq=@vq+(@iq*epcgen[@mx].rsrc)+(@id*epcgen[@mx].xsrc)

epcgen[@mx].s6 = @ed
epcgen[@mx].s7 = @eq

epcgen[@mx].s8 = 0.0

/* obtaining the value of dc link voltage */
@E = sqrt((@ed*@ed)+(@eq*@eq))
@VT = @E/0.6
@Vdc = @E/(0.5*0.6)

epcgen[@mx].v4=@qgen
if (epcgen[@mx].Tf1=0.0)
epcgen[@mx].v5=@pgen
else
epcgen[@mx].v5=@pgen
endif
epcgen[@mx].v6=@iq
epcgen[@mx].v7=@id
epcgen[@mx].v8=sqrt((epcgen[@mx].itr*epcgen[@mx].itr)+(epcgen[@mx].iti*epcgen[@mx].iti))
epcgen[@mx].v9=sqrt((@id*@id)+(@iq*@iq))
epcgen[@mx].v10=0.0

```

```

epcgen [@mx].v11=0.0

epcgen [@mx].v12=@Vdc
epcgen [@mx].v13=@VT

epcgen [@mx].ds0 = 0.0
epcgen [@mx].ds1 = 0.0
epcgen [@mx].ds2 = 0.0
epcgen [@mx].ds3 = 0.0
epcgen [@mx].ds4 = 0.0
epcgen [@mx].ds5 = 0.0
epcgen [@mx].ds6 = 0.0
epcgen [@mx].ds7 = 0.0
epcgen [@mx].ds8 = 0.0
epcgen [@mx].ds9 = 0.0

channel_head [0].type = "pg"
channel_head [0].cmin = 0.
channel_head [0].cmax = 150.0
channel_head [1].type = "qg"
channel_head [1].cmin = -50.0
channel_head [1].cmax = 50.0
channel_head [2].type = "vt"
channel_head [2].cmin = 0.
channel_head [2].cmax = 1.050
channel_head [3].type = "qwindup"
channel_head [3].cmin = 0.
channel_head [3].cmax = 1.050
channel_head [4].type = "qcmd"
channel_head [4].cmin = 0.
channel_head [4].cmax = 1.050
channel_head [5].type = "pcmd"
channel_head [5].cmin = 0.
channel_head [5].cmax = 1.050
channel_head [6].type = "iqcmd"
channel_head [6].cmin = 0.
channel_head [6].cmax = 1.050
channel_head [7].type = "ipcmd"
channel_head [7].cmin = 0.
channel_head [7].cmax = 1.050
channel_head [8].type = "Icurr"
channel_head [8].cmin = 0.
channel_head [8].cmax = 1.050
channel_head [9].type = "Icmd"
channel_head [9].cmin = 0.
channel_head [9].cmax = 1.050

break
case OUP:
break
endcase
end

```

Appendix B. Three Generator Equivalent System Data

B.1 Power flow solution

The power flow solution along with the power demand and generation at each bus is as tabulated in Table B.1.

Table B.1: Power Flow Solution for the three generator equivalent system

Bus Number	V(pu)	Ang(deg)	P_d (MW)	Q_d (MVAR)	P_g (MW)	Q_g (MVAR)
1	1.040	0.0	0.0	0.0	71.6	27.0
2	1.025	9.3	0.0	0.0	163.0	6.7
3	1.025	4.7	0.0	0.0	85.0	-10.9
4	1.026	-2.2	0.0	0.0	0.0	0.0
5	0.996	-4.0	125.0	50.0	0.0	0.0
6	1.013	-3.7	90.0	30.0	0.0	0.0
7	1.026	3.7	0.0	0.0	0.0	0.0
8	1.016	0.7	100.0	35.0	0.0	0.0
9	1.032	2.0	0.0	0.0	0.0	0.0

B.2 Dynamic data

The generator, exciter and governor data is as given as in Table B.2, B.3 and B.4 respectively. The reactances in the generator data are given in pu on a 100 MVA base while the time constants and the inertia constant are in seconds. The machine at bus 1 was modeled using the GENSAL model while the other two machines were modeled using the GEN-ROU models. A static exciter EXST1 was used on all machines while the governor model

Table B.2: Generator dynamic data for the three generator equivalent system

Bus Number	MVA	kV	x_d	x'_d	x_q	x'_q	x_ℓ	τ'_{d0}	τ'_{q0}	H
1	247.5	16.5	0.1460	0.0608	0.0969	0.0969	0.0336	8.96	0	23.64
2	192.0	18.0	0.8958	0.1198	0.8645	0.1969	0.0521	6.00	0.535	6.4
3	128.0	13.8	1.3125	0.1813	1.2578	0.25	0.0742	5.89	0.6	3.01

TGOV1 was used as a governor on all machines.

Table B.3: Exciter dynamic data for the three generator equivalent system

Bus Number	T_r	V_{imax}	V_{imin}	T_c	T_b	K_a	T_a	V_{rmax}	V_{rmin}	K_c	K_f	T_f	T_{c1}	T_{b1}	V_{amax}	V_{amin}	X_e	I_{lr}	K_{lr}
1	0.0	0.1	-0.1	1.0	10.0	200.0	0.02	5.0	-5.0	0.05	0.0	1.0	1.0	1.0	5.0	-5.0	0.04	2.8	5.0
2	0.0	0.1	-0.1	1.0	10.0	200.0	0.02	5.0	-5.0	0.05	0.0	1.0	1.0	1.0	5.0	-5.0	0.04	2.8	5.0
3	0.0	0.1	-0.1	1.0	10.0	200.0	0.02	5.0	-5.0	0.05	0.0	1.0	1.0	1.0	5.0	-5.0	0.04	2.8	5.0

Table B.4: Governor dynamic data for the three generator equivalent system

Bus Number	MWcap	R	T_1	V_{max}	V_{min}	T_2	T_3	D_t
1	247.5	0.05	0.5	1.0	0.01	1.0	10.0	0.0
2	192.0	0.05	0.5	1.0	0.01	1.0	10.0	0.0
3	128.0	0.05	0.5	1.0	0.01	1.0	10.0	0.0